The Deccan Plume : geochemistry, petrology coupled with high-resolution paleomagnetic data - geodynamical and environmental consequences at the K-Pg boundary

Karim Malamoud

UNIVERSITÉ DE GRENOBLE

THÈSE

Pour obtenir le grade de

DOCTEUR DE L'UNIVERSITÉ DE GRENOBLE

Spécialité : **Sciences de la Terre, de l'Univers, et de l'Environnement**

Arrêté ministériel : 7 août 2006

Présentée par

Karim Malamoud

Thèse dirigée par **Alexander V. Sobolev**

préparée au sein de **L'Institut des Sciences de la Terre de Grenoble (ISTerre)**
et de **l'Ecole Doctorales Terre, Univers, Environnement (TUE)**

Des Traps du Deccan à la Réunion : Couplage de données géochimiques, pétrologiques et paléomagnétiques – Conséquences géodynamiques à la limite Crétacé-Paléocène

Thèse soutenue publiquement le **29 Septembre 2014**
devant le jury composé de :

M, Dominique, Gasquet
Professeur, Université de Savoie, Président du jury
M, Andy, Saunders
Professeur, University of Leicester, Rapporteur
M, Mike, Widdowson
Professeur, The Open University, Rapporteur
M, Frédéric, Fluteau
Maître de Conférence, Institut de Physique du Globe de Paris, Examinateur
M, Nicholas, Arndt
Professeur, Université de Grenoble, Examinateur
M, Alexander V., Sobolev
Professeur, Université de Grenoble, Directeur de thèse

Université Joseph Fourier / Université Pierre Mendès France /
Université Stendhal / Université de Savoie / Grenoble INP

Université de Grenoble

Institut des Sciences de la Terre de Grenoble (ISTerre)

Thèse

présentée à

l'Université de Grenoble

pour obtenir le grade de

Docteur de l'Université de Grenoble

spécialité « Sciences de la Terre, de l'Univers, et de l'Environnement »

par

Karim Malamoud

Des Traps du Deccan à la Réunion : Couplage de données géochimiques, pétrologiques et paléomagnétiques – Conséquences géodynamiques à la limite Crétacé-Paléocène

Soutenance prévue le 29 Septembre 2014 devant un jury composé de :

M. Andy Saunders	Professeur, University of Leicester	(Rapporteur)
M. Mike Widdowson	Professeur, The Open University	(Rapporteur)
M. Frédéric Fluteau	Maître de conférence, IPGP Paris VI	(Examinateur)
M. Dominique Gasquet	Professeur, Université de Savoie	(Examinateur)
M. Nicholas T. Arndt	Professeur, Université de Grenoble	(Examinateur)
M. Alexander V. Sobolev	Professeur, Université de Grenoble	(Directeur de thèse)

Remerciements

Je tiens tout d'abord tout d'abord remercier mon directeur de thèse, Alexander V. Sobolev, pour m'avoir confié ce sujet et pour m'avoir encadré pendant ces trois années et demie.

Ma gratitude va à Stéphane Guillot, Jean Braun, Etienne Jaillard, Christine Bigot, Carole Cordier, Catherine Chauvel, Valentina Batanova, Valérie Magnin et l'ensemble de l'équipe Géochimie4D à ISTerre Grenoble, ainsi qu'à Olga et Dmitry Kuzmin à l'Institut Max Planck de Mayence, Allemagne, dont l'aide précieuse m'a permis d'achever ce travail.

Un grand merci également à Frédéric Fluteau de l'Institut de Physique du Globe de Paris et à Ivan Vlastelic de l'Université Blaise Pascal de Clermont Ferrand, pour m'avoir très généreusement confié les échantillons nécessaires à l'élaboration de mon travail.

Je remercie aussi Jacky Larnould et Lionel Cachoulet de JEOL Europe SAS pour le partage de leurs expériences et de leurs connaissances en microscopie électronique.

Je tiens à remercier les membres du jury, Andy Saunders, Mike Widdowson, Nicholas Arndt, Frédéric Fluteau et Dominique Gasquet, pour m'avoir aidé à améliorer ce travail en acceptant de l'évaluer.

Je souhaite vivement adresser mes remerciements les plus chaleureux à tous ceux qui m'ont encouragé et soutenu durant ces trois années et demi : ma famille, mes amis, dont ceux des autres bouts du monde, et bien sûr Anne-Sophie.

Mes remerciements vont enfin à mes collègues de promo, amis, anciens et récents. Pour moi, ces six années grenobloises, depuis le master, même si je n'ai pas été aussi présent que je le souhaitais, c'était vous. Merci pour ces moments précieux et inoubliables, parfois trop rares mais toujours chaleureux, passés en votre compagnie. Je ne les oublierai pas. Je vous souhaite la meilleure des chances. Merci.

En contribuant ainsi à l'étude pétrologique et géochimique des provinces magmatiques et de la Terre interne, j'espère que cette thèse saura apporter quelque(s) pierre(s) à l'édifice de la connaissance de ce domaine des sciences de la Terre.

Karim, le 4/08/2014

Longtemps, j'ai voulu être breton. Longtemps, j'ai voulu être corse, ou basque ou serbe ou bosniaque ou tchétchène. Avoir une origine forte, une identité forte. Etre quelque chose, être lié à une terre, un terroir, avoir des racines. Très important les racines… Et puis un jour j'ai trouvé un petit vers de Bertolt Brecht qui disait « Je n'ai pas de racines, j'ai des jambes »
Daniel Mermet 23/01/2014

R é s u m é

Les Traps du Deccan (70/67-65Ma) (Courtillot *et al.*, 1986, Basu *et al.*, 1993, Chenet *et al.*, 2007), les Seychelles 65-62 Ma (Collier *et al.*, 2008) et les iles Mascareignes 60-0 Ma (Mahoney *et al.*, 2002, Murthy, 2002) sont interprétées comme faisant partie d'une série magmatique représentant l'évolution complète d'un panache mantellique, depuis un stade initial, sous une lithosphère continentale – en l'occurrence celle de l'Inde à la fin du Crétacé – jusqu'à un stade final, sous une lithosphère océanique (iles Mascareignes) (Duncan, 1990). L'importance de l'étude des provinces magmatiques telles que celle des Trappes du Deccan, est de deux ordres. D'une part, il y a toujours débat quant aux processus magmatiques capables de générer de l'ordre d'un million de kilomètres cubes de laves en un temps très court (typiquement, moins d'un million d'années) (Anderson, 1994, 2000a, Courtillot *et al.*, 2003, Foulger *et al.*, 2005, Sheth, 2005, 2007, Sobolev *et al.*, 2011). D'autre part, si les éruptions de provinces magmatiques ont été corrélées aux phénomènes d'extinctions de masses aux cours des temps géologiques, les processus par lesquels ces éruptions ont contribué – ou déclenché – de tels évènements ne sont, à ce jour, toujours pas clairement établis (Wignall, 2001, Courtillot & Renne, 2003, Saunders, 2005).

Cette thèse s'appuie sur de précédents travaux par le groupe de travail d'Alexander V. Sobolev sur le recyclage de matériel crustal dans le manteau terrestre en lien avec les processus de mise en place des provinces magmatiques et des iles océaniques (Sobolev *et al.*, 2005, 2007, 2011). Il s'agit d'utiliser des outils pétrologiques et géochimiques (Sobolev *et al.*, 2005, 2007) couplés à des données de paléomagnétisme haute résolution (Chenet *et al.*, 2008, 2009), et à de la modélisation thermomécanique (Sobolev *et al.*, 2011) dans le but de contraindre les processus profonds à l'origine des Traps du Deccan et leurs conséquences au niveau planétaire (extinction de masse).

A plus long terme, une comparaison précise des données relatives aux conséquences environnementales des Traps du Deccan, avec celles correspondant à l'impacte de la météorite de Chicxulub (Alvarez *et al.*, 1980, Schulte *et al.*, 2010), devrait permettre de conclure quant à la contribution respective de ces deux évènements à l'extinction de masse de la fin de Crétacé.

Dans un premier temps, cette thèse propose une réinterprétation des diverses contraintes temporelles sur la durée de l'éruption des Traps du Deccan (datations radiochronologiques, paleomagnétisme, profiles d'altérations, et données paléo-environnementales) et suggère un scénario temporel pour la mise en place de cette province magmatique, le tout principalement

basé sur des données paléomagnétiques de hautes résolution de Chenet et al (2008, 2009). Ce scénario implique que la phase principale de l'éruption des Traps du Deccan s'est produite peu de temps avant la limite Crétacé-Paléogène (Chenet *et al.*, 2007, Keller *et al.*, 2008a, 2012) et qu'elle correspond à la mise en place d'environ $1.10^6 km^3$ de laves en 50ka. Ces chiffres sont équivalents à 150-200 fois le taux d'éruption actuel de l'ile volcanique d'Hawaii (Courtillot *et al.*, 1986).

Ce scénario temporel a ensuite été couplé à des données géochimiques élémentaires qui ont permis de mettre en évidence plusieurs caractéristiques particulières de la composition des laves des Traps du Deccan (Western Ghats). D'abord, les laves des Western Ghats portent une forte signature du grenat (appauvrissement en terres rares lourdes), ce qui indique une origine profonde pour la grande majorité des liquides primaires. Ensuite, ces laves peuvent être globalement divisées en deux catégories, principalement fondées sur l'intensité de l'assimilation crustale qu'elles ont endurée. Cette classification est, dans l'ensemble, comparable aux différences entre « lower formations » et « upper formations » visibles dans les diagrammes isotopiques (Peng *et al.*, 1994). Une observation plus poussée de l'évolution des éléments traces au cours du temps révèle l'existence de plusieurs excursions de courte durée vers des valeurs compatibles avec une très forte assimilation crustale et une absence de signature du grenat. Ces excursions se sont produites juste avant la limite Crétacé-Paléogène et n'ont, d'après notre scénario temporel, pas duré plus de 10-20ka chacune. Il est probable que ces phénomènes correspondent à un unique épisode d'érosion lithosphérique de la plaque indienne par les processus magmatiques dans le manteau sous-jacent. Cette proposition est en accord avec les variations d'épaisseur actuelles de la plaque indienne. Enfin, il est très probable que ces épisodes d'intense assimilation crustale coïncident avec un dégazage magmatique important qu'il serait important de contraindre afin de mieux quantifier le dégazage global lié aux Trappes du Deccan.

Les données relatives aux Traps du Deccan peuvent être comparées à celles des Traps de Sibérie et révèlent d'importantes différences géodynamiques. Il apparaît notamment que l'importante érosion lithosphérique identifiée dans les Traps de Sibérie (Sobolev *et al.*, 2011) n'ait pas eu lieu dans le cas des Traps du Deccan malgré des caractéristiques mantelliques similaires. Cette différence peut être attribuée à la plus grande épaisseur de la plaque indienne, ainsi qu'à l'existence de zones de faiblesses, liées à l'héritage tectonique du bouclier

indien (Murthy, 2002, Biwas, 2005). Ces zones de faiblesses auraient facilité le passage des magmas à travers la plaque de manière à ce qu'une faible proportion d'entre eux seulement ait été impliquée dans les processus de délamination lithosphérique.

Un ensemble de données géochimiques sur olivine ainsi que de modélisation des liquides magmatiques primaires et de leur source (Sobolev *et al.*, 2005, 2007) pour les Traps du Deccan nous ont permis de montrer 1) l'importante contribution d'une source pyroxenitique à la composition des liquide magmatiques primaires (65%), 2) que la gamme de températures potentielles de ces mêmes sources avait due être de l'ordre de 1600°C et 3) que ces dernières contenaient environ 15% de matériel crustal recyclé. Des mesures et calculs similaires appliquées aux laves de la Réunion ont, par ailleurs, montrés des résultats très différents : 50% de liquides pyroxenitiques dans les liquides magmatiques primaires, une température potentielle mantellique de l'ordre de 1500°C et une teneur des sources magmatiques en matériel crustal recyclé de l'ordre de 7%.
Ces résultats sont compatibles avec le modèle de panache mantellique pour la mise en place des provinces magmatiques et des iles océaniques (Morgan, 1971, White & McKenzie, 1989, Coffin & Eldholm, 1994, White & McKenzie, 1995, Courtillot *et al.*, 2003) ainsi qu'avec l'hypothèse du refroidissement séculaire de ces mêmes panaches (Herzberg & Gazel, 2009).

Nous en concluons que l'éruption des Traps du Deccan fut un événement d'une rapidité exceptionnelle et que son implication dans la crise biologique de la fin du Crétacé fut sans doute particulièrement importante. La mise en place des Traps du Deccan a été déclenchée par l'arrivée d'un large panache mantellique sous la lithosphère indienne. L'activité de ce panache mantellique a ensuite participé à la formation de la « Chagos-Laccadive ridge » et des iles Mascareignes. L'activité actuelle du panache du Deccan est localisée sous l'ile de la Réunion. L'épaisseur lithosphérique, relativement comparable à celle de la plaque indienne, permet une comparaison directe entre le stade initial (Deccan) et le stade final (Réunion) du panache du Deccan. Enfin, il apparaît que ce dernier s'est affaiblit (baisse de température d'environ 100°C) et nous en concluons que cette affaiblissement a pour conséquence une plus faible concentration en matériel crustal recyclé.

A b s t r a c t

The Deccan Traps – or Deccan Flood Basalts – 70/67-65Ma (Courtillot *et al.*, 1986, Basu *et al.*, 1993, Chenet *et al.*, 2007), Seychelles 65-62 Ma (Collier *et al.*, 2008) and Mascarene Islands 60-0 Ma (Mahoney *et al.*, 2002, Murthy, 2002) are believed to trace the evolution of a single mantle plume from its initial plume-head stage, under continental lithosphere (India in the Cretaceous and early Palaeogene), to the recent hot spot or ocean island (plume-tail) stage under oceanic lithosphere (Mascarene Islands) (Duncan, 1990). The relevance of Continental Flood Basalts (CFBs), or continental Large Igneous Provinces (LIPs), such as the Deccan Traps is twofold. Firstly, there is on-going debate on the processes capable of generating large volumes of lava (>1 million km^3) in a relatively short time (<1Ma) (Anderson, 1994, 2000a, Courtillot *et al.*, 2003, Foulger *et al.*, 2005, Sheth, 2005, 2007, Sobolev *et al.*, 2011). Secondly, the timing and occurrence of Continental Flood Basalts has been coincident with the mass extinctions of species throughout the history of our planet. There are suggestions that the eruptions of CFBs might have contributed to, or induced such tragedies, however the mechanism for such extinctions has not yet been fully clarified (Wignall, 2001, Courtillot & Renne, 2003, Saunders, 2005). This PhD aims to build on the previous work by Alexander V. Sobolev and colleagues on crustal recycling within the Earth mantle and LIPs/ocean island magmatism (Sobolev *et al.*, 2005, 2007, 2011). The PhD focus will be to apply petrology and geochemistry (Sobolev *et al.*, 2005, 2007) coupled with high-resolution paleomagnetism (Chenet *et al.*, 2008, 2009), and thermo-mechanical modelling (Sobolev *et al.*, 2011) in order to constrain the deep processes behind the Deccan Traps (mantle melting and crustal recycling) as well as the consequences at the surface of the Earth (eruption rates and related degassing). This analysis should provide an idea of the intensity of the Deccan Traps eruption at the Cretaceous-Palaeogene boundary. The environmental consequences that would result from eruptions of this magnitude can be contrasted with the speculated environmental consequences of the Chicxulub impact (Alvarez *et al.*, 1980, Schulte *et al.*, 2010) to make inferences at the respective contribution of the two catastrophic events to the mass extinctions of the end-Cretaceous.

Upon revisiting published time constraints on the Deccan eruptions (radiometric dating, paleomagnetism, inter-flow weathering profiles and paleoenvironmental data), we propose a new, paleomagnetism-based (Chenet *et al.*, 2008, 2009) eruption scenario for the Main Deccan Province (Western Ghats). We suggest that the main phase of volcanic activity occurred just before and ended at the Cretaceous-Palaeogene boundary (Chenet *et al.*, 2007,

Keller *et al.*, 2008a, 2012) and was responsible for the emplacement of about $1.10^6 km^3$ of lavas in ~50kyr. This is equivalent to 150 to 200 times present-day eruption rates in Hawaii (Courtillot *et al.*, 1986).

Coupling of the paleomagnetism-based timeframe with bulk-rock trace element concentrations revealed that Western Ghats lavas feature a strong garnet signature (Heavy Rare Earth Element depletion), indicative of a deep origin. These lavas have two different trace element signatures that correspond to differences in the intensity of crustal assimilation undergone by their rising melts. This classification resembles the general trend between upper and lower formations seen on radiogenic isotope diagrams (Peng *et al.*, 1994). A closer look at the variations of trace element proxies for garnet signature and crustal assimilation through time reveals several transient excursions of combined strong crustal assimilation and absence of the garnet signature. These excursions occurred before the Cretaceous-Palaeogene boundary and are not believed to have lasted more than 10-20ka each. We suggest that these excursions are part of a single and localized plume-induced lithospheric erosion event of the Indian lithosphere by the Deccan plume. This observation is in agreement with present-day estimates for the thickness of the Indian lithosphere. The probability that these short-lived severe crustal assimilation events coincided with catastrophic magmatic degassing is very likely and should be investigated in detail.

A comparison of the Deccan Traps with the Siberian Traps exposes significant geodynamical differences. Most notably, the widespread and extensive lithospheric erosion observed in the Siberian Traps (Sobolev *et al.*, 2011) did not take place in the Deccan Traps, despite similar mantle characteristics. This difference is attributed to 1) a thicker Indian lithosphere and 2) to the existence of weaknesses in the form of pre-existing structural lineaments (Murthy, 2002, Biwas, 2005). These pre-existing structures facilitated the passage of deep mantle-derived magmas and thus precluded or limited their involvement in a freezing-delamination process.

Olivine geochemistry and olivine-based primary melt and source modelling (Sobolev *et al.*, 2005, 2007) in Deccan Traps lavas showed 1) large contributions of pyroxenite-derived melts (65%) to the primary melts, 2) high potential temperatures of the mantle sources (~1590-1600°C) and 3) that the mantle sources of Deccan Traps magmas contained ~15% of recycled crustal material. These observations contrast with those obtained from Réunion Island lavas

(50% of pyroxenite-derived melts, mantle potential temperatures of 1490-1500°C and 7% of recycled crustal material in the sources of Réunion Island magmas.
Our results are compatible with the plume model for LIPs and ocean island magmatism (Morgan, 1971, White & McKenzie, 1989, Coffin & Eldholm, 1994, White & McKenzie, 1995, Courtillot *et al.*, 2003) as well as with a secular cooling of mantle plumes (Herzberg & Gazel, 2009).

We conclude, along with many authors, that the emplacement of the Deccan Traps was a remarkably swift and catastrophic event at the end of the Cretaceous and that it likely played a significant role in the end-Cretaceous mass extinction. These eruptions have been triggered by the arrival of a large hot and enriched plume-head at the base of the India lithosphere, carrying large amounts of recycled crustal material. Subsequent activity of the Deccan plume resulted in the Chagos-Laccadive ridge, the Mascarene Plateau and Islands. The present manifestation of the plume at Réunion Island occurs at a comparable depth, which allows direct comparison with its passed activity in India. The plume has become significantly cooler (plume-tail). We speculate that the lower concentrations of recycled crustal material measured for the sources of Réunion Island lavas are a consequence of the colder temperatures of the final, ocean-island stage of the Deccan plume.

Table of contents

1. INTRODUCTION 17

1.1. LARGE IGNEOUS PROVINCES AND THE PLUME MODEL 18
1.2. LIPS, MASS EXTINCTIONS AND THE DECCAN CASE 22
1.3. THE DECCAN TRAPS, CHICXULUB, AND THE END-CRETACEOUS EXTINCTION – AN ATTEMPT FOR RECONCILIATION 26
1.4. LAYOUT AND GOALS OF THE PHD PROJECT 30

2. GEOLOGICAL SETTING 33

2.1. INDIA IN THE LATE CRETACEOUS 34
2.2. THE STRUCTURE AND GEOLOGICAL UNITS OF THE INDIAN PLATE 35
2.3. THE STRATIGRAPHY OF THE DECCAN TRAPS 36
2.3.1. THE MAIN DECCAN PROVINCE, THE WESTERN GHATS AND RELATED OUTCROPS 37
2.3.2. PERIPHERAL DECCAN VOLCANISM AND MINOR FORMATIONS 41
2.3.2.1. Kutch and Saurashtra (Gujarat) 41
2.3.2.2. Mount Pavagadh 42
2.3.2.3. Narmada-Tapti rift 42
2.3.2.4. Behradi Kodomali kimberlite 42
2.3.2.5. Mumbai volcanics 43
2.3.2.6. The Seychelles and the Laxmi Ridge 44
2.4. THE INDIAN LITHOSPHERE AND THE DECCAN PLUME 46
2.5. REUNION ISLAND 50

3. RE-VISITING THE ERUPTION TIMING OF THE DECCAN TRAPS 53

3.1. RADIOMETRIC DATING OF THE DECCAN TRAPS 54
3.2. HIGH-RESOLUTION PALEOMAGNETISM 55
3.3. BOLE BEDS AND/OR RED BOLES 56
3.4. GIANT PLAGIOCLASE BASALTS 58
3.5. PALEOENVIRONMENTAL DATA 59
3.5.1. INTERTRAPPEAN SEDIMENTS 59
3.5.2. STRONTIUM AND OSMIUM ISOTOPES 61
3.6. FURTHER SPECULATIONS ON THE EMPLACEMENT OF THE DECCAN TRAPS NEAR THE K-PG BOUNDARY 63
3.6.1. CONTINUOUS DECCAN ERUPTION SCENARIO 63
3.6.2. CUMULATIVE VOLUME AND ERUPTION RATES 67
3.6.3. RED BOLES AND QUIESCENCE TIME 67
3.6.4. COUPLING WITH PALEOENVIRONMENTAL INDICATORS 68
3.7. SUMMARY AND PRELIMINARY INTERPRETATIONS 71

4. SAMPLES AND METHODS 77

4.1. SAMPLES 78
4.2. METHODS 78
4.2.1. BULK-ROCK MAJOR AND TRACE ELEMENTS 79
4.2.2. OLIVINES, SPINELS AND MELT INCLUSIONS 80

5. BULK-ROCK GEOCHEMISTRY THROUGH TIME 85

5.1. SAMPLE COMPOSITION AND CLASSIFICATION 86
5.2. MAJOR ELEMENTS CLASSIFICATION 89
5.3. PROXIES FOR SOURCE DEPTH AND CRUSTAL ASSIMILATION 90

5.4. EVIDENCE FOR A RAPID CHANGE IN CRUSTAL CONTAMINATION AT CONSTANT GARNET SIGNATURE DURING THE MAIN VOLCANIC PHASE OF THE DECCAN TRAPS 95
5.5. SUMMARY AND PRELIMINARY INTERPRETATIONS 98

6. OLIVINE PETROLOGY IN THE DECCAN TRAPS AND REUNION ISLAND 103

6.1. SAMPLES 104
6.2. THE THAKURVADI FORMATION 108
6.3. OLIVINE MAJOR AND TRACE ELEMENT COMPOSITION 109
6.4. PYROXENITIC COMPONENT IN THE SOURCE OF DECCAN (THAKURVADI FORMATION) AND REUNION ISLAND (PDN AND PDF) LAVAS 115
6.5. OLIVINE-HOSTED MELT INCLUSIONS 117
6.6. SPINEL INCLUSIONS IN OLIVINE 121
6.6.1. SPINEL COMPOSITION AND FERROUS-FERRIC IRON RATIOS 122
6.6.2. OLIVINE-SPINEL THERMOMETRY 125
6.7. SUMMARY AND PRELIMINARY INTERPRETATIONS 128

7. PRIMARY MELT RECONSTRUCTION AND SOURCE MODELLING 131

7.1. PRIMARY MELT RECONSTRUCTION 133
7.1.1. MELT INCLUSION RE-EQUILIBRATION 134
7.1.2. MELT INCLUSION BACK-FRACTIONATION 135
7.1.3. TRACE ELEMENT COMPOSITION OF PRIMARY MELTS 139
7.2. SOURCE MODELLING 142
7.2.1. GEODYNAMICAL FRAMEWORK 142
7.2.2. GEOCHEMICAL MODELLING 145
7.2.2.1. Model parameterization 145
7.2.2.2. Geochemical modelling results 148
7.2.3. HYDROUS MANTLE MELTING 153
7.2.3.1. Model description 154
7.2.3.2. Hydrous melting and model coupling results 155
7.2.4. SUMMARY OF SOURCE MODELLING RESULTS 159
7.3. DISCUSSION AND LIMITS 161
7.3.1. PRIMARY MELT RECONSTRUCTION 163
7.3.1.1. K_2O, H_2O and temperature correction 163
7.3.1.2. H_2O and Ce 166
7.3.1.3. Primary melt FeO*, spinel olivine temperature and melt inclusion re-equilibration 167
7.3.1.4. Melt inclusion back-fractionation and Fo_{max} 168
7.3.1.5. Melt decompression and temperature correction 169
7.3.1.6. Trace element concentrations in primary melts 171
7.3.2. SOURCE MODELLING 172
7.3.2.1. Partition coefficient variations 176
7.3.2.2. Effects of primitive versus depleted composition of the mantle 179

8. CONCLUSION CHAPTER 183

8.1. GENERAL CONCLUSIONS 184
8.2. PROSPECTS 189

9. APPENDIX 193

I. Stratigraphic nomenclature of the western Deccan basalt formations (Western Ghats) after Peng et al (1994) 195
II. Conceptual timeframe for the emplacement of the Deccan Traps 197

III. Electron Probe Micro Analyser (EPMA) – Basic principles and high-precision analysis 203
III.1. Electron-Probe Micro Analysis – From electrons to X-ray 204
III.2. Electron Probe Micro Analysis – quantification.....213
III.3. High-precision EPMA for olivines 216
III.4. EPMA protocols for specimens other than olivines.....226
III.5. Specifications of the JEOL JXA-8230 at ISTerre, Grenoble (France) 227
III.6. Historical references.....228
IV. Résumé en français 231
IV.1. Objectifs de la thèse.....233
IV.2. Scénario temporel continu de l'éruption des Trapps du Deccan et couplage à la géochimie roche totale 234
IV.3. Analyse pétrologique des olivines des Trapps du Deccan et de l'île de la Réunion 243
IV.4. Reconstitution des magmas primaires et des sources magmatiques des Trapps du Deccan et de l'île de la Réunion 245
IV.5. Conclusions.....247
IV.6. Perspectives 252

10. REFERENCES.....256

1. Introduction

1.1. Large Igneous Provinces and the plume model

The occurrence of basaltic rocks at the surface of the Earth's crust is related to the activity of the mantle underneath it. Three different geological settings can result in such occurrence, two of which are directly related to plate tectonics, namely island arc volcanism (convergent margins), and mid-ocean ridges and intra-plate rifts (extensional tectonics). The third circumstance under which basaltic rocks may be emplaced at the surface of the Earth in large amounts is not related to plate tectonics and yet remains of the utmost importance to the history of this planet (and certainly others, e.g. Lee *et al.*, 2009). Large outpourings of basaltic rocks (and sometimes more evolved volcanic products) have long been reported under the term Large Igneous Provinces and hotspots (Coffin & Eldholm, 1994). Figure 1.1.

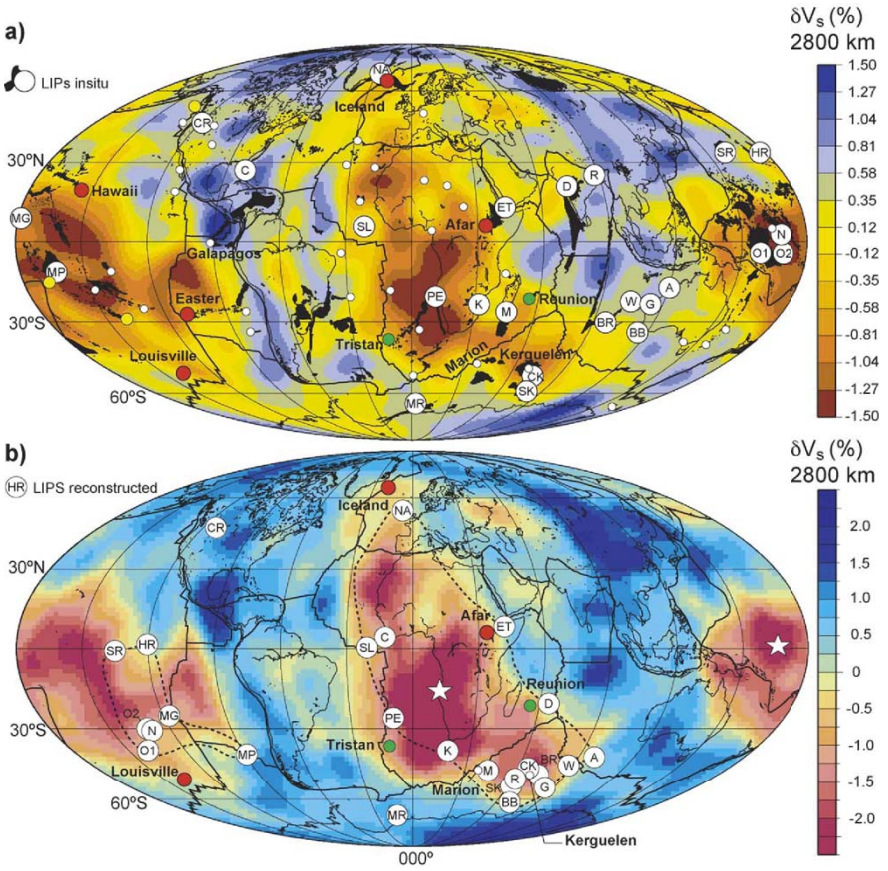

Figure 1.1 – Present-day plate boundaries and tomographic models of shear wave velocity anomalies (∂V_s) at the core-mantle boundary or CMB (note that the tomographic model is different in A and B) and superimposed Large Igneous Provinces or LIPs (black) and hotspots (dots: white, 44 hotspots from Steinberger (2000), red, green and yellow for hotspots argued to have a deep origin according to Courtillot et al (2003) and Ritsema and Allen (2003) at A) present day and B) reconstructed eruption locations back in time. From Burke and Torsvik (2004).

Large Igneous Provinces (LIPs) are defined as large (>$1.10^6 km^3$) outpourings of primarily mafic lithologies (e.g. tholeiites) emplaced over short periods of time (<1Ma) by processes unrelated to "normal" seafloor spreading or subduction. LIPs include continental flood basalts (e.g. the Deccan and Siberian Traps), oceanic plateaus (e.g. the Ontong Java plateau), volcanic rifted margins and aseismic ridges (e.g. the Chagos-Laccadive Ridge), (Coffin & Eldholm, 1994, Saunders, 2005).

No single mechanism or model seems capable of explaining all LIPs in detail. However, the plume model, that states instabilities at the core mantle boundary or CMB (Figure 1.1b) set off plumes (Figure 1.2) that rise towards the overlying lithosphere (Morgan, 1971, White & McKenzie, 1989, 1995), does explain LIPs as a whole.

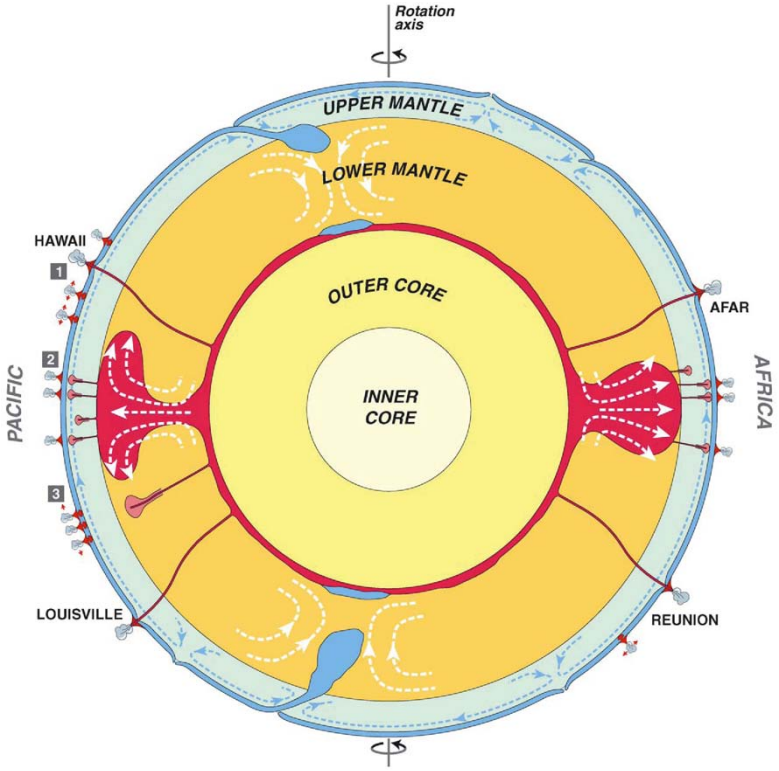

Figure 1.2 –Schematic cross section of the Earth. Three different kinds of mantle plumes as proposed by Courtillot et al: 1) primary plumes, directly originating at the CMB, 2) secondary plumes, derived from larger domes (superswells, Cazenave *et al.*, 1989) near the mantle transition zones and 3) tertiary hotspots with superficial origin (tensile stresses in the lithosphere and decompression melting, Anderson, 2000b). From Courtillot et al (2003).

Mantle plumes have originally been understood as instabilities of purely thermal nature, caused by heat transfer from the outer core (several hundred degrees higher than the lower mantle, Boehler, 1993) to the lower mantle at the CMB. It was not long however, before mantle plume began to be interpreted as part of a crustal and lithospheric recycling scheme

wherein subducting lithosphere is entrained to the CMB by density difference. This subducted lithosphere is stored and heated, and then travels back up, dynamically, by mantle plumes (Chase, 1981, Hofmann & White, 1982, Allègre & Turcotte, 1986, Kogiso *et al.*, 1998). Finally, the consideration that mantle plumes take part in a lithospheric recycling process within the mantle led to the conclusion that they may not be anomalies of purely thermal nature. Instead, the presence of crustal material within plumes result in a chemical anomaly and thus, the idea of thermochemical plumes emerged (Farnetani & Samuel, 2005, Sen & Chandrasekharam, 2011, Sobolev *et al.*, 2011).

The plume model thus stems from:
1) The application of a physical behaviour that was expected for the Earth interior: The Earth mantle lies between two thermal boundary layers, namely the CMB at the bottom and the lithosphere (which involves part of the upper mantle but does not take part in convection) above it, and is likely to be convecting
2) The absence of a relationship between hotspot volcanism and plate tectonics (deep-seated processes, beyond its reach). Several lines of evidence corroborate the existence of mantle plumes:

- Convection plumes are expected to form a large flattened head (~1000km in diameter or more) once they impinge upon the base of the lithosphere (Campbell & Griffiths, 1990). The large plume-head stage is capable of generating very large volumes of melts. This stage corresponds to LIPs emplacement (White & McKenzie, 1995). Once the plume-head has dissipated its energy, a plume-tail or hotspot-stage ensues (Richards *et al.*, 1989a, Campbell & Griffiths, 1990) with much lower rates of melt production and yet much more sustained activity through geological times. This stage then results in a series of seamounts or aseismic ridge, as a result of plate motion above the plume tail or hotspot (Wilson, 1963, Morgan, 1972). Present-day hotspots have indeed been associated with LIPs, e.g. the Chagos-Laccadive Ridge and the Mascarene Islands are associated with the Deccan Traps, (White & McKenzie, 1989, Duncan, 1990, Duncan & Richards, 1991)
- Mantle plumes are anomalies of both thermal and chemical nature that contrast with the physical characteristics of the mantle around it. This contrast is expected to translate in seismic velocity anomalies that can be observed by means of geophysical models (e.g. Kennett & Widiyantoro, 1999, Li *et al.*, 2000, Hammond *et al.*, 2012). It

is nevertheless likely that the scale of plume-tails in the present day mantle is often beyond the reach of geophysical models (Anderson, 2006). Large plume scars have however been reported in the mantle (e.g. Hammond *et al.*, 2012), and large-scale seismic velocity anomalies at the CMB (Large Low Shear Wave Velocity Provinces or LLSVP) have undoubtedly been resolved and do provide sound evidence for the relationship between hotspot volcanism and heterogeneities in the lower mantle (Burke & Torsvik, 2004, Torsvik & Cocks, 2004, Abouchami *et al.*, 2005, Torsvik *et al.*, 2010, Huang *et al.*, 2011, Weis *et al.*, 2011, Payne *et al.*, 2012), Figure 1.1

- Plumes tap deep mantle reservoirs that are more primordial than the upper mantle. This primordial material has undergone far less degassing than shallower parts of the Earth and thus bears typical isotopic signatures of high (>30 Ra) $^{3}He/^{4}He$ (Class & Goldstein, 2005, Herzberg *et al.*, 2013). Similar signatures are also seen in other isotopic systems (Hart *et al.*, 1992)
- The existence of plumes is suggested by the occurrence of primitive lava compositions and/or high-Mg olivine phenocrysts that are indicative of anomalously hot (melt MgO increases with mantle temperature as ~1%/25°C) sources (Campbell & Griffiths, 1990, Sobolev & Nikogosian, 1994, Herzberg & O'Hara, 2002, Campbell, 2005, Herzberg *et al.*, 2007)
- Furthermore, high nickel and low calcium and manganese contents of LIPs and hotspot lavas (Herzberg, 2011) and magnesium-rich olivine phenocrysts (Sobolev *et al.*, 2005, 2007) have been ascribed to the presence of olivine-free lithologies in plumes (pyroxenite and eclogite). Pyroxenite is argued to result from the reaction between eclogite melts (i.e. recycled crust) with the surrounding mantle peridotite. (Yaxley & Green, 1998, Yaxley, 2000, Kogiso *et al.*, 2003, 2004, Sobolev *et al.*, 2005). Eclogite has a low solidus and therefore melts significantly deeper than peridotite in mantle upwelling (Yasuda *et al.*, 1994). The existence of recycled material in plumes has also been suggested by isotopic data, especially osmium (Allègre & Luck, 1980, Roy-Barman & Allègre, 1995, Sobolev *et al.*, 2008)

A number of authors disagree with the plume model, or at least with particular applications of it (e.g. Anderson, 1994, Anderson, 2000a, Sheth, 2005). A comprehensive compilation of non-plume models for the formation of LIPs can be found here: Foulger et al (2005).

The main objection to the plume model comes from the predicted lithospheric response to the arrival of a hot plume. If a plume is regarded as a purely thermal anomaly (thermal plume), the light (because hot) peridotite it contains is expected to induce significant regional uplift of the lithosphere above it, in the order of 0.8-2.5km for a 100 to 300°C temperature excess before any major volcanic activity (Campbell & Griffiths, 1990, Farnetani & Richards, 1994). Such pre-magmatic uplift has been reported for the North Atlantic and Columbia River LIPs (Saunders *et al.*, 2007) yet convincing evidence is still lacking in most other cases: the Siberian Traps (Czamanske *et al.*, 1998), the Emeishan Traps (Peate & Bryan, 2008), the Ontong Java oceanic plateau (Korenaga, 2011), and of course the Deccan Traps (Sheth, 2007).
It has been shown however, that a plume of both thermal (~ 200°C excess temperature) and chemical (carrying 15% of recycled crust) nature (or thermo-chemical plume) is expected to produce only negligible (100-200m) pre-magmatic uplift (Sobolev *et al.*, 2011).

If it is true that no simple unified mechanism is likely to explain all LIPs on the Earth, anti-plume arguments have thus far failed to bring compelling evidence against the plume model. It is therefore likely that the plume model is capable of explaining LIPs on the whole, even though unravelling their every detail may require a number of case-related adaptations. Nevertheless, this PhD does not take a particular geodynamical model for granted but rather consists of a compilation of evidence (uplift, temperature) that consistently rule out the non-plume origin of the Deccan Traps.

1.2. LIPs, mass extinctions and the Deccan case

Mass extinction events (Figure 1.3) correspond to periods in geological times during which the continuous extinction of species and the appearance of new ones was disrupted to such an extent that extinction rates far surpassed speciation rates. Such events have punctuated the history of the Earth and have been observed in the paleontological record for many decades (e.g. Raup & Sepkoski, 1982).

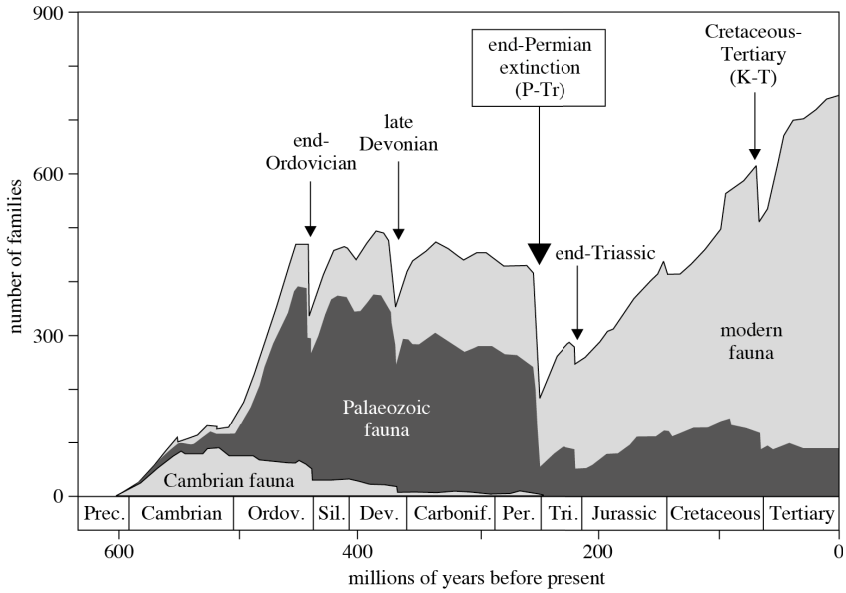

Figure 1.3 –Biodiversity versus time for the past 600Ma and the five most dramatic (the "big five") mass extinctions of the Phanerozoic: End-Ordovician (445Ma), Late-Devonian (375Ma), End-Permian (250Ma), End-Triassic (200Ma) and the Cretaceous-Tertiary (66Ma). From White (2002).

A wealth of potential mass killers have been suggested in the literature, from extra-terrestrial impacts (Alvarez *et al.*, 1980) to LIPs (Courtillot & Renne, 2003, Saunders, 2005), including cosmic rays (Rohde & Muller, 2005, Medvedev & Melott, 2007), Milankovitch cycles (Raup, 1987, Bennett, 1990) and supercontinent formation and break-up (Santosh, 2010).

As in the case of the plume model with respect to LIPs (section 1.1), it is reasonable to contend that no simple and unique mechanism is likely to explain all mass extinction events throughout geological times. Nevertheless, among all possible players, extra-terrestrial impacts and LIPs eruption, for their capacity to release vast amounts of climate-affecting gases over short time periods have dominated the debate for the past thirty years (Alvarez *et al.*, 1980, Courtillot *et al.*, 1986, 1988, Wignall, 2001, Alvarez, 2003, Courtillot & Renne, 2003, Keller, 2005, Saunders, 2005, White & Saunders, 2005, Saunders *et al.*, 2007, Courtillot & Fluteau, 2010).

The strongest historical argument in favour of LIPs as a main trigger of mass extinction events comes from the close-to-perfect correlation through time between the two (Courtillot & Renne, 2003), Figure 1.4.

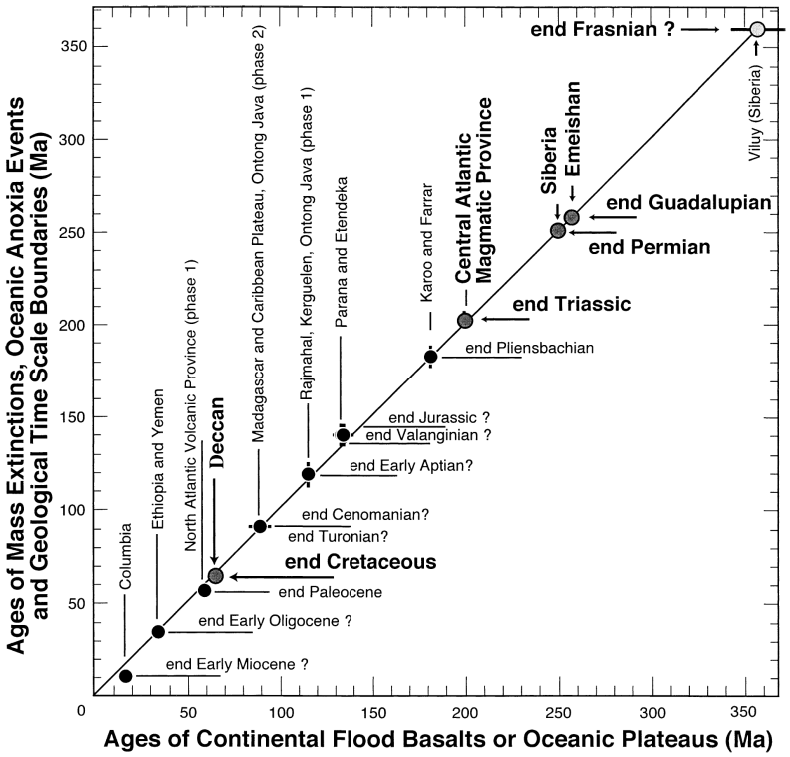

Figure 1.4 –But see also Rampino and Stothers (1988). Correlation between the age of LIPs and mass extinction and ocean anoxia events. From Courtillot and Renne (2003).

The end-Cretaceous (also referred to as KT or K-Pg) extinction is the most recent of the "big five" (Figure 1.3) and appears to correlate rather perfectly with the emplacement of the Deccan Traps (Figure 1.4). This association of the Deccan Traps and the K-Pg extinction has been reported in the literature for the past forty years (Vogt, 1972, Courtillot *et al.*, 1986, 1988, Courtillot & Renne, 2003, Keller *et al.*, 2012). However, and like most other extinction events, the K-Pg crisis has at least one serious alternative scenario: the possibility that the ~65 million years old and 200km-wide impact crater roughly centred on the town of Chicxulub (Yucatan, Mexico) is evidence of a catastrophic extra-terrestrial impact that may well have been sufficient to wipe the dinosaurs out of the Mesozoic world (Alvarez *et al.*, 1980, Schulte *et al.*, 2010). Akin to the debate between pro- and anti-plume proponents, a debate as to which of the extra-terrestrial impact or the large volcanic eruption (Deccan Traps) is to blame for the K-Pg mass extinction, has been raging on for more than thirty years. Both scenarios have been assessed for 1) their age with respect to the Cretaceous-Palaeogene (K-Pg) boundary (Keller *et al.*, 1995) with reports that the Chicxulub impact predated the K-Pg boundary (e.g. Keller *et al.*, 2004a, 2004b, 2007, 2008) or was contemporaneous with it (e.g. Alvarez *et al.*, 1980, Krogh *et al.*, 1993, Norris *et al.*, 2000, Smit, 2004, Schulte *et al.*, 2008, Robinson *et al.*, 2009, Schulte *et al.*, 2010) and conversely for the Deccan Traps (e.g. Courtillot *et al.*, 1986,

1988, Venkatesan *et al.*, 1993, Raju *et al.*, 1995, Allègre *et al.*, 1999, Widdowson *et al.*, 2000, Pande, 2002, Chenet *et al.*, 2007, Keller *et al.*, 2008a, Robinson *et al.*, 2009, Hooper *et al.*, 2010, Keller *et al.*, 2011, 2012) and 2) their respective devastating power with authors arguing that the Chicxulub impact had been able to affect the Earth's troposphere fast enough to trigger an extinction while the eruption of the Deccan Traps certainly spanned several Ma and was thus too slow to bear significant consequences on the global ecosystem (e.g. Pierazzo *et al.*, 2003, Abramov & Kring, 2007, Schulte *et al.*, 2008, 2010). Others argue that the Chicxulub impact was indeed instantaneous but that the sheer size of the Deccan Traps combined with emplacement times much shorter than 1Ma implied that its effect on the climate (through magmatic degassing mostly) would have been orders of magnitude higher than that of the Chicxulub impact (e.g. Sen, 2002, Self *et al.*, 2006, Sen *et al.*, 2006, Chenet *et al.*, 2008, Self *et al.*, 2008a, Chenet *et al.*, 2009, Courtillot & Fluteau, 2010, Keller *et al.*, 2012). The next and final section to this introduction is a modest attempt to untangle and reconcile both sides of this debate. There is nonetheless one last and peculiar aspect to the K-Pg crisis that ought to be kept in mind and that summarizes particularly well the fascinating character of this end-Cretaceous early-Tertiary period. Early in the Jurassic, there was a major shift in the chemistry of the oceans, from a Neritan mode wherein no buffer existed against global acidification, to a Cretan state in which deep-sea unlithified carbonate acted as a buffer against acidification (Ridgwell, 2005). This turning point in geological history correlates with a transition from extremely severe mass extinction events, such as the end-Permian (250Ma) and the end-Triassic (200Ma), themselves associated with particularly voluminous LIPs (the Siberian Traps and the Central Atlantic Magmatic Province) to far less severe crises despite the emplacement of LIPs comparable in size (e.g. the Ontong Java Plateau, the Caribbean Plateau and the North Atlantic Magmatic Province). This transition in the intensity of mass extinction events holds true for all crises since the Jurassic with one notable exception. This exception also happens to be the only such event where a clear combination of intense volcanism and extra-terrestrial impact exists: the K-Pg extinction and the Deccan Traps, Figure 1.5.

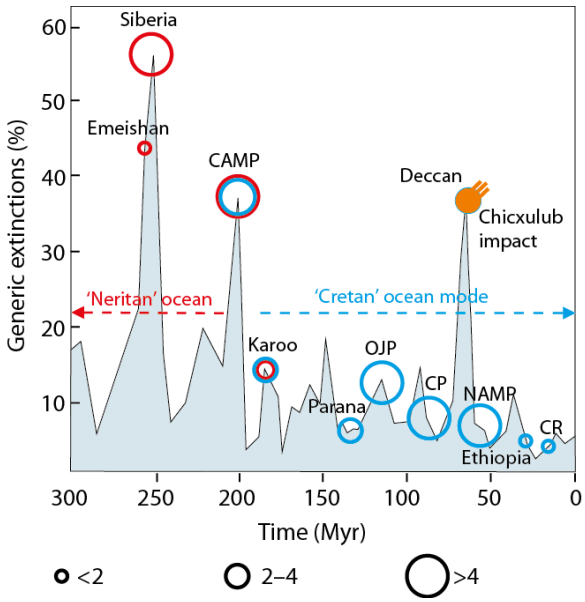

Figure 1.5 –Generic extinction rate versus time for the last 300Ma, major LIPs (circles, diameter is a function of volume in $10^6 km^3$, see below the figure. Blue for oceanic plateaus and red for continental flood basalts) and ocean modes (Neritan and Cretan, see text and Ridgwell, 2005). CAMP: Central Atlantic Magmatic Province, OJP: Ontong Java Plateau, CP: Caribbean Plateau, NAMP: North Atlantic Magmatic Province, CR: Columbia River basalts. From Sobolev et al (2011).

1.3. The Deccan Traps, Chicxulub, and the end-Cretaceous extinction – an attempt for reconciliation

The climate of the Cretaceous was warm (Krassilov, 1973), sometimes extremely so (Huber *et al.*, 2002), and featured a general cooling trend (Krassilov, 1975) that continued on in the Cenozoic, mostly as a result of landmass redistribution and major orogenesis (Molnar & England, 1990, Garzione, 2008, Willenbring & Blanckenburg, 2010), Figure 1.6.

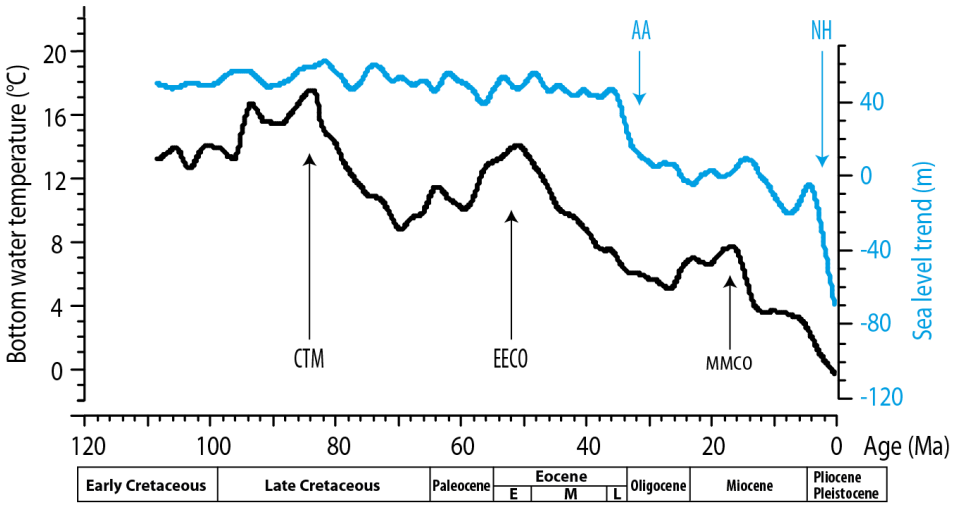

Figure 1.6 – Bottom water temperature and sea level trend since the early Cretaceous from Kent and Muttoni (2013) and Cramer et al (2011). CTM: Cretaceous thermal maximum, EECO: early Eocene climatic optimum, MMCO: middle Miocene climatic optimum. Sea-level drop: AA, inception of Antarctic ice cap and NH inception of the Northern Hemisphere ice sheets.

The paleoclimate of the K-Pg transition has proved more difficult to resolve in detail. The terrestrial record shows opposing trends with reports of cooling (Krassilov, 1975), warming (Wolfe, 1990, Nordt *et al.*, 2002) or a brief low-temperature excursion with recovery early in the Palaeocene (Wolfe & Upchurch-Jr, 1986). The marine record nevertheless provides a better picture (Wilf *et al.*, 2003). Oxygen and carbon (Li & Keller, 1998) as well as strontium (Vonhof & Smit, 1997, MacLeod *et al.*, 2001) and osmium (Ravizza & Peucker-Ehrenbrink, 2003, Robinson *et al.*, 2009) isotopic ratios in marine sediments consistently show a late-Maastrichtian warm event followed by a rapid cooling ending at the K-Pg boundary and further global cooling in the Cenozoic (Burke *et al.*, 1982). Both the extra-terrestrial impact (MacLeod *et al.*, 2001, Wilf *et al.*, 2003, Robinson *et al.*, 2009) and intense volcanism (Li & Keller, 1998, Ravizza & Peucker-Ehrenbrink, 2003, Robinson *et al.*, 2009, Keller *et al.*, 2012) have been proposed as the cause of this global climate change.

The consequences of volcanic eruptions on the climate depends on the composition of the erupted products as well as on their amount and height of ejection (e.g. Robock, 2000). In the case of Continental Flood Basalts, and especially in the case of the Deccan Traps, where both volcanism and/or an extra-terrestrial impact may have contributed to the K-Pg extinction, the average rate of eruption over the entire duration of the flood basalt volcanism is critical (e.g. Self *et al.*, 2006). Indeed, the fact that the Chicxulub impact took only seconds to release a noticeable fraction (Pierazzo *et al.*, 2003) of the harmful volatiles (e.g. SO_2, CO_2, NO_x) while

the Deccan Traps released in potentially several millions of years has been in favour of the impact hypothesis (Alvarez *et al.*, 1980, Schulte *et al.*, 2010). On the other hand, if one was to argue that 80% of the Deccan Traps had been emplaced in a few thousands of years and thus released orders of magnitudes more harmful gasses to the atmosphere than an extra-terrestrial impact like Chicxulub – in a timeframe the global environment could not bear – Figure 1 in Schulte et al (2010) would look somewhat different (Chenet *et al.*, 2008, 2009, Courtillot & Fluteau, 2010). In addition, large outpourings of basaltic rocks onto vast areas of continents would also act as a carbon sink through weathering and erosion (Dessert *et al.*, 2001, 2003). Therefore, the surface and volume of Continent Flood Basalts may also be an important variable in assessing the longer-term environmental consequences of volcanism. Finally, an interesting feature of the end-Cretaceous extinction is that it occurred after a major change – during the Mesozoic – in the global ocean chemistry from a 'Neritan' to a 'Cretan' mode wherein deep-sea unlithified carbonates act as buffers against acidification (Ridgwell, 2005, Payne *et al.*, 2010), Figure 1.5. This would make mass-extinction more difficult, at least in the marine realm, whereas it is precisely from the marine record that the end-Cretaceous mass extinction is globally seen. Furthermore, while the major extinction events that preceded the end-Cretaceous, namely end-Permian and end-Triassic, occurred under a Neritan ocean chemistry mode and were indeed intense, reaching 60 and 40% species extinction, all mass-extinction events have been below 20% of generic extinction ever since, except the end-Cretaceous and despite the buffering by deep-sea carbonates (White & Saunders, 2005, Sobolev *et al.*, 2011).

Attempting to untangle the environmental effects of flood basalt volcanism from those of an extra-terrestrial impact seems difficult since the global environmental consequences – as seen in the geological record – of extra-terrestrial impacts and those of large volcanic eruptions are roughly similar: global climate change (warming or cooling), acid rains, increased rainfall, decreased sunlight (Haywood & Boucher, 2000, Robock, 2000, Chenet, 2006, Self *et al.*, 2006). Speculated asteroid-specific consequences would be 1) extensive wildfires (Wolbach *et al.*, 1985, Vonhof & Smit, 1997) although evidence of their occurrence seems to be lacking (Belcher *et al.*, 2003, Cripps *et al.*, 2005) and 2) slope failure as a result of seismicity (Olsson *et al.*, 1997, Klaus *et al.*, 2000, Norris *et al.*, 2000) even though not all slope failures near North America match this postulate despite being in the vicinity of the impact zone (MacLeod *et al.*, 2003).

These global environmental consequences have been transferred to the geological record mostly as isotopic and chemical excursions in sedimentary deposits and changes in fossil species richness, especially among foraminifera. Yet, the time lag between the actual event taking place (i.e. a huge volcanic eruption or an asteroid impact) and its environmental consequences being recorded in sedimentary rocks can be significant (kyr). For instance, the global ocean mixing time is in the order of thousands of years (MacLeod *et al.*, 2001) potentially averaging many eruptions in the Deccan Traps with one asteroid impact in Yucatan.

High-pressure (e.g. shocked-quartz, fullerene) and PGE-enriched materials intercalated within the sedimentary record suggest the occurrence of an extra-terrestrial impact event (Alvarez *et al.*, 1980, Alvarez, 2003, Parthasarathy *et al.*, 2008). It has been proposed that high-pressure features such as shocked quartz could have been of volcanic origin (Morgan *et al.*, 2004). However, the PGE concentrations in the sources of the Deccan Traps would have been too low (Chalapathi Rao *et al.*, 2013) to explain the K-Pg Ir-anomaly. Therefore, impact signal can be considered as unambiguous in the late-Cretaceous. But this does not help in trying to decipher the consequence of one event versus the other. Adding to the confusion is the fact that the Chicxulub impact has been described as predating the mass extinction (Keller *et al.*, 2004a, 2004b).

Among the frenzy for possible scenarios - and not to mention the possible causes such as several impacts (Hartnady, 1986, Damuth & Johnson, 1989, Chatterjee *et al.*, 2006), sea level change (Hallam & Wignall, 1999) or ecosystem instabilities (McElwain & Punyasena, 2007) – it remains that both events must have occurred close enough to one another to create ambiguous signatures in the sedimentary record, which typically means that the Chicxulub asteroid must have impacted the Earth within a time window of (much) less than a million years (typical resolution of global stratigraphic correlations) around the main phase of volcanism in the Deccan Traps, which immediately precedes the K-Pg boundary. It is also clear that an asteroid the size of Chicxulub (i.e. about 10km in diameter) must have had at least catastrophic *regional* consequences (Campbell *et al.*, 2008, Schulte *et al.*, 2010). The same goes for the Deccan Traps (Self *et al.*, 2006, Keller *et al.*, 2012). Furthermore, the sheer size of the Deccan Traps compared to the rather discreet Chicxulub crater should not be mistaken as a subliminal indication that the Deccan Traps did more damage to Earth than the impact (Alvarez, 2003).

In order to fully grasp the severity of the Deccan Traps eruption and then compare it with models of extra-terrestrial impacts, it is required to 1) better constrain the eruption of the Deccan Traps through time, 2) better constrain the composition of the magmatic sources of these eruptions in order to gain insights as to the geodynamical processes capable of releasing several million cubic kilometres of lavas as well as gigatons of climate-modifying gasses over a relatively short time, and 3) quantify the consequences on the climate – and life.

1.4. Layout and goals of the PhD project

The ultimate goal of this PhD is to re-assess the role of the Deccan Traps as a contributing factor to K-Pg mass extinction event. I aim to understand the deep-Earth processes and magmatism: By reconstructing the composition and physical conditions of the magmatic sources of the Deccan Traps through time, new constraints to melt production and related degassing will be obtained and may be assessed in view of the available literature in order to estimate potential environmental consequences.
This PhD may be considered as a continuation of the work undertaken by Sobolev and co-workers on the Siberian Traps (Sobolev *et al.*, 2011) but in a wholly different setting. While the Siberian Traps have been erupted under a compressive tectonic regime at a time where the world oceans were vulnerable to acidification, the Deccan Traps have been emplaced under extensional tectonic regimes with extremely fast plate motion at a time were the world oceans were buffered against acidification by deep-see unlithified carbonates. An additional difference is the unambiguous simultaneous occurrence of a catastrophic extra-terrestrial impact (Figure 1.5).

A brief introduction on the geological and geodynamic setting of the Indian plate and the Deccan Traps will be followed by four sections, each of them attempting to address on particular and crucial aspect of the Deccan Traps (note however, that the modelling of LIPs-related climate effects is not tackled in this manuscript. An on-going PhD project at the IPGP, Paris (France) is currently attempting to address this issue in the case of the Deccan Traps):

- The duration of the Deccan Traps emplacement and its rate are of the utmost importance to assess the capacity of such an event to affect the global ecosystem. A new timing scenario entirely based on a re-interpretation of the extensive work of Chenet and colleague on paleomagnetic measurements and radiometric dating in the

Western Ghats (Chenet, 2006, Chenet *et al.*, 2007, 2008, 2009) as well as on literature review will be proposed

- The timing scenario will be coupled to bulk-rock major and trace element data (Bonnefoy, 2005). This step will allow for source depths and crustal assimilation to be assessed through time, with implications on melt productivity and degassing
- Olivine phenocrysts in picritic samples from both the Deccan Traps (plume-head stage) and Réunion Island (plume-tail stage) will be investigated for 1) the existence of an olivine-free lithology in the source of the Deccan Traps magmas, with implications on melt productivity, plume-lithosphere interactions and degassing, 2) the volatile (K_2O, H_2O, Cl, SO_2) contents of those magmas and 3) their primary melt composition and temperature
- In the final section, olivine phenocryst data will be integrated to a modelling framework based on observations from the previous sections (e.g. lithospheric thickness, source pressure, crustal assimilation) that will allow for the sources of the Deccan Traps and Réunion Island to be reconstructed and conclusions to be drawn as to the deep origin of the Deccan magmas

2. Geological Setting

2.1. India in the late Cretaceous

India separated from the Gondwana super-continent in the Jurassic, at 170Ma (Dietz & Holden, 1970). Free of its bond with East-Gondwana, India then embarked in one of the most epic continental drifts in Earth history, covering some 9000km over 160Ma. This remarkable journey was punctuated by many events, such as the breakup of sub-continents (Madagascar, Sri Lanka, the Laxmi Ridge and the Seychelles), the emplacement of the Rajmahal and Deccan Traps, and ended with two episodes of collision first with the Kohistan-Ladakh Arc and finally with Asia at about 50Ma. During these two collision episodes, India's motion was reduced from 20cm/yr to merely 5cm/yr and the highest alpine mountain range, the Himalayas, and the Tibetan plateau arose. This unique string of events has been recently re-visited by Sankar Chatterjee and colleagues (Chatterjee *et al.*, 2012).

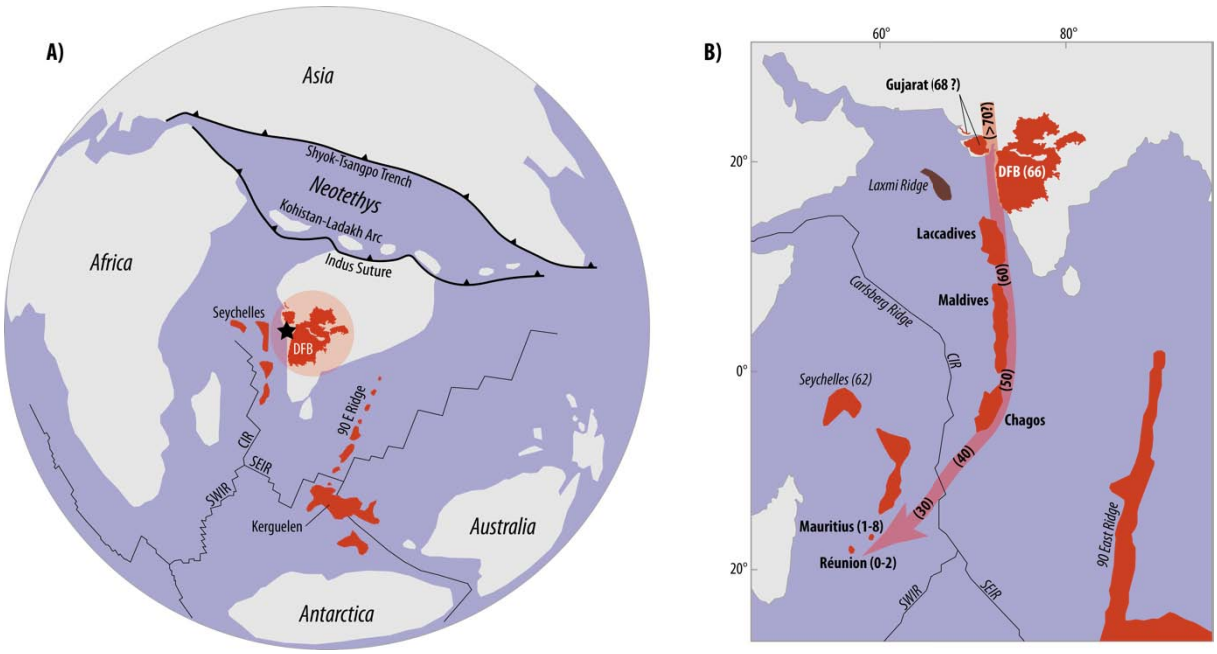

Figure 2.1 – A) India at the K-Pg boundary (66Ma). DFB: Deccan Flood Basalts. Light red, transparent area shows the postulated size of the Deccan plume head (White & McKenzie, 1989). Black start: speculated location of plume centre. CIR: Central Indian Ridge. SWIR: South West Indian Ridge. SEIR: South East Indian Ridge. Red areas show traces of intraplate volcanism. Modified from Chatterjee et al. (2012) and Duncan et al. (1990). B) Deccan plume path (red arrow) in the Indian Ocean with corresponding ages in Ma (Duncan, 1990) from the early Deccan activity north of Gujarat, India, until its current location at Réunion Island. The earliest manifestations of the Deccan plume have been identified near the Tethyan Suture north of Gujarat (Mahoney *et al.*, 2002, Kerr *et al.*, 2010). The age range proposed for the Seychelles is that of the breakup from the Indian plate (Collier *et al.*, 2008). The Laxmi Ridge is a micro-continent with significant ultramafic underplating (Minshull *et al.*, 2008), see section 2.3.2.6. Modified from Mahoney et al. (2002).

During the late Cretaceous, near the Creataceous-Paleogene (K-Pg) boundary and during the eruption of the Deccan Traps, the Indian plate was located in the Indian Ocean with the Gulf

of Cambay (between the Gujarat peninsula and the Konkan coast) roughly centred on today's Réunion Island (Chatterjee *et al.*, 2012) (Figure 2.1a). At this time, the Indian plate motion was in the order of 20cm/yr, which converts into 200km/Ma. This figure is an important one to consider when investigated volcanic phenomena that have spanned several Ma, such as the emplacement of the Deccan Traps.

Subsequent traces of the Deccan plume are to be found in the Seychelles micro-continent that separated from the Laxmi Ridge (Minshull *et al.*, 2008) and Indian plate at about ~62Ma (Collier *et al.*, 2008), and further resulted in the formation of the Chagos-Laccadive ridge (60-40Ma), the Mascarene plateau (30Ma), Mauritius (1-8Ma) and Réunion Island (0-2Ma) (Duncan, 1990, Mahoney *et al.*, 2002), Figure 2.1b.

The generally accepted plume model for the origin of the Deccan Traps and subsequent traces of intraplate volcanism have been heavily criticized by proponents of a rifting model (e.g. Sheth, 2005). According to this model, part of the age progression of Figure 2.1b would not be valid or explained by the plume model. For example, the Chagos-Laccadive ridge have been created by large scale crack propagation, which would result in a similar age progression (Sheth, 2005).

2.2. The structure and geological units of the Indian plate

The Indian plate consists of several Archean to late-Precambrian cratonic units and fold belts forming what is commonly referred to in the literature as the Indian Shield. A number of rifts have also developed at different times along inherited Precambrian structures. (Murthy, 2002, Ray *et al.*, 2008). The Indian Shield is blanketed by Palaeozoic and Mesozoic deposits, Cretaceous to Palaeogene basalts resulting from the eruption of the Deccan Traps, and Quaternary, mostly detrital, sediments (Figure 2.2).

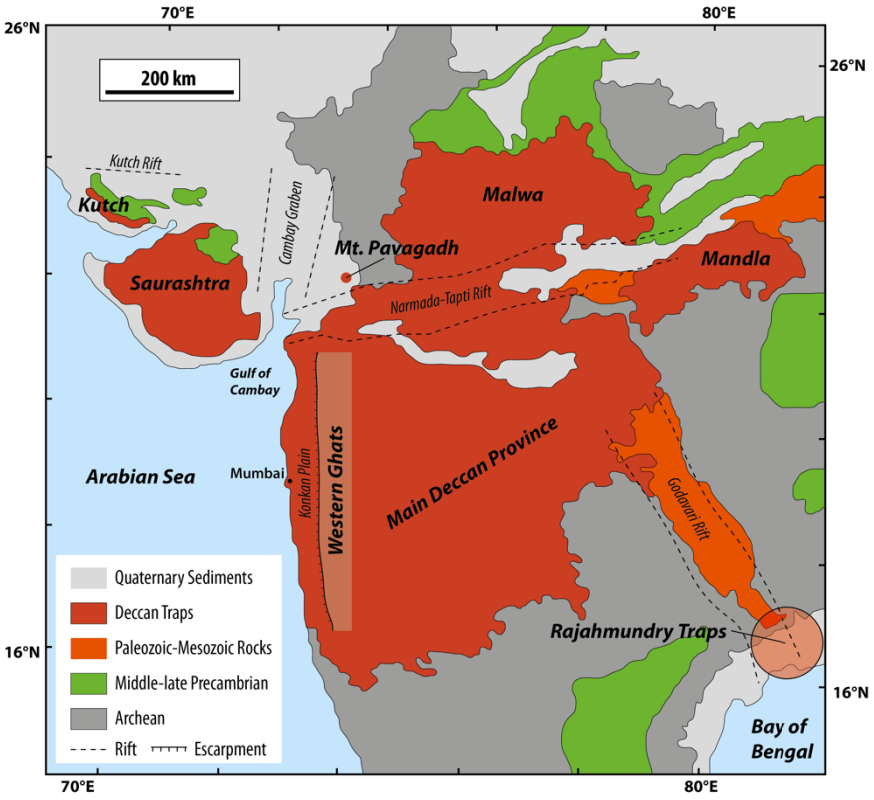

Figure 2.2 - Simplified geological map of western India. Modified from Krishnamurthy et al. (2000)

2.3. The stratigraphy of the Deccan Traps

The present coverage of the Deccan Traps is in the order of 500,000km^2 with an initial extent presumably twice as high and a volume of 1 to 2.10^{6}km^3 (Mitchell & Widdowson, 1991, Sen, 2001, Jay & Widdowson, 2008). Note also that as Deccan-related intrusions have been reported in both the Seychelles (Owen-Smith *et al.*, 2013) and eastern India (Chalapathi Rao *et al.*, 2011a), the original extent of the Deccan Traps still remains very much speculative.

The Deccan Traps are subdivided into geographical units or provinces (Figure 2.3) and the lava flows building the Traps are classified into sub-groups and formations (Figure 2.4).

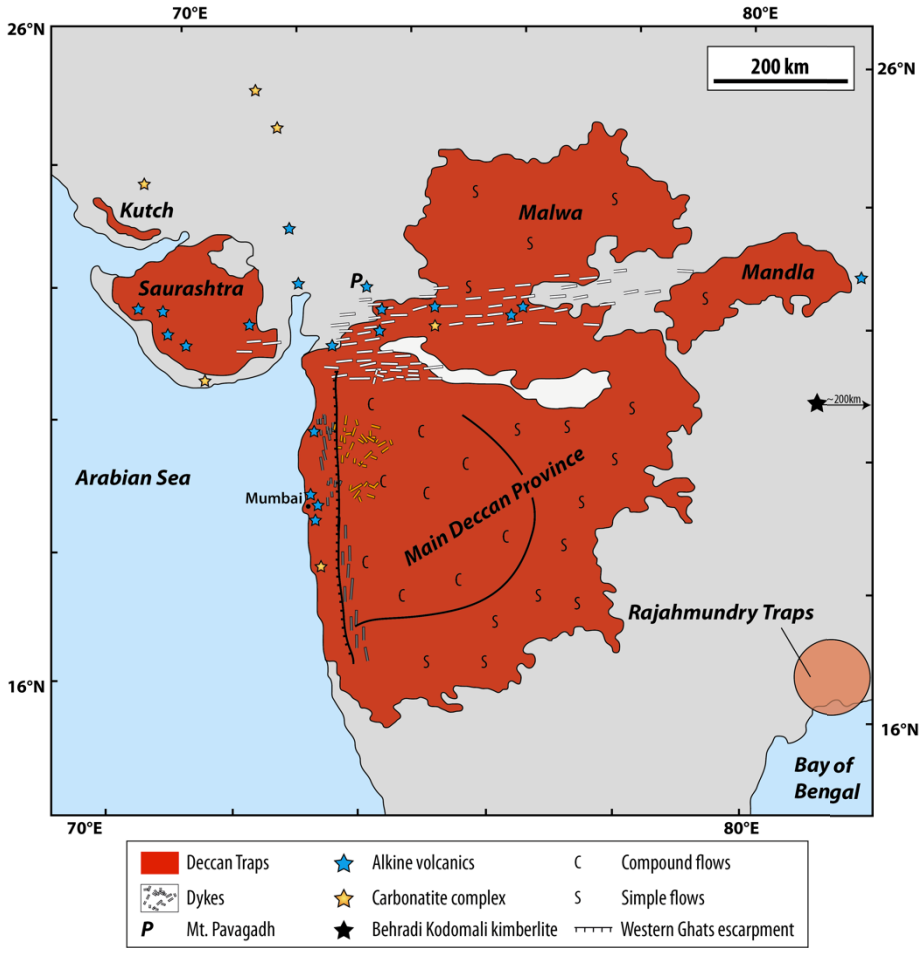

Figure 2.3 - Structure and provinces of the Deccan Traps. Alkali complexes, carbonatites and kimberlite occurrences related the Deccan Traps (Subba Rao, 1972, Woolley & Kjarsgaard, 2008, Vanderkluysen *et al.*, 2011). General structure or the lava flows (simple or compound flows) (Sen, 2001). Main dike swarms (white: Narmada-Tapti swarm, green: Nasik-Pune swarm, grey: Coastal swarm). Rajahmundry Traps, Krishna-Godavari Basin (Baksi *et al.*, 1994, Baksi, 2001, Self *et al.*, 2008b).

2.3.1. The Main Deccan Province, the Western Ghats and related outcrops

The Main Deccan Province (Figure 2.4) is the most extensive and voluminous lava sequence in the Deccan Traps. The maximum thickness of the Main Province is reached along the Indian west coast, at the Western Ghats escarpment. It has a general shield-like structure centred on the Nasik-Pune dyke swarm that gradually thins towards the east and south forming a ~3° slope. Along this trend compound flows gradually transition to simple flows about 200km from the Nasik-Pune swarm. The average length or extent of lava flows is unclear yet larger than 100km. However, Pahoehoe-to-aa flow type transitions that would drastically limit flow propagation have been reported (Duraiswami *et al.*, 2004, Duraiswami

et al., 2013). The shield-like structure of the Main Province is also seen in the general prograde structure of the lava flows: the youngest formations are to be found away to the east and south on the Nasik-Pune swarm, (Figure 2.4). The lava flows of Malwa, Mandla and those of the Rajahmundry Traps are similar to those of the Main Province. The outcrops of Rajahmundry have been linked to the Ambenali and Mahabaleshwar formations (Baksi *et al.*, 1994, Baksi, 2001, Self *et al.*, 2008b) and would have originated from eruption centres in the Western Ghats (coastal dyke swarm, Figure 2.3) thereby forming the longest (>1000km) lava flows ever reported on Earth (Self *et al.*, 2008b).

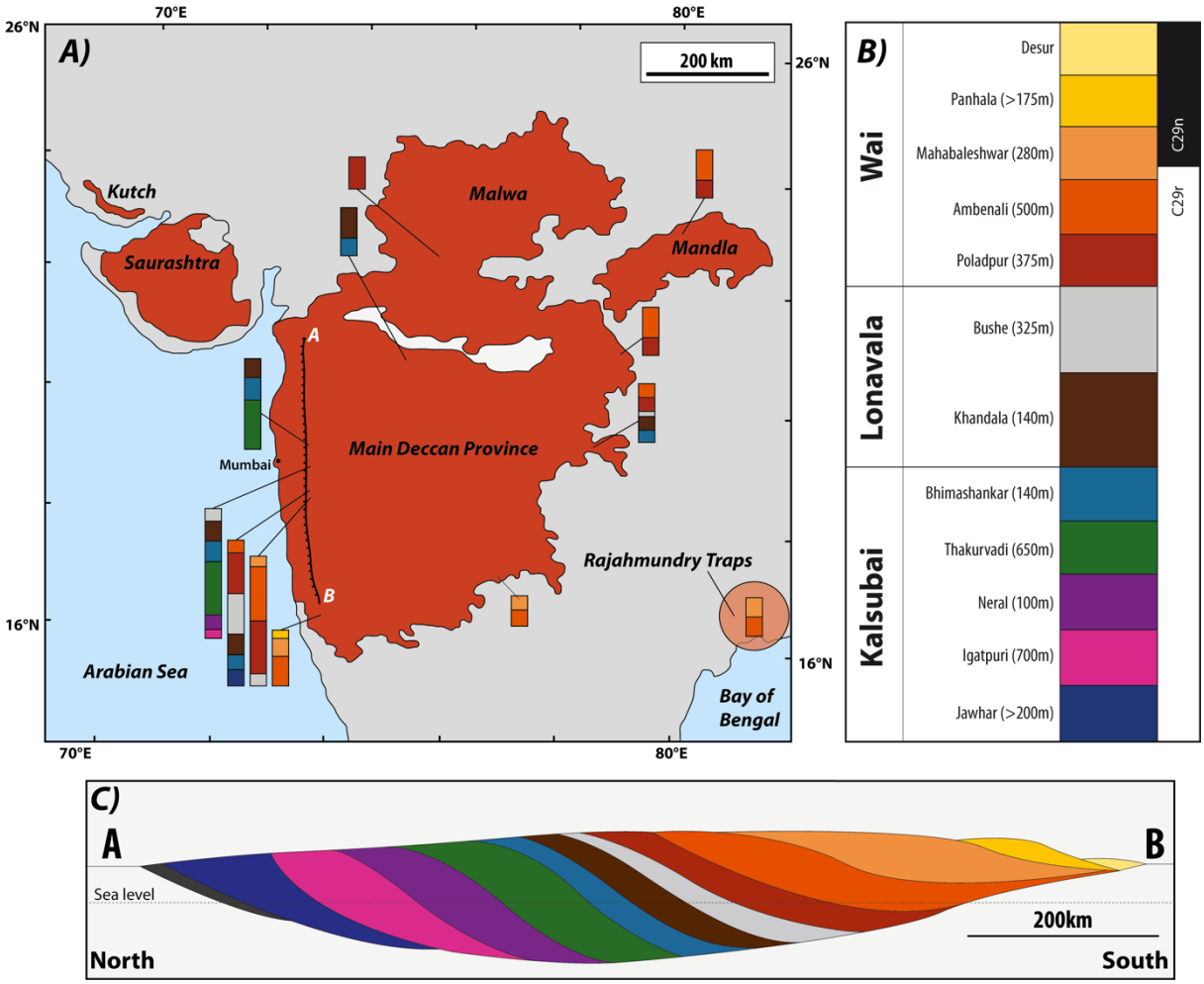

Figure 2.4 – Structure of the Main Deccan Province and associated areas (Malwa, Mandla and the Rajahmundray Traps). A) Present-day extent of the Deccan Traps, location of the cross section (C), and stratigraphic columns for various locations of the Main Deccan Province (Vanderkluysen *et al.*, 2011), colour codes as of B). B) Full stratigraphic column, subgroups and formations (with corresponding thickness) of the Main Deccan Province (Chenet *et al.*, 2009). C) Schematic north-south cross section of the Western Ghats (A) form Chenet et al. (2009).

The Main Deccan Province mostly consists of differentiated tholeiites with minor occurrences of alkaline (Narmada: Subba Rao, 1972, Central Main Province: Talusani, 2010) and felsic products (Mumbai area: Melluso *et al.*, 2002, although these clearly postdate the emplacement of the Main Deccan Province, Hooper *et al.*, 2010). The tholeiites have been divided into three sub-groups and twelve formations originally recognized upon simple field observations, later confirmed and slightly modified using isotopes, major and trace element compositions (e.g. Mahoney, 1984, Lightfoot, 1985, Beane *et al.*, 1986, Devey, 1986, Mitchell & Widdowson, 1991, Peng *et al.*, 1994), Figure 2.4b and appendix I.

The following brief description of the subgroups is taken from Beane et al. (1986):
The first five formations (Kalsubai subgroup) are also referred to in the literature as *lower formations*. They consist of massive amygdaloidal compound flows that make up for more than 50% (~2000m) of the total composite thickness of the Main Deccan Province or Western Ghats. They have higher average Mg# than the above-lying formations and a wide range of compositions from picritic flows (Mg# > 60) to evolved lavas featuring large (>cm) plagioclase phenocryst, the Giant Plagioclase Basalts (Mg# < 45).
The Lonavala subgroup (~15% of total thickness) consists of only two formations (Khandala and Bushe) that are easily recognized in the field by their simpler and less massive structure (especially Khandala) than that of the Kalsubai subgroup. The Lonavala subgroup has a lower average Mg# than the Kalsubai formations. Bushe has the highest $(^{87}Sr/^{86}Sr)_t$ of all Deccan Traps formations (Figure 2.5) despite two picritic flows. Its large compound flows are also much more massive than those of Khandala and allow for easy identification in the field.
The Wai subgroup (35% of total thickness) is the final subgroup and comprises five formations (Poladpur, Ambenali, Mahabaleshwar, Panhala and Desur). Panhala and Desur are very poorly preserved and Desur has been virtually eroded away. The Bushe-Poladpur transition is readily noticed in the field by a transition from massive amygdaloidal flows (Bushe) to simple flows (Poladpur and above). Poladpur appears to be the most extensive formation of the Deccan Traps (Figure 2.4) (Mahoney *et al.*, 2000). The composition of the Wai subgroup is on average the most evolved of the Main Province although it contains no Giant Plagioclase Basalts. Wai also lacks major picritic flows and is thus evolved and more homogeneous than the flows of Kalsubai and Lonavala. Ambenali has the lowest $(^{87}Sr/^{86}Sr)_t$ and $\delta^{18}O$, and the highest $\varepsilon Nd_{(t)}$ of all Main Province tholeiites (Peng *et al.*, 1994), Figure 2.5.

Finally, the Mahabaleshwar formation recorded the C29r-C29n geomagnetic reversal (Chenet *et al.*, 2008).

The location of the Main Deccan Province formation in Nd, Sr and Pb isotopic spaces reveals a hidden diversity of the Deccan Traps tholeiites (Mahoney, 1984, Lightfoot, 1985, Peng *et al.*, 1994), Figure 2.5.

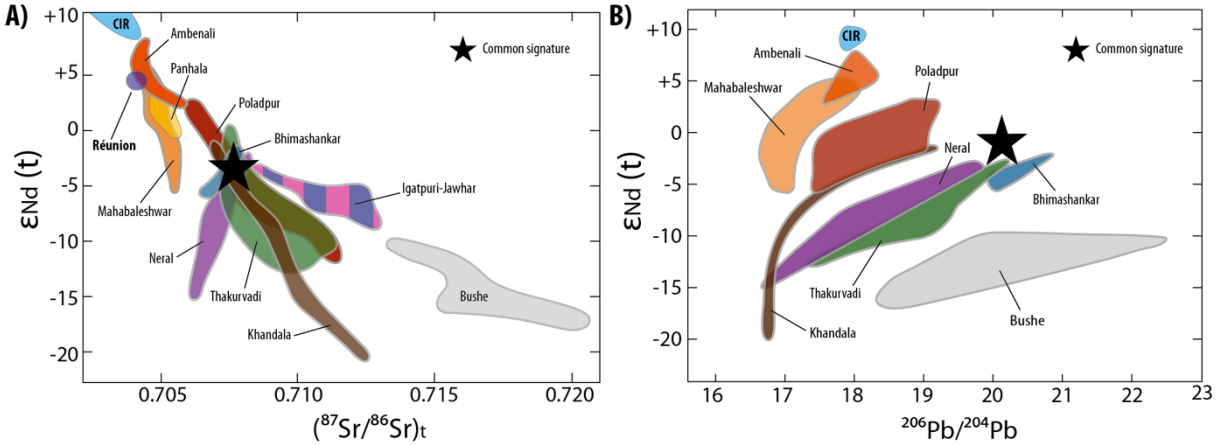

Figure 2.5 – Isotope diagrams from Peng et al. (1994). A) Location of the Main Deccan Province formations in the Nd-Sr isotope space. Réunion (Fisk *et al.*, 1988) and Central Indian Ridge (CIR, Mahoney *et al.*, 1989) shown for comparison. B) Similar to A) for the Nd-Pb isotopic space. All lower formations (Jawhar-Igatpuri to Bushe) converge towards a Common Signature (Peng *et al.*, 1994) suggesting several stages of contamination and evolution of the magmas as well as source different from those of the Ambenali-Mahabaleshwar-Panhala trend.

Figure 2.5 shows that Ambenali is the least contaminated formation of the Deccan Traps with the lowest $(^{87}Sr/^{86}Sr)_t$ and the highest εNd(t) of all Deccan formation. Ambenali has been described as a mixture of MORB- and Réunion-like mantle and considered as a common parental for the other formations of the Main Province (Lightfoot & Hawkesworth, 1988, Mahoney, 1988, Lightfoot *et al.*, 1990). Subsequent contamination would result from at least two stages of contamination by 1) the lower crust, responsible for the *common signature* and 2) several upper crustal end-members resulting in radiating trends from the common signature towards lower εNd(t) and $^{206}Pb/^{204}Pb$ (Peng *et al.*, 1994). Peripheral Deccan-related lavas however do not all fall within this framework (e.g. Melluso *et al.*, 2006). The details of the isotopic evolution of the Deccan Traps formations are however much less straightforward (Chatterjee & Bhattacharji, 2008, and references therein, Bhattacharya *et al.*, 2013) and beyond the scope of this introduction.

2.3.2. Peripheral Deccan volcanism and minor formations

A number of volcanic products have been reported in the literature as the result of peripheral and/or early activity of the Deccan Traps. Despite their rather minor character, these observations are important in order fully to apprehend the extent and dynamics of the Deccan Traps in both space and time. These manifestations are common to all continental flood basalt provinces (Jerram & Widdowson, 2005) and mostly consist of alkaline magmatism (e.g. Subba Rao, 1972 and references therein). Figure 2.3 shows the location of peripheral alkaline magmatism associated with the Deccan Traps.

2.3.2.1. Kutch and Saurashtra (Gujarat)

The lavas of Kutch and Saurashtra have partly preceded, in C30n, and accompanied the emplacement of the Main Deccan Province (C29n) (Basu *et al.*, 1993, Courtillot *et al.*, 2000, Mahoney *et al.*, 2002, Melluso *et al.*, 2006, Paul *et al.*, 2008, Sen *et al.*, 2009). However, the lava flows of Gujarat are not the earliest manifestation of the Deccan plume. Volcanic rocks with isotopic signatures similar to present-day Réunion have been identified further north in Pakistan (south Tethyan suture zone, Figure 2.1). These outcrops predate those of Gujarat lavas by about 2Ma (Kerr *et al.*, 2010) and the possibility of even older manifestations of the Deccan plume has been evoked (Mahoney *et al.*, 2002). In Gujarat, the sedimentary sequence intercalated between both periods of volcanic activity bears evidence of the K-Pg boundary (Courtillot *et al.*, 2000). The lava pile of Gujarat is much thinner than in the Western Ghats and in the order of hundreds of meters, increasing to about 1.5km in the south (e.g. Kaila *et al.*, 1985, Melluso *et al.*, 1995, Peng & Mahoney, 1995). It is discontinuous and affected by faulting (Biwas, 2005, Guha *et al.*, 2005). Despite the faults and rifts, the outcrops are now extremely limited due to the extensive blanketing of the area by quaternary sediments (Figure 2.2). The composition of the lavas of Kutch and Saurashtra differs markedly from the Main Province Tholeiites. Alkali and magnesium contents are generally higher and picritic basalts are common (Krishnamurthy & Cox, 1977, Melluso *et al.*, 1995, Peng & Mahoney, 1995, Krishnamurthy *et al.*, 2000, Melluso *et al.*, 2006). Carbonatites have also been reported on several locations in Gujarat and in the Narmada-Tapti rift (Gwalani *et al.*, 1993, Simonetti *et al.*, 1995, Viladkar & Schidlowski, 2000, Paul *et al.*, 2008 and references therein). Tholeiites do occur in both Kutch and Saurashtra yet no corresponding feeder system has been reported

thus far. It is likely that they have been emitted further south by the feeder dykes of the Western Ghats (Sen *et al.*, 2009).

2.3.2.2. Mount Pavagadh

Mount Pavagadh (Figure 2.3) is an isolated outcrop consisting in a ~500m-thick section (5km across) made of syn-Deccan (Kaneoka & Haramura, 1973), flat-lying lava flow remnants. The section of Mt. Pavagadh is bimodal with alkaline basalt (sometimes picritic) building most of its structure while the upper third is felsic (dacite and rhyolite). No connection of this section with any other Deccan outcrop has yet been established (Sheth & Melluso, 2008).

2.3.2.3. Narmada-Tapti rift

The Narmada-Tapti rift is a complex area in many respects. First, it is an intraplate rift wherein ubiquitous and intense normal faulting syn- and, to a lesser extent, post-Deccan (Kaila *et al.*, 1985, Ju *et al.*, 2013) renders flow correlation – with the rest of the Deccan Traps as well as within the rift itself – much more difficult than for the Main Province (Subbarao *et al.*, 1999, Shrivastava & Pattanayak, 2002). In addition, Deccan volcanism has resulted in large-scale partial remagnetization of many sections (Prasad *et al.*, 1998). A third complication comes from the fact that both Western Ghats-like tholeiites (Peng *et al.*, 1998, Chandrasekharam *et al.*, 1999, Shrivastava & Pattanayak, 2002, Vanderkluysen *et al.*, 2011) and alkali products (Subba Rao, 1972, Gwalani *et al.*, 1993, Simonetti *et al.*, 1995, 1998, Chalapathi Rao *et al.*, 2012) have been emplaced in this area.
Amongst the variety of alkaline rocks of the Narmada-Tapti area, the Abma Dongar carbonatites is certainly the most studied one (e.g. Gwalani *et al.*, 1993, Simonetti *et al.*, 1995, Viladkar & Schidlowski, 2000, Ray *et al.*, 2003) for their geodynamic implications (mantle volatile content: Ray *et al.*, 2003, temperature, amount of melting: Ernst & Bell, 2010).

2.3.2.4. Behradi Kodomali kimberlite

Although other instances of kimberlites have been reported in Indian (e.g. Gregory *et al.*, 2006, Lehmann *et al.*, 2010), the Behradi Kodomali kimberlite is the only such rock that has an end-Cretaceous age (Chalapathi Rao & Lehmann, 2011, Chalapathi Rao *et al.*, 2011b). The

occurrence of kimberlites associated with the eruption of the Deccan Traps is an important geodynamic indicator suggesting that 1) significant heat transfer from the plume the surrounding cratonic root and 2) the Indian lithosphere was thick at the time and location of the Behradi Kodomali kimberlitic intrusion (Chalapathi Rao & Lehmann, 2011, Chalapathi Rao *et al.*, 2011b). See section 2.4 for a discussion of the lithospheric thickness beneath the Indian plate.

2.3.2.5. Mumbai volcanics

Mumbai is located some 80km to the west of the Western Ghats on the coastline (Konkan plain (Figure 2.2 and Figure 2.3). In this area, the lava sequence of the Main Deccan Province (Figure 2.4) is brought to sea-level by a weak north-south anticline structure parallel to the Western Ghats and resulting in a low angle westward dip of the lava flows towards the Arabian Sea: the Panvel Flexure (Hooper, 1990, Dessai & Bertrand, 1995, Sheth, 1998). The area of Mumbai and especially Salsette Island feature alkaline felsic rocks that contrast drastically with the underlying Deccan tholeiites: the Salsette subgroup (Sethna, 1999). Although the latter clearly postdate the main volcanic phase of the Deccan Traps by about 2-3Ma (Lightfoot *et al.*, 1987, Sethna, 1999, Cripps *et al.*, 2005, Hooper *et al.*, 2010, Sheth & Pande, 2013), isotopic signatures resemble those of the Main Deccan Province tholeiites (Lightfoot *et al.*, 1987, Sheth *et al.*, 2013). The Salsette subgroup has thus been interpreted as resulting from the foundering of earlier, underlying grabbroic intrusions related to the ubiquitous Main Deccan Province tholeiites (Lightfoot *et al.*, 1987). Several intrusions related to Main Deccan Province formations (Figure 2.4) have also been reported in this area. Hooper et al. (2010) identified three distinct sets of dykes in the Mumbai area based on chemistry and orientation (Group1: Wai-like composition, random trends; Group2: Kalsubai-like composition, clear north-south trend; Group3: Salsette-like composition, clear north-south trend, cross cut Group1 and 2) and argued for a post-Deccan extension (Laxmi Ridge and Seychelles breakup) of the Indian west coast and a syn-Deccan formation of the Panvel Flexure (see also Hooper, 1990). However, this interpretation has recently been challenged by the discovery of a new 62-63Ma sedimentary sequence within the Salsette subgroup (Sheth & Pande, 2013), casting doubts as to a syn-Deccan formation of the Panvel Flexure.

2.3.2.6. The Seychelles and the Laxmi Ridge

The Seychelles are made of Precambrian granitic terrains and Cretaceous-Tertiary alkaline to tholeiitic intrusions (Devey & Stephens, 1992). Similarities between the latter and the Deccan Traps have been reported (Devey & Stephens, 1991, 1992, Owen-Smith *et al.*, 2013). The tholeiitic dykes of the Seychelles share similarities with the Bushe formation in the Deccan (Devey & Stephens, 1992). In the same way, it has been suggested that the Seychelles tholeiitic and alkaline intrusions correspond to the culmination of volcanic activity in the Deccan (Owen-Smith *et al.*, 2013). However, the published $^{40}Ar/^{39}Ar$ and U-Pb ages reported for these intrusions (63-63.5Ma, Ganerød *et al.*, 2011) may not coincide with the actual culmination of the volcanism in the Deccan Traps (Chenet *et al.*, 2007) but rather to post-Main Province activity (Hooper *et al.*, 2010).

An important unknown regarding the end-Cretaceous early-Palaeogene geodynamics of the Seychelles with respect to the Indian plate stems from the existence of a ~500km-long negative gravity anomaly (Sandwell & Smith, 1997) associated with evidences of pre-geomagnetic chron C28 (Gradstein *et al.*, 2004) of a an early spreading centre: respectively, the Laxmi Ridge and the Gop Rift (Bhattacharya *et al.*, 1994, Malod *et al.*, 1997), Figure 2.1. The Laxmi Ridge is generally described as a micro continent (Talwani & Reif, 1998, Dietmar Müller *et al.*, 2002) with significant ultramafic underplating that became separated from 1- the Indian plate by transient, presumably syn-Deccan, extensional regime (Gop Rift) and 2- (later) from the Seychelles by the onset of the Carlsberg Ridge, which then accommodated all subsequent seafloor spreading in the Arabian Sea (Minshull *et al.*, 2008, Eagles & Hoang, 2014), Figure 2.6. See also Huismans and Beaumont (2011) for two-stage breakup modelling.

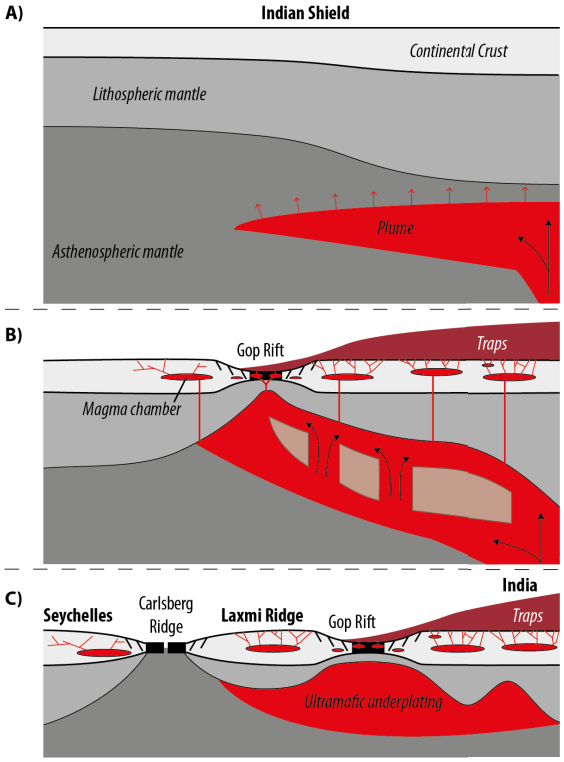

Figure 2.6 – Possible scenario for the formation of the Laxmi Ridge (adapted from Minshull *et al.*, 2008). A) Arrival of the plume beneath the Indian plate. B) Lithospheric erosion and delamination by the plume. Onset of extensional regime along the Indian west coast. Formation of the Gop Rift. Deccan volcanism. C) Post-Deccan formation of the Carlsberg Ridge and Seychelles breakup. Gop Rift inactive.

The age of the India-Laxmi Ridge breakup is difficult to constrain because the magnetic anomaly sequence within the Gop Rift is too short (Bhattacharya *et al.*, 1994). The oldest magnetic anomaly recorded in the Arabian Basin (east side of the Carlsberg Ridge) is C28n (63.1-64.1Ma, Gradstein *et al.*, 2004) on the Seychelles Plateau (Todal & Edholm, 1998, Collier *et al.*, 2008). The Gop Rift must therefore be older than C28n. Plate reconstructions also argue in favour of a pre-C28n Laxmi-India breakup (Royer *et al.*, 2002). Minshull et al. (2008, and references therein) argued for a formation of the Gop Rift in C29r only (0.8Ma) and hence contemporaneous with the emplacement of the Main Deccan Province (Chenet *et al.*, 2007). Alternatively, it is possible that the Gop Rift recorded C31r (68.7-71.0Ma, Gradstein *et al.*, 2004). In this case, it can be interpreted as an early extensional regime resulting from the thermal incubation of the Deccan plume, which resulted in significant underplating of both the Laxmi Ridge and Gop Rift (Collier *et al.*, 2008, Armitage *et al.*, 2011, Arora *et al.*, 2012, Eagles & Hoang, 2014). This would relate the onset of the Gop Rift to the reactivation of existing rifts further north (Narmada, Kutch, Cambay) caused by the changes in tectonic regime within the Indian plate due to the arrival of the Deccan plume (Biwas, 2005, Ju *et al.*, 2013). Considering the roughly north-south orientation of the Gop

Rift, it is reasonable to speculate speculate that the Gop Rift could also be contemporaneous with the early extension episode that resulted in the coastal dyke swarm (Vanderkluysen *et al.*, 2011, Ju *et al.*, 2013), Figure 2.3, and indeed contemporaneous with the emplacement of the Main Deccan Province. However, the early extensional regime responsible for the Gop Rift could also date back to the separation of Madagascar (90Ma, Chatterjee *et al.*, 2012 and references therein), even though further extension as well as significant ultramafic underplating were caused by the Deccan plume in the late-Crataceous and the Seychelles breakup in the early Palaeogene (Arora *et al.*, 2012).

2.4. The Indian lithosphere and the Deccan plume

The lithosphere-asthenosphere transition is boundary layer of both thermal and mechanical nature that constitutes the sole of mechanically coherent tectonic plates (Artemieva, 2009). The interactions between this boundary layer and an impinging mantle plume are of critical importance in understanding Large Igneous Provinces (Saunders *et al.*, 2007). The impingement of a plume on the lithosphere-asthenosphere boundary creates large anomalies of thermal (Morgan, 1971) and chemical (Hofmann & White, 1982) nature that will affect the above-lying plate in a variety of ways and that will ultimately result in thermal anomalies, thinned lithosphere, extension and chemical variations in lavas after the onset of volcanism. These traces of plume activity will remain and can thus be investigated as means to reconstruct plume-related processes (e.g. Saunders *et al.*, 2007, Sobolev *et al.*, 2011). The thickness of the lithosphere directly determines the depth at which primary magmas will be released from their source – however, the actual depth of melting may be slightly different from the lithosphere-asthenosphere boundary (~10km deeper) due to the existence of a plume freezing zone beneath the lithosphere (Watson & McKenzie, 1991). Plume-induced lithospheric erosion will thus affect the depth and amount of melting of primary melt sources, and consequently induce variations in the composition of lavas (Sobolev *et al.*, 2007, 2011). It is also believed to affect plate motion (thinner lithosphere = faster continental drift, e.g. Kumar *et al.*, 2007). The thickness of the Indian lithosphere is therefore a parameter of prime importance in trying to understand the magmatic activity responsible for the Deccan Traps.

The Indian plate is a craton (Figure 2.2). Lithosphere thicknesses of cratons are usually large (≥ 200km) (James *et al.*, 2001, Carlson *et al.*, 2005, Artemieva, 2006, 2009, Eaton *et al.*,

2009, Griffin *et al.*, 2009). Artemieva (2006) proposed that the Precambrian units of Indian Shield were 140 to 200km thick while the Narmada-Tapti area (Figure 2.2) would reach only 80 to 110km. Lehmann et al. (2010) suggested an average thickness of 164km for India. Arora et al. (2012) identified a thickness gradient along the Indian west coast: 120km in the Mumbai area, smoothly decreasing to 95km towards the Laxmi Ridge (west) before transitioning to true oceanic lithosphere west of the Laxmi Ridge. Interestingly, Arora and colleagues also noted a significant thickening 450km southeast of Mumbai (160km). In this area (450km southeast of Mumbai and farther in this direction), there is a steep east-west lithospheric thickness gradient with 165km beneath onshore India decreasing to 65km to the west at the Laccadive Islands (oceanic lithosphere) close to the hypothetical plume path (Arora *et al.*, 2012), Figure 2.7.

Petrological data, to some extent, argue in favour of a generally thick, yet locally thinner Indian lithosphere. Both Precambrian and late Cretaceous diamond-bearing Kimberlites have been reported in India (Lehmann *et al.*, 2010 and references therein), section 2.3.2.4, which implies a lithospheric thickness greater than 140km (Chalapathi Rao & Lehmann, 2011). In the same way, alkali volcanics (Subba Rao, 1972) and (e.g. Sen, 2001, Karmalkar *et al.*, 2005, Talusani, 2010) and garnet-bearing mantle sources also hint at lithospheric thicknesses greater than 80km (Walter, 2014). At the same time, magmatic source rocks in the spinel stability field have also bee reported, especially in Saurashtra, Kutch and in the Cambay-Narmada Tapti junction area (e.g. Sen, 2001, Melluso *et al.*, 2006, Sen *et al.*, 2009), implying shallow lithosphere-asthenosphere boundary (<80km).

Kumar et al. (2007) proposed a very different scenario wherein the Indian lithosphere would have been thinned to about 100km by a large plume before or immediately after (no later than 130Ma) breakup with Gondwana (167Ma). Kumar and co-workers proposed that the very thin Indian lithosphere was directly responsible for the very fast drift of the Indian plate towards Asia. However, this proposition is at odd with several key observations: 1) It fails to explain the existence of Deccan-related kimberlites, lamprophyres, carbonatites and related alkaline lavas. 2) Present-day observations clearly indicate that, except along the Indian west coast, the lithosphere is thicker than 120km. 3) Plumes are known to erode and rejuvenate the continental lithosphere (e.g. Foley, 2008, Sobolev *et al.*, 2011), which implies that the present-day Indian lithosphere must be thinner than it was prior to the impingement of the Deccan plume. Therefore, unless large scale underplating can account for the difference between the Cretaceous lithosphere thickness range proposed by Kumar et al. (2007) and the

range proposed by the various authors quoted in the earlier paragraphs, the proposition that the Indian lithosphere was thin prior to the arrival of the Deccan plume may be considered incorrect. It has also been proposed that the Deccan plume itself was responsible for faster divergence rates of the Indian plate (Eagles & Hoang, 2014).

Sobolev et al (2011) suggested – on the basis of thermo-mechanical modelling of plume-lithosphere interactions – that no lithosphere erosion and subsequent LIPs magmatism would occur if the initial lithospheric thickness was greater than 140-150km.
In this manuscript, it is argued that the Cretaceous lithospheric thickness of the Indian shield was similar to present-day in its central part – i.e. 160-200km (Artemieva, 2006, Priestley & McKenzie, 2006) – and that there was an westward thickness gradient from there so that the Deccan Plume impinged upon a 140km-thick lithosphere beneath the Nasik-Pune dyke swarm (Figure 2.3), and even shallower lithosphere-asthenosphere boundary in Gujarat where spinel-facies mantle sources have been reported (Sen *et al.*, 2009). The cratonic Indian lithosphere has subsequently been eroded and underplated by the Deccan plume, very much in the manner described by Foley (2008) and Sobolev et al. (2011), see also Figure 2.6 of this manuscript, see also Sen and Chandrasekharam (2011). The present-day Indian lithospheric thickness speculated in this PhD thesis is assumed to be very close to a combination of the observations made by Arora et al. (2012), Artemieva (2006) and Priestley and McKenzie (2006). Figure 2.7.

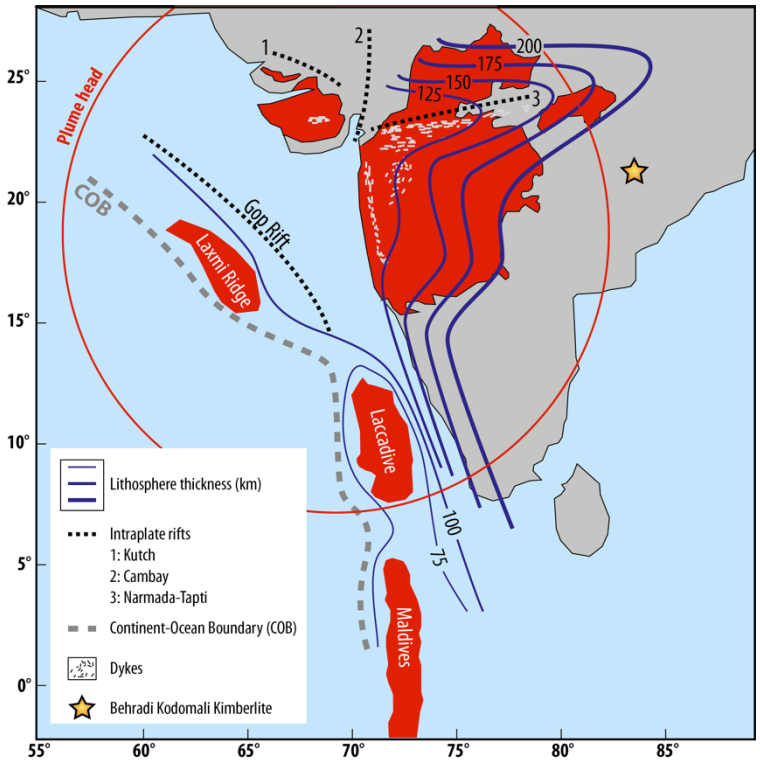

Figure 2.7 – Present-day lithosphere thickness beneath India and the Deccan Traps (based on: Artemieva, 2006, Priestley & McKenzie, 2006, Arora *et al.*, 2012), main rift systems (Figure 2.2), Continent-Ocean Boundary (Arora *et al.*, 2012) major dyke swarms (Figure 2.3), speculated size and location of the Deccan plume at 66Ma (White & McKenzie, 1989) and Deccan-related Kimberlite occurrences: Behradi Kodomali (63-65Ma, Chalapathi Rao & Lehmann, 2011).

The scenario proposed on Figure 2.7 accounts for most of the field observations discussed above:

- The present-day Indian lithosphere is thinner towards centre of the speculated end-Cretaceous location of the Deccan plume centre (White & McKenzie, 1989)
- It is thinner beneath the main feeder dyke swarms (Vanderkluysen *et al.*, 2011, Ju *et al.*, 2013) and intraplate rifts (Murthy, 2002, Bhattacharji *et al.*, 2004, Meert *et al.*, 2010). The postulated thickness beneath Narmada-Tapti and Gujarat (100-125km) fails to explain the occurrence of spinel-facies mantle source rocks in those areas (e.g. Sen, 2001, Melluso *et al.*, 2006, Sen *et al.*, 2009). However, the possibility of large and localized variations of the lithospheric thickness due to erosion by the Deccan plume and/or subsequent thickening due to ultramafic underplating (Foley, 2008, Sobolev *et al.*, 2011) would easily explain that locally mantle source rocks were at depths <80km
- A locally thinned lithosphere would also account for the occurrence of very different volcanic products in relatively small areas of the Deccan Traps: e.g. Lamprophyres (Chalapathi Rao *et al.*, 2012), carbonatites (Gwalani *et al.*, 1993, Ray *et al.*, 2003) and

magmas with shallow sources (e.g. Sen, 2001, Melluso *et al.*, 2006, Sen *et al.*, 2009) in the Cambay-Narmada area (Figure 2.2 and Figure 2.3)

- Lithospheric thickness anomalies along the Narmada-Tapti rift and the Indian west coast are consistent with paleostress modelling on the Indian plate and syn-Deccan extensional events (e.g. Hooper *et al.*, 2010, Ju *et al.*, 2013)
- The Indian lithosphere is also thinner along the beginning of the Deccan plume path in the Indian Ocean (Laccadive and Maldive archipelago) (Laccadive and Maldives archipelago, Duncan, 1990)
- Figure 2.7 is also consistent with the thick lithosphere required for the emplacement of the Behradi Kodomali diamond-bearing kimberlite complex during the main Deccan volcanic phase (Lehmann *et al.*, 2010, Chalapathi Rao & Lehmann, 2011)

2.5. Réunion Island

Réunion Island is the present-day expression of the Deccan plume (Duncan, 1990, Mahoney *et al.*, 2002), Figure 2.1. The emerged part of the island is about 70×50km while the whole volcanic edifice is about 200km in diameter on the ocean floor (Figure 2.8). It is located on early-Palaeogene lithosphere (Duncan, 1990, Fretzdorff & Haase, 2002) that is about 120km-thick (Ellam, 1992), and therefore close to the maximum possible thickness of the oceanic lithosphere (see also Ellam, 1992 for maximum oceanic lithosphere thickness). The plate motion at Réunion Island has been estimated at about 20mm/yr (DeMets *et al.*, 1994).

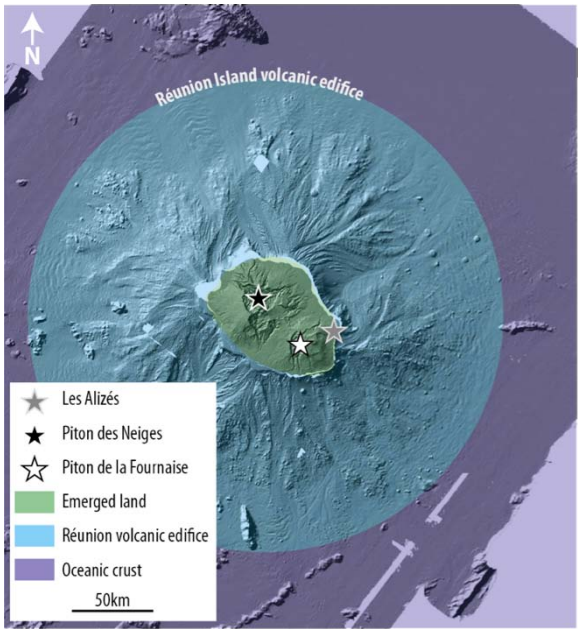

Figure 2.8 – Topography of Réunion Island. Modified from Le Friant et al. (2011)

The Réunion Island includes two or three different volcanoes:
Les Alizés volcano would be the oldest (>4Ma: Smietana, 2011) but its existence is being debated (e.g. Le Friant *et al.*, 2011). It woud have ceased its activity at about 400ka (Smietana, 2011, and references therein).
Piton des Neiges volcano was established shortly after Les Alizés (Upton & Wadsworth, 1965, Gillot *et al.*, 1994). Its latest period of activity was dated at 12ka (Deniel *et al.*, 1992).
Piton de la Fournaise volcano is the current active centre of eruption. It became active around 400ka (Oehler *et al.*, 2008). Proponents of the existence of Les Alizés volcano argue that Piton de la Fournaise was built after the collapse of the previous (Lénat *et al.*, 2001, Oehler *et al.*, 2008).

Réunion Island is an oceanic island similar to Hawaii (Moore & Clague, 1992) in the sense that it is related to a hotspot (the tail stage of the Deccan plume, Duncan, 1990). Nevertheless, if the Hawaiian model of Moore and Clague (alkalic pre-shield, tholeiitic shield building and alkalic post-shield stages) holds for Piton des Neiges (e.g. Upton & Wadsworth, 1965), it has been challenged by reports of differentiated alkaline rock corresponding in age and location with the earliest activity of Piton de la Fournaise (Albarède *et al.*, 1997). These observations may nevertheless be reconciled with the standard Hawaiian ocean island model if the differentiated lavas previously attributed to Piton de la Fournaise belonged instead to an older edifice, namely Les Alizés volcano (see Smietana, 2011 and related publications for a thorough discussion of the structure and evolution of Réunion Island).

3. Re-visiting the eruption timing of the Deccan Traps

It has been known for some time that the main eruptions of Deccan Traps occurred in the late Cretaceous to early Danian. This first age estimation of the onset of Deccan volcanism was based on paleontological studies of underlying sedimentary deposits beneath and in contact with Deccan lavas: the Lameta Formation (Courtillot *et al.*, 1986, Buffetaut, 1987, Salil *et al.*, 1997). An early-Tertiary age had been assigned to intertrappean deposits of the Mumbai area (top of the Deccan Traps section) as early as the late nineteenth century (Blanford, 1867), and still earlier activity of the Deccan Plume (up to 99Ma) has been reported in present day Pakistan (Mahoney *et al.*, 2002). However, such an early trace of Deccan plume activity is somewhat inconsistent with paleogeographic reconstructions (Roddaz *et al.*, 2011, Chatterjee *et al.*, 2012).

A more detailed chronology of the eruptions is difficult to establish. The required resolution is at the order of centuries to millennia. At this level traditional radiochronology is of little use and the marine sedimentary record is often too coarse. Despite these rather stringent constraints, very valuable information as to the relative timing can be obtained from high-resolution paleomagnetism, weathered basalt horizons (Bole Beds), Giant Plagioclase Basalt flows, biostratigraphic and pelagic carbonate Os isotopic ratios.

3.1. Radiometric dating of the Deccan Traps

Although radiometric dating is of limited use when trying to obtain the details of the remarkably swift events that occurred in the late Cretaceous to early Danian, the method did provide the first absolute time constraints to this series of events by showing that the eruption of the Deccan Traps started prior to and straddled the K-Pg boundary. See Chenet et al. (2007, Figure 4) and Courtillot et al. (1986, Figure 4) for a compilation of radiometric dating for the Deccan Traps.

Moreover, recent ^{40}K-^{40}Ar dating (Chenet *et al.*, 2007) shed new lights on the Deccan Traps by showing that the eruption occurred in three different phases: Phase 1 predates the K-Pg boundary by about 2Ma, Phase 2 occurred just before and ended at the K-Pg boundary and Phase 3 happened ~2-300ka later in the Danian and therefore post-dates the K-Pg boundary.

3.2. High-resolution paleomagnetism

The main eruptions of the Deccan Traps are known to straddle three to four geomagnetic chrons, namely C30r, C30n, C29r and C29n (Courtillot *et al.*, 1986), the most intense ones having occurred in C29r.

Recently, Chenet and co-workers (Chenet, 2006, Chenet *et al.*, 2007, 2008, 2009) carried out an extensive field campaign during which they sampled every lava flow in the Western Ghats resulting in an almost complete, 3.5km-thick composite section of the main Deccan province (Figure 2.4), from the north near Igatpuri, to Mahabaleshwar in the south. The unique spatial resolution of their dataset paved the way for a new interpretation of paleomagnetic data that is based on variations of the paleomagnetic mean site directions: Applying today's magnetic secular variations of 2-3° per century, and assuming it was similar in the Cretaceous, they were able to identify directional groups wherein a sequence of lava flows feature magnetic directions that are statistically similar, thereby suggesting they erupted during a period of less than a century. Moreover, no thick weathered horizons (Bole Beds, see section 3.3) were found within directional groups, which further supports a rapid emplacement.

Thirty such directional groups (or single eruptive events) have been identified in this manner, implying a total eruption time of 300 to 3000 years. Lava flows outside directional groups (41 in all) cannot be temporally constrained in the same way, as pole wander paths cannot be predicted over several hundreds of years. By assuming a total time of emplacement of 10 to 100 years – based on volcanological observations at the Roza flow field, Columbia River Basalt (Thordarson & Self, 1998) and the frequent lack of weathering features – for each of the 41 individual flows, their total time of emplacement varies between 410 and 4100 years. Hence, the combined eruption time of the Western Ghats lava pile would have been between 1000 and 7000 years, plus an unknown intervening quiescence time. It should nevertheless be stressed that faster emplacement rates for both directional groups and/or individual flows cannot be ruled out as instances of extremely fast (days to months) variations the geomagnetic field have been identified elsewhere on Earth from both sedimentary (Valet *et al.*, 1986, Channell & Lehman, 1997) and volcanic (Coe *et al.*, 1995, Bogue & Glen, 2010) formations.

Chenet et al. (2008) and Gérard et al. (2006) attempted to evaluate the extent of these quiescence periods and proposed that thin (cm-thick) weathered horizons (thin red boles) may have formed over a few years (typically 10) while thicker ones (m-thick) would have required several thousands of years. Thin red boles (38 in all) being negligible compared to the 6 thick

ones reported, Chenet and co-workers arrived at an estimated 300,000 years of quiescence time based on red boles only, plus an unknown duration where time gaps have not been recorded. This is an order of magnitude larger than the eruption time proposed above. Nonetheless, the possibility that red boles or bole beds may not necessarily imply long volcanic quiescence, however thick they may be, will be discussed in section 3.3.

This high-resolution paleomagnetic data agrees with the episodic character of the Deccan Traps eruption seen at coarser timescales in geochronological (Chenet *et al.*, 2007), petrological (Self *et al.*, 2008b) and paleontological (Keller *et al.*, 2008a) data with a first and minor phase in early C30n, followed by a second and most intense phase in mid-C29r, which is believed to contain – or to have ended at – the K-Pg boundary and, finally, a third phase beginning early in C29n and followed by minor volcanic events and rifting for a few millions of years on (Hooper *et al.*, 2010, Sheth & Pande, 2013). This high-resolution paleomagnetic dataset also, and most importantly, shows that the three main phases are themselves made of shorter ones of extreme intensities (directional groups). It provides a very high precision in the relative timing to within the uncertainties regarding the quiescence time, which now becomes the most important unknown.

Similar observations of discontinuous activity with large pulses, and intervening but difficult-to-measure quiescence periods, have been reported using the same method in Siberia (Pavlov *et al.*, 2011) and Karoo (Moulin *et al.*, 2011).

3.3. Bole Beds and/or Red Boles

Bole beds are weathered basalt horizons intercalated in a lava flow sequence. They are also referred to in the literature as intrabasaltic layers or flood basalt hosted paleosols. Their colour varies according their oxidation state, composition and grain size distribution from grey-blue to green or red. Sayyed (2013) provides an extensive review on bole beds and their potential use as palaeoclimatic indicators of environmental changes.

In the Deccan Traps, bole beds are mostly red and thick (m-thick) or thin (cm-thick). Green boles also occur but are far rarer. Overall, bole beds are more numerous towards the top of the Western Ghats composite section (Sen, 2001, Chenet *et al.*, 2008, 2009). They have been reported in the literature ever since the early publications on the Deccan Traps and their interpretation has remained controversial. They have been argued to be sediments, weathered basalts or pyroclastites (e.g. water pools filling topographical lows), paleosols, or basalts

metasomatized by hydrothermal alteration. See Chenet et al. (2008), Sen (2001) and references therein.

Green boles feature contacts with both under- and over-lying flows, which are sharper than those of red boles. Their colour is due to the presence of Mg in the form of chlorite. Overall, there seem to be a general consensus that green boles are altered ash deposits, probably equivalent to today's andosols or volcanic ash soil. High concentrations of K and Rb also argue in favour of aeolian ash transportation. (Ghosh *et al.*, 2006). However, F. Fluteau (IPGP, personal communication) observed a green bole continuous with a red bole in the field.

In the case of *red boles*, the boundary with the underlying lava appears interstratified and amygdaloidal while the contact with the overlying flow is generally sharp. Their colour results from the presence of Fe^{3+} in the form of geothite. Their chemical composition clearly indicates that red boles are the result of basalt weathering (Ghosh *et al.*, 2006). Furthermore, Ghosh and co-workers argued that red boles had clear characteristics of developing soils, such as shrinkage cracks, clay and secondary minerals as well as partially dissolved plagioclase grains (Sayyed, 2013). Paedogenesis from fresh basalt is known to take several thousands of years (Patino *et al.*, 2003) and this observation supports the idea that red boles took a long time to form. Nevertheless, concentrations in immobile elements (e.g. Al, Fe^{3+}) differ from that of laterites, which suggests processes different and probably shorter than paedogenesis (Widdowson *et al.*, 1997). In the same way, Sayyed and Hundekari (2006) compared red boles to modern Deccan soils and concluded that the bole beds have not undergone intense chemical weathering or paedogenesis. Srivastava et al. (2012) recently proposed that recycling and redeposition by surface runoff, infiltration and ponding was the most likely process of bole bed formation in the Deccan Traps. In other words, most bole beds are interpreted by Srivastava and colleagues as detrital deposits governed by shallow streams. Moreover, Srivastava et al also stress that signs of paedogenesis or lateritization in Deccan bole beds are in fact seldom unequivocal.

In the field, red boles also appear to be associated with Giant Plagioclase Basalt flows (Sen, 2001, Higgins & Chandrasekharam, 2007). See section 3.4.

3.4. Giant Plagioclase Basalts

Giant Plagioclase Basalts (GPB) differ from any other Deccan lavas in that they contain plagioclase phenocrysts that are abundant (up to 25mod%) and large (up to 30mm in length) whilst most other Deccan products only contain very low amounts of small phyric plagioclase. GPBs are the most evolved lavas of the Main Deccan Province. They occur as 5-to-10m-thick flows at the top of the lowest formations of the Western Ghats (Kalsubai sub-group (Figure 2.4), although their occurrence in Wai subject to debate (Deshmukh *et al.*, 1977)) and have therefore been of great help in mapping this part of the lava section (Hooper *et al.*, 1988, Subbarao *et al.*, 2000). Many GPBs have also been emplaced directly on red boles (Deshmukh *et al.*, 1977, Beane, 1988, Sen, 2001). Although uncommon, GPBs have been observed in other volcanic settings (Naslund, 1984, Cullen *et al.*, 1989, Furman *et al.*, 1991).

The relevance of GPBs in understanding the rate of the Deccan Traps eruption stems from the fact that the large plagioclase phenocrysts are believed to have formed over the entire life-span of a magma chamber. Therefore, the time taken by the large phenocrysts to grow is believed to be equal to the eruption time of the formation they belong to (Hooper *et al.*, 1988, Sen, 2001, Borges, 2007, Higgins & Chandrasekharam, 2007, Borges *et al.*, 2013). Plagioclase phenocrysts would have crystallized in convecting, upper crustal magna chambers. Being buoyant, they would accumulate near the top of the chamber and increased in size in response to the continuous supply of magma. After the end of an eruption cycle, a new magma pulse – of a new formation – would eject the Giant Plagioclase magma, sometimes on top of red boles, after a period of dormancy (Sen, 2001, Higgins & Chandrasekharam, 2007). Thus, finding out how long the phenocrysts took to reach their large size is similar to measuring the eruption time of an entire formation. This has been made possible by the application of diffusion/relaxation modelling of $^{87}Sr/^{86}Sr$ zoning in the plagioclase phenocrysts (Borges, 2007, Borges *et al.*, 2013). Such studies yielded maximum residence times of 780 years for 5cm crystals and suggest that the peak of volcanic activity lasted a minimum of 21,000 years, including some periods of dormancy as several GPBs have been erupted onto red boles. These observations also mostly preclude the possibility of (upper) crustal assimilation in the Deccan Traps and argue in favour of large volumes of melts being extracted from an enriched source with low solidus temperatures (e.g. eclogite, Borges, 2007, Borges *et al.*, 2013). Yet, as Borges and co-workers duly noted, high bulk-rock $^{87}Sr/^{86}Sr$

ratios indicative of crustal contamination occur in the Deccan Traps, especially in Mg-rich units (e.g. Bushe formation). Such a pattern may be explained by either rapid and turbulent melt transport through cracks that can efficiently assimilate fragments of wall-rock (Huppert & Sparks, 1985) or by lower crustal assimilation. In the Deccan case, turbulent transport through the crust may also explain the rare yet sometimes extremely abundant xenoliths of in some dykes (Ray *et al.*, 2008).

3.5. Paleoenvironmental data

Paleoenvironmental temporal constraints stem from various proxies in the sedimentary record: high-resolution biostratigraphy and isotopic ratios in marine sediments. Unfortunately, this valuable information can only be pinpointed in time by means of assumptions and models. These include sedimentation rates and chemical precipitation models (Kyte *et al.*, 1993), inter-correlation with other sections that have been precisely dated (e.g. by radiochronology, magnetostratigraphy, biostratigraphic age determination, Coccioni *et al.*, 2004), correlation with astronomical cycles (Boulila *et al.*, 2011) and magnetostratigraphy itself (Cande & Kent, 1995, Gradstein *et al.*, 2004, Robinson *et al.*, 2009, Keller *et al.*, 2011). The uncertainties inherent to these models generally limit the resolution to greater than a few tens or hundreds of thousands – if not millions – of years (Burke *et al.*, 1982, Pegram *et al.*, 1992, Peucker-Ehrenbrink & Ravizza, 2000, Nordt *et al.*, 2002, Wilf *et al.*, 2003, Keller *et al.*, 2011). This is true for both absolute and relative timeframes. Nevertheless, the importance of paleoenvironmental data remains twofold: 1- it provides a tool for tracking climatic variables such as paleotemperatures (oxygen and carbon isotopes), proxies for erosion rates and sources (osmium isotopes) and species diversity (foraminifera) over several hundreds of thousands of years and thereby provides useful information as to Deccan-induced climate/environmental change. 2- it is especially useful in trying to untangle the footprint of the Chicxulub impact versus that of Deccan volcanism because the rate at which both of these events occurred is extremely different (seconds versus tens to hundreds of millennia).

3.5.1. Intertrappean sediments

There are several instances of intertrappean sediments in the Deccan Traps, including some that were of great help to the first attempts to determine the age of the Deccan Traps

(Blanford, 1867, Bajpai & Prasad, 2000, Khosla & Sahni, 2003, Cripps *et al.*, 2005, Singh *et al.*, 2007, Bajpai *et al.*, 2013). Unfortunately, most of these sediments comprise freshwater to estuarine facies and may thus not be correlated to global sedimentary and paleontological data. Such material may be used to monitor relative and local environmental and faunal changes yet they are of no use when it comes to biostratigraphic age determination, or more generally to tracing the global consequences of the emplacement of the Deccan Traps and the role it played with respect to the end-Cretaceous mass extinction (Jaiprakash *et al.*, 1993, Raju *et al.*, 1995, 1996).

The Krishna-Godavari Basin of southeast India is very promising in this respect. It contains marine deposits that are intercalated with lava flows in the Rajahmundry area (Baksi *et al.*, 1994, Raju *et al.*, 1995, 1996, Keller *et al.*, 2008a, 2011). These lava flows have long been recognized as being part of the Deccan Traps (Venkaya, 1949), thereby forming what has been recognized as the longest (~1000km) lava flows so far known on Earth (Self *et al.*, 2008b). The association of the Rajahmundry Traps with the main Deccan province was confirmed on a variety of grounds, mainly magnetostratigraphic and geochemical (Duncan & Pyle, 1988, Lightfoot *et al.*, 1990, Subbarao & Pathak, 1993, Banerjee *et al.*, 1996, Baksi, 2001, Jay & Widdowson, 2008). Furthermore, the lava flows of the Rajahmundry Traps have been identified as members of the Ambenali and Mahabaleshwar formations (Self *et al.*, 2008b).

Keller and co-workers (Keller *et al.*, 2008a, 2009c, 2011) carried out intensive biostratigraphic and magnetostratigraphic fieldwork in the Rajahmundry Traps. They were able to bring new valuable insights as to the age and timing of the Rajahmundry traps – and therefore of the final stages of volcanism in the main Deccan province – as well as on the faunal changes during their emplacement. First and foremost, the Rajahmundry Traps encompass the end of C29r (Maastrichtian) and the beginning of C29n (Danian) and hence straddle the K-Pg boundary, which is located in C29r (Courtillot *et al.*, 1986, Renne *et al.*, 2013). Moreover, it appears that the mass extinction was underway in C29r prior to the eruption of the first so-called mega-flow found in the Krishna-Godavari basin as planktic foraminiferal species richness had already suffered a 50% loss (Keller *et al.*, 2012). The eruption of the first mega-flow was followed (or accompanied) by a further 50% drop in species richness and the extinction was complete by the end of phase 2 (Chenet *et al.*, 2007) after the eruption of the next three to four pre-K-Pg boundary mega-flows of reversed

polarities (C29r). No recovery of species diversity has been observed in between both sets of mega-flows. Phase 3 (Chenet *et al.*, 2007) started near the C29r-C29n reversal and is expressed in the Rajahmundry area by four other mega-flows of normal polarity (C29n). At this time, no major faunal diversity loss have been recorded, which suggests a lower intensity of volcanism and/or that post-phase 2 species had adapted to high stress conditions. Finally, full recovery took place only after phase 3. (Keller *et al.*, 2011, 2012). These observations suggest that phase 2 of Deccan volcanism (i.e. Jawhar to lower-Ambenali, Figure 2.4) alone might have been responsible for the K-Pg mass extinction. In addition, paleomagnetic data and biozone ages require that 260 to 380ka elapsed between phase 2 and phase 3 mega-flows. Nevertheless, it has been suggested that pahoehoe to a'a flow type transition has recently been advocated as a possible limiting factor to the development of very extensive lava flows (Duraiswami *et al.*, 2003, 2013). As a result, Duraiswami and colleagues have proposed multicentre eruptions in order to explain the similarities of the Rajahmundry Traps with the Western Ghats lavas.

3.5.2. Strontium and osmium isotopes

The variations of $^{87}Sr/^{86}Sr$ (Burke *et al.*, 1982) and $^{187}Os/^{186}Os$ (Pegram *et al.*, 1992) in sedimentary marine carbonates over geological times provides a unique record of the origin of the detrital material supplied to the ocean: the erosion of mantle-derived rocks (e.g. oceanic islands or ridges) gives isotopic signatures significantly different from that of continental crust weathering products (DePaolo & Ingram, 1985, Hess *et al.*, 1986, Hodell *et al.*, 1989). Both seawater Sr and Os isotopic records show similar patterns throughout the Cenozoic (Pegram *et al.*, 1992). However, these isotopic systems are fundamentally different (Peucker-Ehrenbrink & Ravizza, 2000) and these differences are extremely relevant in the case of the end Cretaceous extinction. First, an extra-terrestrial impact could reset the $^{187}Os/^{188}Os$ to non-radiogenic values while not affecting the marine Sr record. Several authors have attempted to use Sr isotopes in order to constrain the origin (impact versus volcanism) of the end-Cretaceous extinction (Vonhof & Smit, 1997, MacLeod *et al.*, 2001). However, most of them used Sr as a proxy for continental weathering and argued that impact-induced climate change was to blame for changes in weathering intensities, even though acid rains and wetter climate could have been caused by intense volcanism (Self *et al.*, 2006, Self *et al.*, 2008a, Ganino & Arndt, 2009, Sobolev *et al.*, 2011). Secondly, the residence time of Os in seawater (10-40ka)

is shorter than that of Sr (2-4Ma) (Pegram *et al.*, 1992, Hodell, 1994, McArthur *et al.*, 1998, Peucker-Ehrenbrink & Ravizza, 2000). Such a short residence time – which nevertheless remains longer than ocean mixing times (~10^3yr) (MacLeod *et al.*, 2001) – could prevent a complete homogenization of the seawater $^{187}Os/^{186}Os$ in isolated ocean basins (Robinson *et al.*, 2009). At the same time, it offers a much higher resolution record of the global paleoclimate by keeping traces of short-periodic fluctuations such as glacial-interglacial cycles (Oxburgh, 1998) that would otherwise be buffered in the Sr isotopic system wherein only long-term forcing, such as tectonics, may be seen (Burke *et al.*, 1982, Hodell *et al.*, 1989, Hodell, 1994).

Os isotopes have been used in the past to trace the onset and the environmental consequences of Large Igneous Provinces (Cohen & Coe, 2002, Turgeon & Creaser, 2008) but these findings lacked independent validation of their timing (Robinson *et al.*, 2009).

Robinson et al. (2009) recently published high-resolution marine $^{187}Os/^{188}Os$ data coupled with PGE concentrations from late-Cretaceous pelagic carbonate sections at Deep Sea Drilling Program (DSDP) site 525 in the Atlantic, DSDP site 577 in western Pacific and Ocean Drilling Program (ODP) site 690 in the Weddell Sea as well as a the subaerial Bottaccione section in Italy (Premoli-Silva & Sliter, 1995). Using appropriate age models, Robinson and colleagues were able to increase the temporal resolution of their sampling to 40-100ka and as much as 15ka for special interest samples. Furthermore, coupling with PGE concentrations and published isotopic and paleomagnetic data produces a very coherent $^{187}Os/^{186}Os$ dataset between the four sampling sites. Two $^{187}Os/^{186}Os$ excursions, one early in C29r and the second just before the K-Pg boundary lasting between 100 and 200ka, have been identified from this record (Robinson *et al.*, 2009, Figure 5). It has been suggested that the outpouring of the Deccan basalts on the Dharwar Craton would have removed a source of radiogenic Os by preventing the felsic rocks of the craton from being eroded away (Ravizza & Peucker-Ehrenbrink, 2003). Moreover Ravizza and co-workers proposed that the Os inventory of the Deccan basalts was too low (Allègre *et al.*, 1999) to account for the changes observed in seawater composition. Nevertheless, the Os inventory of Deccan may not be so straightforward because high Os concentrations have been observed in Deccan laterites (Wimpenny *et al.*, 2007). As to the role of the Deccan Traps with respect to the K-Pg extinction, Robinson et al. (2009) point out that that despite its duration (~0.3Ma), the initial decrease in $^{187}Os/^{188}Os$ in C29r seems to have had no consequences on the environment. On the other hand, paleontological (Keller *et al.*, 2011, 2012), paleomagnetic (Chenet *et al.*,

2008, 2009) and ^{40}K-^{40}Ar (Chenet *et al.*, 2007) data show that the actual first Deccan phase (<10% of total volume) occurred in C30n or C30r and that the second and main Deccan phase – responsible for 80% of the total volume – occurred in C29r and led to the K-Pg extinction while a third phase (20% of total volume) took place after the extinction in C29n. It is thus likely that the decline in $^{187}Os/^{186}Os$ seen by (Robinson *et al.*, 2009) in early C29r was a consequence of the early Deccan eruptions and its associated background activity while the second and sharper $^{187}Os/^{186}Os$ excursion was the consequence of the actual second – according to (Chenet *et al.*, 2007) – and main phase of Deccan volcanism (80% of total volume) that ultimately led to the extinction (Keller *et al.*, 2012). However, the fact that no $^{187}Os/^{186}Os$ excursion is seen earlier in C30n casts significant doubt as to either the age, and intensity of the earliest activity of the Deccan Traps, or the sedimentary age models.
Finally, PGE concentrations and $^{187}Os/^{186}Os$ excursions in marine pelagic carbonates show no trace of an extra-terrestrial impact (Robinson *et al.*, 2009).

3.6. Further speculations on the emplacement of the Deccan Traps near the K-Pg boundary

By pulling together the information provided by the various proxies mentioned above, as well as by adding hypotheses to those proposed by Chenet and co-workers (Chenet *et al.*, 2007, 2008, 2009), a new interpretation of the timing of the Deccan Traps eruption and the end-Cretaceous extinction has been developed. First, high-resolution paleomagnetic datasets were re-interpreted in order to construct a *continuous* composite section of all Deccan lava flows and assess the consequences in terms of cumulative erupted volume, quiescence time and magma fluxes. This timeframe – very similar to that of Chenet and co-workers – will later (section 5) be coupled with bulk-rock trace element geochemical signatures. Possible correlations between this hypothetical scenario and paleoenvironmental proxies and observations will then be assessed.

3.6.1. Continuous Deccan eruption scenario

This section is dedicated to a re-interpretation of the high-resolution paleomagnetic dataset of Chenet and co-workers (Chenet *et al.*, 2008, 2009) presented in section 3.2.

The continuous composite section of the main province of the Deccan Traps is derived from the following observations and assumptions:

- Sample order and red bole locations have been taken from Chenet et al. (2008, Figure 7) and Chenet et al. (2009, Figure 9). Directional groups (DGs) are from Table 1 of Chenet et al. (2008) and Table 4 of Chenet et al. (2009). Erupted volumes come from Chenet et al. (2009) Table 5. These have been changed to fractions as their data explains only 10 to 25% of the original volume of the Deccan Traps (e.g. Sen, 2001, and references therein)
- SI20 is the oldest (transitional) sample (bottom of the sequence in the field). The possibility that SI13 and SI22, which belong to the Latifwadi formation, could be older than SI20 has been ruled out. SI20 has thus been thought to have the age of the C30r-C30n magnetic transition, 67.61Ma (Cande & Kent, 1995), corrected to the latest age estimate of the K-Pg boundary of 66.043±0.043Ma (Renne *et al.*, 2013): Cande and colleagues assumed a K-Pg age of 65.0Ma, which implies a 1.043Ma correction to the age of 67.61Ma for the C30r-C30n transition (67.61 + 1.043 = 68.653Ma). The possibility that the lower Western Ghats sequence might have in fact recorded the C31n-C30r transition at 67.735 + 1.043 = 68.778Ma (Chenet *et al.*, 2009) was not considered here
- The K-Pg boundary has been identified in the Rajahmundry traps/Krishna-Godavari Basin of southeastern India as being contained within the early Ambenali formation (Knight *et al.*, 2003, Baksi, 2005, Keller *et al.*, 2008a). Cande and Kent (1995) noted that the K-Pg boundary is expected to have occurred 250ka after the C29r-C29n reversal. This constraint is accounted for by assigning the age of the K-Pg to sample MB22 (i.e. first sample of the oldest directional group in Ambenali)
- Thin red boles form over 10 years while thick ones do so over 50ka (Chenet *et al.*, 2008, 2009) and they have all been reported. Note that this probably is incorrect. On the other hand red boles appear hard to trace over long distances in the field and may instead correspond to local topographical infill. This suggests that the eruption might have continued as well as stopped completely during times of red bole formation. See section 3.3
- Single Eruptive Events (SEE), last for 100 years (Chenet *et al.*, 2008, 2009). On the other hand, the time between single flows outside SEE and/or between SEEs themselves has been assumed to be equal to 1ka. This is likely too long as 1) thin red

boles form within 10 years and were not systematically observed above or below single flows, and 2) most contacts between flows, even outside directional groups, are perfectly preserved and show no trace of alteration. Nevertheless, provided that today's 3° secular variation of the magnetic pole applies to K-Pg times, differences in paleomagnetic directions in excess of 3° requires that any pair of event with such a difference be separated by more than a century. Yet very fast excursion in the order of several degrees per month have been identified in the geological record (Coe *et al.*, 1995, Bogue & Glen, 2010)

- Early and peripheral Deccan products (Subba Rao, 1972), the Panhala and Desur formations (Peng *et al.*, 1994) above Mahabaleshwar and the Mumbai volcanics (Salsette subgroup) (Hooper *et al.*, 2010, Sheth *et al.*, 2013) have not been sampled by Chenet and colleagues and were excluded in this scenario
- In the same way, the absence of erosion hiatuses along is assumed
- Finally, this section does not consider the possibility of unreported lava flows. In other words, the sample set of Chenet and co-workers is assumed to be exhaustive – and non-redundant

The resulting composite section is illustrated on Figure 3.1 below.

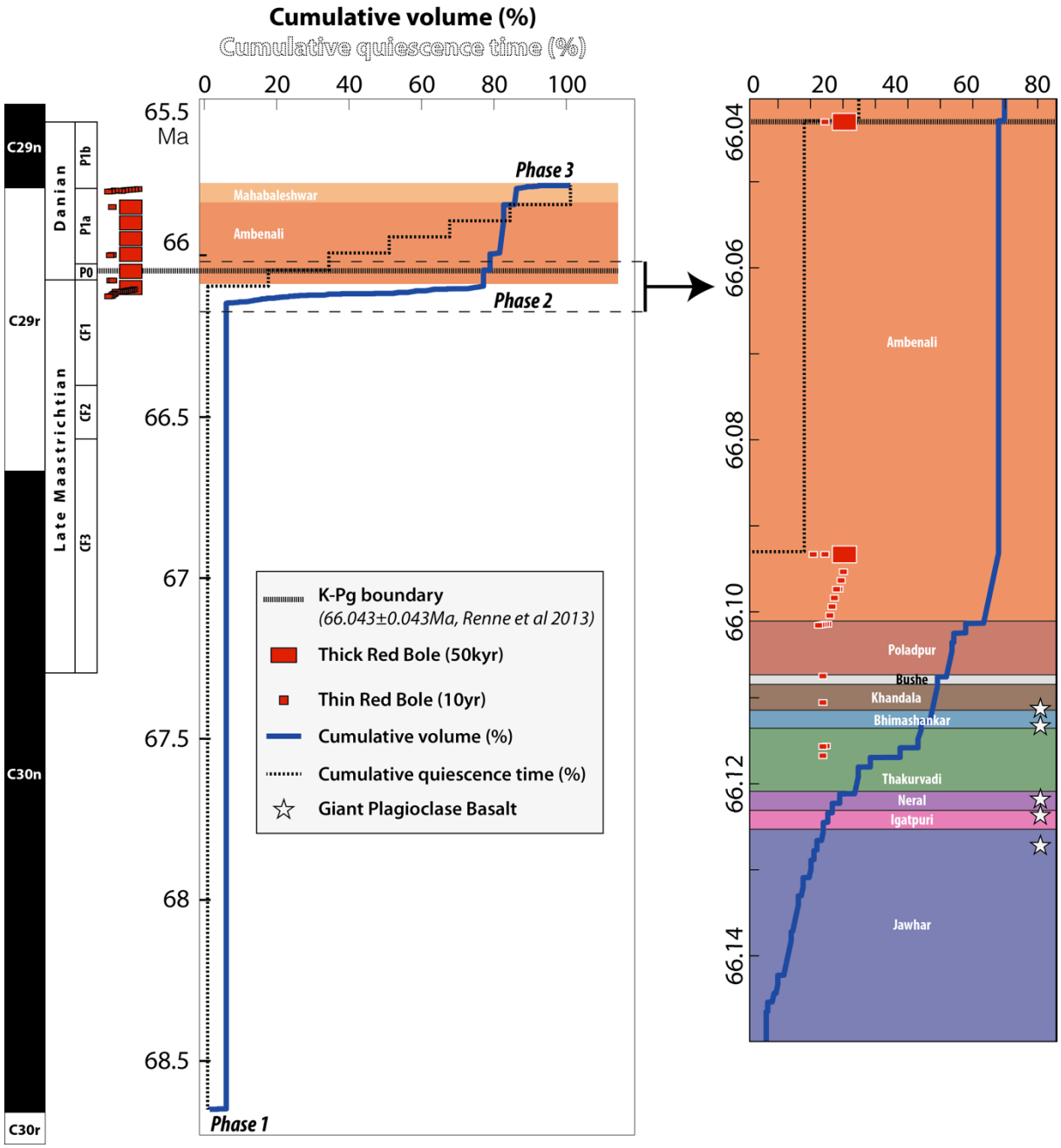

Figure 3.1 - Re-interpretation of the Deccan eruption timeframe based on the radiometric dating and main phases from Chenet et al. (2007) and the high-resolution paleomagnetism from Chenet et al. (2008, 2009). From left to right: magneto-stratigraphy from Cande and Kent (1995) recalculated for K-Pg boundary at 66.043±0.043 Ma (Renne *et al.*, 2013), biozones from Keller et al. (2012), red boles locations, cumulative volume and quiescence time locations from Chenet et al. (2008, 2009). The leftmost figure is an enlargement of phase 2 (Chenet *et al.*, 2007). Giant Plagioclase Basalts locations from Subbarao et al. (2000).

3.6.2. Cumulative volume and eruption rates

Figure 3.1 shows a very discontinuous picture wherein phase 1, responsible for merely less than 10% of the total volume of the Western Ghats occurred at the C30r-C30n reversal, more than 2Ma before the main eruption (phase 2 and 3) and the K-Pg boundary. Phase 2 is responsible for 70-80% of the total volume and spans 50 to 100ka and ends with the K-Pg boundary (hypothesis) in early-Ambenali. Phase 3 accounts for 10-20% of the total volume and is represented by the Mahabaleshwar formation (Panhala and Desur are excluded). Note that the GPB strontium isotopes diffusion and relaxation models mentioned in section 3.4 (Borges *et al.*, 2013) were not integrated to this framework.

Phase 2 would have been responsible for the emplacement of 8.10^5 km^3 of lavas over about 50ka. If the total volume of the Western Ghats was in the order of 1.10^6 km^3 (Sen, 2001, Courtillot & Renne, 2003), the average eruption rate of phase 2 (and in fact for any of the three phases when considered individually) would be in the order of $16km^3/yr$. This is equivalent to 160 times the eruption rates of today's Hawaii: $0.1km^3/yr$ (Courtillot *et al.*, 1986). The average rate over the full emplacement of the Western Ghats ($1.10^6 km^3$ over about 3Ma) looks somewhat different: $0.3km^3/yr$.

3.6.3. Red boles and quiescence time

Figure 3.1 shows the occurrence of red boles along the section and the corresponding cumulative quiescence time considering that thick red boles take 50ka to form while thinner ones do so over only a decade. It is clear that thin red boles are negligible in this timeframe (Chenet *et al.*, 2008, 2009). However, it is important to keep in mind that bole beds in general are difficult to trace over large distances in the field and could thus be of limited lateral extent (F. Fluteau, personal communication). Moreover, GPBs have been described as being associated with red boles in the field (Sen, 2001, Higgins & Chandrasekharam, 2007) whereas red boles were not systematically reported at GPB locations by Chenet and co-workers (Figure 3.1). This indicates that some red boles have likely not been reported.

Figure 3.1 shows a rather surprising relationship between cumulative quiescence time and cumulative erupted volume: the occurrence of large eruptions identified by the existence of directional groups is coeval with the appearance of red boles in the field. This surprising relationship is primarily due to the fact red boles develop on the lava flows themselves.

Therefore, if no flow is reported, e.g. between phase 1 and 2, no red bole will be observed and the cumulative quiescence time will not increase. It is nevertheless noteworthy that neither bole bed nor any sign of erosion seems to have been observed between phase 1 and 2.

Phase 2 contains a significant number of thin red boles, especially towards its end in Ambenali and the occurrence of the first thick red bole of the section. This thick red bole predates the first directional group of Ambenali and the K-Pg since it was hypothesized that the latter was located at the first sample of the first directional group in Ambenali following its proper identification in the Rajahmundry traps, Krishna-Godavari basin, in intertrappean sediments surrounded by Ambenali lavas (Knight *et al.*, 2003, Baksi, 2005, Keller *et al.*, 2008a). Therefore, in this scenario, the K-Pg boundary occurs 50ka after the end of the paroxysmal emplacement of phase 2. This seems in agreement with the fact that the K-Pg boundary is contained within intertrappean sediments in the Rajahmundry traps that are surrounded by sets of mega flows (Self *et al.*, 2008b, Keller *et al.*, 2011, 2012), suggesting lower volcanic intensities at this time.

Phase 3 happens about 300ka after the end of Phase 2. This time constraint again hinges upon the occurrence of thick red boles (6 in all). This duration of 300ka is in agreement with biozones in the oceanic sedimentary record: P0 + P1a ≈ 300ka (Keller *et al.*, 2012). Finally, Phase 3 recorded the C29r-C29n reversal with 7 flows with transitional polarities and 10 with normal polarities.

The Panhala and Desur formation were not included in this section and do not constitute a large body of lava flows.

3.6.4. Coupling with paleoenvironmental indicators

The interpretation of high-resolution paleomagnetic data has been taken one step further by attempting a coupling with paleoenvironmental proxies (Figure 3.2). Amongst the variety of available proxies, only two were considered for the following reasons:

- Paleotemperatures of seawater is a good indicator of the global warming and cooling that might have been caused by intense volcanism and/or extra-terrestrial impact, both presumed causes of the K-Pg extinction
- High-resolution $^{187}Os/^{188}Os$ in deep-sea unlithified carbonates decreases with increasing erosion, increasing rainfall and decreasing cratonic surface exposed to erosion (granitic rocks have a high $^{187}Os/^{188}Os$). Coupled with PGE abundances,

$^{187}Os/^{188}Os$ also helps identifying impact signals (reset of $^{187}Os/^{188}Os$ to undradiogenic values combined with Ir anomaly and Sr isotopes decoupling). Finally, the resolution of the $^{187}Os/^{188}Os$ data published by Robinson et al. (2009) is much finer than e.g. $^{87}Sr/^{86}Sr$ and hence of higher relevance here. See section 3.5.2

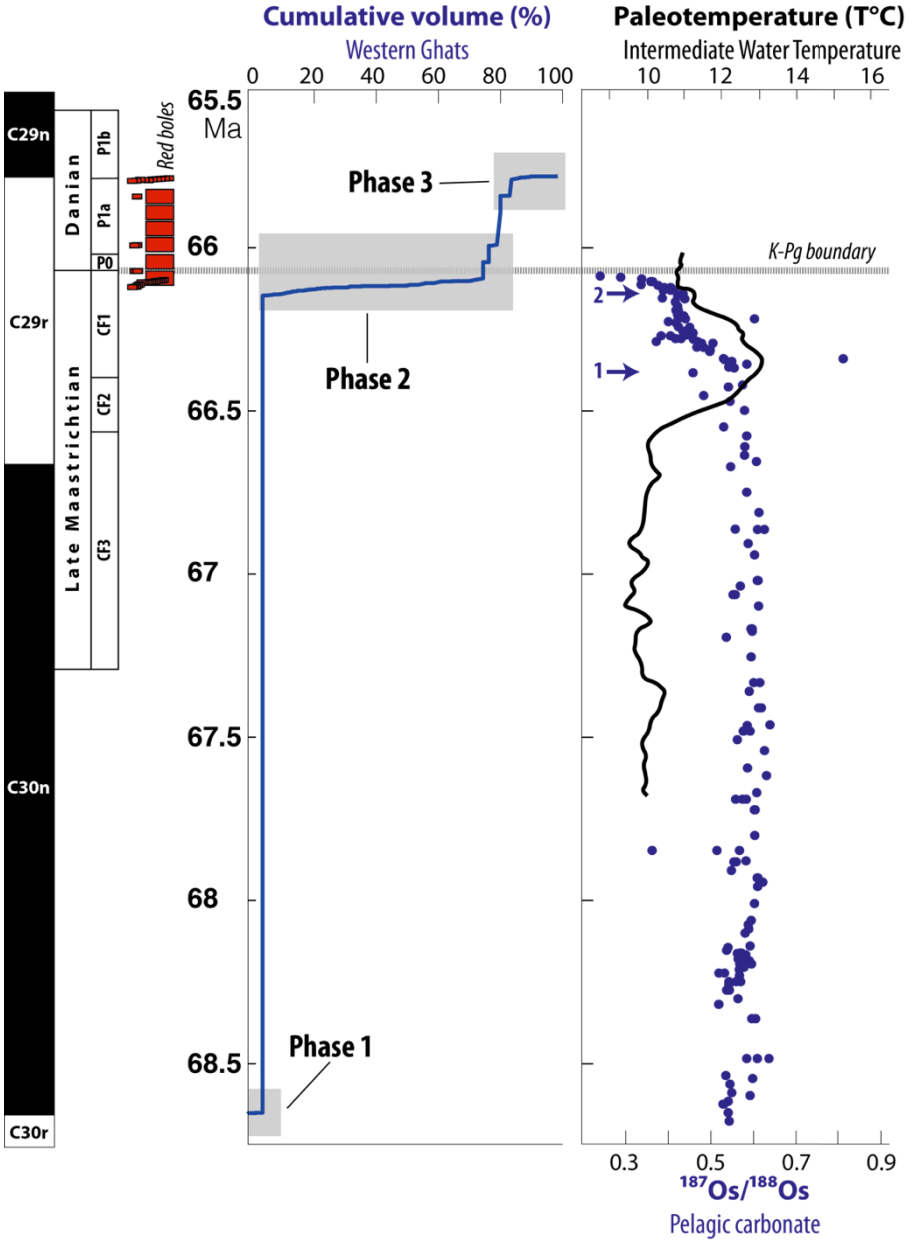

Figure 3.2 - Coupling of the continuous Deccan eruption scenario (Figure 3.1) with paleoenvironmental data. From left to right: magnetostratigraphy from Cande and Kent (1995) recalculated with the K-Pg boundary at 66.043±0.043 Ma (Renne *et al.*, 2013), biozones from Keller et al. (2012), red boles locations from Chenet et al. (2008, 2009), cumulative emplaced volume of the Western Ghats (blue solid line) interpreted from Chenet et al. (2009), paleotemperatures (black solid line) from Li and Keller (1998) and $^{187}Os/^{188}Os$ in pelagic carbonates (blue dots) from Robinson et al. (2009) recalculated for K-Pg at 66.043±0.043Ma (Renne *et al.*, 2013). The blue arrows point at the initial (1) and second (2) drop in $^{187}Os/^{188}Os$ identified by Robinson and co-workers.

The reader should be aware of potential age discrepancies between the biozones (Keller *et al.*, 2012), the cumulative Deccan volume estimate based on Chenet et al. (2008, 2009), the evolution of intermediate seawater temperatures (Li & Keller, 1998) and the high-resolution $^{187}Os/^{188}Os$ (Robinson *et al.*, 2009). All three variables have been re-adjusted to the magnetostratigraphy of Cande and Kent (1995) and latest K-Pg age estimation of 66.043±0.043Ma (Renne *et al.*, 2013). It thus seems reasonable to argue that the K-Pg boundary is properly located in all three datasets. However, any data lying in between polarity reversals and before the K-Pg boundary may suffer from uncertainties pertaining to sedimentation rates and global distribution and evolution of foraminiferal fauna, which homogenization is not instantaneous contrary to geomagnetic reversals. Despite these inconvenience, several important observation can be done and double-checked in the available literature.

Paleotemperatures (Li & Keller, 1998) show evidences of a late Maastrichtian warming (~ 66.5 – 66.3Ma) followed by a cooling near the K-Pg boundary (Vonhof & Smit, 1997, MacLeod *et al.*, 2001, Ravizza & Peucker-Ehrenbrink, 2003, Robinson *et al.*, 2009). The $^{187}Os/^{188}Os$ record does not fluctuate throughout C30n (0.5 – 0.6) with the exception of one point (0.35 at 67.8Ma). It then starts to decrease towards 0.4 at 66.4Ma. This first drop is followed by a second, sharper excursion down to 0.35 starting a few tens of thousands of years before the K-Pg. The dataset does not continue into the Danian. There are also two outsiders at 0.6 and 0.8 between the first and second decrease. Note that the details of the fluctuations in paleotemperatures should not be over-interpreted with respect to the osmium isotope data due to the potential discrepancies mentioned above. Nevertheless, it seems that either of the following proposition is true: 1) The onset of the late-Cretaceous cooling is coeval with the initial drop (1) in $^{187}Os/^{188}Os$. 2) The onset of the late-Cretaceous temperature variations (warming and cooling) is coeval with the general decreasing trend in $^{187}Os/^{188}Os$. Robinson and colleagues (Robinson *et al.*, 2009) also measured PGE abundances along the sections sampled for osmium isotopes and found no evidence of extra-terrestrial impact.

Another mismatch appearing on Figure 3.2 concerns the onset of the warming event at 66.5Ma – which has been attributed to volcanism (Li & Keller, 1998) – with respect to the beginning of phase 2 (66.15Ma) in the Deccan. The Western Ghats composite section of Chenet et al (2008, 2009) does not include the earliest and peripheral formations of the Deccan Traps, namely, the Latifwadi formation and the mostly alkali outcrops of Gujarat. However, the Latifwadi formation has been assigned to phase 1 (Chenet *et al.*, 2007) while

the Gujarat (Saurashtra and Kutch) lavas are considered older than any Deccan tholeiites, and therefore the Latifwadi formation (Sen *et al.*, 2009).

In the same way, phase 1 – which clearly occurred ~2Ma before Phase 2 (Chenet *et al.*, 2007) – is not seen in the osmium isotope record.

These mismatches emphasize that Figure 3.2 must be handled with care.

Finally, the species richness at the El Kef section (the stratotype of the K-Pg boundary) swiftly drop by 50% between biozones CF1 and P0 and then further decreases into the early-Danian (Keller *et al.*, 1995, 2008a). This catastrophic change is too instantaneous to be coupled to the Deccan eruption model presented here, with the exception of phase 2 of the Deccan Traps emplacement, which might have been shorter than speculated here (e.g. shorter red bole formation – see section 3.3 – shorter time gaps between individual flows and during the emplacement of directional groups – see sections 3.2 and 3.4).

3.7. Summary and preliminary interpretations

The emplacement of the Western Ghats occurred in three different phases (Figure 3.1) (Chenet *et al.*, 2007):

- Phase 1 (10% of total volume) at the C30r-C30n reversal (~68.65Ma)
- Phase 2 (70-80% of total volume in 50ka) in C29r (~66.10Ma). Phase 2 ends at the K-Pg boundary
- Phase 3 (10-20% of total volume) after the K-Pg boundary at the C29r-C29n reversal and continued on in early C29n (~65.8Ma). It is represented by the Mahabaleshwar formation in this section
- Earlier Deccan products (Gujarat), peripheral volcanics (Subba Rao, 1972) and the formations above Mahabaleshwar (Panhala, Desur and the Salsette subgroup) where not considered here. Their contribution to the total volume of the Deccan Traps is however believed to be in the order of 10% or less (Paul *et al.*, 2008, Hooper *et al.*, 2010)

Phase 2 alone would be responsible for the end-Cretaceous extinction (Keller *et al.*, 2012). It would have released about 8.10^5 km^3 (Sen, 2001, Courtillot & Renne, 2003) of lavas in 50ka (Figure 3.1), which corresponds to about 160 the current eruption rate of today's Hawaii: $0.1km^3/yr$ (Courtillot *et al.*, 1986). Furthermore, phase 2 contains 25 paleomagnetic directional groups corresponding to 25 paroxysmal eruptions (Chenet *et al.*, 2009). The

maximum eruption rate reached during these extreme events has been estimated at 160km^3/yr (Thakurvadi formation, Chenet *et al.*, 2009). Note that even using such a high rate, Chenet et al did not match the final volume of 1.10^{6}km^3 proposed for the Deccan Traps (e.g. Sen, 2001, and references therein). These extremely high rates are in agreement with recently published strontium isotope diffusion and relaxation models in Giant Plagioclase Basalts, which suggest that entire formations (i.e. Jawhar, Igatpuri, Neral, Thakurvadi and Bhimashankar) could have been emplaced in less than 1ka (Borges *et al.*, 2013).

Red boles start to appear and become more numerous towards the end of phase 2 (Ambenali). The first thick red bole in early Ambenali combined with the hypotheses as to the location of the K-Pg boundary (see 3.6.1) imply that the latter could have occurred up to 50ka after the end of phase 2. It is also interesting to note that when thick red boles are reported, thin red boles seem to be less so and conversely: the last thick red bole is in early Mahabaleshwar and is followed by many thin red boles. In other words, the occurrence of red boles in the field seems compatible with the observation of paleomagnetic directional groups: no thick red bole has been reported inside directional groups or within any of the main volcanic phases (1, 2 and 3). However, thin red boles have been reported within lava sequences belonging to a directional group, which further support a fast alteration/formation process.

Upon comparing this scenario to seawater paleotemperatures and osmium isotopic ratios in pelagic carbonates (Figure 3.2) the following interpretation can be proposed:

The increasing occurrence of red boles in phase 2 is weakly correlated with the cumulative erupted volume. At the same time, osmium isotopic ratios decrease and seawater paleotemperatures vary (Figure 3.2). This could be tentatively interpreted as the result of volcanism-induced climate change: large volumes of CO_2 and SO_2 are released to the atmosphere leading to climate change (warming and/or cooling of seawater paleotemperatures). Large amounts of SO_2 would also affect the climate by making it wetter (Chenet, 2006). Increased erosion would decrease osmium isotopic ratios and even more so as large amounts of basalts (low $^{187}Os/^{188}Os$) are blanketing a craton (high $^{187}Os/^{188}Os$). Moreover, basalts are much more prone to erosion than cratonic rocks. (Robinson *et al.*, 2009). The details of this scenario are however not so straightforward.

First, phase 1 is not seen in the high-resolution osmium isotopic record despite the C30r-C30n reversal being recorded in both Deccan lavas and osmium isotope sections (Chenet *et al.*, 2007, Robinson *et al.*, 2009). It is speculated that the low intensities of this initial volcanism were not sufficient to affect the global oceanic osmium budget. The Western Ghats tholeiitic

eruptions were preceded and probably accompanied by alkali basalt (Subba Rao, 1972, Sen *et al.*, 2009), carbonatites (e.g. Ray *et al.*, 2003, and references therein) and kimberlites (Chalapathi Rao & Lehmann, 2011, and references therein) in the north, northwest and northeast (Figure 2.3). These volcanic events were of much lower intensities than those of the main province, and therefore might have had limited consequences on the environment.

Furthermore, in this scenario (Figure 3.1 and Figure 3.2), the onset of the well-documented late-Cretaceous warming and cooling events, that are roughly coeval with the osmium isotope excursions of Robinson et al and biozones CF2 and CF1 of Keller and colleagues (Figure 3.2), happen 0.5Ma before the onset of phase 2. However, both temperature variations (Li & Keller, 1998) and isotope excursions (Vonhof & Smit, 1997, MacLeod *et al.*, 2001, Ravizza & Peucker-Ehrenbrink, 2003, Robinson *et al.*, 2009) have been interpreted as being caused by the eruption of the Deccan Traps. The re-interpretation proposed in this section concur with the fact that late-Cretaceous warming and the first $^{187}Os/^{188}Os$ excursion of Robinson et al (Figure 3.2) – which is also seen in other isotopic systems (Li & Keller, 1998, Ravizza & Peucker-Ehrenbrink, 2003) – was certainly caused by volcanism (outpouring of large volumes of basalts on a craton and important contribution of the eruptions to the atmospheric pCO_2). Nevertheless, the timescale of the first $^{187}Os/^{188}Os$ excursion of Robinson et al (~0.3Ma), which is similar to that of the late-Cretaceous warming, is incompatible with both the duration of phase 2 (Chenet *et al.*, 2007) and the fact that it contains the K-Pg boundary (Keller *et al.*, 2011). Moreover, Robinson and co-workers point out that no major damage to the environment had been observed by the end of the first $^{187}Os/^{188}Os$ excursion and concluded that the Deccan Traps must have contributed little to the end-Cretaceous extinction. Yet this is again inconsistent with the observations made in the Krishna-Godavari basin wherein 1- the Deccan Traps appear clearly associated with the loss in species richness in biozone CF1 and 2- phase 2 appear to contain or end at the K-Pg boundary (Keller *et al.*, 2011, Keller *et al.*, 2012). In the same way, the duration and intensity of the initial $^{187}Os/^{188}Os$ excursion seems inconsistent with the existence of paroxysmal eruption seen as paleomagnetic directional groups or Giant Plagioclase Basalt flows. Nor is it consistent with the fact that the most voluminous of these paroxysmal eruptions occurred in mid-phase 2 (160km3/yr in the Thakurvadi formation, Chenet *et al.*, 2009). Finally, the very limited number of red boles in the first half of phase 2 indicates that volcanic repose was extremely limited. None of the above argues in favour of phase 2 being responsible for the first $^{187}Os/^{188}Os$ excursion.

The sharper second $^{187}Os/^{188}Os$ excursion (Figure 3.2) is more compatible with phase 2 of the eruption although it has been attributed to the Chicxulub impact (Robinson *et al.*, 2009). The final cooling is also compatible with volcanism (SO_2).

At this stage, major discrepancies in age models cannot be ruled out. For example, Ravizza and Peucker-Ehrenbrink (2003) place the main phase of Deccan volcanism at C30n-C29r, which is very different to what Chenet and co-workers proposed (Chenet *et al.*, 2009).

If the second $^{187}Os/^{188}Os$ excursion indeed corresponds to phase 2 – which would then match all other observations: directional groups, Giant Plagioclase Basalts, biozones and red bole frequencies – one has to find an explanation for the first $^{187}Os/^{188}Os$ excursion (Figure 3.2). The latter has been measured in samples featuring a reverse paleomagnetic orientation. If it is a trace of early Deccan activity, this reverse polarity would be that of C30r and therefore imply a mismatch greater than 2Ma in either sedimentary age models or in the radiometric dating of Chenet et al. (2007). 2Ma is twice greater than the average error bars of Chenet et al and such a mismatch in sedimentary age models coupled to paleomagnetic measures (Robinson *et al.*, 2009) is highly unlikely. Moreover, as mentioned above, several authors have reported excursions in isotopic systems at this time and over similar periods. It may therefore be asserted that the pre-K-Pg $^{187}Os/^{188}Os$ decrease in pelagic carbonates (first + second excursions) did happen in C29r in the last 0.5Ma of the Cretaceous.

How is it possible to accommodate the gap between phase 1 and 2 (>2Ma) and the existence of pre-phase 2 $^{187}Os/^{188}Os$ excursion (~0.5Ma before the K-Pg while phase 2 seems to have lasted 50ka and ended at the K-Pg)? It has been suggested that the Chicxulub impact could have predated the K-Pg boundary by as much as 0.3Ma (Keller *et al.*, 2004a, 2004b, Schulte *et al.*, 2008). However, Alvarez (2003) pointed out that if there was a time interval greater than 0.1Ma between the main phase of the Deccan Traps and the Chicxulub impact it would be easily seen in K-Pg sections. Alternatively, the possibility of several extra-terrestrial impacts in the late Cretaceous has been suggested (Keller *et al.*, 2003). However, it is reasonable to expect that isotope excursions resulting from impact would be sharper that the first excursion of Robinson et al. Not to mention that the observation of similar excursions in strontium isotopes rules out the implications of extra-terrestrial impact as a possible explanation for this early $^{187}Os/^{188}Os$ excursion (see references above and section 3.5.2).

A different scenario would involve the Deccan plume. Sobolev et al. (2011) have shown that the incubation of a plume beneath the lithosphere could generate a very significant degassing of the volatiles contained in the plume itself thereby causing significant damage to the

environment before any magma has actually been erupted. Such a scenario requires knowledge of the volatile content of the magmas. This aspect will be dealt with in a later section 6.5. It also implies that the degassing alone is capable of creating an excursion in volcanism-sensitive isotopic systems. It is reasonable to assert that injecting large amounts of CO_2, SO_2 or HCl to the atmosphere would affect the climate (e.g. temperature variations, higher rainfall). Nevertheless, the new source of low $^{187}Os/^{188}Os$ and $^{87}Sr/^{86}Sr$ material available to the erosion that freshly outpoured basalts represent and the combined loss of material with high isotopic osmium and strontium ratios (cratonic rocks being covered by Deccan basalts) remain unaccounted for.

At last, incompleteness of the sampling cannot be ruled out. Considering the large volume and extent of the main Deccan province, it is possible that that flows – or red boles, for that matter – have been missed between phase 1 and 2 or during phase 2 itself. For instance, the Bushe-Poladpur transition section of Chenet et al is not complete (Chenet *et al.*, 2009, Figure 1). Moreover, the volume estimation proposed by Chenet and co-workers merely accounts for less than 30% of the published estimations for total Deccan Traps volumes (e.g. Sen, 2001, and references therein). A significant missing volume may lie to the west, in the Laxmi Ridge (Minshull *et al.*, 2008) or on the Seychelles micro-continent (Owen-Smith *et al.*, 2013). In addition, dyke swarms and paleo-stress modelling on the Indian plate (Vanderkluysen *et al.*, 2011, Ju *et al.*, 2013) combined with paleotopography (Hooper *et al.*, 2010, Sheth & Pande, 2013) argue for a symmetrical emplacement of the main Deccan province (i.e. on either sides of today's Indian west coast). In that case, the underestimated volume calculated by Chenet et al (2009) would pertain to an underestimated lateral extent and not to unreported flows that would instead add to the overall thickness of the Western Ghats. It thus seems unlikely that missing flows in this composite section would account for significant volumes with respect to phase 2, which also limits, if not preclude, the role of potentially unreported flows in explaining the first $^{187}Os/^{188}Os$ excursion.

4. Samples and methods

4.1. Samples

The samples used in this project were assembled in an attempt to constitute a time-lapsed picture of the Deccan plume, from its initial stage beneath the Indian plate until today at Piton de la Fournaise, Réunion Island, in the Indian Ocean. However, no fieldwork was carried out during this project. This work is therefore solely based on existing samples obtained from the Institut de Physique du Globe de Paris (IPGP, France), the Université Blaise Pascal (Clermont Ferrand, France) and previous projects of Alexander V. Sobolev at the Max Plank Institute, Mainz (Germany).
The main sample set has been collected at the IPGP in Paris, France, with the invaluable help of Frédéric Fluteau and consists in 219 unheated drill cores collected in the Western Ghats for paleomagnetism during Anne-Lise Chenet's Ph.D project in the mid-2000s (Chenet, 2006, Chenet *et al.*, 2007, 2008, 2009)

A second, more limited, set has been collected at the Université Blaise Pascal in Clermont Ferrand (France) with the help of Ivan Vlastelic. It covers the most recent activity of the Deccan Plume: Piton de la Fournaise, Réunion Island. It contains both picritic basalts (MgO > 20wt%) and steady-state basalts (MgO < 10wt%). A.V. Sobolev also provided one sample for Piton de la Fournaise (OPF) and another for Piton des Neiges (RU11), both picritic in composition.

A third, minor, set consists in 5 samples (MgO = 5-14%) from northwest Deccan (Gujarat) collected by A.V. Sobolev's team in the late 2000s. This set has been lost at some point during the project. Its contribution to this project is therefore very limited.

4.2. Methods

This project uses the above-mentioned sample sets in two different ways. First, bulk-rock trace element data are coupled with existing high-resolution paleomagnetic measurements (Chenet *et al.*, 2008, 2009), (section 5.4). This allows for observing the evolution of trace element signatures at the resolution offered by high-resolution paleomagnetism (ca. 100 years) and enables to draw new conclusions as to the big picture of the Deccan eruption. Secondly, in-situ analysis of olivine phenocrysts and their inclusions (spinel and melt

inclusions) were carried out in order to have access to the primary melt compositions, source lithologies and pressure-temperature environment.

4.2.1. Bulk-rock major and trace elements

The IPGP provided bulk-rock major and trace element analyses for 144 drill cores (out of 175 used for paleomagnetic measurements) from the Western Ghats. They were processed at the CRPG (Nancy, France) by Inductively-Coupled Plasma Mass-Spectrometry (ICP-MS). This dataset has been acquired during an MSc project at the IPGP (Bonnefoy, 2005) but were never published. I have been offered to re-visit and publish this data on the occasion of this Ph.D project.

In order to confirm the quality of the dataset a number of randomly selected samples have been re-analysed at the Max Planck Institute for Chemistry (Mainz, Germany) by LA-ICP-MS and yielded positive results.

Table 4–1 Comparison of trace element concentrations (ppm) for a selection of samples from the CRPG database of Bonnefoy (2005) with LA-ICP-MS results obtained for the same samples at the Max Planck Insitute for Chemistry (Mainz, Germany). Δ% is the relative error. Large errors for Pb concentration are due to the LA-ICP-MS method: Pb is volatized by the laser spot.

Sample:	KD04			KD04			VT08			VT09		
	Mainz	CRPG	Δ%	Mainz	CRPG	Δ%	Mainz	CRPG	Δ%	Mainz	CRPG	Δ%
Rb	3.06	2.79	4.6	2.64	2.40	4.7	11.27	18.71	24.8	22.64	21.67	2.2
Ba	116.53	113.36	1.4	102.15	107.12	2.4	189.01	190.95	0.5	108.05	120.18	5.3
Th	1.85	1.85	0.1	1.78	1.86	2.4	2.39	2.35	0.9	3.07	2.89	3.0
U	0.52	0.44	8.5	0.43	0.46	2.6	0.42	0.50	8.0	0.63	0.70	5.4
Nb	8.60	6.94	10.7	8.53	7.26	8.0	10.41	8.06	12.7	5.85	5.56	2.6
Ta	0.54	0.56	1.5	0.52	0.56	3.8	0.66	0.63	1.8	0.41	0.47	6.1
La	10.85	11.17	1.5	11.11	11.20	0.4	15.56	15.55	0.0	10.39	10.55	0.7
Ce	27.08	25.21	3.6	26.27	25.19	2.1	32.60	32.96	0.6	22.23	23.52	2.8
Pb	1.51	2.58	26.3	0.89	2.65	49.7	1.76	2.51	17.5	1.76	2.15	10.0
Pr	3.32	3.34	0.3	3.30	3.38	1.2	4.23	4.43	2.3	3.11	3.38	4.2
Nd	15.38	14.86	1.7	15.18	14.98	0.7	19.51	19.03	1.2	15.57	15.35	0.7
Sr	211.78	211.24	0.1	219.66	208.43	2.6	250.24	227.50	4.8	184.21	194.85	2.8
Sm	3.61	3.84	3.0	3.90	3.88	0.2	4.96	4.89	0.7	4.35	4.40	0.6
Zr	86.68	93.02	3.5	94.20	94.50	0.2	147.57	139.79	2.7	117.55	116.38	0.5
Hf	2.26	2.56	6.1	2.29	2.58	6.0	3.61	3.74	1.8	3.17	3.25	1.2
Eu	1.30	1.33	0.9	1.28	1.38	3.7	1.57	1.60	0.9	1.40	1.51	3.8
Ti	10492.57	8779.86	8.9	10631.83	8553.20	10.8	12478.85	9250.46	14.9	9300.65	8772.78	2.9
Gd	3.56	4.11	7.1	3.80	4.17	4.6	4.92	5.22	2.9	4.82	4.84	0.2
Tb	0.56	0.63	5.8	0.59	0.64	4.3	0.78	0.81	1.4	0.81	0.76	3.1
Dy	3.44	3.65	3.0	3.80	3.68	1.6	5.17	4.75	4.2	5.00	4.56	4.6
Ho	0.66	0.72	4.4	0.72	0.70	1.2	0.98	0.92	3.2	1.02	0.87	7.9
Y	15.95	18.93	8.5	17.40	19.30	5.2	24.21	25.65	2.9	24.22	24.30	0.2
Er	1.87	1.89	0.6	1.90	1.85	1.5	2.64	2.43	4.2	2.75	2.30	9.0
Tm	0.26	0.26	1.8	0.28	0.26	4.0	0.36	0.35	1.2	0.37	0.33	5.1
Yb	1.66	1.66	0.1	1.65	1.68	0.7	2.41	2.23	3.8	2.38	2.06	7.2
Lu	0.21	0.25	7.1	0.24	0.25	2.0	0.35	0.34	1.9	0.35	0.31	6.0

This dataset is available on demand from the PhD candidate.

4.2.2. Olivines, spinels and melt inclusions

In order to apply olivine petrology (major and trace element analysis of olivine phenocrysts and their melt and spinel inclusions), samples with MgO > 6-7wt% (olivine field) have been investigated for olivine phenocryst occurrence by simple observation with a magnifying glass. In addition, phyric samples have all been hand crushed and observed with traditional microscopy in an attempt to separate olivine phenocrysts for further processing. This part of the project has been carried out at the Max Plank Institute for Chemistry in Mainz (Germany)

under the supervision of Olga and Dmitry Kuzmin. Despite the significant number of Deccan samples (>200), only 8 turned out to be olivine-phyric: KUR1, NAK1 and NAK2 (Kutch, Gujarat); VT02 and VT08 (Jawhar formation); VT09 (Igatpuri formation); KD04 and KD06 (Thakurvadi formation). On the other hand, all Réunion samples provided by Ivan Vlastelic at the University of Clermont Ferrand, France, proved olivine-phyric, despite sometimes low MgO contents (<7wt%).

Table 4–2 summarizes the content of the sample set used in this PhD project.

Table 4–2 – Olivine-bearing samples processed during this PhD project. Sample names in underlined bold font are for those that returned data compatible with olivine petrology, primary melt and source modelling (see text below). *Olivine: High-Precision EPMA for major and trace elements of olivine cores, Melt inclusions: High-Precision EPMA of homogenized olivine melt inclusions, Spinels: EPMA of olivine spinel inclusions for applying Al olivine-spinel thermometry. For analytical procedures, see appendix III

Province	**Area**	**Sample name**	**Location**	**Age**	**Formation**	**MgO(wt%)**	**Analysis***	***References***
Deccan	Kutch	KUR1	? (Kutch)	Cretaceous		10.772	Olivine	
Deccan	Kutch	NAK1	Nakhatrana	Cretaceous		12.805	Olivine	
Deccan	Kutch	NAK2	Nakhatrana	Cretaceous		14.032	Olivine	
Deccan	Western Ghats	**KD04**	Devale-Ghoti	K-Pg	Thakurvadi	12.712	Olivine + Melt inclusions + Spinels	*(Chenet et al., 2009)*
Deccan	Western Ghats	**KD06**	Devale-Ghoti	K-Pg	Thakurvadi	12.216	Olivine + Melt inclusions + Spinels	*(Chenet et al., 2009)*
Deccan	Western Ghats	VT02	Val River-Trimbak	K-Pg	Jawhar	8.337	Olivine	*(Chenet et al., 2009)*
Deccan	Western Ghats	VT08	Val River-Trimbak	K-Pg	Jawhar	7.768	Olivine	*(Chenet et al., 2009)*
Deccan	Western Ghats	VT09	Val River-Trimbak	K-Pg	Igatpuri	8.652	Olivine + Spinel	*(Chenet et al., 2009)*
Réunion	Piton des Neiges	**RU11**	Cilaos	Quaternary		25.20	Olivine + Spinel	*(Sobolev & Nikogosian, 1994)*
Réunion	Piton de la Fournaise	**OPF**	Rivière de l'Est	Quaternary		22.44	Olivine + Spinel	*(Sobolev & Nikogosian, 1994)*
Réunion	Piton de la Fournaise	**TI1602**	East flank	01 to 08/1931		29.14	Olivine + Melt inclusions + Spinels	*(Albarède et al., 1997)*
Réunion	Piton de la Fournaise	**GB1961**	Grand Brûlé	04/1961		24.04	Olivine + Melt inclusions + Spinels	*(Albarède & Tamagnan, 1988)*
Réunion	Piton de la Fournaise	**SR1977**	Piton Sainte Rose	03 to 04/1977		24.74	Olivine	*(Albarède & Tamagnan, 1988)*
Réunion	Piton de la Fournaise	**0202-053**	Enclos Fouqué	16/01/2002		>20	Olivine + Melt inclusions + Spinels	*(Vlastélic et al., 2005)*
Réunion	Piton de la Fournaise	**0502-263**	Plaine des Osmondes	26/02/2005		24.00	Olivine + Melt inclusions + Spinels	*(Vlastélic et al., 2007)*
Réunion	Piton de la Fournaise	813-1	Grand Brûlé	26/02/1981		7.40	Olivine	*(Vlastélic et al., 2009)*
Réunion	Piton de la Fournaise	871-82	Enclos Fouqué	6/01/1987		7.05	Olivine	*(Vlastélic et al., 2009)*
Réunion	Piton de la Fournaise	997-272	Enclos Fouqué	27/07/1999		6.58	Olivine	*(Vlastélic et al., 2005)*
Réunion	Piton de la Fournaise	0607-271	Southwest flank	27/07/2006		6.90	Olivine	*(Vlastélic et al., 2007)*

The olivine-phyric samples (Table 4–2) have been hand-crushed in order to separate their olivine phenocrysts. These were embedded in epoxy resin mounts suitable for Electron-Probe Micro-Analyser (EPMA), carefully polished and coated with ~15nm of carbon under secondary vacuum.

The data acquisition was carried out on a JEOL JXA8230 EPMA at ISTerre, Grenoble, France.

The EPMA operating conditions were:

- Olivine: 25kV, 900nA
- Melt inclusions: 15kV, 12nA and 20kV, 200nA (for trace elements)
- Spinels: 20kV, 50nA

An exhaustive description of the EPMA protocols, operating conditions and analytical capabilities of the JEOL JXA8230 used in this project can be found in appendix III along with a simple explanation of the physical principles behind electron-probe micro analysis. See Table 4–3 for a summary of the olivine high-precision EPMA dataset of this PhD.

Table 4–3 - Summary of the final (corrected and filtered) content of the olivine dataset. Olivine: number of mineral grains analysed and total number of measurements (in brackets). Melt inclusions: total number of melt inclusions analysed (one analysis per inclusion). Spinels: total number of spinels analysed (one analysis per spinel). T° estimations: total number of spinel-olivine temperature estimations with standard deviation < 10°C (total number with standard deviation < 5°C in brackets). The total time of acquisition (without probe calibration time and erroneous measurements) is estimated at 1100 hours. PdN: Piton des Neiges. PdF: Piton de la Fournaise.

Origin	Sample	Olivines	Melt inclusions	Spinels	T° estimation
Deccan	KD04	251 (711)	158	207	42 (16)
	KD06	177 (374)	109	77	17 (9)
	VT02	108 (64)	-	-	-
	VT08	79 (85)	-	-	-
	VT09	90 (112)	-	4	2 (1)
Réunion (PdN)	RU11	100 (196)	-	35	29 (14)
Réunion (PdF)	OPF	106 (194)	-	31	21 (7)
	TI1602	167 (565)	68	40	44 (19)
	GB1961	155 (406)	51	6	36 (18)
	SR1977	99 (146)	-	1	-
	0202-053	153 (381)	53	1	29 (15)
	0502-263	148 (342)	57	9	20 (8)
	813-1	17 (20)	-	-	-
	871-82	34 (32)	-	-	-
	997-272	11 (20)	-	-	-
	0607-271	14 (0)	-	-	-

The olivine (Table 4–3) and the Deccan bulk-rock (section 4.2.1) datasets are available on demand from the PhD candidate. Please note that the bulk-rock compositions of all Réunion samples is already published and available from the GEOROC online database (corresponding references in Table 4–2).

In sections 6 and 7 on olivine petrology and olivine-based source modelling, only high-MgO samples that returned data compatible with olivine petrology, primary melt and source modelling (bold, underlined in Table 4–2, MgO > 12wt%) will be described.
The lower-MgO samples of Table 4–2 (regular font, MgO < 12wt%) and the Kutch samples (lost during this project) have nonetheless been integrated to the database of this PhD and are available as Excel files along with the other datasets produced during this PhD. The poor quality of the data with respect to the goals of this project pertains to 1) low MgO contents (8wt% or lower), implying that olivine was not the only silicate phase in equilibrium with the solidifying lava and 2) the presence of sulphides and varying oxidation state of Fe in the Gujarat (Kutch) samples with MgO > 10wt%, which resulted in large variations in olivine trace elements.

The Deccan samples KD04 and KD06 are to be compared with RU11, OPF, TI1602, GB1961, SR1977, 0202-053 and 0502-263 from Réunion Island. Both sets are regarded as early, plume head stage and late, plume tail stage of the Deccan plume respectively. The emphasis will be on the consequences of the new observations on the emplacement of the Deccan Traps in the late-Cretaceous. The implications of these observations on the geodynamics of Réunion Island will be discussed as well, although the contribution of this work to the understanding of Réunion Island is somewhat limited. In this context, the latter is rather considered as a present-day end-member used for comparison.

5. Bulk-rock geochemistry through time

5.1. Sample composition and classification

The re-visited eruption scenario (Figure 3.1 and Figure 3.2) has been supplemented by coupling with bulk-rock major and trace element geochemistry using a dataset provided by the IPGP, Paris, France (Bonnefoy, 2005), section 4. The samples cover 144 of the 175 sampling sites of Chenet and colleagues (Chenet *et al.*, 2008, 2009) and span all Deccan formations in a homogeneous manner. Figure 5.1 below shows the composition of the samples in the volcanic rock classification diagram of Le Bas et al. (1986). The sample set has been divided into two subsets, one for the lower formations (Igatpuri-Jawhar to Bushe) and the other for the upper formations (Poladpur to Mahabaleshwar) in order to account for the significant differences between both parts of the Western Ghats section that has been thoroughly reported in the literature (see for example: Peng *et al.*, 1994). These differences are perhaps best illustrated by isotope ratios (Figure 2.5).

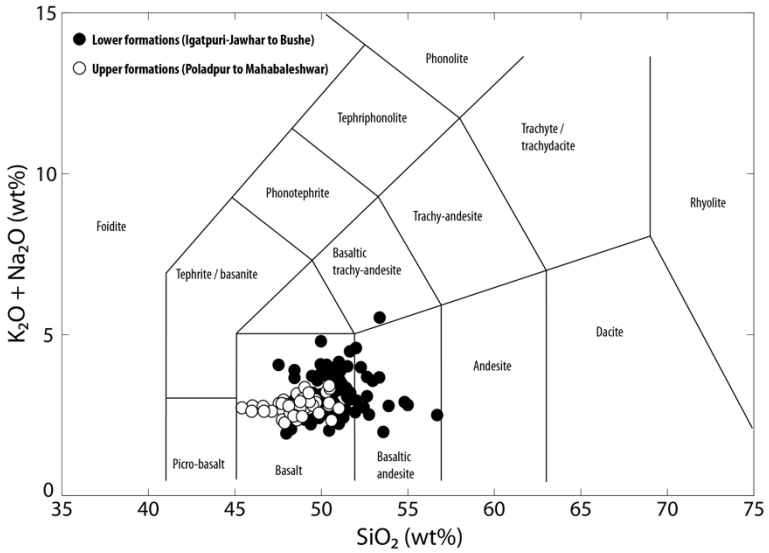

Figure 5.1 – Composition of the dataset of (Bonnefoy, 2005) in the volcanic rocks classification diagram of Le Bas et al (1986).

Most samples are unsurprisingly tholeiitic and range from picrites (n = 2) to basaltic andesite. Mg# ($\frac{Mg}{Mg + Fe}$) ranges from 0.31 to 0.63 in the lower formations, and from 0.32 to 0.53 in the upper formations with a global average (lower and upper formations) of 0.46. The lower formations therefore span a wider compositional range than the upper formations (Figure 5.1).

The division between lower (Igatpuri-Jawhar to Bushe) and upper (Poladpur to Mahabaleshwar) formations has been refined by carrying statistical classification (K-Means

clustering) based on the trace element concentrations of the sample set as a whole. The result of the trace element-based classification (Figure 5.2) is similar to the division between lower and upper formations overall, with a limited number of exceptions: three samples of Poladpur and three more from Mahabaleshwar appear to be more compatible with lower formations trace element concentrations and one sample from Bhimashankar is more compatible with the upper formations.

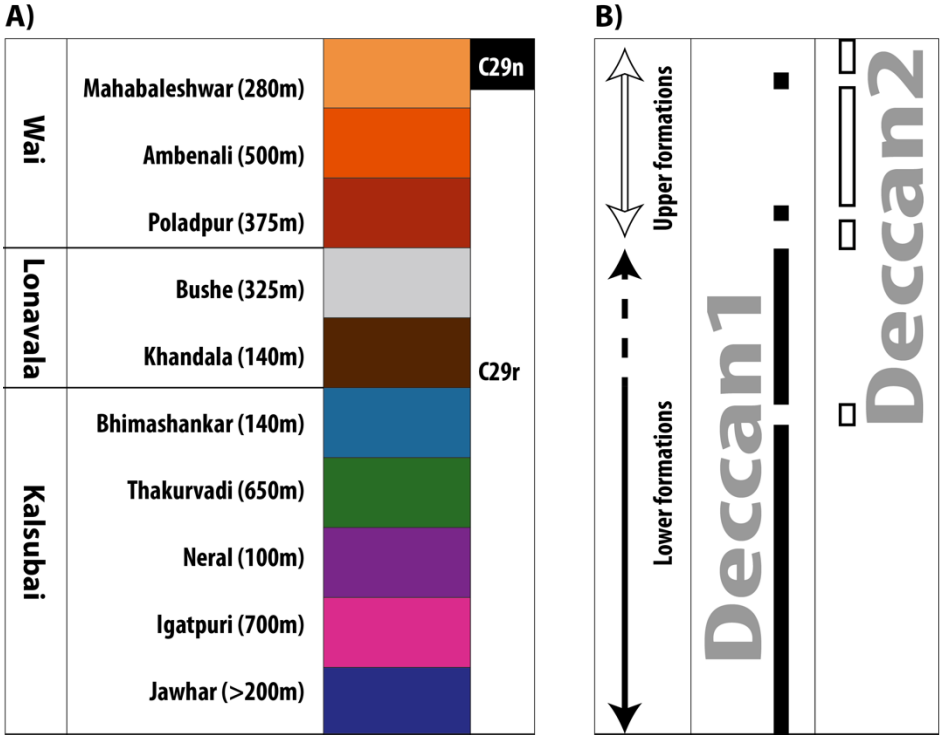

Figure 5.2 – A) Western Ghats stratigraphy modified from Chenet et al (2009). B) Differences between the division in lower (Igatpuri-Jawhar to Bushe) and upper formations (Poladpur to Mahabaleshwar), e.g. Peng et al (1994) and the Deccan1 and Deccan2 subsets identified from trace element-based statistical analysis (K-Means clustering), Figure 5.3.

Two classes thus replace the division between lower and upper formations: Deccan1, corresponding to the lower formations with limited exceptions in the upper formations and Deccan2, which is mostly represented by the upper formations with one exception in Bhimashankar. Figure 5.2 and Figure 5.3. Both classes mostly differ in trace element concentrations indicative of crustal contamination and will be described and interpreted further in this section.

Extended trace element spectra are shown in Figure 5.3a.

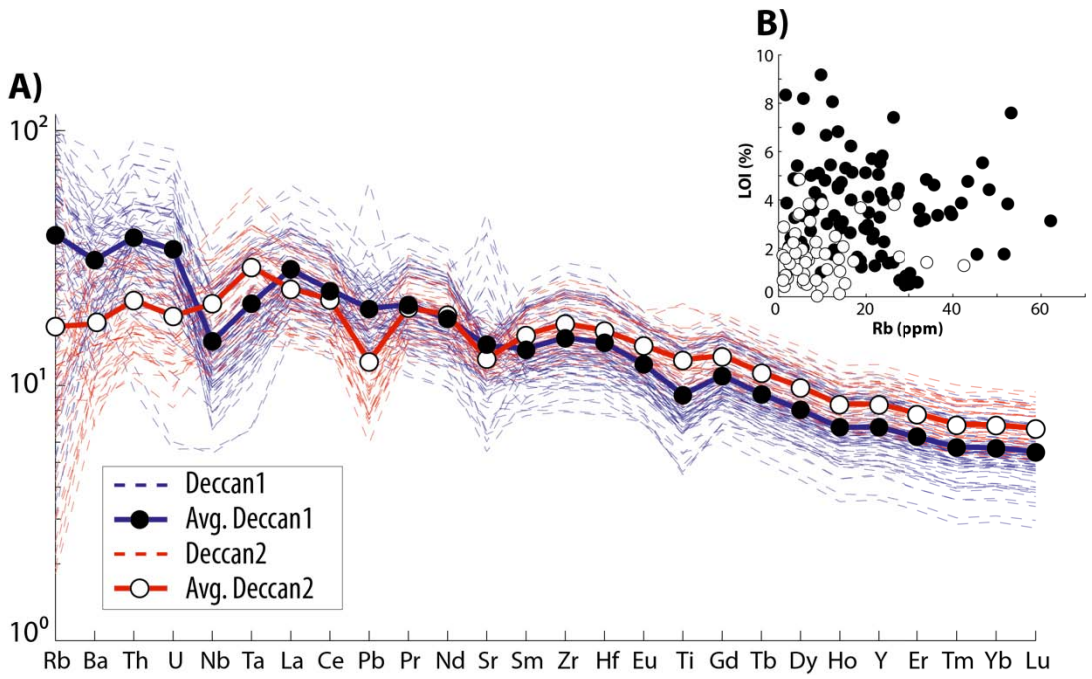

Figure 5.3 – A) Extended trace element spectrum for the 144 Western Ghats samples normalized to primitive mantle (Hofmann, 1988). Deccan1 and Deccan2 (see text and Figure 5.2) have been defined by K-Means clustering on trace element concentrations. B) Bulk-rock Rb content versus Loss On Ignition (LOI) of the samples. High Rb contents and large loss on ignition imply significant weathering of the sample.

Highly variable alkaline contents (e.g. Rb) is thought to be primarily caused by weathering (Figure 5.3b, Rb versus LOI), which all Deccan Traps outcrops bear significant traces of, considering the tropical latitudes under which India has been located since late-Cretaceous times.

All samples feature significant Heavy Rare Earth Element (HREE, Gd to Lu) depletion relative to moderately incompatible rare earths (MREE, Sm to Gd). Elements other that rare earths are widely scattered with both positive and negative anomalies for Pb, Sr and Ti.

Figure 5.3 shows that the average extended trace element spectra of Deccan1 and Deccan2 are mostly different from Rb to Sm and parallel from Sm to Lu. Deccan1 has a strong Nb anomaly resulting in higher Th/Nb and lower Nb/La than Deccan2. The latter, on the other hand, has a stronger Pb anomaly, which results in higher Ce/Pb compared with Deccan1. Deccan2 also has a Sr anomaly slightly more significant and HREE concentrations slightly higher than Deccan1. Ti anomalies are slightly more negative in Deccan1 and finally, Deccan1 and Deccan2 are strikingly parallel from Gd to Lu.

In the next sections, the origin of the Deccan1 and Deccan2 subsets will be investigated and their occurrence will be coupled with the high-resolution timeframe of the Deccan Traps eruption presented in section 3.6.

5.2. Major elements classification

Magma differentiation processes (i.e. fractional crystallization, crustal assimilation and magma mixing) become apparent upon plotting bulk-rock major element versus MgO content, Figure 5.4.

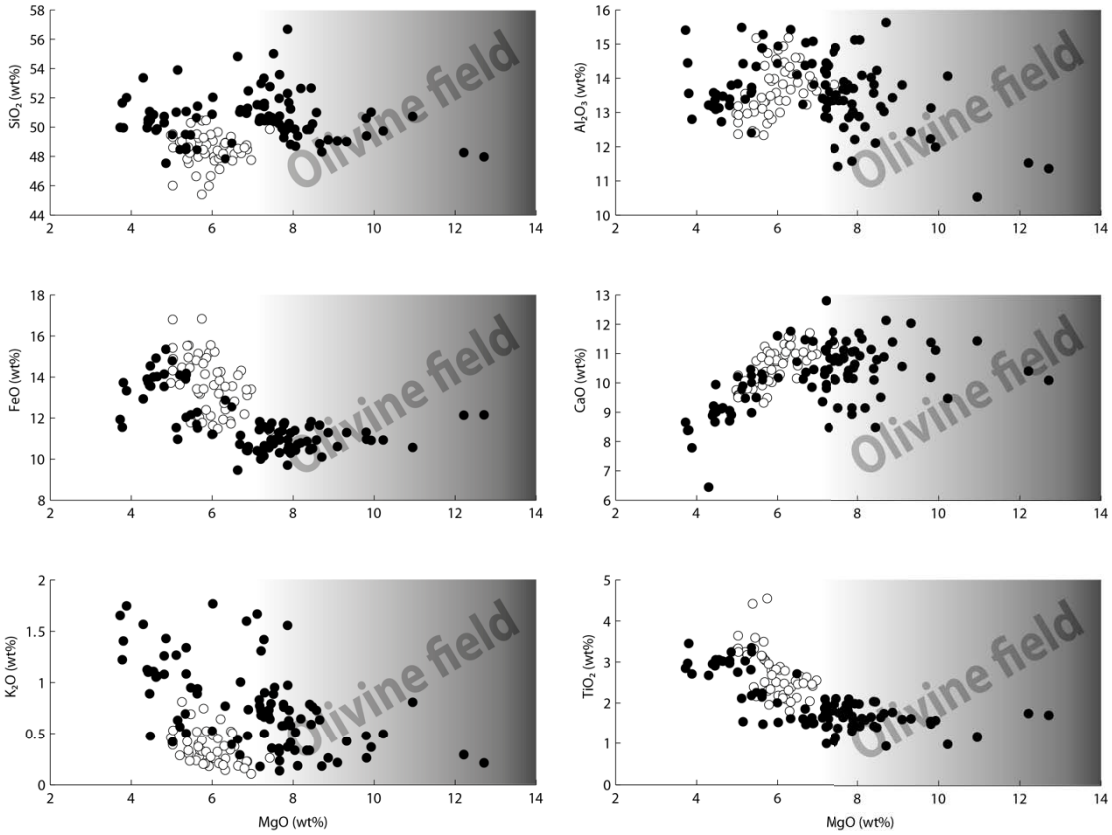

Figure 5.4 - Major elements diagrams for both Deccan1 and Deccan2 subsets identified from trace elements (Figure 5.2 and Figure 5.3). Deccan1: black dots. Deccan2: open circles. Olivine field = MgO > 7wt%, see text.

In Figure 5.4, higher MgO contents are indicative of more primitive lava compositions (note the two picritic samples to the right of every plot). Deccan2 appears to be more homogeneous and on average more evolved than Deccan1. Deccan1 MgO content ranges from 3.7 to 12.7wt%, while Deccan2 ranges only from 5.0 to 7.4wt%. Moreover, at a given MgO content, Deccan2 is slightly lower in SiO_2, Al_2O_3 and K_2O and slightly higher in FeO and TiO_2 than Deccan1.

Each plot on Figure 5.4 feature a general trend shift in the vicinity of MgO = 7wt%. This kink shows the boundary between the olivine stability field (towards higher MgO contents), and further fractional crystallization and/or cumulation of other minerals, such as pyroxenes and feldspars (towards lower MgO contents). The dispersion away from this fractionation trend indicates that other processes occurred during magma differentiation (e.g. crustal assimilation). These processes will be investigated using trace elements.

5.3. Proxies for source depth and crustal assimilation

The depth of magmatic sources and the existence of crustal contamination are two important parameters to consider in understanding the emplacement of a Large Igneous Province (LIP) (Arndt *et al.*, 1993, Sobolev *et al.*, 2011). Major element concentrations (Figure 5.4) suggest that Deccan Traps magmas have suffered significant amounts of fractional crystallization that was likely coupled with crustal assimilation. Therefore, their composition cannot be regarded as representative of the primary melt from which they derive, which makes it considerably more difficult to infer about their origin in the mantle.

The depth of magma sources is indicative of the thickness of the lithosphere beneath the eruption centre. This has implications in calculating the pressure-temperature conditions of a magmatic source as well as its amount of melting (section 7). When examined through time, it shows whether significant erosion of the lithosphere by the plume head – or thinning due to tectonic extension – has occurred during the emplacement of the LIP. This will in turn affect the LIP's late-stage pressure-temperature-melting source conditions (P,T,f). The depth of the magmatic sources is usually estimated from the fractionation between MREE and HREE. Gd/Yb_n (MREE/HREE, normalized to primitive mantle) increases with the steepness of the HREE pattern (Figure 5.3). HREE are extremely compatible with garnet and hence, steep HREE patterns, or high Gd/Yb_n (>1.6, Sobolev *et al.*, 2011) suggest 1) a garnet-bearing source, 2) that garnet remained in the restite after melting occurred, and 3) that the source did not melt sufficiently to exhaust the garnet it contains. Similarly, higher Gd/Yb_n may not be entirely due to higher source pressure, but can also be related to lower amounts of melting (or both…). Alternatively, low Gd/Yb_n (<1.6, Sobolev *et al.*, 2011) means that either all garnet has been exhausted from the magmatic source by high degrees of melting or because of low garnet content, or that the source was not in the garnet stability field (P > 1.5-2GPa for

pyroxenite: Lambart *et al.*, 2009, Lambart *et al.*, 2013, P > 2.4GPa for peridotite: Walter, 2014).

The relevance of crustal contamination (or assimilation) is twofold. First and foremost, crustal contamination modifies the composition of the rising magmas and blurs the source signal they contained. It renders the reconstruction of primary melts more difficult, if not impossible, which precludes proper estimation of the sources P,T,f conditions. On the other hand, crustal contamination returns valuable information as to the processes occurring between the source and the eruption centre (fractionation and assimilation in magma chamber, simple fractionation and low degrees of wall rock assimilation in large magma chambers or large assimilation and limited fractionation upon fast and turbulent transport). In the absence of radiogenic isotope data, crustal assimilation can be assessed using ratios of trace elements that have distinct concentrations in mantle melts and in the crust. Assimilation Fractional Crystallization (AFC: DePaolo, 1981) was not used during this PhD project. See Bhattacharya et al (2013) and Chatterjee and Bhattacharji (2008) for recently published applications of AFC to the Deccan Traps.
Nb/La_n and Th/Nb_n are proxies for crustal contamination. Nb/La_n increases with decreasing contamination because of the general negative Nb anomaly of the continental crust (Rudnick & Gao, 2003). Th/Nb_n varies in the opposite way, as Th/Nb ratios are much higher in the crust than in the mantle. In addition, La concentrations being higher in the upper crust and Th being more abundant in the lower crust, these trace element ratios also help decipher whether one of the other crustal component was preferentially involved in the contamination process (Rudnick & Gao, 2003).

The subsets Deccan1 and Deccan2 identified in the preceding paragraph (section 5.1) mostly differ by their light incompatible trace element contents and feature a remarkably similar HREE pattern (Figure 5.3). This dichotomy is further investigated by considering ratios of elements that vary with incompatible element patterns or HREE steepness: Nb/La_n, Th/Nb_n, Ce/Pb and Gd/Yb_n (Figure 5.5).

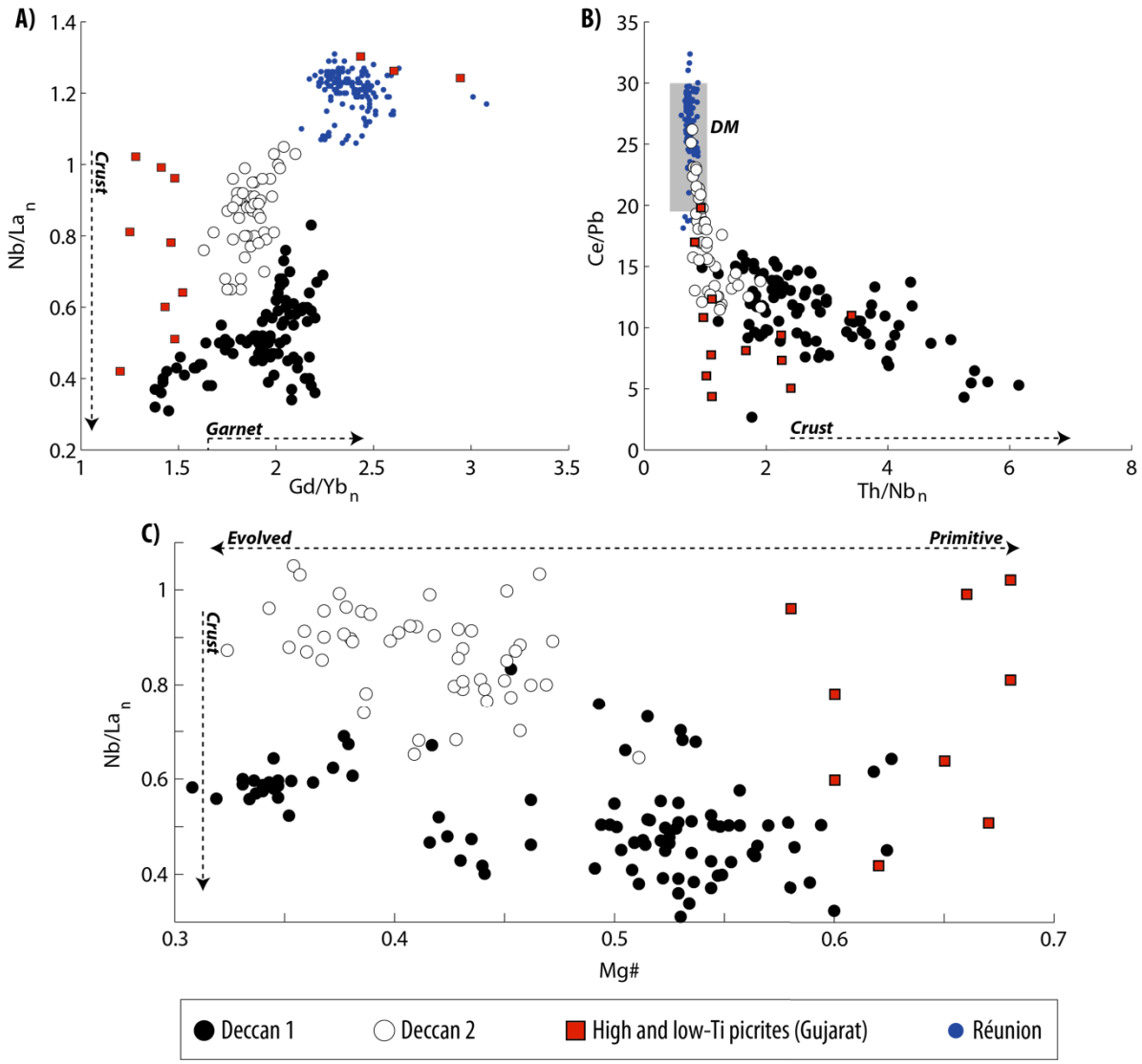

Figure 5.5 - Incompatible trace element ratios for the Deccan1 and Deccan2 subsets (Figure 5.2 and Figure 5.3). Gujarat high-Ti picrites (Melluso *et al.*, 2006) and Réunion lavas (GEOROC database). A) Nb/La_n reflects lithophile elements enrichment. Gd/Yb_n shows variations in Heavy Rare Earth Elements (HREE) patterns that are a proxy for garnet signature in the source of magmas. Values above 1.6 (Sobolev *et al.*, 2011) suggest a source in the garnet stability field (P > 1.5-2GPa for pyroxenite: Lambart *et al.*, 2009, Lambart *et al.*, 2013, P > 2.4GPa for peridotite: Walter, 2014). Trace element abundances normalized to primitive mantle (Hofmann, 1988) B) Th/Nb_n and Ce/Pb variations are another way of illustrating the enrichment of magmas in incompatible elements with respect to average mantle and crustal values. Grey area "DM": Depleted Mantle values (Workman & Hart, 2005). For crustal values, see (Rudnick & Gao, 2003). C) Nb/La_n versus Mg#. Deccan2 tends to be more evolved and less contaminated than Deccan1, see text.

Figure 5.5a and b return the following ranges in trace element ratios:

Deccan1: Nb/La_n = 0.31 to 0.83 (average: 0.51); Th/Nb_n = 0.95 to 6.15 (average: 2.77); Ce/Pb = 2.68 to 15.92 (average: 11.26); Gd/Yb_n = 1.38 to 2.24 (average: 1.92)

Deccan2: Nb/La_n = 0.65 to 1.05 (average: 0.86); Th/Nb_n = 0.77 to 1.91 (average: 1.07); Ce/Pb = 11.46 to 26.20 (average: 16.86); Gd/Yb_n = 1.63 to 2.10 (average: 1.87)

Nb/La_n, Th/Nb_n and Ce/Pb unambiguously indicate that Deccan1 underwent significant crustal assimilation and that both lower (low Nd/La_n) and upper (high Th/Nb_n) crustal components were involved. Deccan2 on the other hand, appears to have assimilated significantly less crustal material and seems to include almost uncontaminated end-members (Nb/La_n = 1.05, Th/Nb_n = 0.77, Ce/Pb = 26.20). Figure 5.5a and b.
Upon considering Figure 5.5a and b together with Figure 5.4 (major element concentrations) and Figure 5.5c (Nb/La_n versus Mg#), a rather non-trivial relationship arises: Deccan2 is more homogeneous and on average more evolved (lower Mg#) than Deccan1 and yet it is less contaminated by crustal material (lower Th/Nb_n and higher Ce/Pb and Nb/La_n) both at a given Mg# and with respect to the highest Mg# end-members of Deccan1. Such a correlation of ratios that decrease with crustal contamination (e.g. Nb/La_n) and Mg# had already been noted in early publications on the Deccan Traps (Cox & Hawkesworth, 1985, Devey & Cox, 1987) and is an important observation to consider in interpreting the dynamics of magma transport in the Deccan Traps. It should be noted however, that the incompatible trace elements ratios presented in Figure 5.5 merely provide qualitative estimates and must not be used as direct indicators for quantifying the amount of crustal assimilation undergone by the magmas as the characteristics of both the contaminants and the sources may have varied through time (Peng *et al.*, 1994, Chatterjee & Bhattacharji, 2008).

The HREE patterns of both Deccan1 and Deccan2 subsets are compared using Gd/Yb_n (Figure 5.5a). Deccan1 (Gd/Yb_n = 1.38 to 2.24, average: 1.92) covers a wider range of Gd/Yb_n than Deccan2 (Gd/Yb_n = 1.63 to 2.10, average: 1.87) and reaches slightly higher values (2.24) than the latter (2.10). Both subsets clearly bear significant garnet signature: $Gd/Yb_n > 1.6$ (Sobolev *et al.*, 2011). Moreover, this signature seems unaffected by the varying crustal assimilation suggested by Th/Nb_n, Ce/Pb and Nb/La_n. Alternatively, higher absolute concentrations of HREE in Deccan2 (Figure 5.3) imply that these magmas could have been formed by lower degrees of melting (a comparable range of Mg# between Deccan1 and Deccan2 (Figure 5.4) rules out the role of fractionation).

Figure 5.6 allows comparison of Western Ghats with the Gujarat high-Ti picrites, Réunion Island and the Siberian Traps (Norilsk).

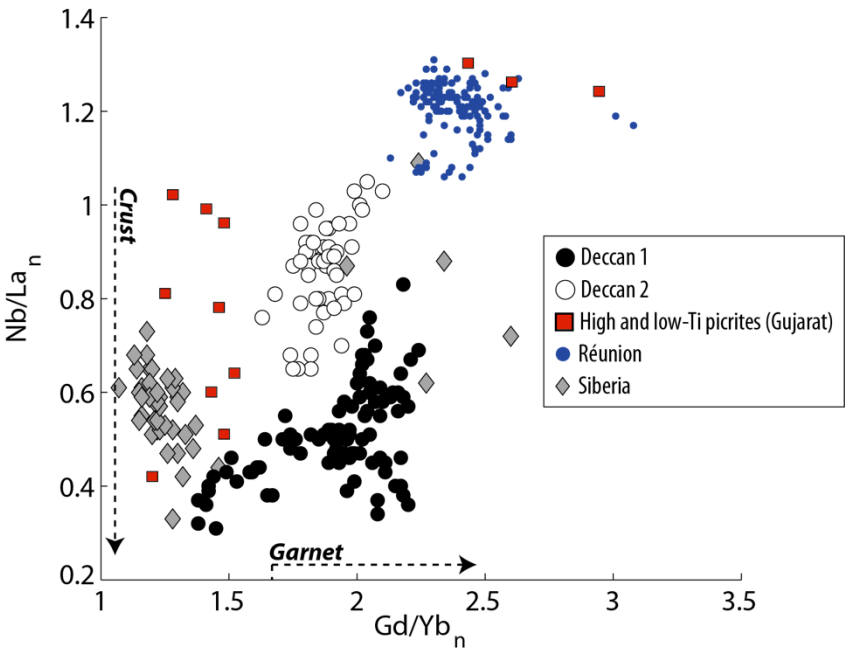

Figure 5.6 – Similar to Figure 5.5a for comparison with Siberian samples from Sobolev et al (2011): Nb/La_n reflects lithophile elements enrichment. Gd/Yb_n shows variations in Heavy Rare Earth Elements (HREE) patterns that are a proxy for garnet signature in the source of magmas. Values above 1.6 (Sobolev *et al.*, 2011) suggest a source in the garnet stability field (P > 1.5-2GPa for pyroxenite: Lambart *et al.*, 2009, Lambart *et al.*, 2013, P > 2.4GPa for peridotite: Walter, 2014). Trace element abundances normalized to primitive mantle (Hofmann, 1988)

The Siberian samples have lower average Gd/Yb_n (shallower source) than the Deccan-Réunion suite while the average Nb/La_n remains comparable to Deccan1. Several outliers with $Gd/Yb_n > 2$ can be noted. They belong to the lower part of the Norilsk section (Sobolev *et al.*, 2011). The Siberian dataset did not include Pb concentration hence it is not shown in the Ce/Pb versus Th/Nb_n diagram (Figure 5.5b).

The high-Ti picrites of Gujarat have been described as OIB-like and similar to recent Réunion Island shield lavas on the basis of trace element and isotopes while other Gujarat volcanics appear rather MORB-like and likely related to a combination of local rifting and remote/early plume activity (Melluso *et al.*, 2006, Sen *et al.*, 2009), section 2.3. Despite low Gd/Yb_n of some of them implying shallow depths of melting, which can be assigned to the existence – and syn-Deccan reactivation – of intra-cratonic rifts in Gujarat (e.g. Biwas, 2005), high-Ti picrite can be seen as resulting from the early flood basalt activity of the Deccan plume (after incubation and early manifestations dating back to at least 70Ma, Figure 2.1) while products of Réunion Island unambiguously constitute the final, present day end member of the plume evolution (Roy, 2003). A global correlation in Gd/Yb_n versus Nb/La_n and Ce/Pb versus Th/Nb_n between Gujarat High-Ti picrites, Deccan2 and Réunion Island (oceanic crust) can be noted. This general correlation does not include Deccan1 (e.g. Nb/La_n and Gd/Yb_n only

appear correlated at $Gd/Yb_n < 1.6$. Above this threshold, the correlation disappears and the scattering is large). It is therefore possible that the assimilation processes of Deccan1 were specific to this subset and not representative of the Deccan system as a whole (Gujarat – Western Ghats – Réunion Island).

5.4. Evidence for a rapid change in crustal contamination at constant garnet signature during the main volcanic phase of the Deccan Traps

The samples used for paleomagnetic observations and those used in bulk-rock major and trace element analysis have been collected at the same locations (section 4). Therefore, the subsets of Western Ghats lavas identified earlier (Deccan1 and 2, Figure 5.3a) can be assigned a relative age by using the re-visited Western Ghats eruption timeframe of Figure 3.1 (section 3.6). Figure 5.7 combines Figure 3.1 with incompatible trace element ratios that increase with garnet signature (Gd/Yb_n) and that decrease with crustal contamination (Nb/La_n) from Figure 5.5a.

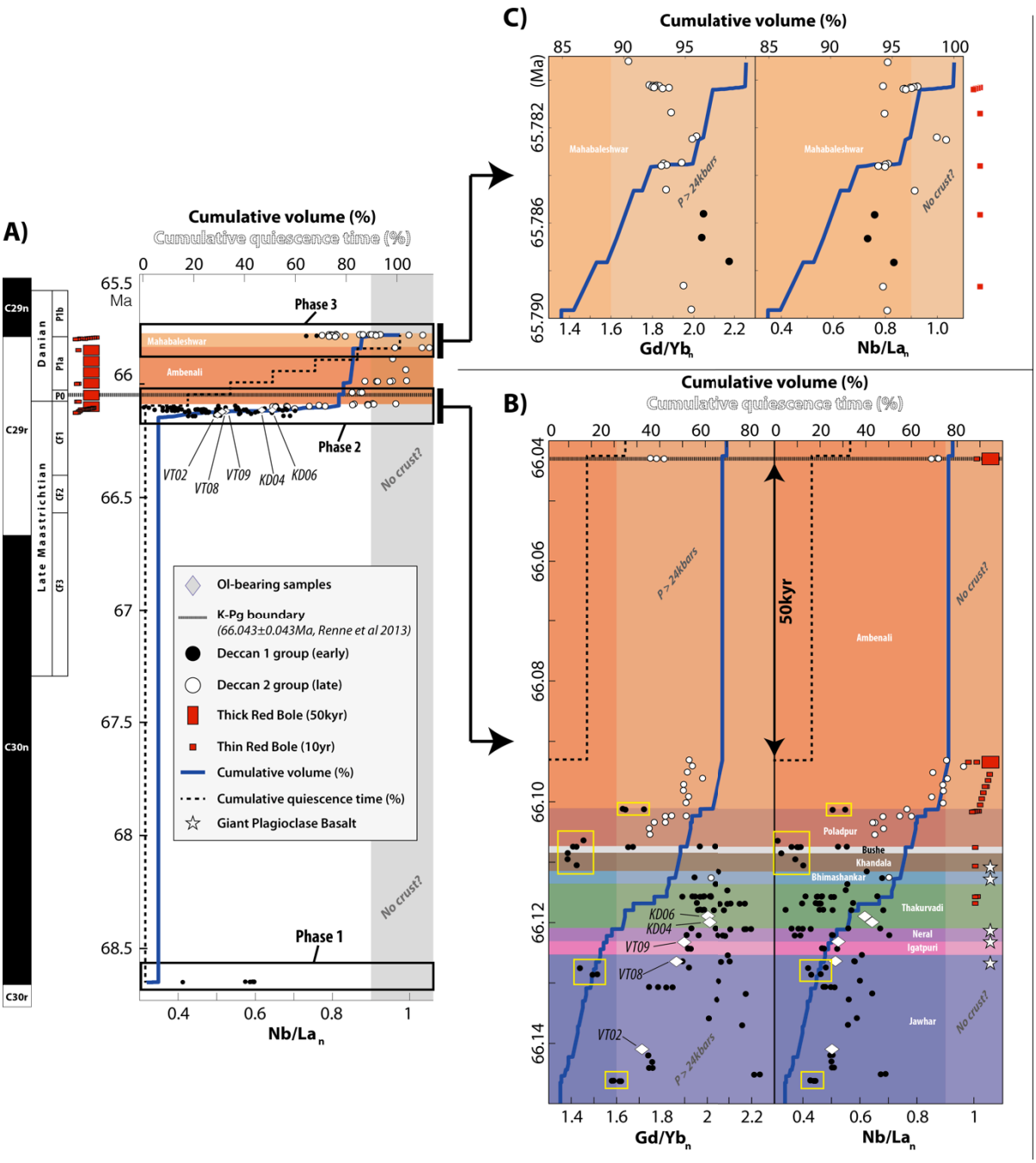

Figure 5.7 - Western Ghats eruption timeframe coupled with bulk-rock trace element data. This figure is a combination of the Deccan eruption timeframe Figure 3.1 (section 3.6) and Figure 5.5a in this section. A) Full timespan of the Western Ghats emplacement with the three main eruption phases determined by Chenet et al (2007) based on ^{40}K-^{40}Ar dating. B) Enlargement of the main Deccan eruption phase (Phase 2). C) Enlargement of the final Deccan phase (Phase 3, Mahabaleshwar only) White diamonds indicates the occurrence of olivine-bearing samples (section 4). Shaded areas: Gd/Yb_n > 1.6 for P > 2.4GPa (Lambart *et al.*, 2009, 2013, Walter, 2014) and Nb/La_n > 0.9 (labelled "no crust?") for limited crustal assimilation (Rudnick & Gao, 2003). Yellow rectangles indicate events of low Gd/Yb_n and Nb/La_n see text

The Deccan1 subset spans the lower formations from Jawhar to Bushe with the exception of one lava flow in Neral. All reported olivine-bearing samples are found between Jawhar and Thakurvadi and bear clear evidence of crustal contamination ($Nb/La_n < 0.7$). On the other hand, Deccan2 occurs mostly in the upper formations, from Poladpur to Mahabaleshwar (with three exceptions). Ambenali (Deccan2) clearly appears as the most homogeneous and least contaminated (Peng *et al.*, 1994, Melluso *et al.*, 2006, Chatterjee & Bhattacharji, 2008, Bhattacharya *et al.*, 2013) formation of the entire section and with respect to both major and trace element ratios (Gd/Yb_n varies between 1.75 and 2.10 while Nb/La_n ranges form 0.85 to 1.05).

A swift geochemical transition occurs in Khandala, Bushe and Poladpur, towards the end of phase 2. Both Khandala and Bushe have the lowest Gd/Yb_n of the entire section (Bushe however shows large variations between 1.41 and 2.04) and the lowest values of Nb/La_n (<0.4). This transition continues in Poladpur (that also has one flow with very low Nb/La_n = 0.31) where the Deccan1 subset ends. With few exceptions, Gd/Yb_n and Nb/La_n are correlated and both increase in Poladpur and early Ambenali. This major transition in incompatible trace element ratios occurs during the second half of phase 2 and seems – considering the hypotheses regarding this timeframe (section 3.6) – to end in early-Ambenali, with the K-Pg boundary. A remarkable feature of this Khandala-Bushe-Poladpur compositional transition is the fact that, based on the near-absence of thin red boles and the occurrence of directional groups (DGs) significant quiescence time can be ruled out (Khandala: three single flows. Bushe: one DG with five flows yet one thin red bole (DG Bushe1). Poladpur: five single flows and two DGs of four flows each (DGPA1 and DGPA2, the latter spans three thin red boles). It is therefore likely that this transition occurred within less than 20ka (Figure 5.7b). Directional Groups (DGs) are reported in appendix II.

Along the same lines Figure 5.7b further reveals that Deccan1 comprises four events, indicated by yellow rectangles on the figure, wherein both Gd/Yb_n and Nb/La_n are low, and that all bear evidence of fast emplacement:

- In lower Jawhar at 66.145Ma, four flows within one DG of five flows (DGJW1, one flow without compositional data): $Gd/Yb_n \sim 1.6$ and $Nb/La_n \sim 0.4$
- In upper Jawhar at 66.128Ma, three flows from two DGs of two flows each (DGSI2 and DGMKKI5. The last flow of the latter has $Gb/Yb_n = 1.9$ and is a Giant Plagioclase Basalt (section 3.4), white star on Figure 5.7): $Gd/Yb_n \sim 1.45$ and $Nb/La_n \sim 0.45$

- In Khandala, Bushe, early-Poladpur between 66.110 and 66.105Ma, with respect to Bhimashankar and late Poladpur-Ambenali. This event is made of three single flows of Khandala, one DG with five flows and one thin red bole (DG Bushe1) of Bushe and one single flow of Poladpur: Gd/Yb_n ~ 1.45 and Nb/La_n ~ 0.3-0.4. This event corresponds to the Khandala-Bushe-Poladpur transition described in the preceding paragraph, late-Poladpur excepted
- In late-Poladpur at 66.101Ma, three flows from one DG (DG PA2) with three thin red boles. Gd/Yb_n = 1.63 to 1.72 and Nb/La_n 0.50 to 0.77. This excursion is separated from the main Khandala-Bushe-Poladpur transition mentioned above by four single flows and one DG of four flows (DG PA1)

Directional Groups (DGs) are reported in appendix II.

Phase 3 (Mahabaleshwar, Figure 5.7c) is more heterogeneous than Ambenali yet less than phase 2. Gd/Yb_n (1.7 – 2.2), which is on average higher than phase 2 (1.4 – 2.2) while Nb/La_n is clearly higher (0.7 – 1.0). Two phase 3 samples have been classified as Deccan1 due to their lower Nb/La_n (Figure 5.3 and Figure 5.7c).

5.5. Summary and preliminary interpretations

Section 3.6, based on previous work from Chenet and colleagues (Chenet *et al.*, 2007, 2008, 2009) and further literature review, exposed a very hectic unwinding of the Deccan Traps emplacement with three main phases separated by 2.5Ma (phase 1 to phase 2) and 0.3Ma (phase 2 to phase 3) and eruption rates that would have been close to $20km^3/yr$ on average and potentially skyrocketing to $160km^3/yr$ within some directional groups (Thakurvadi formation, DG TH2, Chenet *et al.*, 2009). This somewhat heterogeneous picture is now complemented by bulk-rock major and incompatible trace elements.

There appear to be a clear chemical dichotomy along the Western Ghats section. This difference has been identified using bulk-rock incompatible trace elements (Figure 5.5) and also affects major element compositions (Figure 5.4). Figure 5.3 shows this dichotomy in terms of trace element signatures that differ to the left of Sm (incompatible elements) while the HREE signatures (to the right) are strikingly parallel (Ti-anomaly excepted). Two subsets of Western Ghats lavas were thereby proposed: Deccan1 has lower average Nb/La_n and is slightly more enriched in incompatible elements than Deccan2 (Figure 5.3 and Figure 5.5). Furthermore, indices that vary with crustal contamination (e.g. Nb/La_n) are on the whole

reversely correlated with indices showing the primitiveness of lava compositions (e.g. Mg#, Figure 5.5 and Figure 5.4) (Cox & Hawkesworth, 1985, Devey & Cox, 1987). Deccan1 therefore seems more primitive (higher average Mg#) and yet more contaminated (lower average Nb/La_n) than Deccan2.

Upon plotting the incompatible trace element ratios of Figure 5.5 through time (Figure 5.7), it appears that a clear transition from the Deccan1 to Deccan2 occurred in late phase 2 (Chenet *et al.*, 2007) in the Khandala, Bushe and Poladpur formations. Within these formations, Nb/La_n increases from ~ 0.4 to > 0.8 and Gd/Yb_n increases from ~ 1.4 to > 1.9, implying that magmatic sources were not in the garnet stability field early in this transition (Khandala and Bushe) but that they indeed were by the end of it (Ambenali), and that crustal assimilation almost stopped at the same time. The relative timeframe suggests that this transition has occurred in less than 20ka and remained until the end of the Deccan Traps eruptions (Figure 5.7).

In addition to the Khandala-Bushe-Poladpur transition, there appear to be occasional excursions of both low Gd/Yb_n and Nb/La_n that also bear evidence of remarkable swiftness in lower (1 DG = 100 years) and upper (2 DGs = 200 years) Jawhar, in Khandala-Bushe with respect to Bhimashankar and Poladpur-Ambenali (4 single flows (4000 years) + 1 DG (100 years) + 2 thin red boles (20 years) = 4200 years based on section 3.6) and late-Poladpur (1Dg and three thin red boles = 130 years) (yellow rectangles Figure 5.7). On these occasions, Gd/Yb_n and Nb/La_n are correlated and low ($Gd/Yb_n < 1.7$ and $Nb/La_n < 0.5$, Figure 5.6) implying both shallow sources and significant crustal contamination. No such excursion is reported for Ambenali and Mahabaleshwar (Figure 5.7c)

Except for these excursions, Gd/Yb_n and Nb/La_n are not correlated: both Deccan1 and Deccan2 have an average Gd/Yb_n ~ 2 despite average Nb/La_n of ~ 0.5 and ~ 0.9 respectively (Figure 5.5a). Therefore, both Deccan1 and Deccan2 mostly differ by the extent to which they have assimilated crustal components. This is also clearly seen in the trace element patterns (Figure 5.3) and in Ce/Pb and Th/Nb_n (Figure 5.5b).

Figure 5.6 shows a comparison of the Deccan Traps and the Siberian Traps (Sobolev *et al.*, 2011). It appears that garnet signature is absent from most Siberian lava flows, except early ones, which contrasts with the almost ubiquitous $Gd/Yb_n > 1.6$ in the Deccan Traps.

Sobolev et al (2011) have shown that a plume can significantly erode the lithosphere and reduce its thickness (e.g. by more than 50% in about 50ka). Sobolev and colleagues further

argued that in the Siberian case, widespread lithospheric erosion resulted in a sharp drop in Gd/Yb_n (from > 1.6 to <1.5, Figure 5.6) clearly suggesting that the magmatic sources were no longer in the garnet stability field and that the depth of the lithosphere-asthenosphere boundary had been reduced to < 80km. However, Sobolev et al. also contended that the widespread lithospheric thickness reduction caused by the Siberian plume would not have been of the same magnitude if the lithosphere had been thicker (> 130km).

The trace element variations in Deccan Traps lavas reported in this manuscript are compatible with what Sobolev et al (2011) expected for 1) plumes impinging upon thick lithosphere (e.g. 140km) and 2) early release of mantle melts via pre-existing weaknesses within the lithosphere (Murthy, 2002, Biwas, 2005). In this situation, plume-induced lithospheric erosion would be more limited and localized than in the case a thinner and less permeable lithosphere. In the Siberian Traps Sobolev and colleagues (Sobolev *et al.*, 2011) noted that the erosion of the Siberian craton by magmatic processes (melt freezing and delamination) had been very large due to the absence of pre-existing potential pathways for melt transport towards the surface. However localized, the erosion of the Indian lithosphere may still result in hot plume material being brought very close to the crust, inducing decompression melting and crustal assimilation due to heat advection beneath the crust as well as within conduits by turbulent melt transport (Huppert & Sparks, 1985). The typical timescale required for this lithospheric erosion process to be completed has been shown, by numerical modelling, to be in the order of 50ka. This is compatible with the duration of phase 2 of the Deccan Traps eruption (~ 70-80% of the total speculated volume of the Main Deccan Province in ~ 50ka, Figure 5.7b). It is speculated that the 3 or 4 Gd/Yb_n and Nb/La_n excursions could belong to the same erosion event. The sudden "rebound" of Gd/Yb_n and Nb/La_n in Poladpur may be accounted for by the fact that fertile peridotite is denser than e.g. harzburgite. Thus, it is possible that the pathway created by lithospheric erosion became sufficiently clogged by light restite for Gd/Yb_n to increase again significantly (> 1.6). The coeval decrease in crustal assimilation would be due to coating and exhaustion of the conduits wall rock by previous melts.

The upper formations (Wai subgroup) were erupted under this same final regime (deep source, low contamination) as suggested by the quiescence periods (thick red boles) and comparatively lower emplaced volumes (Figure 5.7a), despite the significant extent of the Wai subgroup on the field (Self *et al.*, 2008b, Vanderkluysen *et al.*, 2011).

Bhattacharya et al (2013) identified spikes of high $\delta^{18}O$, low $\varepsilon Nd(t)$ and high $^{87}Sr/^{86}Sr(t)$ compatible with isolated yet significant crustal inputs in late-Poladpur and early-

Mahabaleshwar (no data available for the lower formations). Note that these contamination events are not seen on Figure 5.7c in Gd/Yb_n and Nb/La_n and are thus likely to have been of much lower intensity than those of the lower formations (Figure 5.7b). Bhattacharya et al. proposed that only two phenomena could explain their observations: 1) A different plumbing system is used for each new formation (with the exception of Ambenali) and crustal contamination drops once this new feeder system has been coated by rising magmas. 2) All magmas come from the same chamber. This chamber is fed by magmas that may have had different sources and/or crustal contamination histories. The erupted lavas are the products of various degrees of mixing within this common chamber.

It is likely that their first proposition is incorrect, as it has been shown that all three major Deccan dike swarms have been active almost simultaneously during the emplacement of the Main Deccan Province (Vanderkluysen *et al.*, 2011). However, the second proposition fits two important features of the upper formations and is likely to by more realistic. First, the composition of Deccan2 lavas is on average more evolved and less heterogeneous than that of Deccan1 (Figure 5.4), suggesting that Deccan2 melts were stored in order for them to have homogeneous and evolved compositions. Secondly, the isotopic trends of the Mahabaleshwar and Poladpur formations are different (higher $^{87}Sr/^{86}Sr_{(t)}$ in Poladpur lavas, Figure 2.5). Therefore, the contamination history could have been different.

Finally, the localized lithospheric erosion scenario proposed in the above is in agreement with the present-day Indian lithospheric thickness (localized thinning in the vicinity of the Nasik-Pune swarm and along the west coast but preservation of the Indian Shield to the east, Figure 2.7), with paleostress field modelling on the Indian plate at the time of the Deccan Traps (Ju *et al.*, 2013) as well as with the broad shield-like structure and compound flows centred on Nasik-Pune swarm (Subbarao *et al.*, 2000) (Figure 2.3).

6. Olivine Petrology in the Deccan Traps and Réunion Island

Olivine are used as a mean to access deep magmatic processes. The minor and trace element composition of high-forsterite olivines allows elemental signatures to be related to olivine-free material in the source of primary magmas (Sobolev *et al.*, 2005, 2007). The composition of host olivine and spinel inclusions is used to calculate aluminium partitioning between them, which has been related to magmatic temperatures (Wan *et al.*, 2008, Sobolev *et al.*, 2013, Coogan *et al.*, 2014). Finally, the composition of olivine-hosted melt inclusions is a proxy for primary melt major element composition (Sobolev, 1996, Sobolev *et al.*, 2005), primary melt water content (e.g. Dixon *et al.*, 2002, Almeev *et al.*, 2007, Médard & Grove, 2008) and magmatic temperatures (Sobolev & Nikogosian, 1994, Bureau *et al.*, 1998b, Danyushevsky, 2001, 2002a, Schiano, 2003, Danyushevsky & Plechov, 2011).

All olivine phenocrysts and inclusions have been analysed by Electron-Probe MicroAnalyser at ISTerre, Grenoble, France. Details as to the analytical protocols used during this project are presented in appendix III.

Examples of olivine compositions are listed in Table 6–3 and full datasets are available from the corresponding author.

This section begins with a brief presentation of the samples and reminder on the Thakurvadi formation of the Main Deccan Province (for a reminder on the geological setting of Réunion Island, see 2.5). It will then be dedicated to olivine and inclusions (spinel and melt) compositional data. Their use for primary melt reconstruction and source modelling will be dealt with in section 7.

6.1. Samples

The olivine-bearing samples collected for this PhD project are all reported in Table 4–2 (section 4). However, this section only considers those that fell within the compositional range required for the application of the methods of Sobolev et al (2005, 2007). In other words, this section is based of samples bearing olivine with forsterite content above ~80.
The sample set used for olivine analysis is described consists of 2 samples from the Thakurvadi formation in the Main Deccan Province (KD04 and KD06), 6 samples from Piton de la Fournaise (PdF), Réunion Island (OPF, TI1602, GB1961, SR1977, 0202-053 and 0502-

263) and 1 sample from Piton des Neiges (PdN), Réunion Island (RU11). The Deccan samples will be systematically compared to the Réunion Island samples as early and present-day stages of the Deccan plume respectively.

The major and trace element composition of the selected picritic, olivine-phyric samples is given on Table 6–1 below and their normalized trace element patterns are shown on Figure 6.1.

Table 6–1 - Major and trace element compositions of samples selected for olivine petrology, primary melt and source modelling. See Table 4–2 (section 4) for references. Note that no bulk-rock composition was found for sample 0202-053, which has only been analysed for lead isotopes (Vlastélic *et al.*, 2005). PdF: Piton de la Fournaise; PdN: Piton des Neiges.

	Deccan		Réunion (PdF)					(PdN)
(wt%)	KD04	KD06	T1602	GB1961	0502-263	SR1977	OPF	RU11
SiO_2	47.97	48.27	43.84	44.49	44.83	44.61	45.86	43.40
TiO_2	1.71	1.75	1.28	1.31	1.49	1.48	1.58	1.33
Al_2O_3	11.36	11.53	7.12	8.36	8.03	8.46	7.98	7.60
FeO*	12.17	12.13	13.38	12.63	12.88	12.74	12.04	12.20
MnO	0.18	0.18	0.19	0.19	0.19	0.19	0.19	0.17
MgO	12.71	12.22	26.29	22.82	24.00	22.64	22.44	25.20
CaO	10.09	10.40	5.84	6.62	6.51	6.70	6.46	5.90
Na_2O	1.72	1.78	1.28	1.36	1.53	1.42	1.45	1.90
K_2O	0.21	0.29	0.36	0.41	0.39	0.47	0.52	0.50
P_2O_5	0.20	0.21	0.15	0.17	0.20	0.16	0.19	0.18
Cr_2O_3							0.14	0.22
LOI	2.07	2.44					0.68	0.55
Total	100.39	101.19	99.73	98.36	100.05	98.87	99.51	99.15
(ppm)								
Rb	*2.40*	*2.79*	*7.40*	*10.00*	*8.72*	*11.00*	*12.30*	*12.00*
Ba	*107.12*	*113.36*	*58.09*	*114.20*	*63.30*	*128.50*	*94.80*	*86.00*
Th	*1.86*	*1.85*	*0.84*	*1.52*	*1.07*	*1.56*	*1.60*	*1.25*
U	*0.46*	*0.44*	*0.24*	*0.49*	*0.26*	*0.56*	*0.38*	*0.25*
Nb	*7.26*	*6.94*	*9.28*		*11.36*			
Ta	*0.56*	*0.56*	*0.60*		*0.70*			*0.84*
La	*11.20*	*11.17*	*8.20*		*9.12*		*11.99*	*10.52*
Ce	*25.19*	*25.21*	*18.60*	*28.40*	*21.59*	*28.20*	*22.90*	*25.60*
Pb	*2.65*	*2.58*						
Pr	*3.38*	*3.34*	*2.45*		*2.81*			
Nd	*14.98*	*14.86*	*10.69*	*16.60*	*12.48*	*15.90*		
Sr	*208.43*	*211.24*	*141.71*	*286.20*	*178.60*	*301.40*		
Sm	*3.88*	*3.84*	*2.46*	*4.06*	*3.05*	*3.74*	*3.50*	*3.13*
Zr	*94.50*	*93.02*	*69.88*	*103.00*	*101.00*	*103.00*	*101.00*	*76.00*
Hf	*2.58*	*2.56*	*1.88*		*2.29*		*2.83*	*2.53*
Eu	*1.38*	*1.33*	*0.85*	*1.39*	*1.09*	*1.23*	*1.37*	*1.02*
Gd	*4.17*	*4.11*	*2.58*	*4.00*	*3.06*	*4.06*		
Tb	*0.64*	*0.63*	*0.38*		*0.54*		*0.52*	*0.45*
Dy	*3.68*	*3.65*	*2.27*	*3.79*	*2.74*	*3.21*		
Ho	*0.70*	*0.72*	*0.42*		*0.54*			
Y	*19.30*	*18.93*	*10.95*		*15.69*			
Er	*1.85*	*1.89*	*1.10*	*1.93*	*1.40*	*1.62*		
Tm	*0.26*	*0.26*						
Yb	*1.68*	*1.66*	*0.91*	*1.66*	*1.14*	*1.31*	*1.44*	*1.21*
Lu	*0.25*	*0.25*	*0.13*		*0.17*			

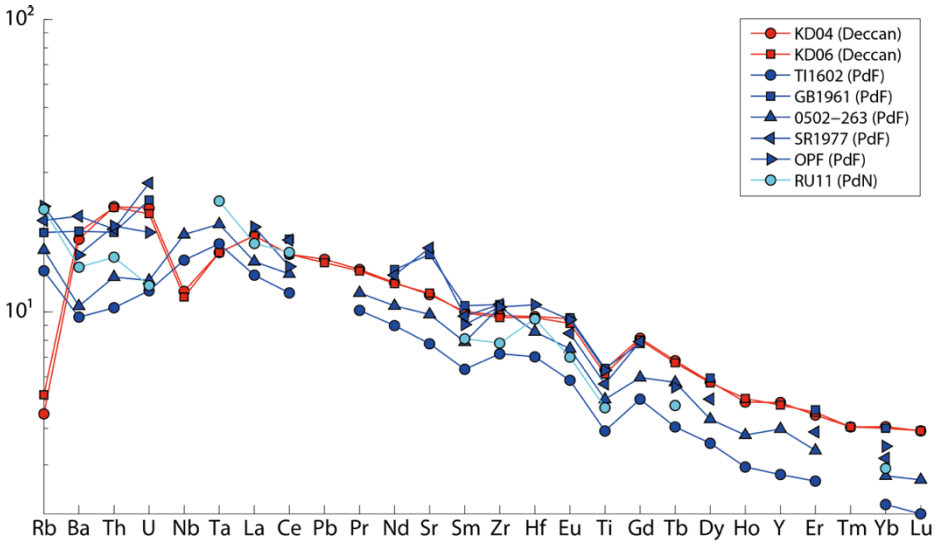

Figure 6.1 - Trace element patterns normalized to primitive mantle (Hofmann, 1988) of the samples selected for olivine petrology, primary melt and source modelling (Table 6–1). PdF: Piton de la Fournaise; PdN: Piton des Neiges.

KD04 (Mg# = 0.65) and KD06 (Mg# = 0.64) belong to the Thakurvadi formation. Their trace element composition is characterized by low Nb/La_n (0.64 and 0.62 respectively), Th/Nb_n (1.95 and 2.03, respectively) and Ce/Pb (9.50 and 9.77 respectively) and high Gd/Yb_n (2.01 and 2.00 respectively). These characteristics are compatible with the Deccan1 signature identified in section 5.1. Deccan1 corresponds to a highly contaminated by both upper (low Nb/La_n) and lower (high Th/Nb_n) crust that builds the lower two thirds of the Western Ghats lava pile. It can however be noted that KD04 and KD06 have low Th/Nb_n and Ce/Pb and that their Deccan1 membership solely stems from their low Nb/La_n. These samples are therefore contaminated by one or more upper crustal components and the implication of the lower crust in their trace element signature seems minimal. Their garnet signature, identified from $Gd/Yb_n > 1.6$ (Sobolev *et al.*, 2011), suggest that their primary magmas originated at pressures greater than 2.4GPa (Walter, 2014).

KD04 and KD06 compatible with Type 2 picrites of Krishnamurthy et al (2000), i.e. Fo generally <86 while Type 1 picrites occur in the alkaline to transitional series of Gujarat and have Fo contents between 86 and 92.

The Réunion Island samples have Mg# between 76 and 80, indicative of higher forsterite contents than KD04 and KD06. Their trace element signatures feature strong garnet signature ($Gd/Yb_n = 1.95 – 2.5$) and no indication of continental crust assimilation ($Th/Nb_n < 0.8$, $Nb/La_n > 1.1$ and $Ce/Pb > 20$ (Figure 5.5) as Réunion Island is located on oceanic crust.

See section 2.5 for a presentation of the geological setting of Réunion Island.

6.2. The Thakurvadi formation

The Thakurvadi formation is the second last formation of the Kalsubai subgroup (Figure 6.2).

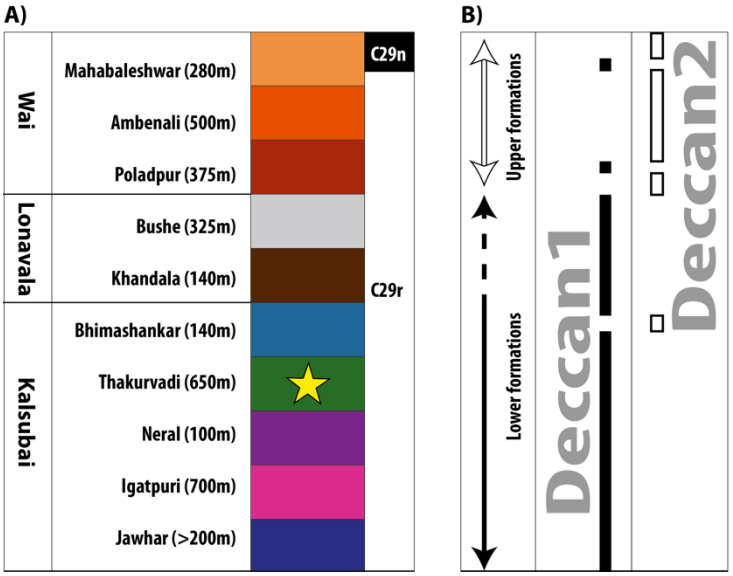

Figure 6.2 - A) Western Ghats stratigraphy modified from Chenet et al (2009). Yellow star indicates the location of the KD04 and KD06 olivine-bearing samples analysed during this project. B) Differences between the division in lower (Igatpuri-Jawhar to Bushe) and upper formations (Poladpur to Mahabaleshwar), e.g. Peng et al (1994) and the Deccan1 and Deccan2 subsets identified from trace element-based statistical analysis (K-Means clustering), section 5.1

Most of its outcrops are located in the Western Ghats. Nevertheless, the chemical signature of the Thakurvadi formation has been identified in all three main feeder dyke systems of the Deccan Traps (Vanderkluysen *et al.*, 2011), Figure 2.3 (section 2.2). The chemical characteristics of the Thakurvadi formation after Peng et al (1994, and references therein) are given in Table 6–2.

Table 6–2 - Chemical characteristics of the Thakurvadi formation and its various sub-units from Peng et al. (1994). The full version of this table with all Deccan formations is given in appendix I

Member or chemical type (CT)	($^{87}Sr/^{86}Sr$)t	Avg. Mg#	TiO2%	Avg. Ba/Zr	Avg. Zr/Nb
Thakurvadi CT	0.7073-0.7080	58	1.8-2.2	0.8	12.0
Water Pipe Member	0.7099-0.7112	59/71	1.4-1.6/1.0-1.1	1.5/1.3	12.3/12.0
Paten Basalt		58	1.0	1.3	15.2
Thakurvadi CT	0.7067-0.7070	58	1.8-2.2	0.8	12.4
Ashne	0.7068	62	2.0-2.1	1.2	9.6
Thakurvadi CT	0.7080-0.7084	58	1.8-2.2	0.8	11.6
Jammu Upper	0.7112	34	2.7	1.6	9.8
Patti Middle	0.7099	46	2.2-2.3	1.5	8.4
Lower Member	0.7066-0.7067	56	1.7-2.0	1.1	11.2

Chenet et al. (2009) reported 25 flows belonging to 5 different directional groups, 2 single flows, and 3 thin red boles, all located within a directional group. One of the 5 directional groups of the Thakurvadi formation is the thickest (200m) of the Western Ghats composite section. Chenet et al calculated an eruption rate of 160km^3/yr for this paroxysmal event.
The Thakurvadi samples used in this section (KD04 and KD06) are from the bottom flows of the formation, just above Neral and do not belong to any directional group (see Figure 5.7 section 5.4, and appendix II). Trace element concentrations and Mg# (section 6.1 above) are consistent with the Lower Member chemical type (Table 6–2) as well as with the Deccan1 signature discussed in section 5. Sr isotope ratios were not measured during this PhD.

KD04 and KD06 are the only Deccan samples presented for olivine geochemistry in this manuscript. None of the few other Deccan samples analysed during this PhD had MgO content (and olivine forsterite) compatible with primary melt and source modelling (MgO < 8wt% and Fo << 80). KD04 and KD06 will be systematically compared to the Réunion Island, PdN (RU11) and PdF (OPF, TI1602, GB1961, SR1977, 0202-053 and 0502-263).

6.3. Olivine major and trace element composition

Olivine phenocrysts in volcanic rocks contain a wealth of information as to the origin and evolution of magmas. Under the low-pressure conditions of crustal magma chambers, olivine is the first silicate mineral to crystallise in mantle-derived melts (P < 10kbars, Green & Ringwood, 1967). The composition of high-forsterite olivine will thus directly reflect that of

the primary melt. In addition, during their growth, olivine crystals trap a number of valuable indicators of primary melt compositions and temperature. Spinel inclusions and the partitioning of aluminium with the host olivine carry information as to the magmatic temperatures at the time of olivine crystallisation (Wan *et al.*, 2008, Sobolev *et al.*, 2013, Coogan *et al.*, 2014). In the same way, olivine growth sometimes results in small volumes of magma being trapped within the phenocrysts. Such melt inclusions carry information as to the composition and temperature of the surrounding magma.

Sections 6.3 and 6.4 deal with olivine phenocryst compositions. Melt and spinel inclusions will be considered in sections 6.5 and 6.6.

Examples of olivine compositions from all samples investigated in this section are presented in Table 6–3, below.

Table 6–3 - Examples of olivine compositions for the selected Deccan and Réunion Island samples (PdN: Piton des Neiges; PdF: Piton de la Fournaise). Oxides concentrations in wt%. Xpx_{Mn} and Xpx_{Ni} from Sobolev et al (2005, 2007)

	Deccan		Réunion (PdF)						(PdN)
Sample	KD04	KD06	TI1602	GB1961	0202-053	0502-263	SR1977	OPF	RU11
SiO_2	39.55	39.78	39.83	39.83	39.64	39.73	39.93	39.83	41.19
TiO_2	0.0130	0.0150	0.0180	0.0170	0.0220	0.0190	0.0170	0.0170	0.0140
Al_2O_3	0.0370	0.0500	0.0310	0.0340	0.0490	0.0360	0.0310	0.0310	0.0550
FeO	16.86	16.00	15.12	15.00	14.73	14.28	14.73	15.38	10.15
MnO	0.2290	0.2240	0.2180	0.2190	0.2100	0.2050	0.2160	0.2270	0.1530
MgO	43.40	44.14	45.06	44.94	45.11	45.43	45.34	44.80	49.26
CaO	0.3140	0.2800	0.2810	0.3060	0.2640	0.2750	0.2910	0.2970	0.2830
NiO	0.2960	0.2970	0.2690	0.2600	0.2780	0.2910	0.2710	0.2560	0.3570
CoO	0.0250	0.0260	0.0250	0.0250	0.0250	0.0240	0.0240	0.0250	0.0230
Cr_2O_3	0.0620	0.0640	0.0400	0.0400	0.0580	0.0500	0.0370	0.0360	0.0820
ZnO	0.0180	0.0120	0.0150	0.0140	0.0150	0.0150	0.0130	0.0120	0.0080
P_2O_5	0.0150	0.0230	0.0110	0.0230	0.0560	0.0120	0.0140	0.0130	0.0140
Na_2O	0.0040	0.0040	0.0060	0.0080	0.0060	0.0050	0.0080	0.0040	0.0030
Total	100.82	100.92	100.92	100.72	100.46	100.37	100.92	100.93	101.58
Fo	82.11	83.10	84.16	84.23	84.52	85.01	84.59	83.85	89.64
Ni ppm	2 327	2335	2117	2043	2182	2285	2131	2014	2808
Ni*	0.115	0.108	0.09	0.087	0.091	0.091	0.088	0.088	0.074
Mn/Fe	0.0140	0.0140	0.0144	0.0145	0.0142	0.0143	0.0146	0.0147	0.0151
Ni/(Mg/Fe)/1000	1.165	1.091	0.916	0.879	0.918	0.926	0.892	0.891	0.746
Ni/Co	11.7	11.5	10.9	10.5	11.2	12.2	11.1	10.1	15.6
Xpx Mn	0.68	0.59	0.50	0.47	0.54	0.52	0.45	0.43	0.36
Xpx Ni	0.78	0.70	0.52	0.48	0.52	0.53	0.49	0.49	0.34

$$Fo = \frac{\frac{MgO}{M_{MgO}}}{\frac{MgO}{M_{MgO}}+\frac{FeO}{M_{FeO}}} \times 100 \quad (6.1)$$

$$Ni^* = NiO \times \frac{FeO}{MgO}\ (wt\%) \quad (6.2)$$

$$Xpx_{Ni} = 10.5402 \times Ni^* - 0.4368 \quad (6.3)$$

$$Xpx_{Mn} = 3.48 - \left(2.071 \times \frac{Mn}{Fe} \times 100\right)\ (ppm) \quad (6.4)$$

Figure 6.3 shows the compositional range for all Deccan and Réunion Island samples with respect to the reference dataset of Sobolev et al. (2007).

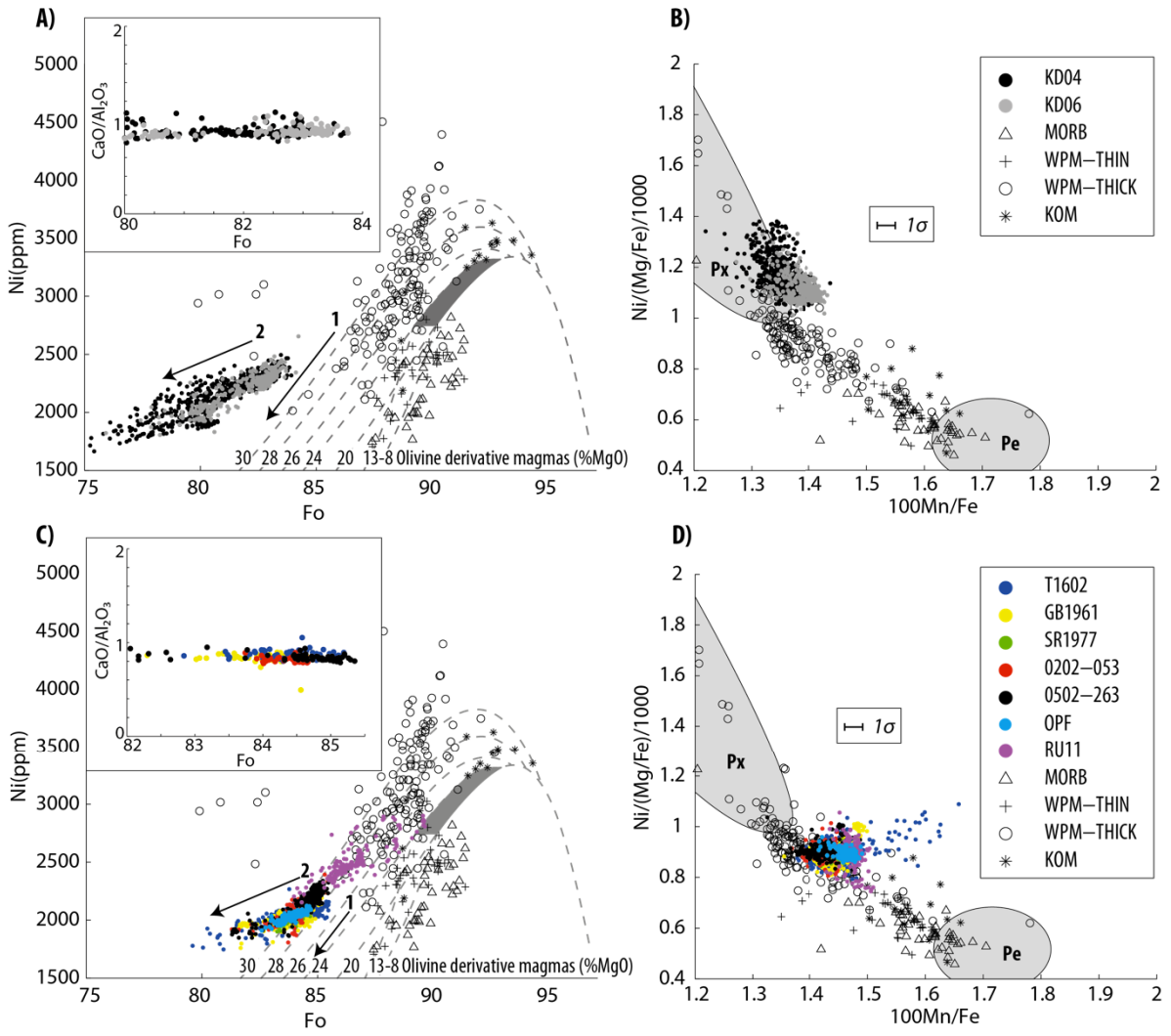

Figure 6.3 - Olivine phenocrysts compositional range for the Deccan Traps (A and B) and Réunion Island (C and D) samples from high-precision EPMA (900nA, 25kV) and corresponding error bar when necessary (no error bar implies 1σ error smaller than symbols). The dataset of Sobolev et al. (2007) is also shown for comparison: MORB: Mid-Ocean Ridge Basalts, WPM-Thin: Within Plate Magma Thin lithosphere, WPM-Thick: Within Plate Magma Thick lithosphere, KOM: Komatiites. A and C: Ni (ppm) and Fo (mol%) contents with superimposed peridotite melting model of Herzberg (2011): the path followed by both Réunion and Deccan olivines (arrow 2) is different from that expected for purely peridotitic melts (arrow 1). This trend could be explained by the coeval crystallisation of large amounts of clinopyroxenes (Herzberg *et al.*, 2013). CaO/Al_2O_3 of olivine melt inclusions (section 6.5) versus Fo is shown in an inset in A and C of the figure. Constant CaO/Al_2O_3 at any Fo clearly rules out the possibility of significant coeval clinopyroxene crystallisation. B and D: Ni/(Mg/Fe)/1000 and 100Mn/Fe; Px: pyroxenitic source field and Pe: peridotitic source field form Sobolev et al (2007)

KD04 and KD06 (Deccan Traps, Thakurvadi formation, Figure 6.3a) have similar Fo (74.1 to 83.9 and from 75.9 to 84.2mol% respectively) and Ni (1665 to 2496 and 1807 to 2655ppm respectively) contents. This range of Fo content along with the bulk-rock compositions presented in section 6.1 are compatible with fractionated (Fo < 86), cumulate, tholeiitic-picritic Type2 olivines described by Krishnamurthy et al. (2000) and are therefore the most

forsteritic olivine that can be found in the Main Deccan Province, alkali peripheral volcanics (Figure 2.3) excepted (e.g. Krishnamurthy *et al.*, 2000, Melluso *et al.*, 2006).

The Réunion Island (Piton de la Fournaise) samples (TI1602, GB1961, SR1977, 0202-053 and 0502-263, Figure 6.3c) have overall higher and less scattered Fo (Fo = 79.5-85.5) than the Deccan samples KD04 and KD06. Their Ni content ranges from 1869 to 2413ppm. RU11 from Réunion Island (Piton des Neiges) has significantly higher Fo olivines than both Piton de la Fournaise and Deccan Traps (Thakurvadi formation) samples (Fo = 84.0-89.6). Ni contents range from 1747 to 2341ppm for Piton de la Fournaise samples and from 2154 to 2901ppm for RU11 (Piton des Neiges).
The Ni-Fo trends of the Deccan Traps (Thakurvadi formation) and Réunion Island samples of parallel with the Ni content of Réunion Island samples about 400ppm lower than that of the Deccan Traps (Thakurvadi formation) samples at equal Fo.

The forsterite content of olivine phenocrysts decreases with the fractionation of their associated melt (Bowen, 1928, Roeder & Emslie, 1970). Moreover, mantle olivines have Fo contents in the order of 90-92 (e.g. Herzberg, 2011, Foley *et al.*, 2013). It is therefore important to use *volcanic* olivines with the highest possible Fo content for primary melt reconstruction and thermometry (section 7) (Sobolev *et al.*, 2005, 2007).

Ni being more compatible with olivine than pyroxenes while Mn behaves in the opposite fashion, Sobolev and colleagues (Sobolev *et al.*, 2005, 2007) noted that Ni enrichment and Mn deficiency in high-forsterite olivines – and therefore in primary melts – could be linked to the existence of an olivine-free lithology in the mantle, namely pyroxenite. The fractional crystallization of olivine from a primary melt induces a progressive decrease in Fo content of the crystallizing olivines, associated with a decrease in Ni (compatible with olivine) and an increase in Mn (incompatible with olivine). Therefore, as long as it is the only crystallizing mineral (Figure 5.4), olivine Ni enrichment over Mg/Fe and Mn depletion over Fe remain nearly constant and can thus be used as a proxy for pyroxenite-derived melts in the magmatic sources (Sobolev *et al.*, 2007).

Figure 6.3a shows significant divergence of the Deccan samples from peridotitic melt crystallisation paths (Herzberg, 2011) caused by Ni excess (~1000ppm at Fo80). Herzberg

and colleagues (Herzberg *et al.*, 2013) also established that Ni-excess trends such as those of Figure 6.3a (and b) could be accounted for by the coeval crystallization of large amounts of clinopyroxenes. However, the inset of Figure 6.3a (and b) show constant CaO/Al_2O_3 of olivine-hosted melt inclusions at any Fo whereas clinopyroxene crystallisation would induce a decrease of this ratio. This clearly rules out the possibility of significant coeval crystallisation of clinopyroxene during olivine fractionation.

Ni normalized to Mg and Fe versus Mn/Fe ratio (Figure 6.3b) indicates that the composition of KD04 and KD06 olivine phenocrysts (Deccan Traps) is closer to that expected for melts derived from pyroxenitic sources due to Mn deficiency (Sobolev *et al.*, 2007).

The Réunion Island samples are more compatible with a peridotitic source than KD04 and KD06 from the Deccan Traps although some degree of divergence with equilibrium olivines from purely peridotite-derived magmas (Figure 6.3c) still occurs (Ni excess of about 500ppm at Fo80). Mn deficiency (Figure 6.3d) is also more limited than that of KD04 and KD06 (Figure 6.3b). Several analyses of TI1602 from Piton de Fournaise (Réunion Island) show significant divergences from the pyroxenite-peridotite trend in Mn/Fe (Figure 6.3d). This feature likely pertains to perturbation of the oxidation state of Fe during olivine crystallization (TI1602 also bears the lowest Fo olivines of the Réunion Island sample set) and merely results in a limited number of outliers that do not significantly affect the significance of the primary melt signature within this sample. Although not discussed here, similar perturbations of both Ni and Mn have been observed in the Réunion Island steady-state basalts samples (MgO ~7wt%) and lower MgO Deccan Traps samples analysed during this PhD, Table 4–2 (section 4).

6.4. Pyroxenitic component in the source of Deccan (Thakurvadi formation) and Réunion Island (PdN and PdF) lavas

The amount of pyroxenite melt in the sources of mantle-derived magmas (Xpx has been related to Ni excess (Xpx_{Ni}) and Mn deficiency (Xpx_{Mn}) in high-Fo magmatic olivines (~Fo90) by Sobolev et al. (2005, 2007) as:

- [illegible] (6.5)

  Where: [illegible] (6.6)

- [illegible] (6.7)

Figure 6.4 shows the evolution of Xpx with Fo for Deccan Traps and Réunion Island samples.

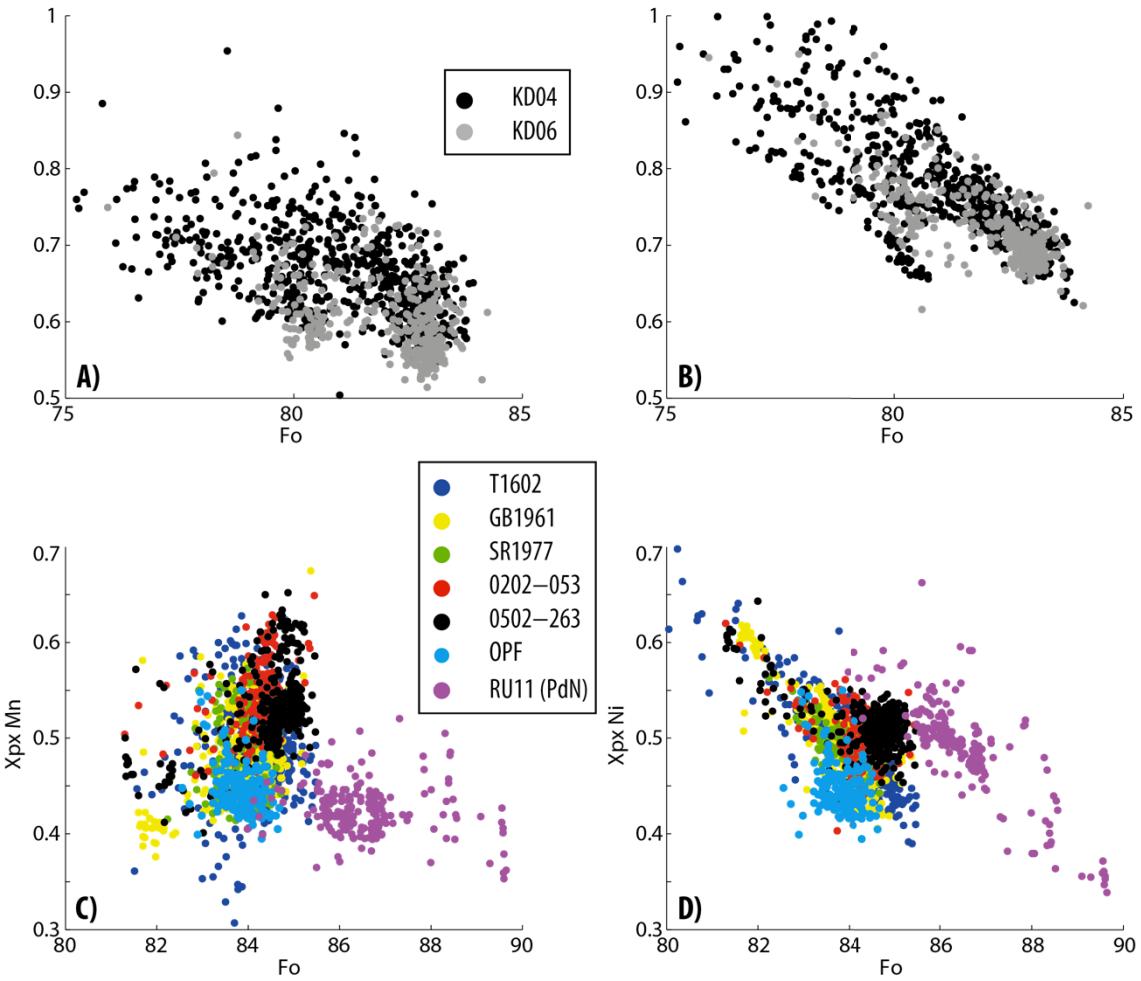

Figure 6.4 – Raw (see text) pyroxenitic component (Xpx) in the sources of Deccan Traps Thakurvadi formation (A and B) and Réunion Island Piton des Neiges (PdN) and Piton de la Fournaise (C and D) magmas based on Ni excess (Xpx_{Ni}) and Mn deficiency (Xpx_{Mn}) versus Fo number.

All samples exhibit variations of Xpx > 10% at any Fo value while the overall ranges of Xpx, irrespective of the Fo content, varies by more than 40% (Figure 6.4). The Deccan Traps samples (Figure 6.4a-b) feature a reverse correlation of Xpx and Fo that converges towards Xpx = 0.55-0.65 at maximum Fo. This relationship also exists yet is less clear for the Réunion Island samples (Xpx = 0.4-0.5, Figure 6.4c-d). Olivines from RU11 (Piton des Neiges) clearly have distinct Xpx in both Ni and Mn spaces with respect to Piton de la Fournaise samples. This implies a slightly different source composition for Piton des Neiges with a more limited involvement of pyroxenitic components. However, the relatively low pyroxenitic component of RU11 at high Fo (Xpx ~ 0.35 at Fo ~ 90) should be handled with care as most (>80%) Xpx estimates for this sample are in the order of 0.40-0.45. It is possible that high-Fo (>88) olivines from RU11 are different from those with lower Fo~86 (e.g. metasomatized peridotite xenocrysts?).

The few wild variations of Xpx seen on Figure 6.5 are not observed on Figure 6.4 and yet correlate, to some extent at least, with a fractionation trend (decreasing Fo). It is likely that the perturbations of the Xpx indices of Figure 6.5 is the result of processes related to magmatic fractionation and cumulate formation, such as varying oxidation state of Fe and the crystallisation of other (non-silicate) phases (e.g. sulphides) (Krivolutskaya *et al.*, 2012).
These effects can be filtered out by finding the best correlation of Xpx_{Ni} and Xpx_{Mn} (largest population at the highest Fo), Figure 6.5.

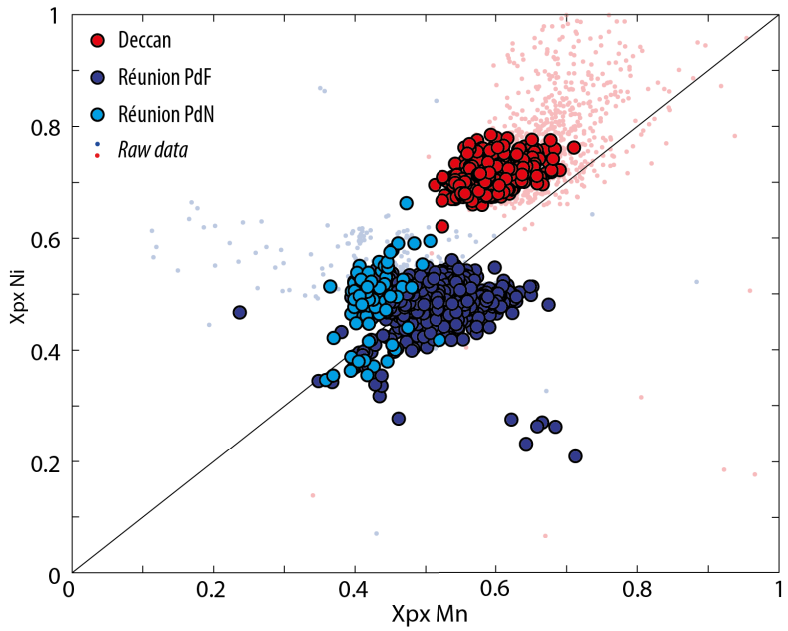

Figure 6.5 - Correlation of pyroxenitic component estimations from Ni excess (Xpx_{Ni}) and Mn deficiency (Xpx_{Mn}). Raw data: not filtered for analytical mistakes (e.g. bad totals, compositional discrepancies and poor probe calibration). No systematic trend was noted at any locality and hence samples of PdF and Deccan Traps have all been plotted together.

Réunion Island (PdF) and Deccan Traps samples on Figure 6.5 have been plotted by location and not separately, as in Figure 6.4, because no significant difference in Xpx was observed at each location. A few outliers, especially for Réunion Island (PdF), still exist but Figure 6.5 allows for proper average pyroxenitic components to be estimated for all three localities. The average pyroxenitic component of the Deccan Traps samples (Thakurvadi formation) is of 0.65 and of 0.5 for Réunion Island (PdF). Piton des Neiges (Réunion Island) has a slightly lower average (0.45), which is due to its more limited Mn deficiency (Figure 6.3d and Figure 6.4). Although not representative of the whole sample, low Xpx grain of Figure 6.4c-d should be investigated more thoroughly for potential records of xenocrystic origin.

6.5. Olivine-hosted melt inclusions

Melt inclusions are small volumes of melt that have been trapped by growing olivine phenocrysts during crystallisation. They are the most direct proxy for primary melt reconstruction.

Inclusion-bearing olivines have all been processed at the Vernadsky Institute in Moscow by A.V. Sobolev as follows: separated olivine grains containing crystallized melt inclusions were

heated to 1180-1220°C in a vertical furnace for 30 minutes and quenched under controlled oxygen fugacity, corresponding to the QFM buffer.

All the melt inclusions analysed by EPMA during this project are larger than 8µm in diameter in order to allow for large excitation volumes of high-current EPMA analysis (appendix III).

Figure 6.6 is an overview of measured (non-equilibrated) olivine melt inclusions and examples of compositions are given on Table 6–4.

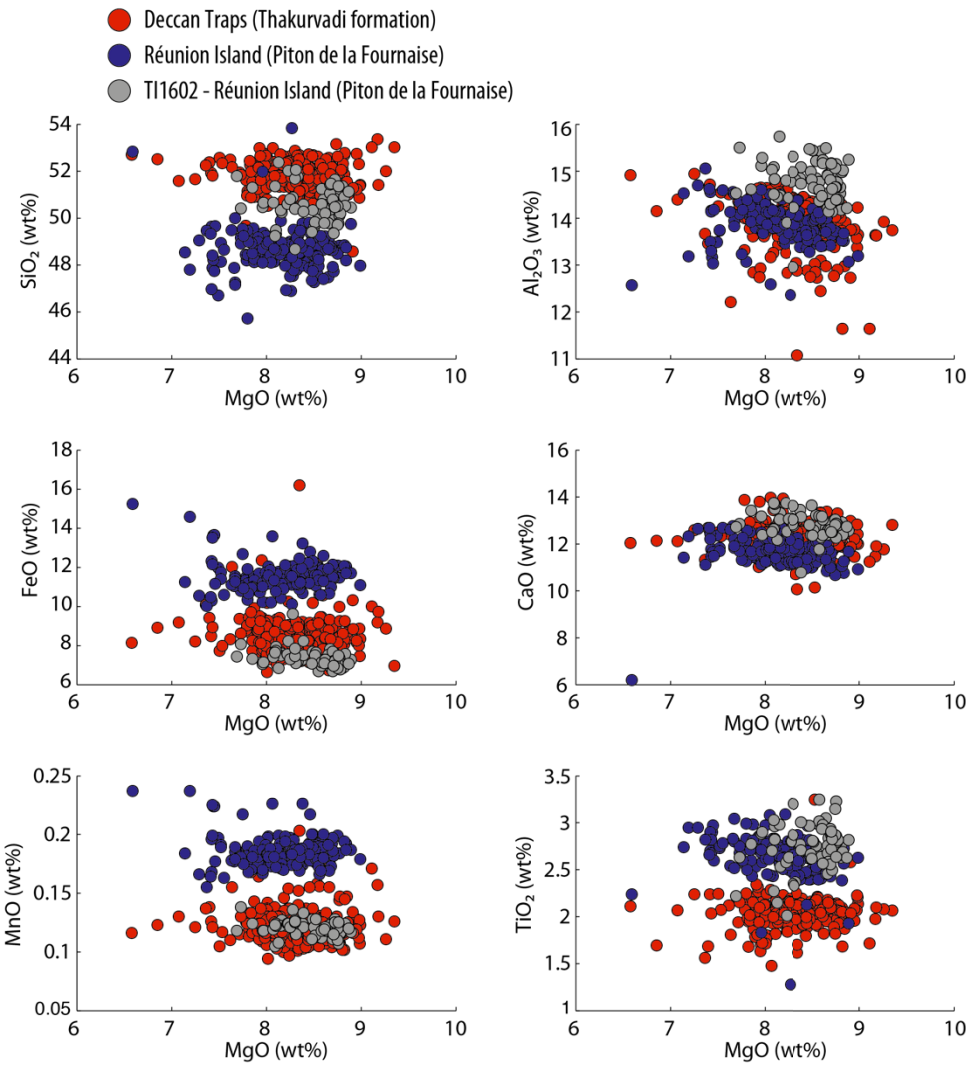

Figure 6.6 – Measured compositions of non-equilibrated (Danyushevsky *et al.*, 2000a) olivine melt inclusions for Deccan Traps (red) and Réunion Island Piton de la Fournaise (bleu, except TI1602 which is in grey) samples.

Table 6–4 - Examples of melt inclusion compositions for the selected Deccan Traps and Réunion Island samples (RU11 from Piton des Neiges was not analysed for melt inclusions). Oxides concentrations in wt%.

	Deccan		Réunion (PdF)			
Sample	KD04	KD06	TI1602	GB1961	0202-053	0502-263
SiO_2	51.87	51.78	50.61	48.41	49.03	48.64
Al_2O_3	14.24	14.58	14.6	14.12	14.06	13.79
FeO_{tot}	8.08	8.79	7.15	11.87	11.2	11.5
MgO	8.82	7.9	8.58	8.04	7.98	8.7
CaO	12.07	11.99	11.78	11.76	11.18	11.07
TiO_2	2.09	1.89	3.25	2.61	2.67	2.62
MnO	0.12	0.13	0.12	0.19	0.19	0.19
Na_2O	2.17	2.31	2.77	2.44	2.36	2.34
K_2O	0.44	0.44	1.08	0.67	0.73	0.65
Cl	0.02	0.02	0.03	0.02	0.02	0.02
S	0.03	0.05	0.04	0.11	0.07	0.12
P_2O_5	0.23	0.18	0.42	0.26	0.41	0.27
Total	100.22	100.06	100.58	100.72	99.89	99.95
Host Olivine						
SiO_2	40.03	39.79	40.14	39.78	40.04	40.17
Al_2O_3	0.0550	0.0290	0.0350	0.0370	0.0340	0.0320
FeO	16.31	18.41	14.93	16.08	14.72	14.29
MgO	43.70	42.37	45.87	44.58	45.05	45.58
CaO	0.2930	0.3190	0.2940	0.2790	0.2670	0.2760
TiO_2	0.0290	0.0160	0.0110	0.0100	0.0100	0.0080
MnO	0.2210	0.2490	0.2120	0.2330	0.2090	0.2050
Cr_2O_3	0.0640	0.0470	0.0350	0.0340	0.0420	0.0440
NiO	0.2860	0.2550	0.2600	0.2500	0.2720	0.2890
CoO	-	-	0.0230	0.0220	0.0220	0.0200
ZnO	0.0140	0.0140	0.0150	0.0140	0.0150	0.0160
P_2O_5	-	-	0.0150	0.0170	0.0200	0.0180
Total	101.00	101.49	101.85	101.34	100.64	100.90
Fo	82.69	80.41	84.56	83.17	84.51	85.04

Melt inclusions of the Deccan Traps samples tend to have slightly higher SiO_2 and lower FeO_{tot}, MnO and TiO_2 for the same MgO than those of PdF. However, TI1602 (Réunion Island, grey on Figure 6.6) has higher SiO_2, Al_2O_3 and CaO and lower FeO and MnO than its counterparts from the same location. Several olivine core measurements of TI1602 returned higher Mn/Fe than the other samples from the same locality (Figure 6.3d) and differences in melt inclusion composition could therefore be ascribed to olivine and magmatic compositions. However, no such difference is observed for any other element including volatiles (Figure

6.4c-d and Figure 6.7). It is likely that Fe-loss from the inclusion occurred due to equilibration of the melt and the host olivine at low temperature (Sobolev & Danyushevsky, 1994)
The volatile contents of melt inclusions are given on Figure 6.7.

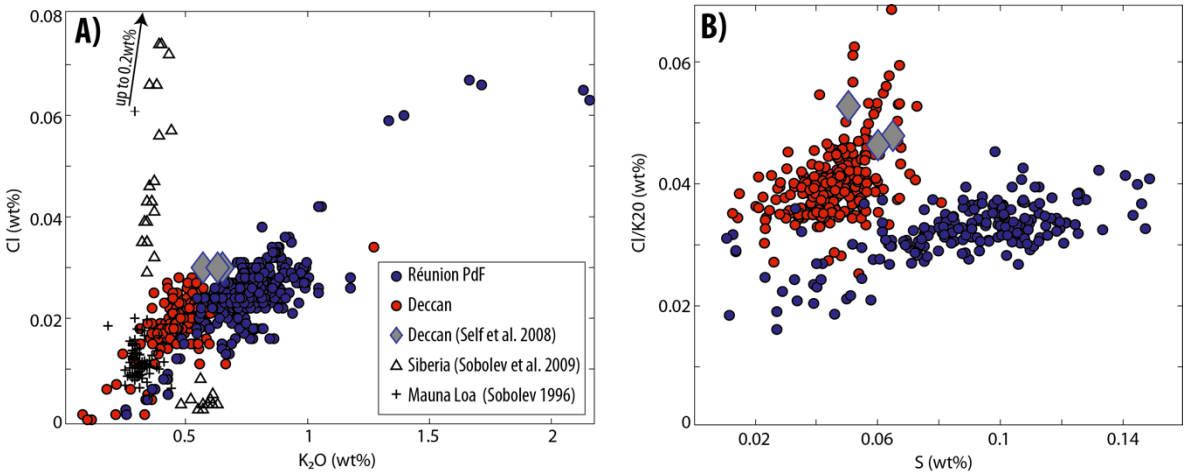

Figure 6.7 - Volatile contents of Deccan and Réunion (Piton de la Fournaise only) melt inclusions and published data for the Deccan Traps (Self *et al.*, 2008a), the Siberian Traps (Sobolev *et al.*, 2009a) and Hawaii, Mauna Loa (Sobolev, 1996). K_2O is not a volatile but it is a proxy for water concentrations in the primary melts (e.g. Sobolev & Chaussidon, 1996, Dixon *et al.*, 2002). The relationship between K_2O and water content is discussed in section 7.3.1.1

The average volatile (K_2O, Cl and S) contents of the Deccan Traps and Réunion Island, PdF melt inclusions are given in Table 6–5.

Table 6–5 – Average volatile contents of melt inclusions and average Fo of the host olivines for the Deccan Traps (Thakurvadi formation) and Réunion Island (Piton de la Fournaise) samples analysed in this section

	Thakurvadi Formation			Réunion Island (Piton de la Fournaise)				
	KD04	KD06	*Avg.*	TI1602	0202-053	0502-263	GB1961	*Avg.*
K2O(wt%)	0.48	0.48	*0.48*	0.78	0.66	0.64	0.72	*0.70*
Cl(wt%)	0.02	0.02	*0.02*	0.02	0.02	0.02	0.02	*0.02*
S(wt%)	0.04	0.05	*0.05*	0.07	0.10	0.09	0.10	*0.09*
Fo	*82*	*82*		*84*	*84*	*84*	*84*	

Self and colleagues (Self *et al.*, 2008a) reported 4 olivine-hosted (Fo 81) melt inclusions and glasses volatile contents for three formations of the Deccan Traps Kalsubai subgroup: Jawhar, Thakurvadi and Neral (Figure 6.2). Their estimations returned similar concentrations of S and Cl, to the most K_2O-rich inclusions of Figure 6.7, with S = 0.07-0.10wt%, Cl = 0.03 wt% and K_2O = 0.4-0.7wt% (Fo = 81).

KD04 and KD06 come from two successive lava flows at the beginning of the Thakurvadi formation (section 6.2). It is therefore likely that both samples shared a similar degassing history. The difference in volatile concentrations between the many inclusions from two closely similar samples of the same formation (KD04 and KD06) analysed during this project and the few inclusions from three different formations of the Kalsubai subgroup published by Self et al cannot be interpreted. On the whole, both datasets are compatible and no conclusion may be drawn as to the evolution of magma degassing during the emplacement of the Kaulsubai subgroup due to limited data.

Matrix glass volatile measurements similar to Self et al (2008a) were carried out on none of the Deccan Traps (Thakurvadi formation) or Réunion Island (Piton de la Fournaise) samples, which precludes magma degassing calculations similar to those of Self and colleagues. It is nevertheless proposed that the degassing of lavas is generally complete and that the amount of volatiles remaining in the rocks is negligible. Thus, volatile concentrations in matrix glasses are not necessarily representative of the amount of undegassed volatiles. (Sobolev, 2014, personal communication).

Réunion Island (Piton de la Fournaise) melt inclusions (Figure 6.7) are also compatible with estimates of Sobolev and Nikogosian (1994, K2O only) as well as Bureau and colleagues (Bureau *et al.*, 1998a, 1998b) for PdF, Réunion Island.

Both Deccan Traps and Réunion Island melt inclusions follow a markedly different trend than the Siberian samples shown on Figure 6.7a for comparison (Sobolev *et al.*, 2009b) and appear closer to Hawaiian and MORB concentrations (Sobolev, 1996, Sobolev *et al.*, 2009a). Figure 6.7b and the difference in Cl/K_2O may hint at different magma degassing processes between the Deccan Traps (Thakurvadi formation) and Réunion Island (Piton de la Fournaise).

6.6. Spinel inclusions in olivine

Spinel inclusions in olivine are used to constrain the oxidation state of Fe and the oxygen fugacity of the melt with respect to the QFM and Ni-NiO oxygen buffers, which has implications for the reconstruction of primary melt compositions from melt inclusions, and the calculation of magmatic temperatures (Borisov & Shapkin, 1990, Nikolaev *et al.*, 1996). In additions, spinel inclusions are used to estimate magmatic temperatures in an way that is independent from petrological models (thereby allowing for independent validation) and that

hinges upon Al partitioning between the spinel inclusion and its host olivine (Wan *et al.*, 2008, Coogan *et al.*, 2014).

6.6.1. Spinel composition and ferrous-ferric iron ratios

Examples of compositional data for olivine spinel inclusions are given on Table 6–6.

Table 6–6 - Examples of spinel compositions for the selected Deccan and Réunion Island samples (PdN: Piton des Neiges; PdF: Piton de la Fournaise). Oxides concentrations in wt%. New total is the total sum of oxides in wt% recalculated for Fe_2O_3 + FeO instead of FeO_{tot}.

	Deccan		Réunion (PdF)					(PdN)
Sample	KD04	KD06	TI1602	GB1961	0202-053	0502-263	SR1977	RU11
SiO_2	0.09	0.06	0.05	0.08	0.07	0.06	0.11	0.11
TiO_2	1.92	2.08	2.36	2.45	2.36	2.39	2.19	1.74
Al_2O_3	16.74	15.03	15.77	16.83	16.17	16.58	18.44	17.89
Cr_2O_3	41.78	42.08	37.64	37.90	40.71	40.06	34.39	43.28
V_2O_3	0.43	0.50	0.27	0.25	0.26	0.27	0.33	0.15
FeO_{tot}	28.51	32.28	33.10	31.66	28.30	27.40	30.82	24.10
MnO	0.25	0.30	0.25	0.28	0.22	0.21	0.21	0.20
MgO	10.02	7.39	9.74	10.00	12.23	12.47	11.84	12.68
NiO	0.17	0.11	0.18	0.17	0.19	0.21	0.19	0.24
ZnO	0.14	0.16	0.10	0.11	0.08	0.07	0.09	0.09
Total	100.04	99.99	99.47	99.75	100.58	99.74	98.60	100.47
FeO	20.84	24.67	21.39	21.31	18.04	17.46	18.29	16.98
Fe_2O_3	8.52	8.46	13.02	11.51	11.40	11.05	13.92	7.92
New total	100.90	100.84	100.77	100.90	101.72	100.84	99.99	101.26
Mg#	0.46	0.35	0.45	0.46	0.55	0.56	0.54	0.57
Fe^{III}#	0.11	0.11	0.17	0.15	0.14	0.14	0.18	0.10
Cr#	0.56	0.58	0.51	0.51	0.54	0.53	0.46	0.56
Al#	0.33	0.31	0.32	0.34	0.32	0.33	0.37	0.34
Cr/(Cr+Al)	0.63	0.65	0.62	0.60	0.63	0.62	0.56	0.62
Fe^{2+}	0.29	0.34	0.30	0.30	0.25	0.24	0.25	0.24
Fe^{3+}	0.11	0.11	0.16	0.14	0.14	0.14	0.17	0.10
Fe^{3+}/Fe_{tot}	0.27	0.24	0.35	0.33	0.36	0.36	0.41	0.30
$(Fe^{2+}/Fe^{3+})_{sp}$	2.72	3.24	1.83	2.06	1.76	1.76	1.46	2.38
$(Fe^{2+}/Fe^{3+})_{liq}$	10.41	13.10	6.18	7.23	5.88	5.88	4.61	8.77

$$Mg\# = \frac{\frac{MgO}{M_{MgO}}}{\frac{MgO}{M_{MgO}}+\frac{FeO}{M_{FeO}}} \quad (6.8)$$

$$Fe^{III}\# = \frac{\frac{Fe_2O_3}{M_{Fe_2O_3}}}{\frac{Cr_2O_3}{M_{Cr_2O_3}}+\frac{Al_2O_3}{M_{AlO_3}}+\frac{Fe_2O_3}{M_{Fe_2O_3}}} \quad (6.9)$$

$$\frac{\frac{}{}}{\frac{}{}+\frac{}{}+\frac{}{}} \quad (6.10)$$

$$\frac{\frac{}{}}{\frac{}{}+\frac{}{}+\frac{}{}} \quad (6.11)$$

$$\quad (6.12)$$

From stoichiometry: $\quad (6.13)$

$$\quad (6.14)$$

Figure 6.8 shows the compositional range of the spinel inclusions analysed during this project.

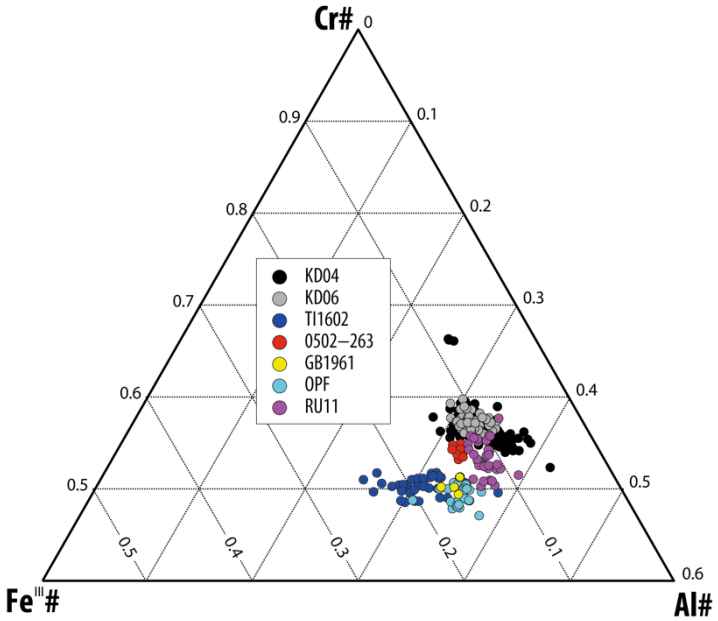

Figure 6.8 – Olivine spinel inclusions for Deccan Traps and Réunion samples.

Spinel inclusions from the Deccan Traps are relatively homogeneous at an average of Fe^{III}# ~ 0.1 (σ = 0.013), Cr# ~ 0.57 (σ = 0.016) and Al# ~ 0.33 (σ = 0.021). The Réunion Island samples are however more heterogeneous and generally less Cr-rich with PdF spinels at about Fe^{III}# ~ 0.12-0.22 (σ = 0.027), Cr# ~ 0.50 (σ = 0.022) and Al# ~ 0.27-0.37 (σ = 0.034), yet 0502-263 (PdF) and RU11 (PdN) have slightly higher (~0.2 units) Cr# (σ = 0.012) and lower Fe^{III}# (σ = 0.018) and Al# (σ = 0.015).

The ferrous-ferric partitioning (Fe^{2+}/Fe^{3+}) of spinel inclusions and the Fo content of the host olivines can be compared with the fractionation paths of published high-Mg glasses and primary melts in order to find the most appropriate oxygen fugacity buffer for melt inclusion-based petrological modelling (section 7.1). Figure 6.9 shows Fe^{2+}/Fe^{3+}_{liquid} versus Fo of the host olivine for spinels in samples where melt inclusions have been analysed: KD04, KD06, TI1602, GB1961 and 0502-263. RU11 from PdN, Réunion Island, is shown for comparison. Data are represented by location for clarity and because no significant difference in Fe^{2+}/Fe^{3+}_{liquid} was noticed among Deccan Traps or PdF samples.

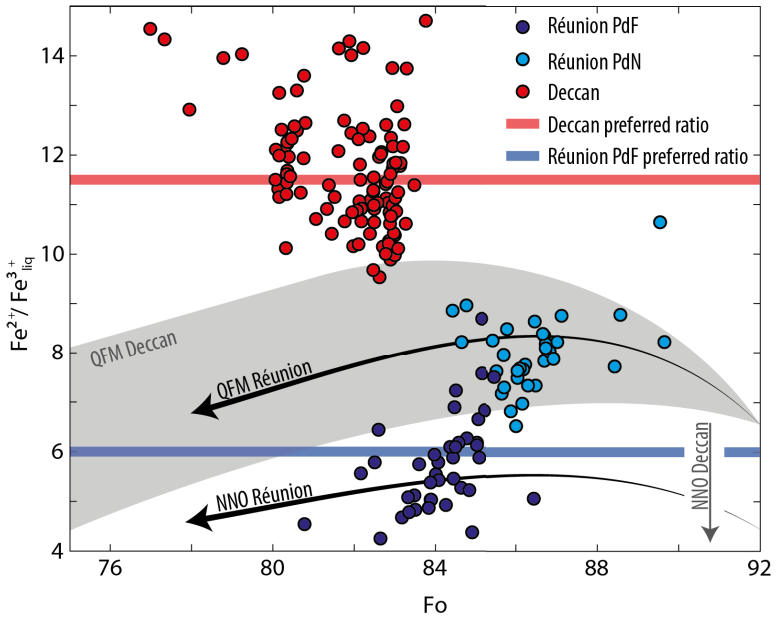

Figure 6.9 – Fe^{2+}/Fe^{3+}_{liq} recalculated from Fe^{2+}/Fe^{3+} of spinel inclusions (Table 6–6) (Maurel & Maurel, 1982) and Fo of the host olivine compared with the evolution of Fe^{2+}/Fe^{3+}_{liq} for the QFM and NNO oxygen fugacity buffers (Borisov & Shapkin, 1990, Danyushevsky & Sobolev, 1996) during the crystallisation of high-MgO glasses and primary melt estimates for the Deccan Traps (grey field: Sen, 1995, Sen & Chandrasekharam, 2011. NNO not in the plot area) and Réunion Island (arrows: Ludden, 1978, Sobolev & Nikogosian, 1994, Famin *et al.*, 2009, Villemant *et al.*, 2009, Salaün *et al.*, 2010). Fe^{2+}/Fe^{3+}_{liq} preferred ratios used for back-fractionation of melt inclusions (section 7) are Fe^{2+}/Fe^{3+}_{liq} = 6 for Piton de la Fournaise and Fe^{2+}/Fe^{3+}_{liq} = 11.5 for the Deccan Thakurvadi samples. PdN: Piton des Neiges. PdF: Piton de la Fournaise. Fractionation carried out using Petrolog (Danyushevsky & Plechov, 2011), P = 1atm, crystallization models: Ford et al (1983) for olivine, Danyushevsky (2001) for clinopyroxene, orthopyroxene and plagioclase.

Figure 6.9 shows that Fe^{2+}/Fe^{3+}_{liq} at PdF is compatible with the Ni-NiO oxygen fugacity buffer while PdN is closer to QFM. In order to apply the most appropriate Fe^{2+}/Fe^{3+}_{liq} in the petrological models presented in section 7, the average Fe^{2+}/Fe^{3+}_{liq} of PdF melts (Fe^{2+}/Fe^{3+}_{liq} = 6) is used. From Figure 6.9, it also appears that there is a linear relationship between Fe^{2+}/Fe^{3+}_{liq} and Fo (in the form $Fe^{2+}/Fe^{3+}_{liq} = a \times Fo + b$) between PdF and PdN. However, this

relationship was not considered because 1) in this particular case, the use of a fixed ratio as opposed to a linear equation has very limited consequences (logarithm) on the oxygen fugacity (Borisov & Shapkin, 1990, Nikolaev *et al.*, 1996) and 2) the linear relationship between PdF and PdN would induce negative values of Fe^{2+}/Fe^{3+}_{liq} at Fo < 78 and thus preclude its use for petrological modelling at low Fo (e.g. melt-liquidus associations and fractionation).

The Deccan Traps spinel inclusions, Figure 6.9, have markedly higher Fe^{2+}/Fe^{3+}_{liq} than both PdF and PdN samples (average Fe^{2+}/Fe^{3+}_{liq} = 11.5). It is also higher than calculated Fe oxidation state versus Fo based on the QFM oxygen fugacity buffer.

Overall, the oxidation state of magmas strongly increases between the Deccan Traps (Thakurvadi formation) and Réunion Island. Moreover, at Réunion Island, the oxidation state seems related to fractionation as Piton de la Fournaise and Piton des Neiges form a single trend of increasing oxidation during fractionation. Figure 6.9.

6.6.2. Olivine-spinel thermometry

Aluminium partitioning between spinel inclusions and their host olivine has been used as an igneous thermometer by Wan et al. (2008) and more recently by Coogan et al. (2014). The olivine-spinel thermometer is expressed as:

$$T(°C) = \frac{10\,000}{0.512+0.873Y_{Cr}-0.91\ln(K_D)} - 273 \quad (6.15)$$

Where:

$$Y_{Cr} = \frac{\frac{Cr_2O_3}{M_{Cr_2O_3}}}{\frac{Cr_2O_3}{M_{Cr_2O_3}}+\frac{Al_2O_3}{M_{Al_2O_3}}} \; and \; K_D = \frac{(Al_2O_3)_{olivine}}{(Al_2O_3)_{spinel}} \quad (6.16)$$

This thermometer is valid within the following range (Wan *et al.*, 2008):

- $0.07 < Y_{Cr} < 0.69$
- $Fe^{3+} < 0.1$
- $Ti < 0.025$

These bounds preclude proper application of the thermometer to the Deccan Traps and Réunion Island samples investigated in this manuscript as most of these have Fe^{3+} and Ti contents beyond the recommendations of Wan et al. (Figure 6.10).

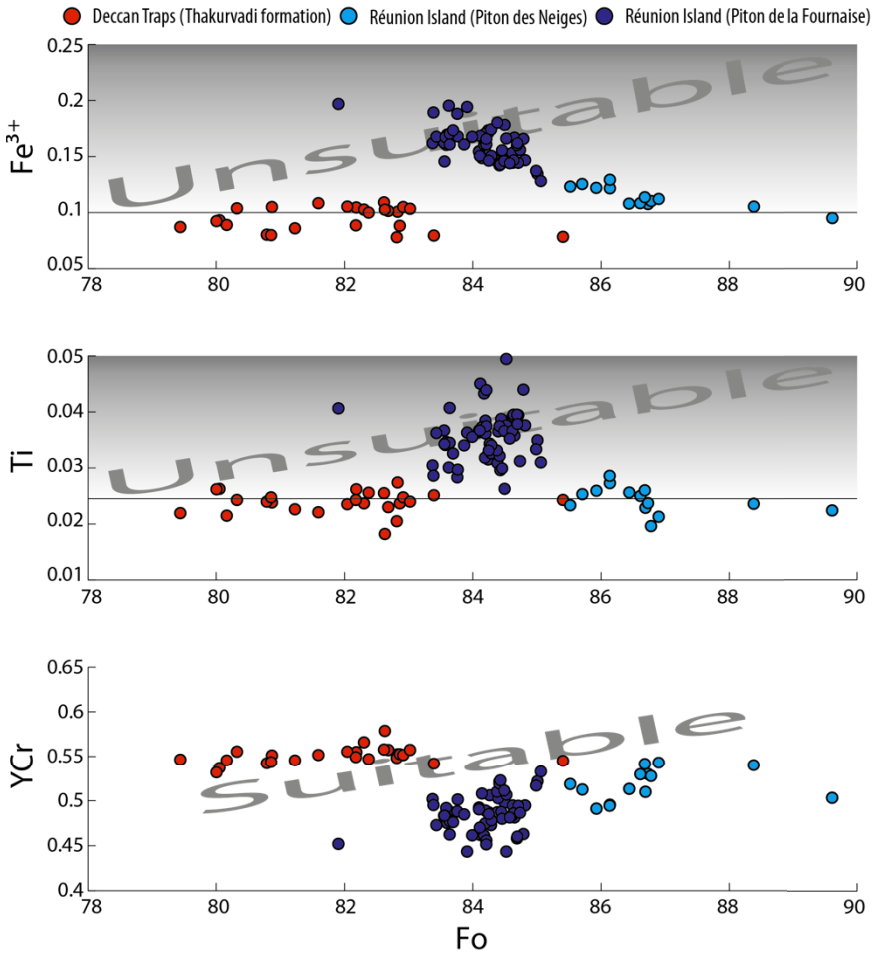

Figure 6.10 – Fe^{3+}, Ti and Y_{Cr} contents of spinel inclusions versus Fo of the host olivines. The suitable and unsuitable ranges of Fe^{3+}, Ti and Y_{Cr} are from Wan et al (Wan *et al.*, 2008)

The olivine-spinel thermometer of Wan et al. (2008) has recently been re-assessed in order to account for Ti variations (Sobolev *et al.*, 2013). Sobolev and colleagues proposed the following formulation:

$$T(K) = \frac{\text{[illegible]}}{\text{[illegible]}} - 273 \quad (6.17)$$

Where:

$$\text{[illegible]} = \frac{\text{[illegible]}}{\text{[illegible]}} \quad (6.18)$$

$$\text{[illegible]} = \frac{\text{[illegible]}}{\text{[illegible]}} \quad (6.19)$$

This new thermometer has been applied to the olivine-spinel dataset presented above (Figure 6.11).

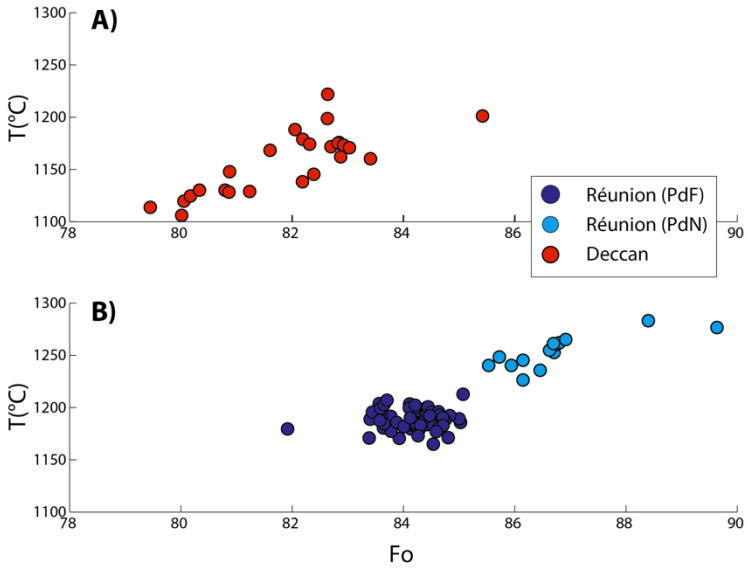

Figure 6.11 – Aluminium olivine-spinel thermometry (Sobolev *et al.*, 2013). Each data point is an average of at least 3 measurements of the same olivine-spinel couple. All olivine-spinel couples with a standard deviation > 5°C have been removed. The precision of the thermometer has been assessed by Sobolev et al. (2013) at ±5°C, which is equivalent to the size of the dot on the figure. 1σ error equal to the diameter of the symbols.

The temperatures returned by Al partitioning between spinel inclusions and host olivines is that of crystallizing olivine cumulates in crustal magma chambers. This is also equivalent to the temperature at which melt inclusions were trapped. Figure 6.11 provides the following results:

- Deccan Traps: 1107-1223 (±5) °C
- Réunion PdN: 1226-1283 (±5) °C
- Réunion PdF: 1165-1213 (±5) °C

Temperatures decrease with Fo as expected during a fractionation sequence and the cooler temperature range observed for the Deccan Traps samples merely pertains to the lower Fo content of the host olivines. Source potential temperature (i.e. the temperature of the mantle source) calculations require melt inclusion-based petrological modelling in order to account for the fractionation undergone by the samples. This process be dealt with in section 7.

6.7. Summary and preliminary interpretations

The olivine dataset presented in this section is the first step towards assembling a reasonable picture of the deep magmatic processes that generated the Deccan Traps and Réunion Island volcanics:

- The primary magmas from which lavas of both localities originated are mixture of peridotite- and pyroxenite-derived (olivine-free) melts. The contribution of pyroxenite to the generation of primary magmas result in Ni excess and Mn deficiency in the composition of the olivine phenocrysts. Based on Sobolev et al. (2005, 2007) it has been estimated that the Deccan Traps (Thakurvadi formation only) high-Fo olivines crystallized from a primary melt made of pyroxenite-derived melt at 65%. In the same way, Réunion Island high-Fo olivine of Piton de la Fournaise (PdF) crystallized from a primary melt composed of 50% of pyroxenite melt. Piton des Neiges returned slightly lower pyroxenitic component (40-45%) while its maximum Fo olivines (Fo ~ 90) suggest even lower involvement of an olivine-free lithology in the formation of primary magmas (Xpx ~ 0.35). This observation requires further investigation and may result from metasomatism of mantle olivines (Foley *et al.*, 2013). Figure 6.3, Figure 6.4 and Figure 6.5
- Homogenized olivine melt inclusions will be used for primary melt reconstruction at Réunion Island (Piton de la Fournaise) and for the Deccan Traps (Thakurvadi formation only) in the next section (7.1). Figure 6.6
- The volatile (S and Cl) contents of melt inclusions (Figure 6.7) are compatible with previous measurements from both localities (Sobolev & Nikogosian, 1994, Sobolev, 1996, Bureau *et al.*, 1998a, 1998b, Self *et al.*, 2008a) and form a trend that is markedly different from that of the Siberian Traps inclusions and similar to MORBs and Hawaiian inclusions (Sobolev *et al.*, 2009a). A significant difference in Cl/K_2O between Deccan Traps and Réunion Island (Piton de la Fournaise) inclusions may imply different degassing processes of magmatic sources between the plume-head stage and the tail stage of the Deccan Plume. No magma degassing calculations can be carried out due to the lack of bulk-rock volatile measurements. It is nonetheless argued that the figure proposed by Self et al (2008a) still hold true (S = 3.5Tg/km^3 and Cl = 1Tg/km^3). However, the very high chlorine concentrations found in Siberian melt inclusions (up to 0.2wt%, Sobolev *et al.*, 2009a) are in stark contrast with those

reported here for the Deccan Traps and Réunion Island. The differences in volatile concentrations between the Siberian and the Deccan Traps should be assessed in details in order to re-evaluate the potential environmental consequence of both LIPs

- Olivine spinel inclusions provided valuable information as to the oxidation state of Fe (Réunion Island Piton de la Fournaise Fe^{2+}/Fe^{3+}_{liq} = 6; Deccan Traps Thakurvadi formation Fe^{2+}/Fe^{3+}_{liq} = 11.5) and oxygen fugacity in the primary magmas of both localities. There is a significant difference between the oxidation state of the Deccan Traps (Thakurvadi formation) magmas (Fe^{2+}/Fe^{3+}_{liq} ~ 11.5) and those of Réunion Island (Piton des Neiges and Piton de la Fournaise, Fe^{2+}/Fe^{3+}_{liq} = 6). In addition, there is a clear correlation of Fe^{2+}/Fe^{3+}_{liq} and Fo between Piton de la Fournaise and Piton des Neiges suggesting that the oxidation state of Réunion Island magmas is related to their degree of fractionation. These trends will be integrated to melt inclusion-based petrological modelling of primary melt (section 7.1). Figure 6.9
- In addition, olivine-spinel aluminium partitioning was used as a magmatic thermometer (Sobolev *et al.*, 2013) and returned the following temperature ranges for crustal magma chambers (Figure 6.11):

  Deccan Traps (Thakurvadi formation only): 1107 – 1223°C

  Réunion Island (Piton des Neiges): 1226 – 1283°C

  Réunion Island (Piton de la Fournaise): 1165 – 1213°C
- The temperature under which spinel inclusions formed is equal to that of melt inclusions trapping by the growing olivine crystals (cumulate formation in crustal magma chambers) and hence, olivine-spinel-based temperature estimates will be used as an independent constrain for melt inclusion re-equilibration and ensuing primary melt modelling (section 7.1)

7. Primary melt reconstruction and source modelling

The purpose of the olivine dataset presented in the preceding section (6) is to be used as a proxy for understanding the deep mantle processes that generated the lavas exposed in the Deccan Traps and at Réunion Island. However, the olivine phenocrysts that have been described earlier crystallized in shallow crustal magma chambers (Figure 7.1) (Sobolev & Nikogosian, 1994, Bureau *et al.*, 1998b) and the information they convey therefore corresponds to the conditions applicable at this pre-eruption stage of magmatic evolution. The path that led to this stage thus has to be unveiled in order for the origin of the magmas to be reconstructed. Such a forward modelling process requires the use of proxies, namely the olivine dataset presented in the preceding section but also bulk-rock trace element composition. It also involves assumptions that may have critical implications and that therefore sometimes represent strong limitations or imply large uncertainties that will be discussed.

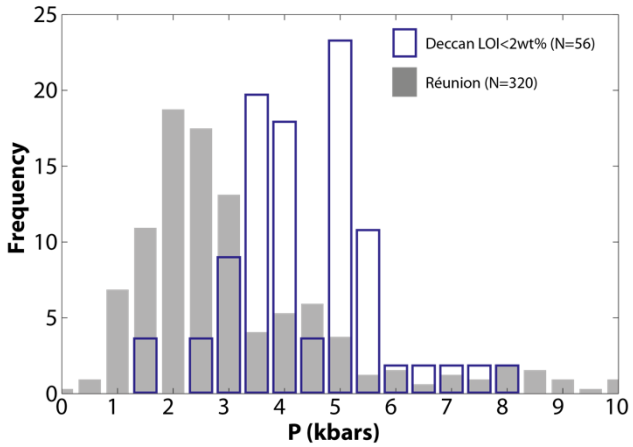

Figure 7.1 – Histograms of the last equilibrium pressure of the olivine-clinopyroxene assemblage for Deccan Traps (Loss on Ignition, LOI, < 2wt%) and Réunion Island lavas with MgO < 7wt%. This result is compatible with independent estimates by Bureau and colleagues (Bureau *et al.*, 1998b). Calculation carried out using the Petrolog software (Danyushevsky & Plechov, 2011)

This section begins with the reconstruction of primary melt compositions, that is, the composition of the magmas after it departed from its source in the mantle and before any other magmatic process such as crustal assimilation or fractionation occurred. This first step is achieved upon re-equilibration and back-fractionation of melt inclusions (section 7.1).

In a second phase, the sources of primary magmas will be modelled and mantle potential temperatures will be calculated.

Finally, the limits of the models used in this section will be briefly discussed.

7.1. Primary melt reconstruction

The composition of primary melts is recalculated from melt inclusion (major and minor elements) and bulk rock (trace element) composition. Melt inclusions were analysed in KD04 and KD06 from the Deccan Traps (Thakurvadi formation) and TI1602, GB1961, SR1977, 0502-263 from Réunion Island (Piton de la Fournaise, PdF). Therefore, the primary melt compositions calculated here are valid for these volcanics only. However, since the composition of the samples used in this PhD are representative of their respective localities (sections 4 and 5), it is reasonable to argue that the primary melt compositions proposed here for Piton de la Fournaise at Réunion Island and for the Thakurvadi formation of the Deccan Traps are applicable to Réunion Island as a whole and to the lower formations of the Deccan Traps (Igatpuri-Jawhar to Bushe) respectively. In the case of the Deccan Traps, it is even possible that primary melt compositions could have been roughly constant for all formations of the Main Deccan Province, as Ambenali-like signatures have been recognized in most of them (Peng *et al.*, 1994), section 5. Nevertheless, if HREE slopes (e.g. Gd/Yb_n) are roughly constant throughout the Western Ghats (Deccan Traps) section, trace element signatures that are indicative of source composition as well as crustal contamination (e.g. Th/Nb_n) indicate strong variations along this same section (Figure 5.5).

The composition of primary melts is recalculated in the following manner and the different steps to this process are detailed in the next sections. 1) Melt inclusion compositions are re-equilibrated with their host olivine for Fe-loss (Danyushevsky *et al.*, 2000a, 2002b). 2) Re-equilibrated melt inclusions are back-fractionated to mantle Fo values (Herzberg, 2011). 3) Primary melt water contents are calculated using K_2O as a proxy and primary melt temperatures are corrected for water content based on Almeev et al. (2007) and Médard and Grove (2008), section 7.3.1.1. 4) Primary melt trace elements are recalculated using their concentration in the bulk rock. TiO_2 and Al_2O_3 are assumed to behave like trace elements during primary melt fractionation. The evolution of TiO_2 and Al_2O_3 during melt inclusion back-fractionation can thus be directly liked to the trace element concentrations in the primary melt by simple cross multiplication using bulk rock trace element concentrations.

All calculations have been carried out using the Petrolog software (Danyushevsky & Plechov, 2011) and Ford et al. (1983). The oxygen fugacity buffer used was a fixed Fe^{2+}/Fe^{3+}

chosen according to Figure 6.9 (Fe^{2+}/Fe^{3+} = 6 for Réunion PdF and Fe^{2+}/Fe^{3+} = 11.5 for Deccan Traps Thakurvadi formation samples).

7.1.1. Melt inclusion re-equilibration

Olivine-hosted melt inclusions are trapped during olivine crystallisation. Subsequent cooling will result in magmatic fractionation within the inclusions themselves. As any low-pressure crystallisation sequence, olivine first appears and crystallizes on the walls of the inclusion. As fractionation proceeds, olivine compositions on the inclusion walls become increasingly Fe-rich. If sufficient volumes of similarly fractionating melt surrounded the host olivine, the latter would also progressively become more Fe-rich. However, within olivine cumulates, from which high-Fo volcanic olivines are extracted, the amount of fractionating melt is not large enough to affect the composition of the olivines phenocrysts. Host olivines in cumulate layers will therefore keep Mg-rich compositions despite decreasing temperatures. The chemical gradient between the increasingly Fe-rich olivine rim crystallizing within the inclusions and the constant high-Mg composition of the host olivine will result in Fe-loss from the inclusion to the host olivine. The small volume of melt inclusions is not sufficient to affect the composition of the host but the composition of the melt inclusion is indeed strongly affected. Melt inclusion re-equilibration consists in adding Fe to measured melt inclusion compositions in order to reconstruct their composition at the time of melt inclusion entrapment during host olivine crystallisation. The amount of Fe that has to be added to the melt inclusions depends of the original Fe content of the primary melt (FeO*) from which the host olivine crystallised. (Danyushevsky *et al.*, 2000a, 2002b). In the present case, FeO* is an unknown and increases with melting pressure. The temperature at which melt inclusions were trapped (i.e. the crystallisation temperature of the host olivine) is the same as that of spinel inclusion formation (i.e. the crystallization temperature of the host olivine). The issue of guessing the right FeO* is addressed by re-equilibrating the melt inclusions for a range of FeO* that covers the temperature range returned by the olivine-spinel thermometer (section 6.6.2). Figure 7.2.

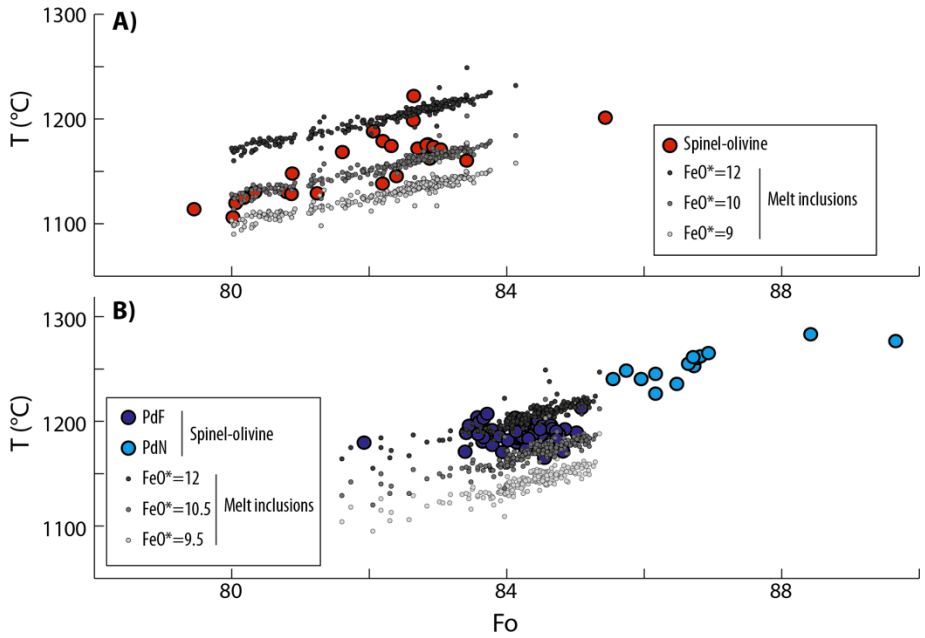

Figure 7.2 - Melt inclusion re-equilibration (Danyushevsky *et al.*, 2000a, 2002b) for different Fe contents of the primary melt (FeO* wt%). Spinel-olivine temperatures (Figure 6.11) used as framework for melt inclusion FeO* estimation. A) Deccan Traps (Thakurvadi formation), B) Réunion Island (Piton de la Fournaise and Piton des Neiges for spinel-olivine thermometry only)

Melt inclusion re-equilibration matches the olivine-spinel thermometer for FeO* = 9 – 12wt% for the Deccan Traps (Thakurvadi formation) samples and FeO* = 9.5 – 12wt% for the Réunion Island (PdF) samples. Although no melt inclusions were analysed in RU11 from PdN, Figure 7.2b shows that FeO* = 9.5 – 12wt% also matches the trend of PdN olivine-spinel temperatures.

7.1.2. Melt inclusion back-fractionation

The re-equilibrated melt inclusions (section 7.1.1) have the composition of the magma surrounding the crystallizing olivines within which they are hosted. In order to access the composition of the primary melt – that of the magma before crystallisation of olivine, which is the first silicate mineral to crystallize in mantle-derived melts at pressure < 10kbars (Green & Ringwood, 1967) – olivine must be added to the composition of the re-equilibrated melt inclusions until equilibrium with Fo contents equal to that of the initial mantle source of the primary melt (Herzberg & O'Hara, 2002). This process is called back-fractionation or reverse-crystallisation. Figure 7.3.

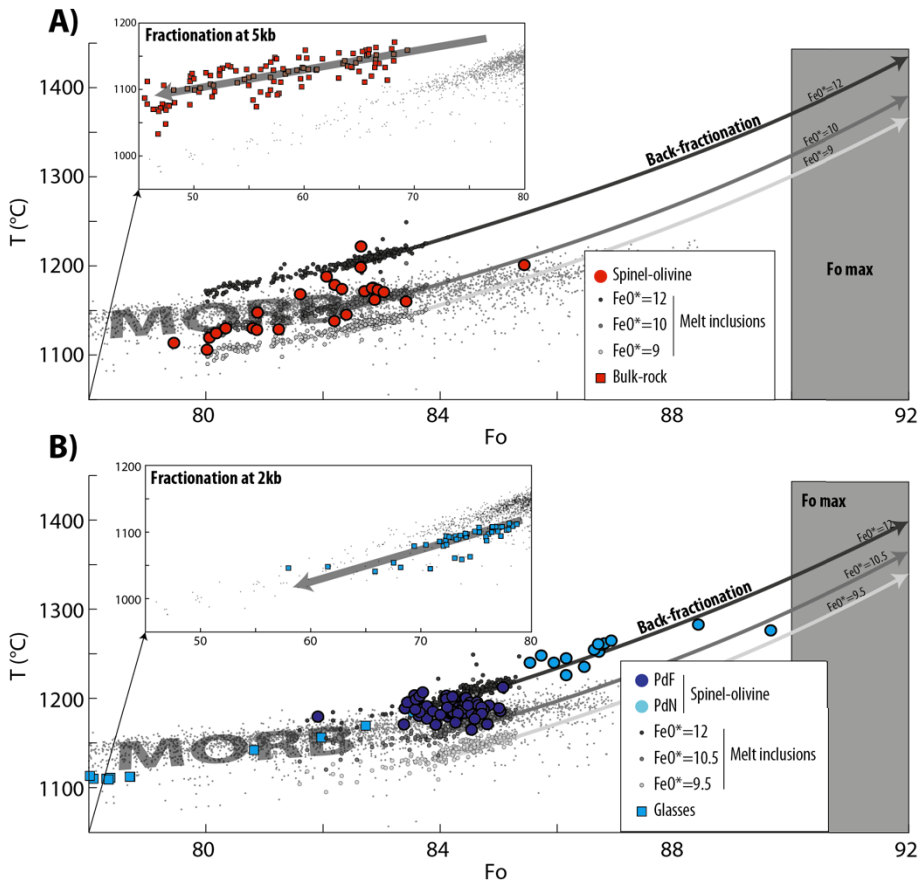

Figure 7.3 - Back-fractionation paths of re-equilibrated melt inclusions (grey arrows) to mantle Fo values (Fo_{max}) for different FeO* (wt%) of primary melts. Spinel-olivine temperature data (Figure 6.11). A) Deccan Traps (Thakurvadi formation) samples. The inset shows bulk-rock (Figure 5.4) melt-liquidus associations and the pressure (kbars) required for the melt inclusion crystallisation paths to match the bulk-rock melt-liquidus associations. B) Réunion Island (Piton de la Fournaise and Piton des Neiges for spinel-olivine thermometry only) samples. The inset shows melt-liquidus associations of glasses (Famin *et al.*, 2009, Villemant *et al.*, 2009, Salaün *et al.*, 2010) and the pressure (kbars) required for them to be matched by the melt inclusion crystallisation paths. Background: compilation of melt-liquidus associations of MORB glasses from GEOROC.

The back-fractionation paths of Figure 7.3 match the spinel-olivine data because the FeO* used in the re-equilibration stage (section 7.1.1) was chosen accordingly. These paths are further validated with bulk-rock compositions (Deccan Traps, Figure 7.3a) and volcanic glasses (Réunion Island, Figure 7.3b) compositions: the melt-liquidus associations of volcanic glasses and bulk-rock compositions (with low loss on ignition) return pressures, temperatures and equilibrium olivine Fo contents that must be matched by fractionation (or crystallisation) of the re-equilibrated melt inclusions at the same pressure (upper crustal magma chamber). In other words, all potential products of the back-fractionated melt inclusions (or primary melts) must be explained by the crystallisation paths of the latter.

The composition of the primary melts is assumed to be equal to the composition of the back-fractionated melt inclusions up to equilibrium with mantle olivine. It thus depends on the maximum Fo (Fo_{max}) used in the back-fractionation process, but also on the initial FeO* used in melt inclusion re-equilibration, which determines the starting point of the back-fractionation paths. Figure 7.4.

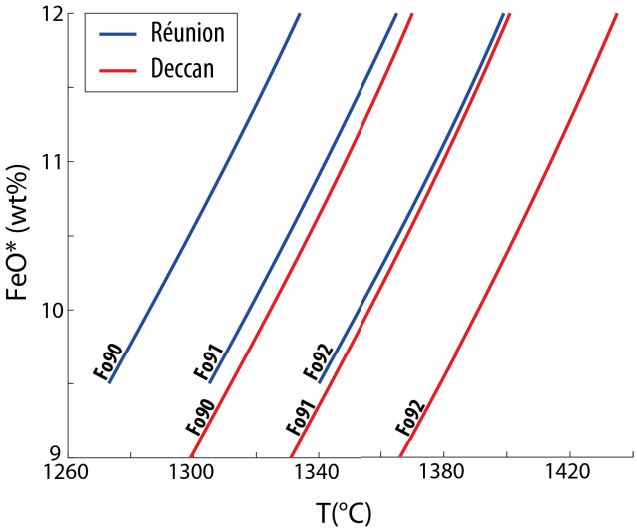

Figure 7.4 – FeO* used in melt inclusion re-equilibration as a function of crustal magma chamber magmatic temperature for different mantle olivine Fo (Fo_{max}, see Figure 7.3). Red: Deccan Traps (Thakurvadi formation). Blue: Réunion Island (Piton de la Fournaise only. No melt inclusions from Piton des Neiges)

The range of low-pressure (upper crustal) magmatic temperatures on Figure 7.4 is 126°C (1273 to 1399°C) for Réunion Island (PdF) between Fo90 / FeO* = 9.5 and Fo92 / FeO* = 12 and 136°C (1299 to 1435°C) for the Deccan Traps (Thakurvadi formation), between Fo90 / FeO* = 9 and Fo92 / FeO* = 12. The temperature increase per unit Fo is 30°C and slightly less (~25°C) per 1% FeO* increase.

The primary melt compositions at different FeO* and Fo_{max}, corresponding to Figure 7.4 are given in Table 7–1.

Table 7–1 – Corresponds to Figure 7.4. Average compositions of equilibrated melt inclusions (underlined italics) and corresponding calculated primary melts or backfractionated melt inclusions (bold) for different Fo_{max} and FeO*. Black bold font: compositions considered relevant for the Deccan Traps and Réunion Island primary melts. Oxides concentrations in wt%. H_2O concentrations calculated as $1.2 \times K_2O$ (section 7.3.1.1)

	SiO_2	TiO_2	Al_2O_3	Fe_2O_3	FeO	MnO	MgO	CaO	Na_2O	K_2O	H_2O	P_2O_5	T (°C)	Fo	FeO*
Deccan Traps	*50.23*	*1.85*	*12.71*	*1.07*	*11.05*	*0.11*	*9.24*	*11.15*	*1.95*	*0.43*	*0.52*	*0.21*	*1196*	*82.3*	*12*
	48.12	**1.46**	**10.01**	**1.08**	**11.16**	**0.09**	**17.26**	**8.78**	**1.54**	**0.34**	**0.41**	**0.17**	**1370**	**90.0**	**12**
	47.73	**1.38**	**9.48**	**1.07**	**11.02**	**0.08**	**19.00**	**8.31**	**1.45**	**0.32**	**0.38**	**0.16**	**1401**	**91.0**	**12**
	47.31	**1.29**	**8.88**	**1.04**	**10.81**	**0.08**	**20.99**	**7.79**	**1.36**	**0.30**	**0.36**	**0.15**	**1435**	**92.0**	**12**
	51.43	*2.01*	*13.78*	*0.89*	*9.20*	*0.12*	*7.68*	*12.09*	*2.11*	*0.47*	*0.56*	*0.23*	*1149*	*82.3*	*10*
	49.38	**1.64**	**11.25**	**0.93**	**9.64**	**0.10**	**14.90**	**9.87**	**1.72**	**0.38**	**0.46**	**0.19**	**1325**	**90.0**	**10**
	48.99	**1.56**	**10.72**	**0.93**	**9.58**	**0.09**	**16.53**	**9.41**	**1.64**	**0.37**	**0.44**	**0.18**	**1357**	**91.0**	**10**
	48.54	**1.48**	**10.12**	**0.92**	**9.48**	**0.09**	**18.44**	**8.88**	**1.55**	**0.35**	**0.41**	**0.17**	**1391**	**92.0**	**10**
	52.02	*2.09*	*14.31*	*0.80*	*8.27*	*0.12*	*6.92*	*12.55*	*2.19*	*0.49*	*0.59*	*0.24*	*1123*	*82.3*	*9*
	50.06	**1.74**	**11.91**	**0.85**	**8.82**	**0.10**	**13.63**	**10.45**	**1.82**	**0.41**	**0.49**	**0.20**	**1299**	**90.0**	**9**
	49.67	**1.66**	**11.40**	**0.85**	**8.81**	**0.10**	**15.19**	**10.00**	**1.74**	**0.39**	**0.47**	**0.19**	**1331**	**91.0**	**9**
	49.22	**1.58**	**10.80**	**0.85**	**8.75**	**0.09**	**17.03**	**9.48**	**1.65**	**0.37**	**0.44**	**0.18**	**1366**	**92.0**	**9**
Réunion Island (PdF)	*48.11*	*2.48*	*13.11*	*1.91*	*10.30*	*0.16*	*9.59*	*11.10*	*2.28*	*0.65*	*0.78*	*0.31*	*1198*	*84.3*	*12*
	46.89	**2.09**	**11.03**	**1.91**	**10.30**	**0.13**	**15.59**	**9.34**	**1.92**	**0.55**	**0.66**	**0.26**	**1334**	**90.0**	**12**
	46.75	**2.04**	**10.78**	**1.90**	**10.25**	**0.13**	**16.37**	**9.13**	**1.87**	**0.53**	**0.64**	**0.25**	**1349**	**90.5**	**12**
	46.60	**1.99**	**10.51**	**1.89**	**10.18**	**0.13**	**17.21**	**8.90**	**1.83**	**0.52**	**0.63**	**0.25**	**1365**	**91.0**	**12**
	46.29	**1.87**	**9.91**	**1.85**	**10.01**	**0.12**	**19.11**	**8.39**	**1.72**	**0.49**	**0.59**	**0.23**	**1399**	**92.0**	**12**
	48.92	*2.64*	*13.98*	*1.67*	*9.00*	*0.17*	*8.34*	*11.83*	*2.43*	*0.69*	*0.83*	*0.33*	*1163*	*84.3*	*10.5*
	47.73	**2.27**	**12.02**	**1.70**	**9.18**	**0.15**	**13.82**	**10.17**	**2.09**	**0.59**	**0.71**	**0.28**	**1299**	**90.0**	**10.5**
	47.58	**2.22**	**11.77**	**1.70**	**9.15**	**0.14**	**14.56**	**9.96**	**2.05**	**0.58**	**0.70**	**0.28**	**1314**	**90.5**	**10.5**
	47.43	**2.17**	**11.51**	**1.69**	**9.12**	**0.14**	**15.35**	**9.74**	**2.00**	**0.57**	**0.68**	**0.27**	**1330**	**91.0**	**10.5**
	47.11	**2.06**	**10.92**	**1.67**	**9.02**	**0.13**	**17.15**	**9.24**	**1.90**	**0.54**	**0.65**	**0.26**	**1365**	**92.0**	**10.5**
	49.44	*2.75*	*14.55*	*1.51*	*8.14*	*0.18*	*7.53*	*12.31*	*2.53*	*0.72*	*0.86*	*0.34*	*1137*	*84.3*	*9.5*
	48.29	**2.40**	**12.69**	**1.56**	**8.41**	**0.16**	**12.62**	**10.74**	**2.21**	**0.63**	**0.75**	**0.30**	**1273**	**90.0**	**9.5**
	48.15	**2.35**	**12.46**	**1.56**	**8.41**	**0.15**	**13.31**	**10.54**	**2.17**	**0.62**	**0.74**	**0.29**	**1289**	**90.5**	**9.5**
	48.00	**2.31**	**12.20**	**1.55**	**8.39**	**0.15**	**14.07**	**10.32**	**2.12**	**0.60**	**0.72**	**0.29**	**1305**	**91.0**	**9.5**
	47.67	**2.20**	**11.62**	**1.54**	**8.33**	**0.14**	**15.79**	**9.83**	**2.02**	**0.58**	**0.69**	**0.27**	**1340**	**92.0**	**9.5**

Table 7–1 summarizes all possible primary melt compositions and magmatic temperatures applicable to the crystallisation environment of the melt inclusions host olivines. At this stage and for further calculations and modelling, choosing one set of Fo_{max} and FeO* is required in order not to drastically augment to number of possible compositional and physical (T°C) scenarios. The average FeO* is derived from the best fit of melt inclusion re-equilibration with spinel-olivine temperatures (Figure 7.2). FeO* = 10wt% for the Deccan Traps (Thakurvadi formation) and FeO* = 10.5wt% for Réunion Island (PdF) were retained for further calculations. The Fo_{max} of Réunion Island (PdF) was fixed at Fo_{max} = 90.5 based on the maximum Fo measured on the Island (Piton des Neiges: Sobolev & Nikogosian, 1994). The Fo_{max} of the Deccan Traps (Thakurvadi formation) was chosen slightly higher at Fo_{max} = 91, also based on observations from the Deccan Traps (Krishnamurthy *et al.*, 2000).

The corresponding primary melt compositions are highlighted on Table 7–1.

7.1.3. Trace element composition of primary melts

Melt inclusion trace element concentrations are not accessible to EPMA and were not measured during this project. However, the use of proxies for trace element behaviour during melt inclusion back-fractionation helps circumvent this limitation. TiO_2 and Al_2O_3 were assumed to behave in a similar way to trace elements and have been used to calculate the trace element concentrations of primary melts from the bulk-rock compositions of the samples analysed for olivines and melt inclusions (Table 6–1). The concentration of a trace element x in the primary melt (PM) is assumed to be related to its concentration in the bulk-rock (BR) in the following way:

$$[x]_{PM} = [x]_{BR} \times \frac{[TiO_2]_{PM}}{[TiO_2]_{BR}} \quad (7.1)$$

or:

$$[x]_{PM} = [x]_{BR} \times \frac{[Al_2O_3]_{PM}}{[Al_2O_3]_{BR}} \quad (7.2)$$

$\frac{[TiO_2]_{PM}}{[TiO_2]_{BR}}$ and $\frac{[Al_2O_3]_{PM}}{[Al_2O_3]_{BR}}$ used for the estimation of primary melt trace element concentrations for the Deccan Traps and Réunion Island are given in Table 7–2 below.

Table 7–2 – Primary melt (Table 7–1)-to-bulk rock (Table 6–1) Al_2O_3 and TiO_2 ratios. Samples from the Deccan Traps are KD04 and KD06 and those from Réunion Island are TI 1602, GB1961, SR1977 and 0502-263

	$\frac{[Al_2O_3]_{PM}}{[Al_2O_3]_{BR}}$	$\frac{[TiO_2]_{PM}}{[TiO_2]_{BR}}$
KD06	0.93	0.89
KD04	0.94	0.91
TI1602	1.65	1.73
GB1961	1.41	1.69
SR1977	1.39	1.50
0502-263	1.47	1.49

The trace element concentrations in the primary melt of Réunion Island (PdF) have been calculated using the same samples processed earlier for olivine-hosted melt inclusions (section 6.5) and used for the reconstruction of primary melts major element concentrations (Table 7–1): TI1602, GB1961, SR1977 and 0502-263. These samples are from Piton de la Fournaise and contain average Fo84 olivines. Note that these are not the highest Fo olivines reported at Réunion Island (Sobolev & Nikogosian, 1994). However their compositions correspond to average olivine-rich basalt of Piton de la Fournaise (Albarède *et al.*, 1997). In

addition, Réunion Island being emplaced onto an oceanic lithosphere, the trace element patterns of these samples is unaffected by (continental) crustal assimilation (Figure 5.6).

On the other hand, crustal assimilation has long been recognized in the Deccan Traps, especially for high-MgO lavas (Figure 2.5 and Figure 5.5) and both of the olivine-bearing samples presented here (KD04 and KD06) are clearly affected by this process (Figure 6.1). This feature of the Deccan Traps lavas, i.e. the most primitive lavas being on average the most contaminated and vice versa, has been evoked in section 5. Several adaptations are therefore required in order to avoid crustal assimilation effects in the reconstruction of the trace element patterns of Deccan Traps primary melts.

Firstly, only a limited set of trace elements has been considered: Th, Nb, La, Ce, Nd, Sm, Gd, Dy, Er and Yb. This set is deemed sufficient to account for incompatible trace element variations due to low amounts of fractional melting as well as to preserve Heavy Rare-Earth Elements (HREE) depletion (garnet signature), which is an important feature of both Réunion Island and Deccan Traps lavas.

Secondly, the compositions of KD04 and KD06 cannot be used as is because of the crustal assimilation they have undergone. Considering the difficulty of properly inferring about the composition of the various crustal components involved in the crustal contamination of Deccan Traps lavas (Peng *et al.*, 1994, Chatterjee & Bhattacharji, 2008, Ray *et al.*, 2008, Bhattacharya *et al.*, 2013), the quantification and correction of crustal assimilation effects in high-MgO lavas was not carried out. Instead, it is assumed that the primary melts of Deccan Traps lavas have had a constant composition throughout the emplacement of the Western Ghats formations and that the trends in radiogenic isotope ratios are entirely due to the variable assimilation of various crustal components (Figure 2.5), (e.g. Peng *et al.*, 1994, Chatterjee & Bhattacharji, 2008). Following this assumption, the trace element concentrations of primary melts were calculated using the TiO_2 and Al_2O_3 contents of backfractionated, olivine-hosted melt inclusion as proxies (Table 7–2). This process is therefore similar to the calculation of Réunion Island primary melts explained above. Nevertheless, the starting trace element composition has to be less affected by crustal contamination than those of KD04 and KD06. It was deemed reasonable to replace the trace element concentrations of KD04 and KD06 by that of the least contaminated (e.g. highest Nb/La_n, lowest Th/Nb_n) sample with an MgO content close-enough to the olivine stability field (MgO > 7wt%, Figure 5.4) so as to restrict magmatic fractionation effects. Among the bulk-rock dataset presented in section 5,

MB23 (Ambenali formation, appendix II) is the sample bearing the most negligible signs of crustal assimilation (Nb/La_n = 0.87, Th/Nb_n = 0.99, Ce/Pb = 18.64) while still being close to the stability field of olivine (MgO = 6.97wt%). The trace element concentrations of MB23 have therefore been chosen for the reconstruction of primary melt trace element concentrations for the Deccan Traps.

Figure 7.5 shows the reconstructed trace element patterns for the primary melt of Deccan Traps and Réunion Island lavas.

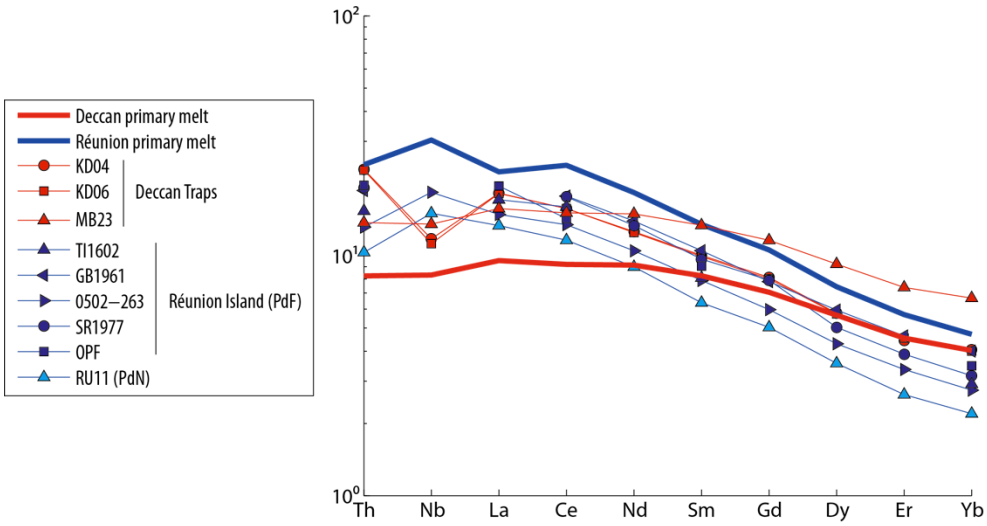

Figure 7.5 – Deccan Traps and Réunion Island primary melt trace element composition, and Deccan Traps (KD04, KD06) and Réunion Island (PdF: TI1602, GB1961n 0502-263, SR1977) samples used in this project. All data normalized to primitive mantle (Hofmann, 1988)

The final, averaged, major and trace element composition of primary melts as well as the magmatic temperatures, equilibrium olivine Fo content and initial FeO* used for melt inclusion re-equilibration are presented in Table 7–3.

Table 7–3 – Major (wt%) and trace element (ppm) compositions of calculated Deccan Traps and Réunion Island primary melt, and corresponding magmatic temperature, equilibrium olivine Fo (Fo_{max}) and initial FeO* used for melt inclusion re-equilibration.

	SiO_2	TiO_2	Al_2O_3	Fe_2O_3	FeO	MnO	MgO	CaO	Na_2O	K_2O	H_2O	P_2O_5	
Decca Traps	48.99	1.56	10.72	0.93	9.58	0.09	16.53	9.41	1.64	0.37	0.44	0.18	
Réunion Island (PdF)	47.58	2.22	11.77	1.7	9.15	0.14	14.56	9.96	2.05	0.58	0.7	0.28	
	Th	Nb	La	Ce	Nd	Sm	Gd	Dy	Er	Yb	T (°C)	Fo_{max}	FeO_{ini}
Decca Traps	0.67	5.13	5.86	14.75	10.87	3.19	3.61	3.61	1.89	1.67	1357	91	10
Réunion Island (PdF)	1.96	18.86	13.82	38.39	21.93	5.25	5.45	4.76	2.38	1.96	1314	90.5	10.5

The primary melts and corresponding magmatic temperatures will now be used in an attempt to reconstruct the sources of Deccan Traps and Réunion Island magmas.

7.2. Source modelling

The olivine dataset presented in section 6 and the primary melt compositions and temperatures reconstructed in the preceding section 7.1 can be utilized as proxies for mantle source composition, amount of melting and potential temperature.

The sources of the Deccan Traps and Réunion Island will be modelled using the approach developed by Sobolev and colleagues (Sobolev *et al.*, 2005, 2007). This model will then be compared with a hydrous mantle melting model (Katz *et al.*, 2003). In a final modelling section, the uncertainties pertaining to both models and their implications for sources of the Deccan Traps and Réunion Island volcanics will be investigated.

7.2.1. Geodynamical framework

Geodynamical framework used in this section has been established by Sobolev and co-workers (Sobolev *et al.*, 2005, 2007). It is based on the plume model (Wilson, 1963, Morgan, 1971) and considers that a mantle plume is not a mere temperature anomaly but that it is also a chemical anomaly: temperature anomalies in the deep mantle are capable of carrying some amounts of ancient, subducted oceanic crust in the form of eclogite. The presence of eclogite in plumes has long been suggested (Hofmann & White, 1982) and has major implications for magmatic processes. The geodynamical framework of this approach is presented in Figure 7.6 and in the text below.

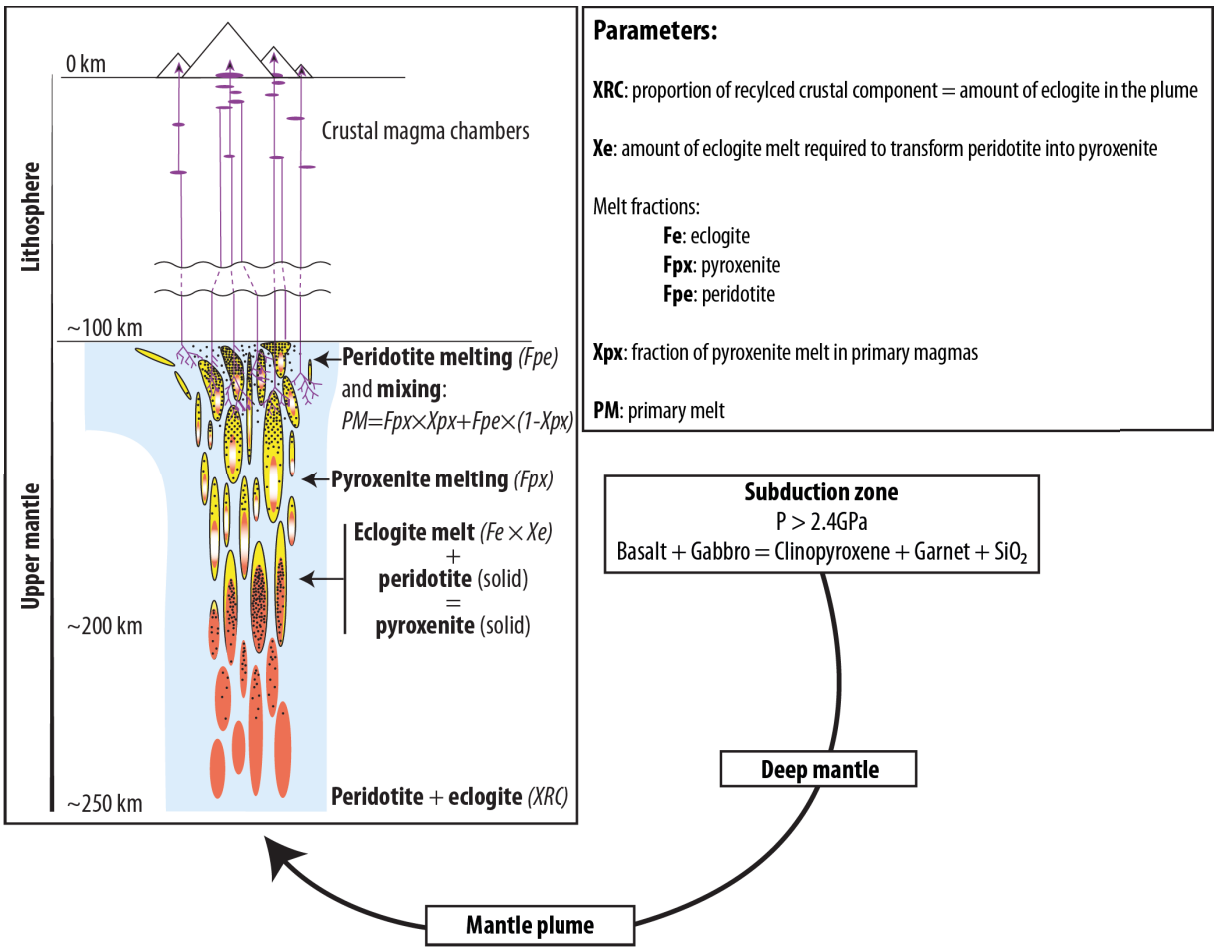

Figure 7.6 – Geodynamical framework used for source modelling, after Sobolev et al (2005, 2007). See text for description.

The framework of Sobolev et al (2005, 2007) shown on Figure 7.6 includes the five following stages:

- Oceanic crust undergoes subduction and is metamorphosed into eclogite at pressures greater than 1.5GPa. The trace element composition of the oceanic crust is modified during subduction using mobility coefficients from (Tatsumi & Hanyu, 2003)
- The dense eclogite sinks in the deep mantle, possibly as deep as the D'' layer. Thermal anomalies in the deep mantle generate convection plumes that can dynamically carry small volumes of eclogite (< 20%). The maximum amount of eclogite that may be carried by a plume corresponding to a temperature anomaly ΔT with respect to ambient mantle (T_p = 1350°C) is obtained after (Leitch & Davies, 2001) as:

$$\Delta T \propto \frac{\alpha \Delta T \rho_e \rho_0}{\rho_m} \quad (7.3)$$

- Where $\Delta\rho_e$ is the excess eclogite in the plume (equal to XRC, Figure 7.6), α (K^{-1}) is the thermal expansivity of the mantle, ρ_e is the density of eclogite (3500kg.m^{-3}) and ρ_0 is the density of the MORB mantle (3300kg.m^{-3})

- Eclogite has a lower solidus than peridotite and thus starts melting at deeper depths than peridotite (~180km) and melt by 40 to 60% (Fe, Figure 7.6) so that only a dense eclogite refractory restite remains and probably delaminates. (Yasuda *et al.*, 1994, Yaxley, 2000, and references therein). The eclogite high-Si melt reacts with the olivine of the surrounding peridotite to produce secondary pyroxenite until all the olivine is exhausted (Rapp *et al.*, 1999, Sobolev *et al.*, 2005). The weight fraction of reacting eclogite melt Xe (Figure 7.6) is considered equal to the olivine mode in the peridotite (Sobolev *et al.*, 2005). The mineral modes in the pyroxenite are calculated as a function of Xe (Table 7–5)
- The secondary pyroxenite also has a lower solidus than peridotite (yet higher that eclogite: Yaxley, 2000, and references therein) and starts melting deeper than peridotite. It also melts by 40 to 60% (Fpx, Figure 7.6). (Yaxley & Green, 1998, Sobolev *et al.*, 2007, 2011)
- Both Fe and Fpx are therefore buffered within 40-60%. As explained, the lower bound of this range is due to low solidi compared with peridotite. The upper bound is the result of melting-induced exhaustion causing the eclogite and pyroxenite to become refractory beyond 60% melting (Na exhaustion: Kogiso & Hirschmann, 2006)
- Finally, the proportion of pyroxenite-derived melt that mix with peridotite-derived melts (*Fpe,* Figure 7.6) is given by *Xpx* (Figure 7.6), which is measured in volcanic olivine phenocrysts (Figure 6.5). This mixture of pyroxenite- and peridotite-derived melt forms the primary melt that will travel to the surface and undergo fractionation and contamination within the crust. The olivine phenocrysts analysed for Ni excess and Mn deficiency in order to characterize the pyroxenitic component *Xpx* have crystallized at shallow depth in crustal magma chambers (Marsh, 2007) and must therefore be chosen among the highest forsterite contents in order to exclude the chemical effects of fractionation and contamination
- The amount of recycled oceanic crust in the form of eclogite in the plume (*XRC*) can be calculated from the melt fractions of eclogite (*Fe*), pyroxenite (*Fpx*) and peridotite (*Fpe*), the fraction of reacting eclogite melt *Xe* and the pyroxenitic component *Xpx* as:

$$XRC = \frac{Xe}{F_e\left(\frac{F_{Px}(1-Xpx)}{Xpx\,F_{Pe}}+\frac{1-F_e}{F_e}X_e+1\right)} \quad (7.4)$$

And the proportions of each lithology in the plume head are obtained from:

$$C_e = XRC(1-F_e) \quad (7.5)$$

$$C_{px} = \frac{XRC\ F_e}{X_e} \quad (7.6)$$

$$C_{Pe} = 1 - C_e - C_{px} \quad (7.7)$$

- The total amount of melting of the hybrid source (pyroxenite + peridotite) is:

$$Tot\ melt\% = F_{Pe}\frac{C_{Pe}}{C_{Pe}+C_{Px}+C_e} + F_{Px}\frac{C_{Px}}{C_{Pe}+C_{Px}+C_e} \quad (7.8)$$

7.2.2. Geochemical modelling

7.2.2.1. Model parameterization

The first modelling approach used in this project consists in calculating the evolution of trace element concentrations through the five stages of mantle convection and magma production described above (section 7.2.1) so that the final primary melt modelled matches the primary melt composition reconstructed from melt inclusion back-fractionation (sections 7.1.2 and 7.1.3).

Mantle and oceanic crust composition

The compositions of the major lithologies upon which this model is based are given in Table 7–4.

Table 7–4 – Compositions of the starting lithologies of the trace element model. PM: Primitive Mantle from Hofmann (1988), DMM: Depleted MORB Mantle from Workman and Hart (2005), OC: average Oceanic Crust from White and Klein (2014). The oceanic crust (OC) is modified during subduction by fluid circulation. This process is implemented here by applying Mobility coefficients (Tatsumi & Hanyu, 2003) to the original oceanic crust composition (OC) thereby creating Eclogite

	PM	**DMM**	**OC**	*Mobility*	**Eclogite**
Th	0.08	0.01	0.21	0.38	0.13
Nb	0.62	0.15	2.77	0.04	2.67
La	0.61	0.19	2.13	0.56	0.94
Ce	1.60	0.55	5.81	0.51	2.86
Nd	1.19	0.58	4.90	0.31	3.39
Sm	0.39	0.24	1.70	0.14	1.47
Gd	0.51	0.36	2.25	0.06	2.12
Dy	0.64	0.51	2.84	0.04	2.74
Er	0.42	0.35	1.85	0.01	1.84
Yb	0.41	0.37	1.85	0.01	1.82
				Subduction	

The peridotite composition is considered to be equivalent to 80% PM and 20% DMM throughout the model (White & McKenzie, 1995). The initial composition of the peridotite that is metamorphosed by eclogite melts and the composition of the peridotite that melts with the pyroxenite are assumed to be equal.

The trace element mobility coefficients of Tatsumi et al (2003) are used to simulate the compositional changes affecting the oceanic crust during subduction. It is possible that trace element mobility during subduction only concerns secondary altered minerals. In this case, the final composition of the processed altered crust could be equal to its original composition before alteration.

Rock and melt modes for eclogite, pyroxenite and peridotite

The rock and melting modes of the lithologies that will undergo melting (i.e. eclogite, pyroxenite and peridotite) are given in Table 7–5.

Table 7–5 – Modes of the peridotite (Walter, 1998, Donnelly *et al.*, 2004), eclogite and pyroxenite (Sobolev *et al.*, 2005) used in the trace element model. m: rock modes, p melting modes for non-modal melting, (see text below), f: coefficients used to calculate the mineral modes of the pyroxenite from those of the original peridotite before metasomatism by eclogite melt:

$\boldsymbol{m_{Px}^{olivine} = m_{Pe}^{olivine} - Xe}$ and is therefore equal to zero

$\boldsymbol{m_{Px}^{Opx} = m_{Pe}^{Opx} + f^{Opx}.Xe}$ where $\boldsymbol{f^{Opx} \in [-0.1\ ;\ -0.5]}$

$\boldsymbol{m_{Px}^{Cpx} = m_{Pe}^{Cpx} + f^{Cpx}.Xe}$ where $\boldsymbol{f^{Cpx} \in [0.86; 1]}$

$\boldsymbol{m_{Px}^{Grt} = m_{Pe}^{Grt} + f^{Grt}.Xe}$ where $\boldsymbol{f^{Grt} \in [0.24; 0.03]}$

$\boldsymbol{m_{Pe}^{i}}$ and $\boldsymbol{m_{Px}^{i}}$ are the modes of mineral i in the peridotite and pyroxenite respectively.

Opx: orthopyroxene, Cpx: clinopyroxene, Grt: garnet

Peridotite	**m**	**p**	**Eclogite**	**m**	**p**	**Pyroxenite**	**m**	**f**	**p**
Ol	0.57	0.08	Coesite	0.1	0.2	Opx	0.064	-0.1	0.1
Opx	0.14	0.14	Opx	0	0	Cpx	0.83	1	0.75
Cpx	0.27	0.53	Cpx	0.55	0.5	Grt	0.106	0.1	0.15
Grt	0.02	0.25	Grt	0.35	0.3				
Sp	0	0	Sp	0	0				

Melting model

The melting of eclogite, pyroxenite and peridotite is described by non-modal aggregate melting (Shaw, 1970):

$$\frac{C_i^l}{C_i^0} = \frac{1}{F}\left(1 - \left(1 - \frac{P_i F}{D_i^0}\right)^{\frac{1}{P_i}}\right) \quad (7.9)$$

Where:

$$D_i^0 = \sum_\phi m_\phi D_i^{\phi/l} \quad (7.10)$$

$$P_i = \sum_\phi p_\phi D_i^{\phi/l} \quad (7.11)$$

For any trace element i, and mineral phase ϕ, C_i^l and C_i^0 are the concentrations of i in the melt and in the restite, respectively. D_i^0 is the average partition coefficient of i in the melting lithology and P_i is the average melting mode, that is the extent to which partition coefficients are affected by the fact that not all mineral phases melt to the same degree (Table 7–5). F is the melt fraction.

Solid/liquid partition coefficients

The partition coefficients implemented in this model are given in Table 7–6

Table 7–6 – Mineral-melt partition coefficients. Olivine, orthopyroxene (Opx), clinopyroxene (Cpx) and garnet partition coefficients from Donnelly et al (2004). Spinel partition coefficients from Kelemen et al (1992) and Murton et al (2005). Coesite partition coefficients from Sobolev et al (Sobolev *et al.*, 2005).

	Olivine	**Opx**	**Cpx**	**Garnet**	**Spinel**	**Coesite**
Th	5.00E-05	5.00E-05	3.00E-03	1.50E-03	0.00E+00	7.00E-06
Nb	4.10E-05	1.00E-04	7.00E-03	4.20E-03	0.00E+00	5.00E-05
La	5.00E-05	5.00E-04	4.20E-02	1.00E-03	1.00E-02	2.00E-04
Ce	6.00E-05	3.00E-03	9.00E-02	7.00E-03	6.00E-04	7.00E-05
Nd	2.00E-04	9.00E-03	1.90E-01	6.00E-02	6.00E-04	3.00E-04
Sm	6.00E-04	1.00E-02	2.80E-01	1.15E-01	1.00E-02	9.00E-04
Gd	9.90E-04	1.60E-02	3.70E-01	8.00E-01	6.00E-04	1.50E-03
Dy	4.00E-03	2.50E-02	4.02E-01	1.40E+00	1.00E-02	2.70E-03
Er	8.70E-03	4.10E-02	4.22E-01	3.20E+00	3.00E-03	1.09E-02
Yb	1.70E-02	4.70E-02	4.32E-01	4.18E+00	1.00E-02	2.40E-02

Potential temperature

Finally, the source potential temperature is calculated from the total amount of melting of the hybrid source (Equation 7.8) as in (Herzberg *et al.*, 2007):

$$T_p = Tot\ melt\% \frac{\Delta S \times T}{C_P} - P \quad (7.12)$$

Where ΔS is the entropy difference between solid and liquid (300 J kg^{-1} K^{-1}), C_P is the specific heat at constant pressure (1200 J kg^{-1} K^{-1}), T (°K) is the magmatic temperature obtained from spinel-olivine and melt inclusion thermometry (sections 7.1.1 and 6.6.2) recalculated at the pressure of the source after (Ford *et al.*, 1983) as $T = T_{spinel/inclusion} + 49P_{GPa}$. Finally, P is the postulated source pressure (P (GPa) = depth (km) / 33). (Katz *et al.*, 2003).

It is therefore critical to estimate pressure appropriately in order to calculate realistic potential temperatures (T_p).

The depth at which primary magmas will be released from their source is thought to be that of the lithosphere-asthenosphere boundary. This depth may be increased by about 10km due to the existence of a plume-head freezing zone (Watson & McKenzie, 1991).

The depth of the lithosphere-asthenosphere boundary beneath India both today and at the K-Pg boundary is a matter of debate (section 2.4). Based on section 2.4 and Figure 5.5 as well as on the stratigraphy of the Deccan Traps (section 2.3), the depth of the lithosphere asthenosphere boundary during the emplacement of the Thakurvadi formation (fourth lowest formation of the Deccan Traps) is estimated to have been in the order of 140km. The depth of the Thakurvadi formation sources is thereafter considered to be in the order of 150km, including the plume-head freezing zone (Sobolev *et al.*, 2005). The pressure corresponding to this depth is 4.5GPa and will be used to calculate potential temperatures in later sections.

Réunion Island is located on early-Palaeogene lithosphere (Duncan, 1990, Fretzdorff & Haase, 2002) that is 110 to 120km-thick (Ellam, 1992). The pressure of primary magma generation at Réunion Island is estimated at 3.5GPa.

7.2.2.2. Geochemical modelling results

The geochemical model was implemented as a simple Excel spreadsheet, which is available from the PhD candidate.

Primary melt simulations were carried out by minimizing the difference between the trace element patterns of the reconstructed primary melts (section 7.1.3) and that of the model by varying the degrees of melting of eclogite (Fe), pyroxenite (Fpx), and peridotite (Fpe) only. The results are presented in Figure 7.7 and Table 7–7.

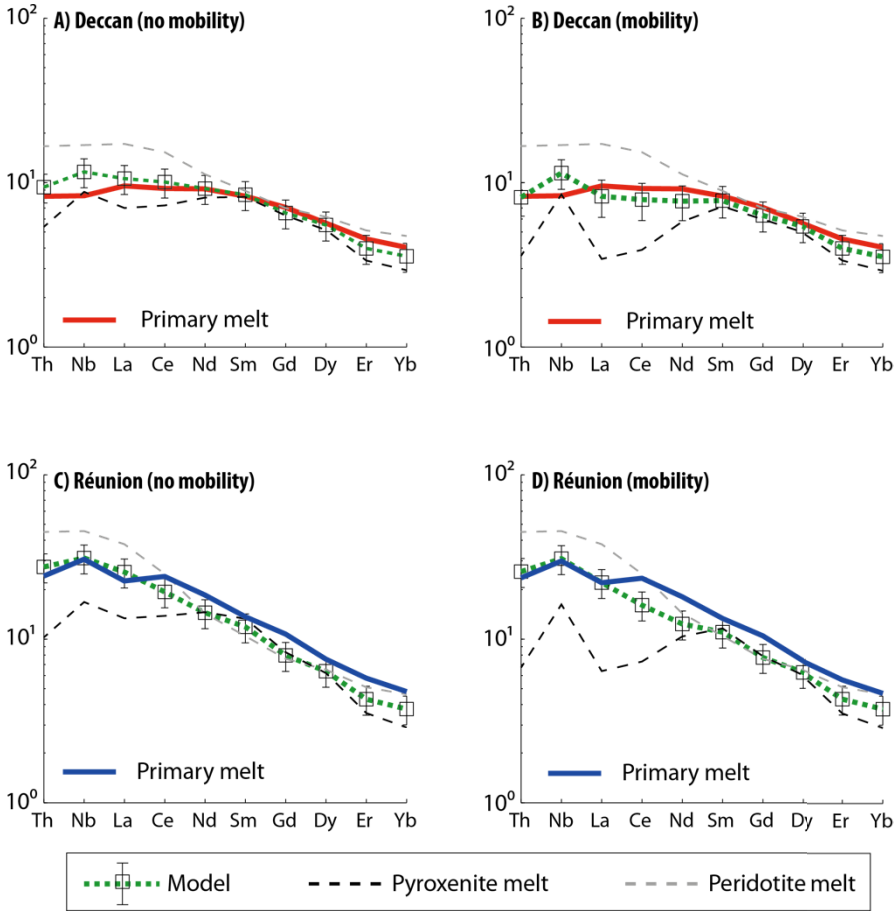

Figure 7.7 – Application of the geochemical mode of Sobolev et al (2005, 2007) to Deccan Traps (A and B) and Réunion Island (C and D) primary melts reconstructed in section 7.1.3. The parameterization of the model is described in section 7.2.2.1 above. The modelled primary melt is calculated as: Xpx × pyroxenite melt + (1-Xpx) × peridotite melt. The distance between the modelled and the reconstructed primary melt has been minimized by varying the degree of melting of eclogite (Fe), pyroxenite (Fpx) and peridotite (Fpe). The model fit is considered acceptable when it describes the reconstructed primary melt within ±20% relative error (error bars on the figure. See also Figure 7.8), Sobolev et al (2005). Two simulations were done for each setting, with (B and D) and without (A and C) mobility coefficients (Tatsumi & Hanyu, 2003) to modify the composition of oceanic crust during subduction. See text for discussion. See Table 7–7 for full model dataset.

Figure 7.7 and Table 7–7 illustrate two different results for each geological setting:

- The first scenario does not involve mobility coefficients, meaning that the composition of the oceanic crust is not affected by subduction and that therefore the eclogite has the same composition as the oceanic crust. The scenario is referred to as *"no mobility"*

- The second scenario uses the mobility coefficients of Tatsumi and Hanyu (2003) in order to simulate oceanic crust elemental loss upon fluid migration during subduction

As mentioned earlier, it is possible that the mobility of trace elements during subduction does not affect the entire crust and is only limited to weathered mineral. It is therefore hypothesised that the *mobility* and *no mobility* scenarios (Figure 7.7) can be considered as two compositional end-members for the recycled component.

For either scenario, the minimum residuals are met for the same set of values of Fe, Fpx and Fpe.

The mobility coefficients of Tatsumi and Hanyu (2003) have been used by Sobolev et al (2005). Nevertheless, the reason for proposing a simulation without them is that these coefficients are very poorly constrained (limited number of publications) and are likely to vary from one setting to another. Furthermore, the large Nb anomaly in the eclogite and pyroxenite induced by the low mobility of Nb compared to that of Th, La, Ce, Nd, and Sm suggested by Tatsumi and Hanyu (2003) (0.04, Table 7–4) seems unrealistically large. It is nonetheless interesting to note that positive Nb anomalies are a common feature of Ocean Island Basalts (Sun & McDonough, 1989), which may carry small amounts of recycled crust (Sobolev *et al.*, 2007).

The relative errors of each scenario (with and without mobility coefficients) for both the Deccan Traps and Réunion Islands are shown on Figure 7.8.

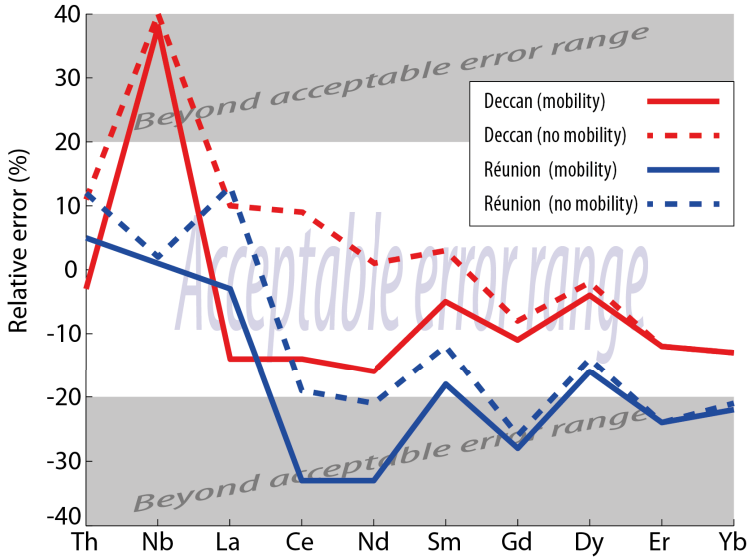

Figure 7.8 – Relative error between reconstructed and modelled primary melts – with and without the mobility coefficients of Tatsumi and Hanyu (2003) – for the Deccan Traps and Réunion Island as in Figure 7.7. Acceptable error range of ±20% as in Sobolev et al (Sobolev *et al.*, 2005)

Figure 7.8 shows that the fit of the reconstructed Réunion Island primary melt is better for Ce, Nd, Sm, Gd, Dy, and Yb without the use of mobility coefficients to describe subduction, that is with a recycled component – or eclogite – similar in composition to the average oceanic crust of Table 7–4 (White & Klein, 2014). On the other hand, the Th and La concentrations of Réunion Island primary melts is better described if their mobility during subduction is close to that proposed on Table 7–4. The Nb anomaly is however, almost perfectly reproduced in either case.

As for the Deccan Traps reconstructed primary melt, either scenario (with or without the loss of mobile elements from the oceanic crust during subduction) fall within the acceptable error range of ±20% proposed by Sobolev et al (2005), except Nb which forms a slightly negative anomaly as opposed to the recycled component (Figure 7.7 Figure 7.8).

Overall, the geochemical model used in this section tends to overestimate the concentrations of incompatible trace elements (Th, Nb, La) and to underestimate that of compatible trace elements (Ce to Yb).

The uncertainties pertaining to the model will be investigated in section 7.3.

The degree of melting of eclogite (Fe), pyroxenite (Fpx) and peridotite (Fpe) returned by the trace element pattern fitting of Figure 7.7 are (Table 7–7):

- Deccan Traps: $Fe = 0.52$, $Fpx = 0.60$, $Fpe = 0.05$
- Réunion Island: $Fe = 0.4$, $Fpx = 0.40$, $Fpe = 0.02$

Finally, the total degree of melting of the hybrid sources, the amount of recycled crust (XRC or eclogite) in the plume, and the corresponding potential temperatures are (Table 7–7):

- Deccan Traps: Tot melt% = 12%, XRC = 14%, $T_p = 1590°C$
- Réunion Island: Tot melt% = 3%, XRC = 6%, $T_p = 1470°C$

Table 7–7 – Geochemical modelling results (Figure 7.7) obtained from the parameterization of the pyroxenitic source model of Sobolev et al (2005) presented in section 7.2.2.1.

		Th	Nb	La	Ce	Nd	Sm	Gd	Dy	Er	Yb	XRC	C*Er*	C*Px*	C*Pe*	Tot. Melt%	T*mes* (°C)	P (Gpa)	Tp (°C)
Deccan / no mobility																			
Peridotite	80% PM / 20% DMM	0.07	0.52	0.53	1.39	1.07	0.36	0.48	0.61	0.40	0.40								
Pyroxenite	X*e* = 0.57	0.26	3.26	2.56	6.97	5.81	1.97	2.09	2.20	0.98	0.85								
Eclogite melt	F*e* = 0.52	0.40	5.33	4.10	11.17	9.39	3.18	3.30	3.40	1.42	1.19								
Peridotite melt	F*Pe* = 0.05	1.33	10.47	10.48	24.47	13.36	3.47	3.56	3.96	2.15	1.94								
Pyroxenite melt	F*Px* = 0.6	0.43	5.44	4.27	11.61	9.64	3.19	3.21	3.29	1.41	1.20								
Final mixing	Xpx = 0.65	0.75	7.20	6.45	16.11	10.94	3.29	3.33	3.53	1.67	1.46	0.14	0.07	0.13	0.81	0.12	1360	4.5	1589
Deccan / mobility																			
Eclogite formation	Mobility	0.38	0.04	0.56	0.51	0.31	0.14	0.06	0.04	0.01	0.01								
	Crust	0.21	2.77	2.13	5.81	4.90	1.70	2.25	2.84	1.85	1.85								
	Eclogite	0.13	2.67	0.94	2.86	3.39	1.47	2.12	2.74	1.84	1.82								
Peridotite	80% PM / 20% DMM	0.07	0.52	0.53	1.39	1.07	0.36	0.48	0.61	0.40	0.40								
Pyroxenite	X*e* = 0.57	0.17	3.15	1.25	3.74	4.16	1.72	1.97	2.13	0.98	0.84								
Eclogite melt	F*e* = 0.52	0.25	5.14	1.80	5.51	6.49	2.75	3.10	3.28	1.41	1.17								
Peridotite melt	F*Pe* = 0.05	1.33	10.47	10.48	24.47	13.36	3.47	3.56	3.96	2.15	1.94								
Pyroxenite melt	F*Px* = 0.6	0.29	5.25	2.09	6.23	6.89	2.79	3.04	3.19	1.41	1.19								
Final mixing	Xpx = 0.65	0.65	7.08	5.03	12.61	9.16	3.03	3.22	3.46	1.67	1.45	0.14	0.07	0.13	0.81	0.12	1360	4.5	1589
Primary melt		**0.67**	**5.13**	**5.86**	**14.75**	**10.87**	**3.19**	**3.61**	**3.61**	**1.89**	**1.67**								
Réunion / no mobility																			
Peridotite	80% PM / 20% DMM	0.07	0.52	0.53	1.39	1.07	0.36	0.48	0.61	0.40	0.40								
Pyroxenite	X*e* = 0.57	0.33	4.17	3.26	8.88	7.31	2.39	2.26	2.28	0.98	0.83								
Eclogite melt	F*e* = 0.4	0.53	6.93	5.32	14.52	12.01	3.92	3.60	3.55	1.41	1.16								
Peridotite melt	F*Pe* = 0.02	3.59	28.19	23.04	39.87	17.05	4.07	3.87	4.17	2.14	1.89								
Pyroxenite melt	F*Px* = 0.4	0.82	10.43	8.16	22.16	17.38	5.19	4.24	3.98	1.49	1.19								
Final mixing	Xpx = 0.5	2.20	19.31	15.60	31.02	17.22	4.63	4.06	4.08	1.81	1.54	0.06	0.04	0.04	0.92	0.03	1320	3.5	1472
Réunion / mobility																			
Eclogite formation	Mobility	0.38	0.04	0.56	0.51	0.31	0.14	0.06	0.04	0.01	0.01								
	Crust	0.21	2.77	2.13	5.81	4.90	1.70	2.25	2.84	1.85	1.85								
	Eclogite	0.13	2.67	0.94	2.86	3.39	1.47	2.12	2.74	1.84	1.82								
Peridotite	80% PM / 20% DMM	0.07	0.52	0.53	1.39	1.07	0.36	0.48	0.61	0.40	0.40								
Pyroxenite	X*e* = 0.57	0.22	4.03	1.56	4.68	5.19	2.08	2.13	2.21	0.97	0.83								
Eclogite melt	F*e* = 0.4	0.33	6.68	2.34	7.16	8.30	3.39	3.38	3.42	1.40	1.14								
Peridotite melt	F*Pe* = 0.02	3.59	28.19	23.04	39.87	17.05	4.07	3.87	4.17	2.14	1.89								
Pyroxenite melt	F*Px* = 0.4	0.54	10.08	3.90	11.68	12.35	4.53	4.01	3.86	1.48	1.18								
Final mixing	Xpx = 0.5	2.06	19.13	13.47	25.78	14.70	4.30	3.94	4.01	1.81	1.54	0.06	0.04	0.04	0.92	0.03	1320	3.5	1472
Primary melt		**1.96**	**18.86**	**13.82**	**38.39**	**21.93**	**5.25**	**5.45**	**4.76**	**2.38**	**1.96**								

7.2.3. Hydrous mantle melting

The geochemical model used in the preceding section 7.2.2 hinges upon the minimization of differences in trace element concentrations between the model and the measured primary melts by varying the melt fraction of eclogite (Fe), pyroxenite (Fpx) and peridotite (Fpe). Because of their low solidus, the melt fractions of eclogite (Fe) and pyroxenite (Fpx) are expected to be large (>40%: Yasuda *et al.*, 1994, Yaxley & Green, 1998) and fairly constant because extensive fractional melting renders the source rock refractory by exhausting Na (Kogiso & Hirschmann, 2006). The combination of low solidus and extensive fractional melting is therefore believed to buffer the melt fraction of both eclogite and pyroxenite within 40-60% (Sobolev *et al.*, 2005). On the other hand, the melt fraction of peridotite is much lower (<10%, Table 7–7) and will depend on the intensity of the temperature anomaly of the plume. In addition, peridotite is the main lithology of the plume head (Deccan Traps ~81% and Réunion Island ~92%, Table 7–7). The melt fraction of peridotite will therefore have considerable implication on the trace element pattern generated by the model as well as on the total amount of melting of the hybrid source (peridotite + pyroxenite).

The hydrous mantle melting parameterization of Katz et al (2003) is combined to the estimates of Fe and Fpx from the geochemical model of Table 7–7. Furthermore, total melt fractions will be calculated for different pressures in order to assess the consequences of the poorly constrained lithospheric thickness of pre-Deccan Traps India on the modelling results (total melt fraction, potential temperature and recycled component in the plume).

7.2.3.1. Model description

The hydrous mantle melting model of Katz et al (2003) for peridotite is expressed as a function of temperature (T), pressure (P), and peridotite water content ($X_{H_2O}^{bulk}$):

$$F_{Pe}\left(P,T,X_{H_2O}^{bulk}\right)=\left[\frac{T-\left(T_{solidus}-\Delta T\left(X_{H_2O}\left(X_{H_2O}^{bulk},P,F_{Pe}\right)\right)\right)}{T_{liquidus}^{lherz}-T_{solidus}}\right]^{\beta_1} \quad (7.13)$$

Where:

- The solidus of the mantle (peridotite) is:

$$T_{solidus}=A_1+A_2P+A_3P^2 \quad (7.14)$$

- The liquidus of dry Lherzolite:

$$T_{liquidus}^{lherz}=B_1+B_2P+B_3P^2 \quad (7.15)$$

- The water-induced lowering of the peridotite solidus:

$$\Delta T\left(X_{H_2O}\right)=KX_{H_2O}^{\Upsilon} \quad (7.16)$$

- The amount of water dissolved in the melt, wherein water is treated as a trace element with a partitioning coefficient similar to Ce, although Katz and colleagues noted that this might have to be reassessed according to the geological setting:

$$X_{H_2O}=\frac{X_{H_2O}^{bulk}}{D_{H_2O}+F(1-D_{H_2O})} \quad (7.17)$$

The values of the different parameters are given in Table 7–8.

Table 7–8 – Parameters used in the hydrous melting model. From Katz et al (2003).

Parameter	For calculating	Value	Units
A_1	$T_{solidus}$	1085.7	°C
A_2	$T_{solidus}$	132.9	°C Gpa^{-1}
A_3	$T_{solidus}$	-5.1	°C Gpa^{-2}
B_1	$T^{lherz}_{liquidus}$	1475.0	°C
B_2	$T^{lherz}_{liquidus}$	80	°C Gpa^{-1}
B_3	$T^{lherz}_{liquidus}$	-3.2	°C Gpa^{-2}
K	$\Delta T(H_2O)$	43	°C wt%$^{-\Upsilon}$
Υ	$\Delta T(H_2O)$	0.75	
D_{H20}		0.01	
β_1	F	1.5	

In this model, ΔT depends on the melt fraction F and F=f(P,T, $X_{H_2O}^{bulk}$) therefore has to be solved using a root finder.

The melt fractions of eclogite (Fe) and pyroxenite (Fpx) are taken from the geochemical model directly (Table 7–7):

- Deccan Traps: *Fe* = 0.52, *Fpx* = 0.60
- Réunion Island: *Fe* = 0.40, *Fpx* = 0.40

7.2.3.2. Hydrous melting and model coupling results

Total melt fraction

The total melt fractions (Tot melt%$_{Deccan}$ = 12% and Tot melt%$_{Réunion}$ = 3%, 7.2.2.2), speculated source pressures (P_{Deccan} = 4.5GPa and $P_{Réunion}$ = 3.5GPa) can be confronted to Fo_{max}, T and FeO* of the reconstructed primary melts (section 7.1) in the framework of Katz et al (2003), Figure 7.9.

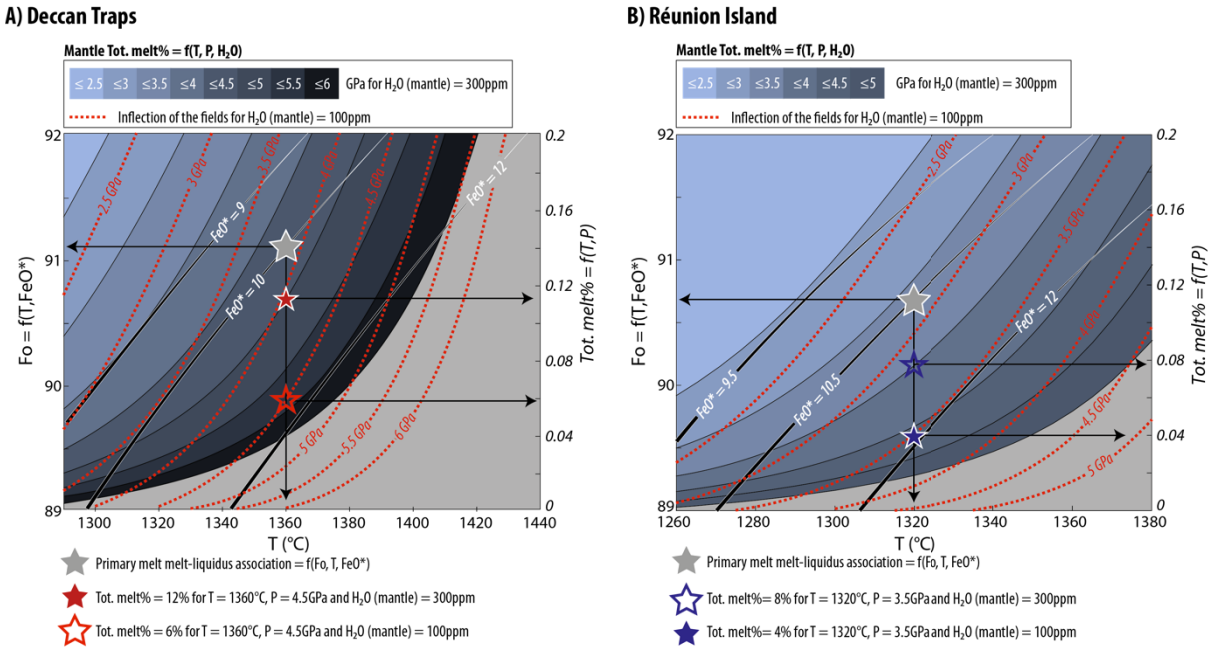

Figure 7.9 – Magmatic temperature (T), pressure (P), primary melt equilibrium olivine maximum Fo (Fo_{max}), Fe_{tot} content of the primary melt (Feo*) and total melt fractions of the hybrid source (Tot. melt%) for A) the Deccan Traps and B) Réunion Island. Right vertical axis: melt inclusions back-fractionation paths Fo_{max} = f(T) for different FeO*, grey star: melt-liquidus association for the reconstructed primary melts (Table 7–1). Left vertical axis: total melt fraction (Tot.melt%) = f(T, P), blue fields: T,P, Tot. melt% relationship for primitive mantle (H_2O_{Mantle} = 300ppm), red dashed isolines: T,P, Tot. melt% relationship for primitive mantle (H_2O_{Mantle} = 100ppm)

Figure 7.9 a and b both read from left to right:

- The melt inclusions back-fractionation paths (section 7.1.2) are plotted as T = f(Fo_{max}, FeO*) where T is the liquidus of the Fo_{max} equilibrium olivine. A set of Fo_{max} and T

correspond to a *FeO** content and conversely. The average *FeO** values of the reconstructed primary melt (section 7.1.1) have been estimated at FeO^*_{Deccan} = 10wt% and $FeO^*_{Réunion}$ = 10.5wt% and correspond to magmatic temperatures of T_{Deccan} = 1360°C and $T_{Réunion}$ = 1320°C at Fo_{max} *(Deccan)* = 91 and Fo_{max} *(Réunion)* = 90.5. The possible range of *FeO** for both localities has also been reported on both Figure 7.9a and b: FeO^*_{Deccan} = 9-12wt%, $FeO^*_{Réunion}$ = 9.5-12wt%

- The hydrous melting model *T*, *P*, total melt fraction (equation 7.8, see section 7.2.2.1) for Primitive and Depleted Mantle water content (300 and 100ppm, respectively) are linked to the $T = f(Fo_{max}, FeO^*)$ relationship by the magmatic temperature *T*: a set of Fo_{max} and *FeO** correspond to a given *T* (T_{Deccan} = 1360°C and $T_{Réunion}$ = 1320°C) and this temperature also corresponds to a total melt fraction at a given pressure and mantle water content.

Figure 7.9a shows that at P = 4.5GPa and for Primitive Mantle water content (300ppm), the Deccan Traps melt fractions are: Fpe = 0.05 and Tot. melt% = 12%, which is similar to estimates of the geochemical model (Table 7–7). If the mantle water content is lower and closer to Depleted Mantle content (100ppm), the total melt fraction at P = 4.5GPa would be of 6%. This possibility may be considered less likely as mantle plumes are generally not made of depleted material (White & McKenzie, 1995). Moreover, hot plumes are expected to melt by more than 6% (Herzberg & O'Hara, 2002, Sobolev *et al.*, 2007). Alternatively, similar total melt fractions of ~12% with mantle water contents of 100ppm would nonetheless be achieved at P = 4GPa.

Figure 7.9b on the other hand, shows that Réunion Island total melt fractions of 3% estimated from geochemical modelling (Table 7–7) are matched by the hydrous melting model only for low mantle water content, similar to Depleted Mantle values (100ppm) at P = 3.5 GPa. Primitive Mantle water content (300ppm) of the Réunion Island source peridotite would require P > 4GPa to match the total melt fractions returned by the geochemical model. The thickness of the lithosphere beneath Réunion Island seem well established (~110km, Ellam, 1992) and it is therefore unlikely that pressures higher than 3.5GPa would be compatible with the sources of Réunion Island magmas.

Potential Temperatures

As explained is section 7.2.2.1, the potential temperature (Tp) of the source can be calculated from total melt fractions (Tot. melt%), magmatic temperature (T) and pressure (P) following Herzberg et al (2007). In much the same way as Figure 7.9, Tp can thus be represented as a function of Tot.Melt%, T, P and mantle water content (Figure 7.10).

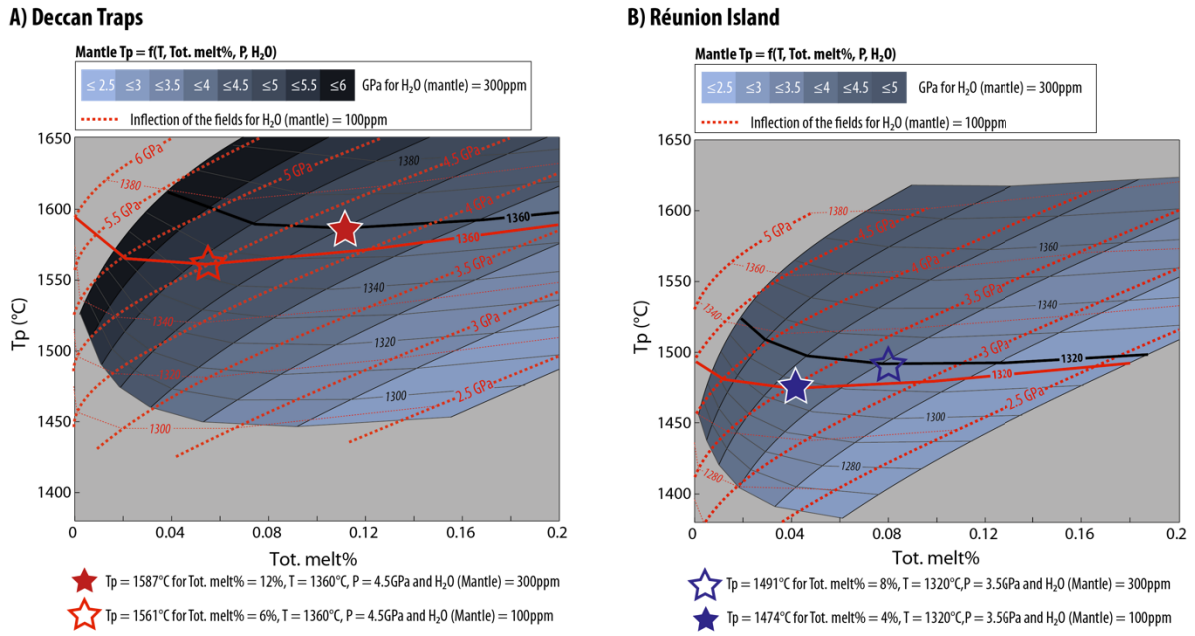

Figure 7.10 –Total melt fractions (Tot. melt%), magmatic temperature (T), pressure (P), mantle water content (H_2O_{Mantle}) and potential temperature (Tp) of the Deccan plume for A) the Deccan Traps and B) Réunion Island. Blue fields: Tp = f(Tot. melt%) for Primitive Mantle water content (300ppm). Thick red dotted lines: Tp = f(Tot. melt%) for Depleted Mantle water content (100ppm). Thin black solid lines: isolines for magmatic temeratures (T) for Primitive Mantle water content. Thin red dotted line: isolines for magmatic temperatures (T) for Depleted Mantle water content. Thick solid red and black lines: isolines for primary melt magmatic temperature (T_{Deccan} = 1360°C and $T_{Réunion}$ = 1320°C, see Table 7–3. Red and blue stars similar to Figure 7.9.

Figure 7.10 illustrates the relationship between total melt fractions of the hybrid source (Tot. melt%), magmatic temperatures (T), pressure (P) and mantle water content for both localities (Deccan Traps and Réunion Island). The total melt fractions of Figure 7.9 for Primitive Mantle water content (300ppm) Tot melt%$_{Deccan}$ = 12% and Tot melt%$_{Réunion}$ = 8% and for Depleted Mantle water content (100ppm) Tot melt%$_{Deccan}$ = 6% and Tot melt%$_{Réunion}$ = 4% are also reported (red and blue stars). The corresponding potential temperatures (Tp) are:

- Deccan Traps: 1587°C for H_2O_{Mantle} = 300ppm and 1561°C for H_2O_{Mantle} = 100ppm
- Réunion Island: 1491°C for H_2O_{Mantle} = 300ppm and 1474°C for H_2O_{Mantle} = 100ppm

In DMM water content is indeed 100ppm, Figure 7.9 suggests that the mantle beneath Réunion Island is more depleted than that of the Deccan Traps because the total melt fractions returned by the geochemical model and those of the hydrous melting model converge for this scenario. It is therefore speculated that the potential temperature of the plume was as high as 1587°C for the Deccan Traps and is 110°C lower at 1474°C beneath Réunion Island.

Recycled component

The amount of recycled crust carried by the plume in the form of eclogite is expressed as equation 7.4 () from the melt fractions of eclogite (Fe), pyroxenite (Fpx) and peridotite (Fpe), the fraction of reacting eclogite melt Xe and the pyroxenitic component Xpx (section 7.2.1). XRC depends on the melt fractions of the three lithologies involved in the plume and will therefore decrease with pressure (P) and increase with magmatic temperature (T). In other words, at a given Xpx, XRC is correlated with potential temperature (Tp).
Furthermore, eclogite is denser than peridotite: $\rho_e \sim 3500 km.m^{-3}$ and $\rho_{pe} \sim 3300 km.m^{-3}$ respectively. The plume does thus not carry eclogite because it is buoyant but rather because the plume is vigorous enough to dynamically drag small eclogite bodies towards the upper mantle (sufficient temperature anomaly with respect to the surrounding mantle). There is therefore a maximum amount of eclogite that a given plume can carry and this amount depends directly on its potential temperature. As a first approximation (Figure 7.11), the maximum amount of eclogite that can be carried by a plume (XRC_{max}) can be related to the temperature anomaly of the plume with respect to MORB mantle ($\Delta T = Tp - Tp_{MORB}$ where $Tp_{MORB} = 1350°C$) and the density difference between eclogite (ρ_e) and peridotite (ρ_{pe}) as $XRC_{max} < \alpha \frac{\Delta T \rho_{pe}}{\rho_e - \rho_{pe}}$ where α is the coefficient of thermal expansivity of the plume. (Leitch & Davies, 2001).

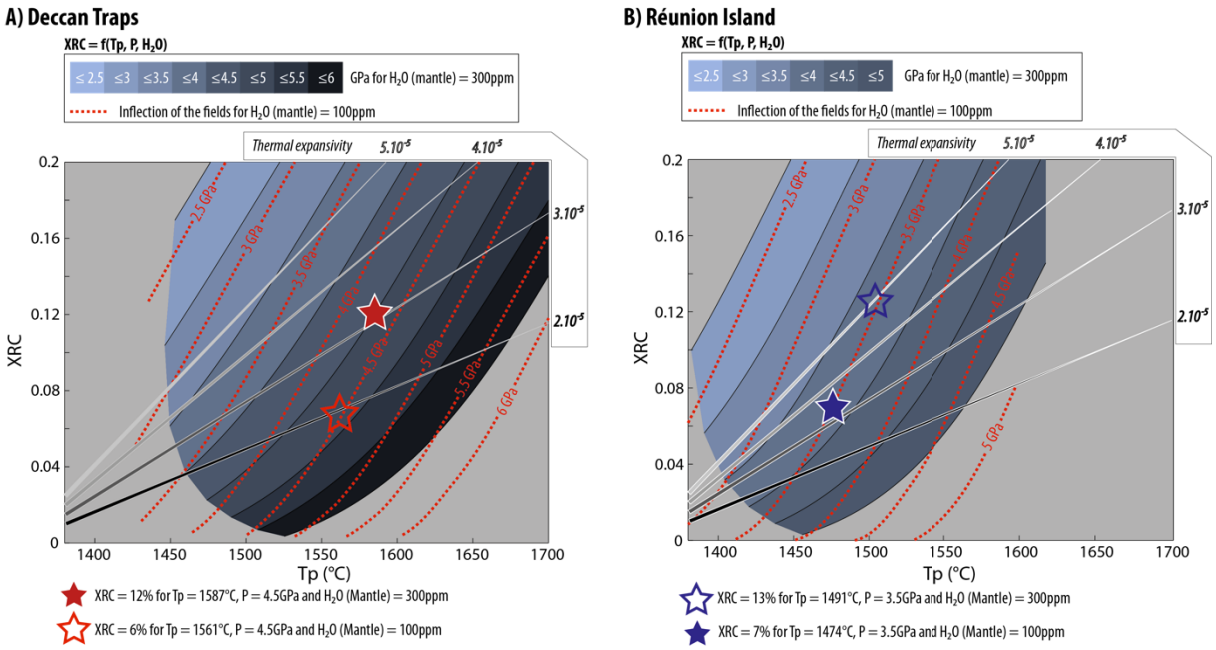

Figure 7.11 – Recycled component carried by the plume (XRC) as a function of potential temperature (Tp), pressure (P), and mantle water content (blue fields: H_2O_{Mantle} = 300ppm, red dotted lines: H_2O_{Mantle} = 100ppm) for A) the Deccan Traps and B) Réunion Island. Red and blue stars from Figure 7.9 and Figure 7.10. Superimposed XRC_{max} = f(Tp) for mantle thermal expansivity ranging from 2.10^{-5} to 5.10^{-5} from Leitch and Davies (2001), section 7.2.1.

From Figure 7.11, Tp_{Deccan} = 1587°C, XRC_{Deccan} = 12% at H_2O_{Mantle} = 300ppm and $Tp_{Réunion}$ = 1474°C, $XRC_{Réunion}$ = 7% at H_2O_{Mantle} = 100ppm return similar thermal expansivity coefficients of ~ 3.10^{-5}. On the other hand, H_2O_{Mantle} = 100ppm for the Deccan Traps and H_2O_{Mantle} = 300ppm for Réunion Island would require significantly different thermal expansivity coefficients of 2.10^{-5} and 5.10^{-5} respectively.

7.2.4. Summary of source modelling results

The application of the geochemical model of Sobolev et al (2005, 2007) (7.2.2), the combination of hydrous mantle melting (Katz *et al.*, 2003) and the calculation of mantle potential temperature based on Herzberg et al (2007), allowed for constraining several characteristics of the mantle sources of the Deccan Traps and Réunion Island, Table 7–9.

Table 7–9 – Summary of the source modelling results.

- H_2O_{Mantle}: mantle peridotite water content
- Xe: fraction of eclogite melt reacting with the surrounding peridotite to produce pyroxenite
- Melt fractions: eclogite (Fe), peridotite (Fpe), pyroxenite (Fpx)
- Xpx: proportion of pyroxenite melt in the primary melt
- XRC: recycled component (amount of eclogite) carried by the plume,
- Proportions of the three lithologies in the plume head: eclogite (Cer), pyroxenite (Cpx), peridotite (Cpe)
- Tot. melt%: total melt fraction of the hybrid source
- T: magmatic temperature (low pressure, close to atmospheric)
- P: source pressure
- Depth: source depth corresponding to source pressure (P)
- Tp: potential temperature of the source

	Deccan	Réunion
H_2O_{MANTLE} (ppm)	300	100
X*e* (%)	57	57
F*e* (%)	52	40
F*pe* (%)	5	2
F*px* (%)	60	40
X*px* (%)	65	50
XRC (%)	12	7
C*er* (%)	7	4
C*px* (%)	13	4
C*pe* (%)	81	92
Tot. Melt%	12	4
T (°C)	1360	1320
P (Gpa)	4.5	3.5
Depth (km)	150	115
Tp (°C)	1587	1474

7.3. Discussion and limits

The final results of the source modelling undertaken in the above sections are summarized in Table 7–7 and Table 7–9 (section 7.2.4). These results are compatible with the following scenario:

The Deccan Traps magmas were generated by a vigorous mantle plume (Tp ~ 1600°C) of primitive composition (DMM component < 20% and H_2O = 300ppm) and carrying recycled oceanic crust in the form of eclogite (XRC ~ 10 – 15%). The Deccan plume reached the thick Indian cratonic lithosphere (thickness ~ 140 – 250km) a few million years before the K-Pg boundary (70 - 68Ma, e.g. Mahoney *et al.*, 2002, Chenet *et al.*, 2007). The multi-level melting of the hybrid (eclogite, pyroxenite, peridotite) source resulted in a total average melt fraction of 10 – 15% (involving 65% of pyroxenite-derived melt, Xpx) considering a depth of melt generation of 150km (4.5GPa). These numbers are compatible with a plume head diameter of > 1000km as suggested by White and McKenzie (1995) in order to generated the sheer 1-$3.10^6 km^3$ of lavas proposed throughout the literature (e.g. Sen, 2001, and references therein). The potential temperature (1600°C), recycled component (XRC = 10-15%) and the pyroxenitic component in mantle derived melts (Xpx = 65%) also comply with the WPM-THICK (Within-Plate Magmas – Thick lithosphere) classification of Sobolev et al (2007). Plume-lithosphere interactions resulted in a significant – yet heterogeneous – thinning of the Indian cratonic lithosphere (section 2.4). Lithospheric thinning is observed in HREE trace element signatures at four different times along the Western Ghats composite section in lower and upper Jawhar, Khandala-Bushe and upper-Poladpur (Figure 5.7). Altogether the four transient episodes of thinning are compatible with one single and localized event of lithospheric erosion (50ka, Sobolev *et al.*, 2011) and periodic clogging by peridotite restite inducing increased source depths thereafter (section 5.5). Nonetheless, the trace element signature of Thakurvadi formation lavas undoubtedly bears evidence of deep origin (Gd/Yb_n > 1.6, Figure 5.7), despite the occurrence of paroxysmal eruption rates ($160 km^3$/yr, Chenet *et al.*, 2009). Overall, the average eruption rate of the main province of the Deccan Traps might have been close to 200 times that of today's Hawaii over 50 000 years (section 3.6). It is tempting to associate lithospheric thinning, at least to some extent, with extensional tectonics related to the rifting of 1) the Laxmi Rigde and 2) the Seychelles after the emplacement of the main Deccan lava pile (Figure 2.1 and Figure 2.6). However, Hooper et al (2010) consistently observed that extension along the Indian West Coast post-dated the emplacement of the

Western Ghats. Moreover, Sobolev et al (2011), indicated that extensional tectonics were not required for plume-induced lithospheric erosion to take place.
More than 60Ma after the emplacement of the Deccan Traps, the Deccan plume was still active and resulted in the building of Réunion Island onto 115km-thick Indian Ocean lithosphere (Ellam, 1992). Piton de la Fournaise is therefore the present day remnant of the Deccan plume. Olivine-based geochemical modelling reveals important changes between the early stage of the Deccan plume and its present-day state at Réunion Island. Potential temperature estimations suggest that it is now cooler by about 50-150°C (Tp ~ 1450-1500°C) and is therefore far less vigorous than at the K-Pg boundary. In the same way, it carries less recycled crustal material (XRC ~ 7%), the total melt fraction of the hybrid source is lower by 10% (Tot. melt% ~ 3-5%) and the contribution of pyroxenite-derived melts to the magmas is lower by about 15% (Xpx = 50%) compared with K-Pg times.

The above scenario supports the proposition that mantle plumes related to Palaeocene Large Igneous Provinces were hotter and melted more extensively than those of modern-day Ocean Islands (Herzberg & Gazel, 2009). Herzberg and Gazel attributed this general temperature change to lower mantle compositional heterogeneities. The outcomes of the geochemical modelling carried out in during this PhD is thus in overall agreement with the current understanding of deep-Earth processes. Nevertheless, several aspects of this modelling could be improved and benefit to the meaning and clarity of the big-picture exposed above.

The different stages of chemical analysis and calculations presented in the previous sections of this PhD, from olivine and inclusions data (section 6) to the application of geochemical models (section 7), all aim at reconstructing the mantle processes, which have their surface manifestation as intraplate volcanics (here, the Deccan Traps and Réunion Island). In a very final stage, these results can be integrated to a 2- or 3D numerical modelling framework in order to infer about the deep processes of the Earth (mantle convection, mantle structure, crustal recycling time and the like), (Sobolev *et al.*, 2011).
Throughout this manuscript, the prime sources of information and proxies for deep-Earth processes are olivine phenocrysts found in lavas that have been erupted onto the surface of the Earth. These olivines crystallized as cumulates in crustal magma chamber that are distant from the processes they are meant to be probes of (mantle melting and crustal recycling) in both space (>100km) and chemical evolution terms (e.g. fractionation, crustal assimilation,

magma mixing). Like any indirect approach and model, the methods used in this PhD project therefore suffer from a number of limitations that must be assessed in order for conclusions to be meaningful.

The all-important aspect of any modelling approach that assessing limitations represents, was only touched upon due to limited time. A first subsection of this discussion is dedicated to uncertainties in the reconstruction of primary melts. It is followed by a brief assessment of the uncertainties and sensitivities in the geochemical models.

7.3.1. Primary melt reconstruction

7.3.1.1. K_2O, H_2O and temperature correction

Electron Micro-Probe Analyser (EPMA) is the only analytical tool used during this PhD project (see appendix III for technical description and analytical protocols). EPMA does not allow for water contents to be directly measured. Yet, the effect of water content on magmatic processes is significant. Most importantly in the present case, H_2O affects melting processes and magmatic temperature estimations in petrological models by lowering the melting points of rocks and minerals (e.g. Danyushevsky, 2001, Katz *et al.*, 2003, Almeev *et al.*, 2007, Médard & Grove, 2008) that have been used in sections 7.1 and 7.2. Note however, that H_2O does not affect the temperature obtained by aluminium-based olivine-spinel thermometry (section 6.6.2). Indeed, these estimates are solely based on the partitioning of Al between olivines and their spinel inclusions and do not depend on liquidus temperatures (Wan *et al.*, 2008, Coogan *et al.*, 2014).

One can circumvent this limitation of EPMA by using K_2O as a proxy for H_2O concentrations. It has indeed been observed that, in magmatic rocks with low (<2%) loss on ignition, both elements are correlated to one another (e.g. Danyushevsky *et al.*, 2000b, Dixon *et al.*, 2002), Figure 7.12.

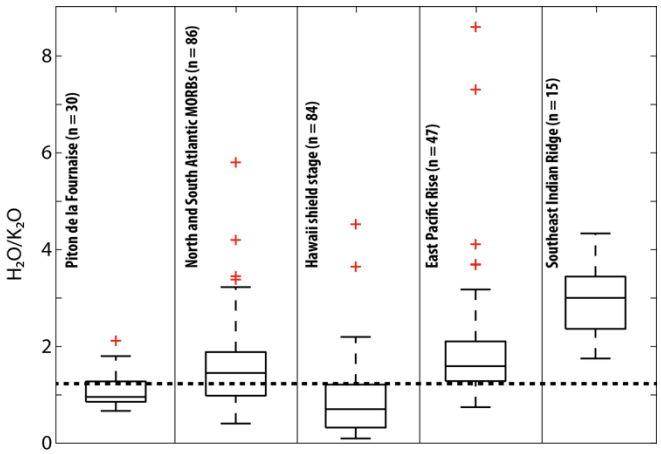

Figure 7.12 – H_2O/K_2O for different geological settings. Melt inclusion and high-MgO glasses (loss on ignition <1%) data compiled from GeoRoc

H_2O/K_2O = 1.2 has been used in this project based on Dixon et al. (2002) and personal communication with A.V. Sobolev. However, the literature data compiled in Figure 7.12 suggest ratios slightly lower than 1 for PdF and Hawaiian shield stage, implying that $H_2O/K_2O < 1$ would probably be more appropriate in the case of the Deccan Traps. This issue was identified too late during this project for any modification of the temperature corrections to be done. Nevertheless, the effect of varying H_2O/K_2O has been evaluated in order to estimate the importance of this parameter on the temperature corrections applied in the calculation of primary melt composition and mantle potential temperature (sections 7.1 and 7.2).

The temperature correction for water content is in the form [illegible] where T_{ini} is the magmatic temperature estimation of any melt fractionation model not directly taking this effect into account, like Ford et al. (1983), which has been used in this project. [illegible] based on Almeev et al. (2007) whom proposed [illegible]. In order to better account for the low amounts of water of hot-spot related magmatic rocks compared with arc volcanics, [illegible] has been chosen in all temperature corrections (best fit of H_2O = 0 to 2.5wt%, Figure 7.13).

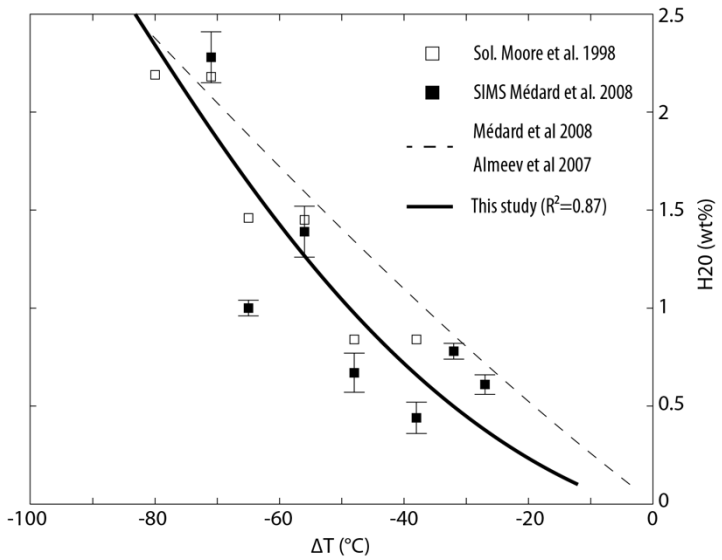

Figure 7.13 – Magmatic temperature correction for low melt water contents. (Moore *et al.*, 1998, Almeev *et al.*, 2007, Médard & Grove, 2008)

The variations of ΔT as a function of K_2O and H_2O/K_2O are shown in Figure 7.14.

K_2O contents of olivine melt inclusions and bulk-rocks from the Deccan Traps and Réunion Island are in the order of 0.5 (±0.2) wt%. From Figure 7.12, H_2O/K_2O for these settings is about 1 (±0.2). Therefore, the maximum effect of H_2O/K_2O on ΔT_{water} is the present case – i.e. H_2O/K_2O = 1 (±0.2) and K_2O = 0.5 (±0.2) wt% – is 10°C.

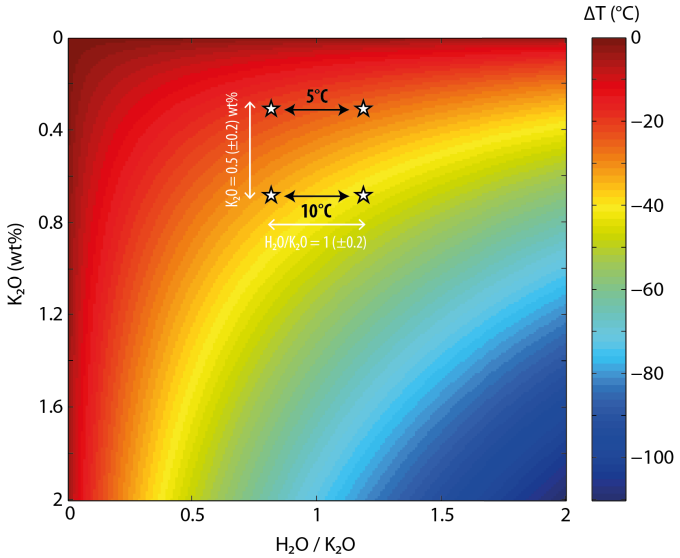

Figure 7.14 – Sensitivity of temperature correction (ΔT) to H_2O/K_2O and K_2O contents

It is therefore possible that all the temperature estimates presented in this manuscript – spinel-olivine aluminium thermometry excepted – are underestimated by about 10°C, which is likely within the error bars of any model. This issues nevertheless needs to be addressed in the future.

7.3.1.2. H_2O and Ce

Cerium can also been used as a proxy to water concentrations in fresh volcanic and mantle rocks (e.g. Dixon *et al.*, 2002). Rare earths were not measured in the olivine-hosted melt inclusions of the Deccan Traps and Réunion Island samples analysed during this PhD. Therefore, no direct relationship between Ce and water was used during this project. Literature and modelled Ce/H_2O are nevertheless proposed in Table 7–10.

Table 7–10 – H_2O and Ce concentrations and ratios in the inputs and results of the application of the geochemical model of Sobolev et al (2005, 2007).

Inputs: Primitive mantle (PM) from Hofmann (1988), Depleted MORB Mantle (DMM) from Workman and Hart (2005), eclogite from Dixon et al (2002). Pe: starting peridotite composition 80% PM and 20% DMM (section 7.2.2).

Outputs: H_2O concentrations in the melts of eclogite, pyroxenite and peridotite were estimated by integrating water to the geochemical model of Sobolev et al (2005, 2007) as a moderately incompatible trace element with $D_{H2O} = 0.01$ as in Katz et al (2003). Uncertainties of ±10ppm on H_2O concentrations are arbitrary and meant to show the consequences on Ce/H_2O (±5 units). The final H_2O contents are those of the reconstructed primary melts (section 7.1) and were determined using K_2O from back-fractionated melt inclusions as a proxy, see above (section 7.3.1.1). Outputs in brackets are for the application of the geochemical model of Sobolev et al (2005, 2007) without the coefficients of Tatsumi et al (2003) for the mobility of trace elements during subduction.

	Deccan			Réunion		
	H_2O (ppm)	Ce (ppm)	H_2O/Ce	H_2O (ppm)	Ce (ppm)	H_2O/Ce
Inputs						
DMM	100	0.55	182	100	0.55	182
PM	300	1.60	187	300	1.60	187
Eclogite	600	6.00	100	600	6.00	100
Pe = PM+DMM	260	1.39	186	260	1.39	186
Outputs						
Eclogite melt	1140 ±10	11 (6)	104 (190) ±5	1480 ±10	15 (7)	99 (211) ±5
Pyroxenite	765 ±10	7 (4)	109 (191) ±5	960 ±10	9 (5)	107 (192) ±5
Pyroxenite melt	1265 ±10	12 (6)	105 (211) ±5	2300 ±10	22 (12)	105 (192) ±5
Peridotite melt	4380 ±10	24	183 ±5	9200 ±10	40	230 ±5
Final	2400 ±10	16 (13)	150 (185) ±5	5800 ±10	31 (26)	187 (223) ±5

Table 7–10 shows that the H_2O/Ce ratios in the final modelled melts (150 or 185 for the Deccan Traps and 187 or 223 for Réunion Island depending on the effect of subduction on the recycled oceanic crust Ce content) are compatible with published estimates for magmatic glasses: $H_2O/Ce \sim 200±50$ (e.g. Dixon *et al.*, 2002).

The combined study of H_2O, K_2O and Ce in rocks and inclusions may prove useful both in terms of having simple proxies to magmatic and mantle water concentrations as well as for

tracing the relative evolution of H_2O, K_2O and Ce in various locations and geological setting around the Earth.

7.3.1.3. Primary melt FeO*, spinel olivine temperature and melt inclusion re-equilibration

FeO* is determined in the melt inclusion re-equilibration stage (section 7.1.1) wherein Fe is added to the inclusion is order to account for its re-equilibration with the host olivine upon cooling. Once this stage is completed, the Fe content of the melt inclusions must be equal to that of the primary melt minus the fraction involved by the crystallisation of the host olivine. Hence, proper estimation of FeO* is crucial in order to appropriately reconstitute the original composition of the melt inclusions. FeO* is also liked pressure: the higher the pressure under which the host olivine crystallised and the inclusions were trapped, the higher FeO*. Therefore higher FeO* also induces higher magmatic temperatures to balance the pressure-induced increase of liquidus (Figure 7.4).

In section 7.1.1, FeO* was determined using the range of temperature and forsterite estimates independently obtained from Al-based olivine-spinel thermometry (Figure 6.11) as a framework upon which melt inclusion compositions can be fitted by varying FeO* (Figure 7.2). Only the FeO* corresponding to the average spinel-olivine temperature was considered for melt inclusion back fractionation (Figure 7.3). Nevertheless, the range of olivine-spinel temperatures is large (±5 to ±25°C) and the minimum and maximum FeO* required to describe this range are FeO* = 9 to 12 for the Deccan Traps samples and FeO* = 9.5 to 12 for Réunion Island samples. The error bar on the re-equilibrated melt inclusion temperature (Figure 7.2) and their back fractionation paths is therefore > ±5°C and < ±25°C.

Alternatively, it is likely that the range of olivine-spinel temperatures (e.g. ±25°C) corresponds to the actual conditions under which the olivines grew. In other words, if an olivine crystallizes while ascending, its liquidus drops accordingly because pressure decreases - and the temperature recorded by the partitioning of aluminium between olivine and spinel inclusions as well as the equilibrium FeO* of the melt inclusions will be lower. The possibility that the scatter in olivine-spinel temperatures and the large range of melt inclusion equilibrium FeO* (Figure 7.2) are records of the physical environment of the growing phenocrysts (Figure 7.15) implies that both olivine-spinel aluminium partitioning and melt inclusion compositions should be considered at the phenocryst scale, i.e. measured in similar

zones (if existing) of the crystal within which they are, and as close as possible to one another.

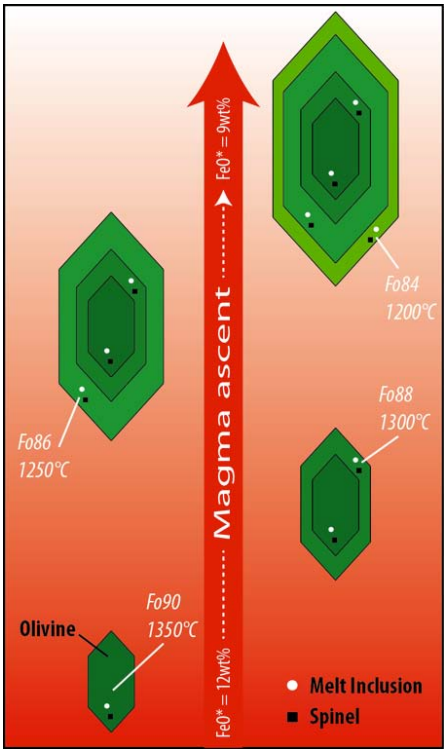

Figure 7.15 – Schematic illustration of the evolution of temperature, Fo and FeO* during olivine growth within an ascending magma and the consequences on measured spinel-olivine temperature and melt inclusion FeO* from 12 to 9wt%. All numbers are indicative only.

The olivine-spinel dataset used for olivine-spinel aluminium partitioning thermometry has been acquired by analysing spinel inclusions and the host olivine in the same area (i.e. one spinel analysis combined with three olivine analyses within 10 to 100µm of the spinel in order to account for possible chemical zoning, see appendix III for EPMA protocols). However, the melt inclusion dataset was obtained without considering the occurrence of spinels in their vicinity. Furthermore, the olivines analysed during this project have been separated by moderate crushing and were therefore fragments of phenocrysts. Future olivine based studies like this one would greatly benefit from the use of thin sections as opposed to epoxy mounts of olivine separates as well as from a phenocryst-scale approach to the coupling between melt inclusion composition and aluminium partitioning between olivine and spinels.

7.3.1.4. Melt inclusion back-fractionation and Fo_{max}

The melt inclusion re-equilibration discussed above (and 7.1.1) is followed by a back-fractionation stage wherein the composition of the primary melt – from which the melt

inclusions and their host olivines were derived – is reconstructed by simply adding (or melting) olivine back into melt inclusions. The resulting melt composition is assumed to be that of the primary melt that was extracted from the mantle/plume-head source. The equilibrium Fo for this melt must therefore be equal to that of the source (Fo = 90-92, e.g. Sobolev *et al.*, 2005, Herzberg, 2011). The equilibrium Fo of the source is thus guessed. This guess can by comforted by making it equal to the maximum Fo olivine observed in the sample or in the province where the samples came from. The Fo of both the Deccan (Thakurvadi formation, Fo ~ 80-86) and Réunion Island (Piton de la Fournaise, Fo ~ 81-86) samples is too low to be in equilibrium with a mantle source (e.g. Herzberg, 2011). It entails that 1) the picritic samples analysed during this PhD are fractionated and 2) this fractionation took place in the olivine stability field (bulk rock MgO > 7wt%, Figure 5.4) and hence simple back-fractionation to higher equilibrium Fo is still possible even though the maximum equilibrium Fo (Fo_{max}), which is that of the source, is unknown (but lies within Fo ~ 91 ±1). The calculations of section 7.1 assume Fo_{max} (Deccan) = 91 and Fo_{max} (Réunion) = 90.5 based on the highest Fo olivine reported in the literature for lava samples from the Deccan Traps (Fo = 91: Krishnamurthy *et al.*, 2000) and Réunion Island (Fo = 90.5: Sobolev & Nikogosian, 1994). If these estimates were incorrect, to uncertainty on magmatic temperature resulting from a Fo range of Fo = 91±1 is ±40°C. Combined with the possible range of FeO* the total uncertainty on temperature in the reconstruction of the primary melt composition by re-equilibration and back-fractionation of melt inclusions is in the order of ±60°C. The consequence of this temperature range on the composition of the primary melts is ±4% Mg#. The full range of possible primary melt compositions is presented in Table 7–1.

7.3.1.5. Melt decompression and temperature correction

The temperature and equilibrium olivine Fo of the primary melt reconstructed upon re-equilibration and back-fractionation of melt inclusions is valid only for shallow depth, where the cumulate they were extracted from crystallised (Ford *et al.*, 1983). The evolution of this primary melt between the magma chamber and the source need to be reconstructed in order to characterize the temperature of the mantle source, Tp (section 7.2.1). Melt transport from the mantle through the lithosphere to the upper crust is believed to take place in dunite or pyroxenite channels in the sub-lithospheric mantle (Kelemen *et al.*, 1995, 1997, Batanova *et al.*, 2011) and in cracks (dykes) in the rigid lithosphere (Marsh, 2007, Maimon *et al.*, 2012).

Nevertheless, these processes are swift enough to leave no record of the occurrence behind so that the actual path followed by the primary melts from their source to the crustal magma chambers where olivine cumulates crystallised cannot be known with absolute certainty. The hypothesis upon which the calculation of potential temperature hinges in the modelling presented above (section 7.2) is shown on Figure 7.16.

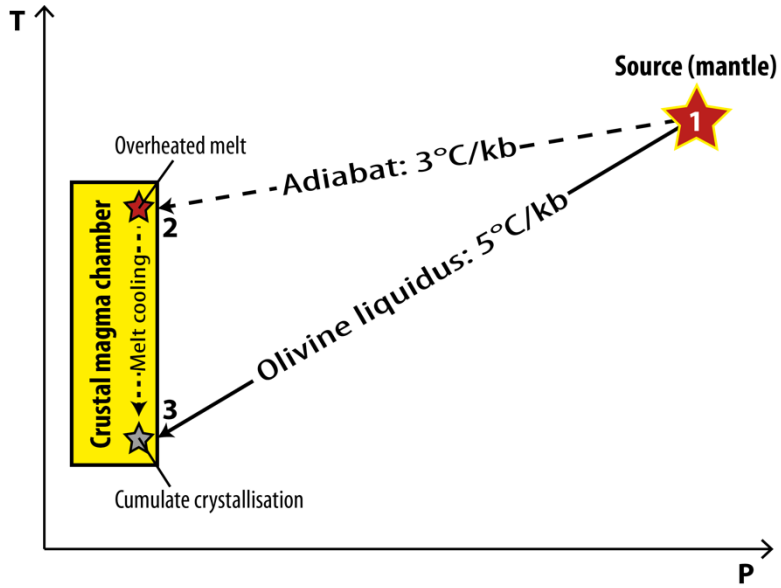

Figure 7.16 – Hypothesis on the temperature evolution of the primary melts upon ascent from their source through the lithosphere towards the crustal magma chambers wherein the analysed olivine cumulates are assumed to have crystallized. 1) Primary melts are extracted from their source at high pressure (lithosphere-asthenosphere boundary) and temperature (potential temperature, Tp). During transport in the lithosphere, melts will be decompressed and cooled. Two different paths can be taken: 2) The primary melt can follow an adiabatic path along which it will cool by ~3°C/kb and arrive in the crustal magma chamber in an overheated state. In this scenario, the overheated melt will cool until it reaches the olivine liquidus and olivine cumulates will begin to crystallise. 3) The primary melt follows the olivine liquidus at about 5°C/kb. In this case, fractionation in the olivine stability field can occur during the ascent of the melt through the lithosphere. The cumulate composition will thus be more evolved than that of the original primary melt and needs to be back-fractionated to a composition in equilibrium with its source. Based on Ford et al (1983).

According to Figure 7.16, once it has been extracted from its source, a primary melt can either be transferred via an adiabatic process or follow the olivine liquidus. If it follows an adiabat (~3°C/kb), the primary melt will arrive overheated (i.e. significantly hotter than the olivine liquidus) in the crustal chamber. Once the melt liquidus is reached, olivine cumulates will crystallize. The Fo content of these olivines will be high and close to the source equilibrium Fo. On the other hand, if the extracted melt exchanges some amount of heat with the surrounding rocks during ascent, it can follow a trajectory below the olivine liquidus (~5°C/kb) and olivine fractionation – although limited – will take place during melt transport.

Therefore, the composition of the melt that subsequently enters the crustal chamber will be further away from the source equilibrium composition. In order for this composition to be reconstructed, back-fractionation to mantle source equilibrium olivine (Fo_{max}) is required. The maximum Fo reported in the melt inclusion host olivines from the Deccan Traps (Thakurvadi formation) and Réunion (Piton de la Fournaise) analysed during this PhD is ~86, which is lower than mantle olivines (Fo90-92: e.g. Herzberg & O'Hara, 2002, Herzberg, 2011). It is thus clear that the primary melt was fractionated in the olivine stability field upon ascent and that the decompression from the source to the crustal chamber was not adiabatic. The actual evolution of a primary melt from its source to the crystallisation of olivine cumulates remains unknown. Nevertheless, most of the olivine fractionation generally occurs in crustal magma chambers as cumulate and allows for high-Fo olivines to be preserved. Occasionally, little fractionation occurs before cumulate formation and results in olivine close to mantle Fo contents being preserved, e.g. Fo90.5 have been reported at Piton des Neiges, Réunion Island (Sobolev & Nikogosian, 1994).

7.3.1.6. Trace element concentrations in primary melts

The concentrations of trace elements in reconstructed primary melts were not measured in olivine-hosted melt inclusions because ppm-level concentrations or rare-earth elements in micrometre-sized glassy inclusions are not accessible to EPMA analysis. Instead, primary melts trace element compositions have been calculated from bulk-rock trace element concentrations measured by Inductively Coupled Plasma Mass Spectrometer (ICP-MS) and from the evolution of EPMA-measured minor elements that behave similarly to trace elements during back fractionation, i.e. Ti and Al. This method is uncertain for two main reasons: 1) Ti and Al and merely proxies. Trace element concentrations in melt inclusions can be measured and directly integrated to the back-fractionation calculations. 2) Deccan Traps magmas are known for (Peng *et al.*, 1994, Sen, 2001, Chatterjee & Bhattacharji, 2008, e.g. Bhattacharya *et al.*, 2013) and were described above (section 5) as bearing signs of crustal contamination, which significantly affect trace element patterns (DePaolo, 1981). The issue was partly circumvented by using only a limited set of trace elements that are less subject to contamination-induced variations. Nevertheless, crustal contamination effects cannot be ruled out and indeed, one may notice for instance that a slight negative Nb anomaly still exists in the Deccan Traps reconstructed primary melt trace element pattern (Figure 7.5). Since this

particular trace element pattern is used in the application of the geochemical model of Sobolev et al (2005, 2007), potential crustal assimilation effects will have consequences on the melt fractions and potential temperatures returned by the model.

7.3.2. Source modelling

The geochemical model of Sobolev et al (2005, 2007) consists in a fit of a primary melt composition that is recalculated from olivine melt inclusions (section 7.1.2) and bulk-rock compositions (section 7.1.3), by a modelled primary melt composition that results from the melting, reaction and mixing of three lithologies: eclogite, reaction pyroxenite and peridotite (section 7.2.1). The main parameters of this model are given in Table 7–11a and Table 7–11b for the coupling with the hydrous melting model of Katz et al (2003). The following observations are proposed:

Only two parameters are directly measured: the pyroxenitic component Xpx and the magmatic temperature at which the olivines of the sample crystallized. The variables used in fitting the reconstructed primary melt composition are the melt fractions of each of the three lithologies: eclogite (Fe), pyroxenite (Fpx) and peridotite (Fpe) (underlined in Table 7–11a and b). The other parameters of the model are averages: the composition of the mantle (peridotite), of the recycled component (eclogite) and their mineral modes. For example, the composition of the mantle could change between the early stage of a mantle plume and its final tail stage by involving progressively more depleted mantle components (White & McKenzie, 1995). This possibility is seen in the second stage of modelling (section 7.2.3.2) using the hydrous melting approach of Katz et al (2003) wherein the Réunion Island (Piton de la Fournaise) case is better described by low, DMM-like mantle water contents. Alternatively, the composition of the recycled component can be affected to various degrees by subduction processes (Dixon *et al.*, 2002, Tatsumi & Hanyu, 2003), average crustal compositions (White & Klein, 2014) or even by metasomatism in the deep mantle (e.g. Foley *et al.*, 2013, and references therein). These parameters will have considerable implication on the final trace element pattern generated by the model. The amount of eclogite melt required to transform peridotite into pyroxenite (Xe) is reasonably well constrained from experiments (Yasuda *et al.*, 1994, Yaxley, 2000, Wang & Gaetani, 2008) but the mineral modes of all three lithologies can be different, particularly the amount of garnet, which strongly modifies the trace element patterns. In the same way, the ranges coefficients given by Sobolev et al (2005) for

calculating the mineral modes in the reaction pyroxenite from those of the original peridotite have sufficiently loose bounds to significantly affect the final trace element signatures. Finally, this model is essentially a melting and mixing model and hence depends greatly on proper estimations of mineral-melt trace element partition coefficients (Table 7–6) and rock melting modes (Table 7–5). Rare Earths partition coefficients are known to depend on mineral chemistry, pressure and temperature (Sun & Liang, 2013). Mineral and melting modes are also expected to vary with at least pressure and temperature (e.g. Walter, 1998). In the end, it is clear that finding the appropriate partition coefficients and compositions for the starting lithologies is the most crucial stage in the application of a model such as that of Sobolev et al (2005, 2007).

Some of the observations exposed above are currently being tested yet full integration of the model sensitivities into the modelling framework by means of e.g. Monte Carlo simulations, was not attempted due to lack of time.

Table 7–11 – Variables and their dependence in A) the model of Sobolev et al (2005, 2007) and B) the coupling of the hydrous mantle melting model of Katz et al (2003). Abbreviations:

- Pe compo, m pe, Fpe: chemical composition of mantle peridotite, mineral modes and melt fraction, respectively
- OC: composition of the average oceanic crust
- m e, Xe, Fe: eclogite mineral modes, fraction of eclogite melt reacting with peridotite to form pyroxenite, eclogite melt fraction, respectively
- m px, Fpx, Xpx: pyroxenite mineral modes, melt fraction and melt fraction involved in the primary melts
- XRC: amount of eclogite (recycled component) in the plume head
- Tot melt: total melt fraction of the hybrid (peridotite + pyroxenite + eclogite restite)
- P: source pressure
- T: magmatic temperature in crustal magma chamber
- Tp: potential temperature of the source

A) Sobolev et al (2005, 2007)

Variables			*Dependencies*													
			Pe Compo	m pe	Fpe	OC	m e	Xe	Fe	m px	Fpx	**Xpx**	XRC	Tot melt	P	**T**	Tp
	Peridotite	Pe Compo	Var														
		m Pe		Var													
		Fpe			Var												
	Eclogite	OC compo				Var											
		m e					Var										
		Xe		+				Calc									
		Fe							Var								
	Pyroxenite	m px						+		Calc							
		Fpx									Var						
		Xpx										**Measured**					
		XRC			+			+	+		+	+	Calc				
		Tot melt			+						+		+	Calc			
		P													Var		
		T														**Measured**	
		Tp												+	+	+	Calc

B) Katz et al (2003)

			Dependencies										
			Fpe	H_2O_{mantle}	Xe	Fe	Fpx	**Xpx**	XRC	Tot melt	P	**T**	Tp
Variables	Peridotite	Fpe	Calc										
		H_2O_{mantle}		Var									
	Eclogite	Xe			Var								
		Fe				Var							
	Pyroxenite	Fpx					Var						
		Xpx						**Measured**					
		XRC	+		+	+	+	+	Calc				
		Melt%	+				+		+	Calc			
		P									Var		
		T										**Measured**	
		Tp								+	+	+	Calc

7.3.2.1. Partition coefficient variations

The partitioning of elements between minerals and melts varies with temperature, pressure and chemistry (e.g. Sun & Liang, 2013). The effect of partition coefficient variations on the trace element pattern generated by the geochemical model of Figure 7.7 (section 7.2.2) was assessed using a compilation of partition coefficients for Th, Nb, La, Ce, Nd, Sm, Gd, Dy, Er and Yb in mafic lithologies from the Geochemical Earth Reference Model (GERM) database. The behaviour of trace elements during melting is mainly controlled by garnet and clinopyroxene (Table 7–6) and hence the trace element compilation from GERM only includes these two phases (Figure 7.17).

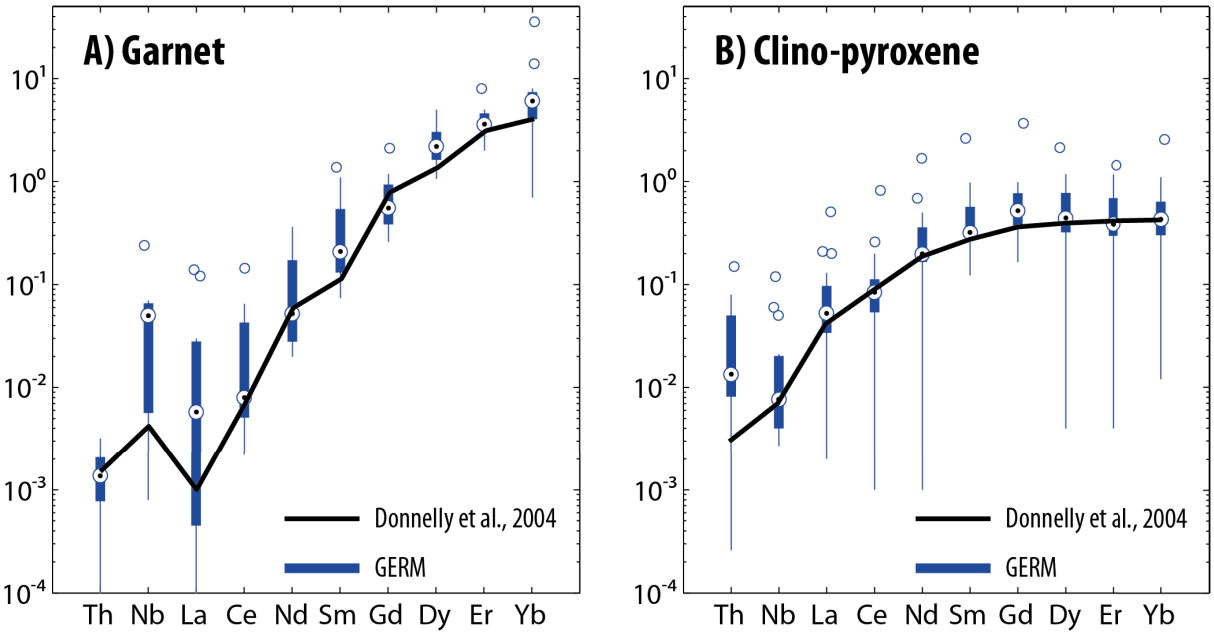

Figure 7.17 – Comparison of the partition coefficients from Donnelly et al (2004) as used in Table 7–6 with a compilation of partitioning coefficients from mafic lithologies and experiments from the Geochemical Earth Reference Model (GERM) represented as a boxplot: black and white dot, median; blue rectangle, inter-quartile; whiskers (blue line), 1th and 99th percentile; blue circles, outliers.

The dataset corresponding to Figure 7.17 is summarized in Table 7–12

Table 7–12 - Partition coefficients for garnet and clinopyroxene from Donnelly et al (2004) as in the application of the geochemical model of Sobolev et al (2005) of section 7.2.2 of the manuscript and a compilation from the Geochemical Earth Reference Model (GERM): compilation of partition coefficients for mafic rock and experiments summarized by statistical indexes: 25th percentile, average, median and 75th percentile

	Donnelly et al 2004	GERM			
Garnet		25th percentile	Average.	Median	75th percentile
Th	1.50E-03	1.00E-03	1.47E-03	1.37E-03	1.70E-03
Nb	4.20E-03	7.10E-03	6.13E-02	5.00E-02	6.19E-02
La	1.00E-03	4.75E-04	2.90E-02	5.80E-03	2.70E-02
Ce	7.00E-03	5.10E-03	2.85E-02	8.00E-03	4.00E-02
Nd	6.00E-02	2.98E-02	1.06E-01	5.20E-02	1.44E-01
Sm	1.15E-01	1.33E-01	3.69E-01	2.09E-01	4.93E-01
Gd	8.00E-01	4.23E-01	7.63E-01	5.54E-01	8.08E-01
Dy	1.40E+00	1.63E+00	2.42E+00	2.20E+00	2.88E+00
Er	3.20E+00	3.48E+00	4.10E+00	3.60E+00	4.47E+00
Yb	4.18E+00	4.05E+00	7.23E+00	6.07E+00	7.36E+00

	Donnelly et al 2004	GERM			
Cpx		25th percentile	Average.	Median	75th percentile
Th	3.00E-03	8.73E-03	3.48E-02	1.35E-02	4.50E-02
Nb	7.00E-03	4.00E-03	2.05E-02	7.70E-03	2.00E-02
La	4.20E-02	3.40E-02	8.46E-02	5.26E-02	9.29E-02
Ce	9.00E-02	5.70E-02	1.14E-01	8.43E-02	1.08E-01
Nd	1.90E-01	1.68E-01	2.95E-01	1.99E-01	3.45E-01
Sm	2.80E-01	2.82E-01	4.74E-01	3.20E-01	5.39E-01
Gd	3.70E-01	3.73E-01	7.10E-01	5.21E-01	7.55E-01
Dy	4.02E-01	3.24E-01	5.93E-01	4.42E-01	7.74E-01
Er	4.22E-01	2.99E-01	5.17E-01	3.87E-01	6.80E-01
Yb	4.32E-01	3.11E-01	5.81E-01	4.31E-01	6.35E-01

This basic assessment of partitioning-induced sensitivity was carried out by simply changing the original coefficients used in the geochemical model (Table 7–6) from those of Donnelly et al (2004) to extreme cases based on the compilation from GERM. The 25th and 75th percentiles of the GERM compilation (Table 7–12) were considered to be sufficiently further apart to constitute an upper and lower bound of possible mineral/melt partitioning in mantle sources. All other model parameters were unchanged and similar to the simulation of Figure 7.7, including the melt fractions of eclogite (Fe), pyroxenite (Fpx) and peridotite (Fpe).

Figure 7.18 presents the effect of such mineral/melt partitioning variations

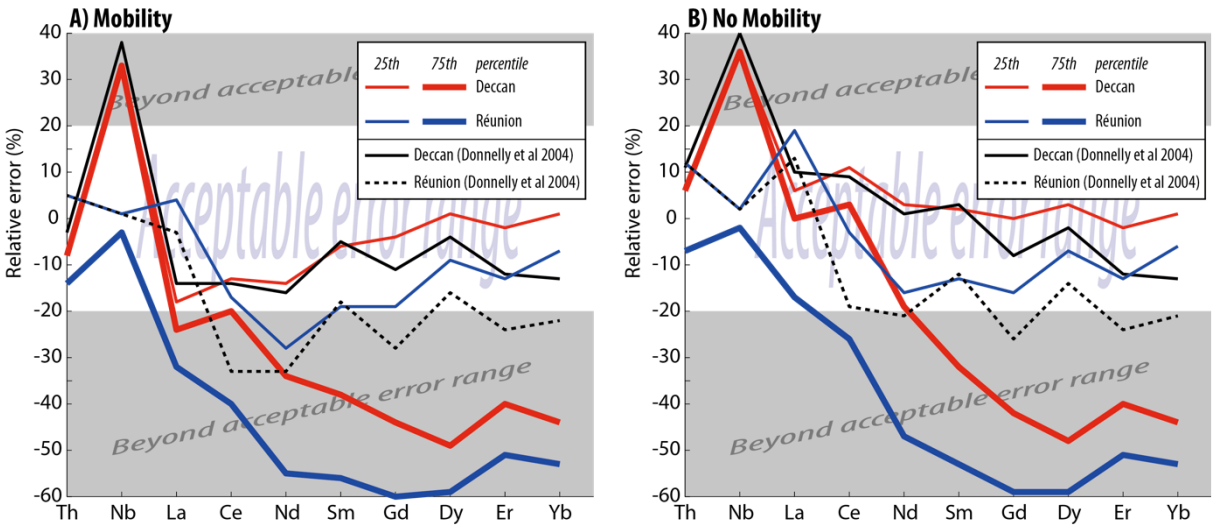

Figure 7.18 - Consequences of partitioning coefficients modification in the application of the geochemical model of Sobolev et al (2005) of section 7.2.2: the minimization of the melt fractions of eclogite, pyroxenite and peridotite where done using the partitioning coefficients of Donnelly et al (2004). The coefficients have then been changed to correspond to the 25th and 75th percentile of the partition coefficient compilation from the Geochemical Earth Reference Model (Table 7–12) and the relative error is reported in the figure for two scenarios: A) mobility coefficients of Katz et al (2003) are applied to the oceanic crust –eclogite transition B) the composition of the eclogite is equal to that of the oceanic crust.

Changes in trace element partitioning mostly affects elements heavier than Nd and the effect on incompatible elements is less significant, as one may expect for low-degree melts (< 20%) of garnet-bearing source.

The patterns corresponding to the 25th percentile of the GERM compilation allows for Réunion Island primary melts to be reproduced within the acceptable error range of ±20% (Sobolev *et al.*, 2005), except for Nd in the *mobility* case (Figure 7.18a).

It is reasonable to argue that lower partition coefficients are more likely to apply to high-temperature sources such as those of Réunion Island and Deccan Traps magmas. In this case, the difference between the coefficients originally used in the model (Donnelly *et al.*, 2004) and those corresponding to the 25th percentile of the GERM compilation suggest that the

geochemical modelling results (Table 7–9) are fairly robust. Nevertheless, Figure 7.18 also suggests that higher partitioning coefficients strongly affect the model generated trace element patterns, to the point of being way beyond tolerable error.

7.3.2.2. Effects of primitive versus depleted composition of the mantle

A further simple sensitivity test of the geochemical model (section 7.2.2) consists in evaluating the consequences of mantle peridotite depletion on the trace element patterns of Figure 7.7. This was carried out much in the same way as the previous section with partitioning coefficients (section 7.3.2.1). In other words, all parameters of the model are preserved, including partitioning coefficients (Donnelly *et al.*, 2004) and the melt fractions of eclogite (Fe), pyroxenite (Fpx) and peridotite (Fpe). The varying parameter is this time the composition of the original peridotite of the model (Table 7–4). Figure 7.7 uses a peridotite made of 80% primitive mantle (Hofmann, 1988) and 20% Depleted MORB Mantle (Workman & Hart, 2005). Figure 7.19 shows the effect of changing the initial peridotite composition from the above-mentioned to 100% primitive mantle or 100% depleted mantle.

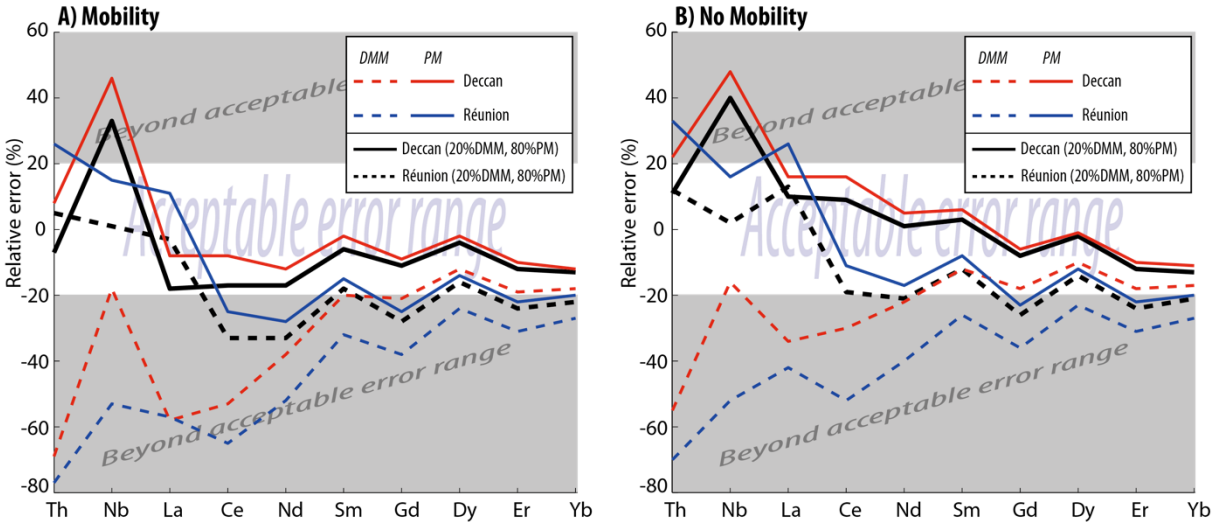

Figure 7.19 - Consequences of mantle peridotite composition on the output of the geochemical model of Sobolev et al (2005) of Figure 7.7: the minimization of the melt fractions of eclogite, pyroxenite and peridotite where done using a mantle peridotite made of 20% Depleted MORB Mantle (DMM) and 80% Primitive Mantle (PM). Mantle peridotite compositions have been changed to 100% DMM or 100% PM and the relative error is reported in the figure for two scenarios: A) mobility coefficients of Katz et al (2003) are applied to the oceanic crust –eclogite transition B) the composition of the eclogite is equal to that of the oceanic crust.

Figure 7.19 shows that most of the effect of involving preferentially primitive and depleted mantle translates into incompatible trace element variations, as anyone would expect. The

model-generated trace element patterns better describe the calculated primary melts when the contribution of primitive mantle in large or exclusive. Nevertheless, if a depleted MORB mantle component happened to be involved at more than 20% at any locality, the incompatible trace element patterns of the model would easily reach beyond the acceptable error range of ±20% (Sobolev *et al.*, 2005). Fortunately, significant (e.g. > 20%) involvement of depleted MORB mantle is unlikely for both the Deccan Traps (Sen, 2001, and references therein) and Réuion Island (e.g. Füri *et al.*, 2011).

8. Conclusion chapter

8.1. General conclusions

This PhD brings new insights as to the emplacement of the Deccan Traps at the K-Pg boundary and the evolution through time of the Deccan Plume, between its early (plume head) stage beneath India and its present-day (plume tail) stage, at Réunion Island in the Indian Ocean.

Based on previous work by Anne-Lise Chenet and colleagues, it has been consistently shown that the eruption of the Deccan Traps at the Cretaceous-Palaeogene transition was fast and that a paroxysmal volcanic event ends at the K-Pg boundary.
Chenet and colleagues brought exceptional constrains as to the duration and dynamics of the emplacement of the Deccan Traps. First, Chenet et al (2007) identified three main phases of volcanism based on ^{40}K-^{40}Ar radiometric dating: Phase 1 predates the K-Pg boundary by about 2Ma, Phase 2 occurred just before and ended at the K-Pg boundary (Keller *et al.*, 2012) and Phase 3 happened ~2-300ka later in the Danian and therefore post-dates the K-Pg boundary. Secondly, Chenet et al (2008, 2009) used paleomagnetism on a comprehensive sample set of the entire Western Ghats section and were able to identify Directional Groups corresponding to sequences of lavas with statistically similar magnetic orientations, implying that any of these sequences must have been emplaced in a century or less. Chenet et al identified 30 Directional Groups (or Single Eruptive Events) and 41 lava flows unrelated to directional groups, suggesting a total eruption time of 300 to 3000 years for the Directional Groups alone and 1000 to 7000 years for all the formations of the Western Ghats. Very fast eruption rates have recently been independently confirmed from diffusion/relaxation modelling of $^{87}Sr/^{86}Sr$ zoning in giant plagioclase phenocrysts (A few hundred years for the emplacement of entire formations, Borges *et al.*, 2013). Chenet et al thus argued that quantifying the intervening quiescence time within the eruption sequence was the most critical issue in order for the rates, total duration and environmental effects of the Deccan Traps eruption to be fully understood. Chenet et al (2008) and Gérard et al (2006) attempted to quantify the span of volcanic quiescence periods along the Western Ghats section from the occurrence and extent of intertrappean weathered horizons (red boles or bole beds, Sayyed, 2013). Upon assuming that centimetre-thick red boles formed over 10 years while meter-thick did so over 50,000 years, Chenet et al proposed that the 38 thin- and 6 thick-red boles

reported in the Western Ghats implied a total cumulated volcanic quiescence time of 300,000 years.

The extensive work of Chenet and colleagues has been re-interpreted in order to implement a continuous timeframe of the Western Ghats section (Figure 3.1) that could be compared with paleoenvironmental data (Figure 3.2) and coupled to bulk-rock geochemistry (Figure 5.7). Considering the uncertainties on volcanic quiescence (section 3.6.3) and magmatic degassing processes (Self *et al.*, 2006, Sobolev *et al.*, 2011) the continuous eruption timeframe of the Western Ghats shows good correlation with intermediate water paleotemperatures (Li & Keller, 1998) and recent high-resolution $^{187}Os/^{188}Os$ records in pelagic carbonates (Robinson *et al.*, 2009). It is thus argued that phase 2 of the Deccan Traps emplacement (Chenet *et al.*, 2007) corresponds to a cataclysmic volcanic event corresponding to the eruption of ~ $8.10^5 km^3$ of lavas in ~ 50ka. The average eruption rate during this event would have been close to $20km^3/yr$ (~ 200 times present-day Hawaii, Courtillot *et al.*, 1986) and occasionally skyrocketing to $160km^3/yr$ (Chenet *et al.*, 2009). This catastrophic event is well correlated with at least the late-Cretaceous cooling as well as both of the strong $^{187}Os/^{188}Os$ negative anomalies reported by Robinson et al (2009). Furthermore, it clearly appears that phase 2 (Chenet *et al.*, 2007) ends with the Poladpur formation (onset of the Wai sub-group) at the K-Pg boundary (Keller *et al.*, 2012) and is followed by significant volcanic quiescence periods, suggested by the occurrences of thick red boles between phase 2 and 3. The occurrence of 6 thick red boles in Ambenali-Mahabaleshwar implies 300ka of volcanic quiescence before the onset of phase 3 in Mahabaleshwar. Interestingly, this estimate of 300ka is similar to those proposed on the basis of radiometric dating (Chenet *et al.*, 2007) and paleontological observations (biozone P1a, Keller *et al.*, 2012). It is also speculated that the formation of thick red boles could have been favoured by a wetter and cooler climate as a result of a volcanically induced late-Cretaceous cooling (Figure 3.2 and section 1.3).

The continuous timeframe of the Western Ghats eruption (section 3.6.1) has been coupled with the bulk-rock major and trace element dataset of Bonnefoy (2005). Two different incompatible trace element signatures have been identified along the Western Ghats section. Deccan1 corresponds mostly to the lower formations (Jawhar to Bushe) and features clear evidence of strong crustal assimilation whereas Deccan2 (Wai subgroup: Poladpur to Mahabaleshwar) shows less or no evidence of crustal contamination and a more evolved and homogeneous composition than Deccan1. The transition between Deccan1 and Deccan2 takes

place during the emplacement of Poladpur and is therefore correlated with the end of phase 2 (Chenet *et al.*, 2007).

The average trace element signature of both Deccan1 and Deccan2 is indicative of deep, garnet bearing sources ($Gd/Yb_n > 1.6$, Figure 5.6), which is at odd with the widespread and significant plume induced lithospheric erosion postulated for LIPs emplacement (Sobolev *et al.*, 2011). Nevertheless, Deccan1 features four transient Gd/Yb_n and Nb/La_n excursions in lower- and upper-Jawhar, Khandala-Bushe and upper-Poladpur compatible with suddenly shallower ($Gd/Yb_n < 1.8$) sources and heavily contaminated melts ($Nb/La_n \sim 0.5$) (Figure 5.7). The fleeting character of these excursions is confirmed by their systematic association with directional groups thereby suggesting that these compositional excursions did not last for more than a few hundred years. It is argued that transient excursions of both low Gd/Yb_n and low Nb/La_n correspond to a localized, plume-induced lithospheric thinning event. The sudden onset of erosional pathways in the Indian lithosphere would lead to extensive decompression melting ($Gd/Yb_n < 1.8$) and large crustal assimilation ($Nb/La_n < 0.6$) caused by the Deccan plume being locally brought close to the crust. The erosional pathways would subsequently become clogged by large amounts of light peridotite restite, causing melts to be again released in the garnet stability field (Gd/Yb_n). Crustal contamination would drop as a result of the previous extensive assimilation. In other words, the magmatic conduits would probably become too refractory for large crustal assimilation to happen. The four excursions reported in Jawhar, Khandala-Bushe and Poladpur altogether span ~ 50ka, which is compatible with the model-based estimation of Sobolev et al (2011). The localized lithospheric erosion in both space and time is also compatible with what Sobolev and colleagues expected for lithospheric thicknesses in the order of 140km (in agreement with the Indian case, section 2.4). It is also compatible with the location of the feeder dykes of the Deccan Traps (Vanderkluysen *et al.*, 2011), Figure 2.3. In addition, it seems reasonable to argue that severe crustal assimilation results in severe magma degassing (Self *et al.*, 2008a, Ganino & Arndt, 2009, Sobolev *et al.*, 2011). All four Gd/Yb_n and Nb/La_n transient negative excursions occurred during phase 2, which ended at the K-Pg boundary. It is thus likely that catastrophic amounts of magmatic gasses were released on these occasions and contributed to the end-Cretaceous extinction.

High-MgO, olivine-phyric samples from the Deccan Traps and Réunion Island have been investigated in order to reconstruct the primary melts and magmatic sources for both localities

– themselves representative of the (early) plume-head and (final) plume-tail stage of the Deccan plume.

High-forsterite olivines (>80) from the Thakurvadi formation of the Deccan Traps, and Piton des Neiges and Piton de la Fournaise (Réunion Island) were processed for high-precision EPMA analysis olivine phenocrysts as well as olivine-hosted melt and spinel inclusions.
The olivine phenocrysts composition from the Deccan Traps and Réunion Island revealed Ni excess and Mn deficiency corresponding to a hybrid mantle source (pyroxenite + peridotite , Sobolev *et al.*, 2005) (Figure 6.3) and with a large contribution of pyroxenite melts to the primary melt compositions: Xpx (Deccan) = 65%, Xpx (Réunion) = 50% (Figure 6.5).
Olivine-hosted melt inclusions from Deccan Traps lavas recorded volatile contents similar to those published by Self et al (2008a) (averages: K_2O = 0.48wt%, Cl = 0.02wt%, S = 0.05wt%) yet much lower in chlorine than the Siberian Traps (Sobolev *et al.*, 2009a). It is however likely that the amount and rate of magmatic degassing were much higher during (or just before: Sobolev *et al.*, 2011) the episodes of strong crustal contamination mentioned earlier (transient Gd/Yb_n and Nb/La_n negative excursions, Figure 5.7). Olivine-hosted melt inclusions from Réunion Island revealed slightly different volatile contents (averages: K_2O = 0.70wt%, Cl = 0.02wt%, S = 0.09wt%). Most notably, Cl/K_2O of Réunion Island inclusions was significantly lower than for the Thakurvadi melt inclusions (Cl/K_2O = 0.30 and 0.40, respectively. But Cl/K_2O is twice higher in Deccan Traps than in Réunion Island olivine-hosted inclusions at a given S content, Figure 6.7b), suggesting slightly different compositions of the magmas either due to crustal assimilation (Figure 5.7) or due to the larger amounts of pyroxenite-derived melts involved in the primary melts of the Deccan Traps lavas (the recycled crustal component could be responsible for chlorine enrichment: Sobolev *et al.*, 2009a, 2011).

Olivine-hosted melt and spinel inclusions have been used to reconstitute the primary melts of the Deccan Traps and Réunion Island lavas (section 7.1). This result has subsequently been integrated into a modelling framework based on geochemistry (Sobolev *et al.*, 2005) and thermodynamics (Katz *et al.*, 2003) allowing for reconstructing the temperature, pressure and composition of the mantle sources of Réunion Island and Deccan Traps lavas (section 7.2). Modelling results revealed clear changes between the plume-head (Deccan Trap) and the plume-tail (Réunion Island) stage of the Deccan plume.

During the emplacement of the Deccan Traps, the Deccan plume was hot (Tp ~ 1590-1600°C) and carried large amounts of recycled crustal material (XRC ~ 14%) compared with other settings (Sobolev *et al.*, 2007). The large recycled component of the Deccan plume at this time precludes significant surface uplift (Sobolev *et al.*, 2011) and thus reconciles the observations of several authors with the plume model (e.g. Saunders *et al.*, 2007, Sheth, 2007). The hybrid source (eclogite + reaction pyroxenite + peridotite) in the plume melted at 4.5GPa by about 12% with a contribution of pyroxenite melts at 65% (Table 7–9). The strong garnet signature of most Deccan Traps lavas (Figure 5.6) suggests that the Indian lithosphere was little affected by plume-related magmatism and thus remained thick throughout the plume-head stage of the Deccan Plume. This feature is most directly explained by 1) the initially deep lithosphere-asthenosphere boundary (140km, section 2.4) and 2) by the limited involvement of magmas in the lithosphere erosion process due to their early escape (before freezing and delamination) towards the surface (Sobolev *et al.*, 2011), probably facilitated by pre-existing weaknesses within the Indian lithosphere itself (e.g. Murthy, 2002).
Some 66Ma later, the Deccan plume remains active beneath Réunion Island in the Indian Ocean. It is now cooler by about 100±50°C (Tp ~ 1490-1500°C) and therefore carries less recycled crustal material (XRC ~ 7%) than at its younger state in the Deccan Traps. The mantle source of Réunion Island lavas is argued to melt by 4% at 3.5 GPa with a contribution of pyroxenite melts at 50% (Table 7–9).

Figure 8.1, is an illustration of speculated plume-lithosphere interactions for the Deccan plume during the Deccan Traps eruption and at present-day Réunion Island. A comparison with the Siberian plume is also included.

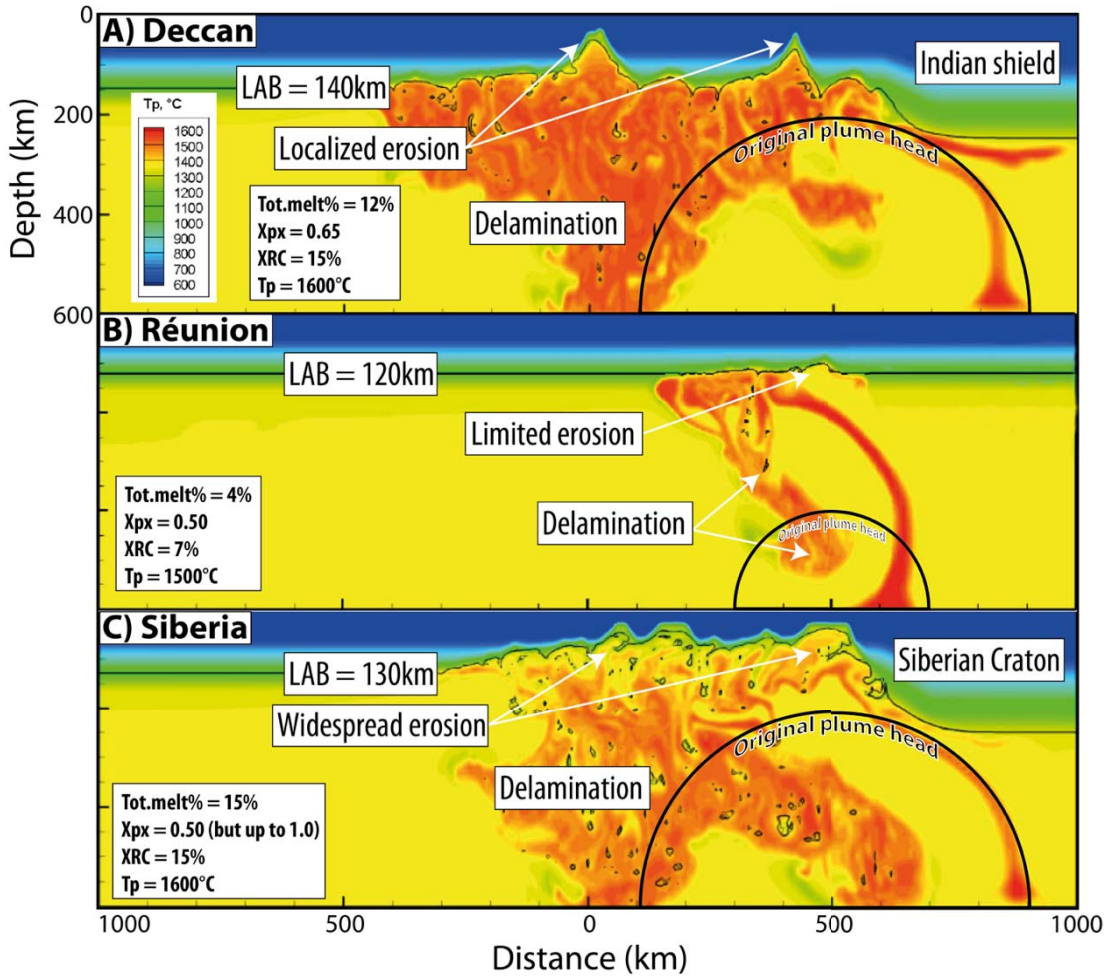

Figure 8.1 – Schematic illustration of the plume-lithosphere interactions based on Sobolev et al (2011) for A) the Deccan Traps (plume-head stage of the Deccan plume), B) Réunion Island (plume-tail stage of the Deccan plume) and C) the Siberian Traps. Colorscale: potential temperature (°C). Model time of the snapshot: 1Myr. Note that this is not an actual simulation of the Deccan plume but a simple modification of a figure from Sobolev et al (2011). A proper thermomechanical model of the Deccan plume is being implemented by S.V. Sobolev at GFZ, Germany

8.2. Prospects

In the concluding paragraphs of her Ph.D, Anne-Lise Chenet (Chenet, 2006) suggested that the immediate prospects of her work be to address the following items:

- Confirm that the Deccan eruption took place in two separate phases by dating the transitional polarity samples of the Latifwadi plateau and investigating the Tapti River area where thick sections have not yet been accurately dated
- Re-sample the Khandala-Bushe and Bushe-Poladpur transitions since the poor outcrops of the Bushe formation did not allow for a fully comprehensive sampling during this project

- Investigate the lower formations, especially in the Narmada River/Rift area in order to better constrain the early phases of Deccan volcanism. However, the Narmada rift has been active post-Deccan making flow-to-flow correlations much more difficult than in the case of the Western Ghats
- Numerical models used in assessing the environmental consequences of the Deccan Traps should be tested on a global – planetary – scale and account for the chemistry and physics of the stratosphere
- Finally, comparing the Deccan Traps with the Karoo province (southeast Africa, 180Ma), where signs of a major extinction are absent despite similar erupted volumes

This new Ph.D project undertaken in January 2011 originally aimed at bringing together geochemistry, petrology and geodynamics in the implementation of a thermo-mechanical numerical model of the Deccan plume through time similar to Sobolev et al (2011). As such, this new project would have been able to address the first three items above-mentioned as part of a Ph.D. fieldwork and would have used the high-resolution paleomagnetic data of Anne-Lise Chenet's Ph.D. as time constraints for the entire main volcanic phase.
Nevertheless, difficulties in the early stages of this project mostly pertaining to the installation of a new JEOL JXA 8230 Electron Microprobe Analyser at ISTerre as well as to the unsuccessful quest for local contacts in India precluded the organisation of a proper field trip. However, full access, granted by Frédéric Fluteau and Vincent Courtillot at the Institut de Physique du Globe (IPGP, Paris, France), to the Western Ghats samples collected and used during Anne-Lise Chenet's PhD (Chenet, 2006), as well as their bulk-rock major and trace element compositional data (Bonnefoy, 2005) enabled us to participate in the study of the Deccan Traps by:

- Revisiting the high-resolution paleomagnetic data and $^{39}Ar/^{40}Ar$ ages of (Chenet, 2006, 2007, 2008, 2009) and reconstructing a continuous timing scenario for the emplacement of the Western Ghats that fits paleao-environmental indicators such as high-resolution $^{187}Os/^{188}Os$ record in pelagic carbonates (Robinson *et al.*, 2009) and global seawater temperatures (Li & Keller, 1998) (section 3.6)
- Coupling this timeframe with bulk-rock compositional variations, allowing for the depth of mantle sources and the assimilation of crustal material to be traced in time throughout the emplacement of the Western Ghats

- Carrying olivine petrology and source modelling (Sobolev *et al.*, 2005, 2007) olivine-phyric, picritic samples from both the Deccan Traps and Réunion Island in order to bring new insights as to the magma sources, their melting conditions, the primary melts generated, and the amounts of volatiles they carried
- Ultimately, the catastrophic eruption rates speculated upon interpretation of these data (70% of the Western Ghats formations in 50,000 years) and the clear correlations with paleoenvironmental proxies, lead the author to conclude that the emplacement of the Deccan Traps must have had cataclysmic consequences on the environment of the late-Cretaceous

The author hopes this manuscript still provides some degree of novelty and advancement to the community despite the extensive use and re-interpretation of published data and the absence of actual fieldwork.

This work would greatly benefit from addressing the following items:

- Fieldwork would allow addressing the first three items of Anne-Lise Chenet's proposed prospects (Chenet, 2006). It would also allow for more olivine-phyric samples to be collected both in the Main Deccan Province and in the peripheral areas of the Deccan Traps (e.g. Gujarat, section 2.3.2). A more coherent dataset would enable for far better constraints on the dynamics of the Deccan Plume
- More specifically, the transient Gd/Yb_n and Nb/La_n negative excursion (Figure 5.7) should be investigated on the field for olivine-phyric samples and olivine-hosted melt inclusions as they may represent periods of catastrophic degassing due to large crustal assimilation and extensive decompression melting
- Fieldwork should be carried out in the Seychelles as Bushe-like compositions have been reported there (Owen-Smith *et al.*, 2013) and may thus correspond to the culmination of the Deccan Traps activity, shortly pre-dating the K-Pg extinction
- The results of source modelling (as in section 7.2) should be implemented in the thermo-mechanical modelling framework of Sobolev et al (2011), in order for the Deccan plume to be compared with other settings, such as the Siberian Traps or the Ontong Java plateau.

9. Appendix

I. Stratigraphic nomenclature of the western Deccan basalt formations (Western Ghats) after Peng et al (1994)

Subgroup	Formation (Max. thickness)	Member or chemical type (CT)	$(^{87}Sr/^{86}Sr)t$	Avg. Mg#	TiO2%	Avg. Ba/Zr	Avg. Zr/Nb
Wai	Desur (100m)		0.7072-0.7080	48	1.6-1.9	1.2	11.4
	Panhala (>175m)		0.7046-0.7055	52	1.6-2.3	0.5	14.8
	Mahabaleshwar (280m)		0.7040-0.7055	47	2.5-4.3	0.5	11.4
	Ambenali (500m)	Ambenali CT	0.7038-0.7044	49	1.9-3.1	0.3	14.4
	Poladpur (375m)	Upper	0.7061-0.7083	52	1.8-2.3	0.4	12.7
		Lower	0.7053-0.7110	56	1.5-2.0	0.7	14
		Sambarkada		43	2.2-2.3	0.9	12.6
		Valvhan	0.7068	42	2.5-2.6	0.9	12.3
		Ambavne		45	2.0-2.1	0.4	14.0
Lonavala	Bushe (325m)	Pingalvadi		61	1.1-1.2	0.8	17.2
		Bushe CT	0.713-0.720	55	1.0-1.3	1.1	15.3
		Shingi Hill	0.718	49	1.3-1.4	2.0	16.2
		Hari	0.7078-0.7079	46	2.0-2.1	1.0	12.9
		Karla Picrite	0.7147	68	1.1-1.2	0.8	19.7
		Bhaja	0.712	58	1.3-1.5	0.6	18.2
	Khandala (140m)	Rajmachi	0.7102	44	2.1-2.5	1.2	14.6
		Khandala Phyric CT		41	2.4-2.8	1.3	13.6
		KA3	0.7107	49	1.7	3.1	12.9
		Madh		58	1.6	2.8	14.0
		Boyhare	0.7102	63	1.2-1.3	2.1	13.7
		KA2	0.7124	57	1.2	3.9	13.5
		Khandala Phyric CT	0.7077	41	2.5-2.8	1.3	13.6
		KA1	0.7094	61	1.0-1.1	1.8	15.4
		Dhak Dongar	0.7071-0.7072	40	2.9-3.1	1.0	13.1
		KCG	0.7098	48	1.4-1.6	1.5	18.7
		Monkey Hill GPB	0.7073	41	3.1-3.4	1.1	12.2
		Girvali GPB	0.7068-0.7074	45	2.8-3.1	0.8	12.1
Kalsubai	Bhimashankar (140m)	Bhimashankar CT	0.7067-0.7076	47	1.9-2.6	0.8	11.7
		Manchar GPB		42	2.9-3.1	0.5	13.2
	Thakurvadi (650m)	Thakurvadi CT	0.7073-0.7080	58	1.8-2.2	0.8	12.0
		Water Pipe Member	0.7099-0.7112	59/71	1.4-1.6/1.0-1.1	1.5/1.3	12.3/12.0
		Paten Basalt		58	1.0	1.3	15.2
		Thakurvadi CT	0.7067-0.7070	58	1.8-2.2	0.8	12.4
		Ashne	0.7068	62	2.0-2.1	1.2	9.6
		Thakurvadi CT	0.7080-0.7084	58	1.8-2.2	0.8	11.6
		Jammu Upper	0.7112	34	2.7	1.6	9.8
		Patti Middle	0.7099	46	2.2-2.3	1.5	8.4
		Lower Member	0.7066-0.7067	56	1.7-2.0	1.1	11.2
	Neral (100m)	Tunnel Five GPB	0.7082-0.7083	36	3.3-3.5	1.0	10.8
		Tembre Basalt		43	2.8-3.0	1.1	10.6
		Neral CT	0.7062-0.7073	62	1.5-1.7	1.2	12.3
		Ambivli Picrite	0.7104	67	1.4-1.5	1.7	18.6
	Igatpuri - Jawhar (>700m)	Kashele GPB	0.7102-0.7122	40	2.6-3.1	1.1	11.5
		Mg-rich Igatpuri		59	1.4-1.9	1.0	13.3
		Igatpuri phyric	0.7107-0.7124	49	1.9-2.2	1.1	14.3
		Thal Ghat GPB	0.7108	36	3.6	0.9	10.7
		HFS-poor Jawhar		51	1.3-1.6	1.5	13.0
		Plag. Phyric	0.7085	38	3.0	1.0	11.7
		Mg-rich Jawhar	0.7128	59	1.4-1.9	1.0	12.7
		Kasara phyric	0.7091	39	2.8-3.0	1.0	10.8

II. Conceptual timeframe for the emplacement of the Deccan Traps

Synthesis of the Western Ghats cross-section (sections 3.6 and 5.4). (Chenet et al., 2008, Chenet et al., 2009).

SEE (Single Eruptive Events) may be seen at the formation or field section level, which induces slightly different interpretations. "Deccan Group" refers to trace element classification. Conceptual timeframe (in Ma) based on the hypotheses explained in section 3.6. Gd/Yb_n: garnet signature, normalized to Hofmann (1988). Nb/Lan: crustal signature, normalized to Hofmann (1988). Blue sample names are for duplicates, red for missing bulk-rock data, underlined bold fonts for olivine-bearing samples. Light and dark grey lines highlight directional groups. K-Pg boundary (Renne et al., 2013) at MB22. Finally, the first two letters of sample names correspond to their section, the next two digit to the sampling site and the last two are for the drill core ID as several drill cores have been collected at each sampling site. For a graphical representation of this table, see Figure 5.7. Bulk-rock compositional data obtained at the SARM Nancy, France. Only two Giant Plagioclase Basalts were identified in the sample set among at least 5 such flows reported in the Deccan Traps (Sen, 2001, and references therein), section 3.4.

Sample *(Red boles)*	Formation	SEE (section)	SEE (formation)	Deccan Group	Magneto-stratigraphy	^{40}K-^{40}Ar age (Ma)	Timeframe (Ma)	Gd/Yb_n	Nb/La_n	Cumulative volume (%)
MB0203	Mahabalesh war (280m)			2		64.1 ± 0.9	65.779260	1.684	0.809	100
MB0407		DG_PA6		2			65.780260	1.785	0.791	99
MB0503		DG_PA6		2			65.780272	1.820	0.923	91
MB0608		DG_PA6		2			65.780285	1.802	0.924	91
MB0702 *(thin)*		DG_PA6		2	C29n		65.780297	1.833	0.910	91
MB0807 *(thin)*		DG_PA6		2			65.780320	1.812	0.897	91
MB1104 *(thin)*		DG PA6		2			65.780342	1.799	0.901	91
MB1202		DG_PA6		2			65.780365	1.808	0.873	91
MB1701 *(thin)*		DG_PA6		2			65.780377	1.880	0.870	91
MB0905 *(thin)*		DG_PA6		2			65.780400	1.849	0.879	91
MB2705				2	C29r / C29n		65.781410	1.890	0.797	91
WA0405		DG_WA2		2			65.782410	2.012	0.998	91
WA0306		DG_WA2		2			65.782510	1.992	1.034	90
MB2805		DG_PA5		2	C29r / C29n		65.783510	1.941	0.811	90
MB1005 *(thin)* *(thin)* *(thin)*		DG_PA5		2	C29r / C29n		65.783543	1.854	0.800	88
MB1811		DG_PA5		2	C29r / C29n		65.783607	1.868	0.773	88
MB1901		DG_PA5		2	C29r / C29n		65.783640	1.843	0.799	88
WA0708 *(thin)*				2			65.784640	1.866	0.913	88
WA0801				1			65.785650	2.046	0.759	87
WA0503				1			65.786650	2.038	0.732	87
WA0902 *(thin)*				1			65.787650	2.175	0.833	86
WA0607				2			65.788660	1.950	0.791	86
MB2901 *(thick)*				2			65.789660	1.987	0.807	85
MB3002	Ambenali (500m)	DG_PA4		2			65.839660	2.037	1.051	85
MB2009 *(thin)*		DG_PA4		2			65.839710	2.096	1.032	82
MB1407 *(thick)*		DG_PA4		2	C29r		65.839770	1.777	0.962	82
WA1001 *(thick)*				2			65.889770	1.966	0.956	82
WA1102				2			65.939770	2.018	0.990	81

Sample *(Red boles)*	Formation	SEE (section)	SEE (formation)	Deccan Group	Magneto-stratigraphy	^{40}K-^{40}Ar age (Ma)	Timeframe (Ma)	Gd/Yb_n	Nb/La_n	Cumulative volume (%)
(thick)										
MB1305				2			65.989770	1.842	0.992	80
MB1601				2			65.990770	1.891	0.955	80
(thin)										
MB1505				2			65.991780	1.871	0.884	79
WA0104		DG_WA1	DG AM1	2		64.6 ± 0.9	65.992780	1.876	0.949	79
(thin)										
WA0205		DG_WA1	DG AM1	2			65.992840	1.891	0.914	78
MB2105			DG AM1	2			65.992890	1.826	0.917	78
(thick)										
(thin)										
MB2309		DG_PA3		2			66.042900	1.749	0.871	78
MB2606		DG_PA3		2			66.042950	1.776	0.876	76
MB2208		DG_PA3		2		64.8 ± 0.9	**66.043000**	1.810	0.851	76
(thin)										
(thick)										
(thin)										
PA0105				2			66.093020	1.920	0.904	76
PA0208				2	C29r		66.094020	1.934	0.964	75
(thin)										
PA0309				2			66.095030	1.912	0.856	75
(thin)										
PA1005				2			66.096040	1.979	0.907	74
(thin)										
(thin)										
PA1104				2			66.097060	1.896	0.891	74
(thin)										
PA0804				2			66.098070	1.895	0.893	73
(thin)										
PA0905				2			66.099080	1.918	0.852	73
(thin)										
PA19				2			66.100090	1.906	0.892	72
(thin)										
(thin)										
PA1804	Poladpur (375m)	DG_PA2		2			66.101110	1.627	0.765	71
(thin)										
PA17		DG_PA2			C27r?	62.2 ± 0.9	66.101153			66
(thin)										
PA1602		DG_PA2		1			66.101197	1.721	0.548	66
(thin)										
PA1504		DG_PA2		1			66.101240	1.639	0.504	66
PA0709		DG_PA1		2			66.102240	1.843	0.740	66
PA0601		DG_PA1		2			66.102290	1.907	0.781	62
PA0507		DG_PA1		2			66.102340	1.815	0.681	62
PA0403				2			66.103340	1.815	0.653	62
PA0417				2			66.103340	1.766	0.645	62
PA1404				2			66.104340	1.744	0.683	62
PA1307				2			66.105340	1.747	0.652	61
PA1208				1	C29r		66.106340	1.454	0.311	61
MN03	Bushe (325m)		DG Bushe 1	1			66.107340	1.967	0.523	60
MN0305			DG Bushe 1	1			66.107340	2.035	0.554	57
(thin)										
BU01		DG_BU1	DG Bushe 1	1			66.107370	1.408	0.360	57
BU0204		DG_BU1	DG Bushe 1	1			66.107390	1.423	0.392	57
BU0305		DG_BU1	DG Bushe 1	1			66.107410	1.672	0.380	57
BU0406		DG_BU1	DG Bushe 1	1			66.107430	1.651	0.384	57
MN04	Khandala (140m)			1			66.108430	1.385	0.324	57
MN0504				1			66.109430	1.384	0.373	57
(thin)										
MN0608				1			66.110440	1.424	0.401	56
MN07	Bhimashankar (140m)			1			66.111440	2.052	0.624	56
KK0109			DG BH1	2			66.112440	1.944	0.702	55
MN0907			DG BH1	1	Trans.		66.112540	2.017	0.678	52
KK0410	Thakurvadi (650m)	DG_KK2		1			66.113540	2.037	0.556	52
KK0607		DG_KK2		1			66.114540	2.093	0.550	51
KK0805			DG TH3	1			66.115540	2.015	0.661	51
MN08			DG TH3				66.115551			46
KD1507		DG_KD3	DG TH3	1			66.115562	2.011	0.467	46
KD13		DG_KD3	DG TH3	1	C29r		66.115573	1.986	0.409	46
(thin)										
KD2206		DG_KD3	DG TH3	1			66.115594	1.934	0.451	46
KD1803		DG_KD3	DG TH3	1			66.115606	1.946	0.466	46
KD1603		DG_KD3	DG TH3	1			66.115617	1.982	0.465	46
KD1704		DG_KD3	DG TH3	1			66.115628	1.890	0.449	46
(thin)										
KD12		DG_KD3	DG TH3	1			66.115649	1.968	0.509	46
KD25		DG_KD3	DG TH3	1			66.115660	2.016	0.499	46
KD20		DG_KD2	DG TH2	1			66.116660	1.954	0.576	46
KD21		DG_KD2	DG TH2				66.116677			37
MN11		DG_MN3	DG TH2	1			66.116693	2.107	0.445	37
(thin)										
MN1208		DG_MN3	DG TH2	1			66.116720	2.170	0.460	37
MN1309		DG_MN3	DG TH2	1			66.116737	2.147	0.397	37

Sample *(Red boles)*	Formation	SEE (section)	SEE (formation)	Deccan Group	Magneto-stratigraphy	^{40}K-^{40}Ar age (Ma)	Timeframe (Ma)	Gd/Yb_n	Nb/La_n	Cumulative volume (%)
KK0707		DG_KK3	DG TH2	1			66.116753	2.093	0.462	37
KK0204		DG_KK3	DG TH2	1			66.116770	2.059	0.452	37
KD1104		DG_KD1	DG TH1	1			66.117770	1.968	0.458	37
KD0505		DG_KD1	DG TH1	1			66.117787	1.986	0.471	33
KD0707		DG_KD1	DG TH1	1			66.117803	2.078	0.339	33
KD24		DG_KD1	DG TH1				66.117820			33
KD0301		DG_KD1	DG TH1	1			66.117837	1.959	0.504	33
KD02		DG_KD1	DG TH1	1			66.117853	1.978	0.570	33
KK0303			DG TH1	1			66.117870	2.029	0.682	33
KD0603				1			66.118870	2.003	0.617	33
KD04				1			66.119870	2.011	0.644	33
MN1502	Neral (100m)	DG_MN1		1			66.120870	1.930	0.559	32
MN1602		DG_MN1		1			66.120890	2.037	0.671	28
MN1807		DG_MN1		1			66.120910	2.197	0.360	28
MN1905		DG_MN1		1			66.120930	2.175	0.384	28
MN2002		DG_MN1		1			66.120950	2.168	0.399	28
MN21		DG_MN1		1			66.120970	2.106	0.427	28
KD0107			DG NE1	1			66.121970	1.909	0.502	28
MN14		DG_MN2	DG NE1	1			66.121995	2.073	0.703	25
MN1705		DG_MN2	DG NE1	1			66.122020	2.049	0.505	25
KK0505		DG_KK1	DG NE1	1			66.122045	1.962	0.391	25
KK0902		DG_KK1	DG NE1	1	C29r		66.122070	2.083	0.371	25
NA06	Igatpuri (700m)		DG IG2				66.123070			25
VT10			DG IG2				66.123120			24
VT0901			DG IG2	1			66.123170	1.898	0.524	24
SI0108		DG_SI5	DG IG1	1			66.124170	1.915	0.467	24
NA05		DG_SI5	DG IG1				66.124203			23
SI0201		DG_SI5	DG IG1	1			66.124237	1.915	0.474	23
VT0705			DG IG1	1			66.124270	1.927	0.520	23
SI0304	Jawhar (>200m)			1			66.125270	2.095	0.607	23
KI13		DG_MKKI6	DG JW6				66.126270			22
MK0304 ***GPB***		DG_MKKI6	DG JW6	1			66.126303	2.103	0.580	21
VT0803a		DG_VT2	DG JW6	1			66.126337	1.891	0.515	21
VT0803b		DG_VT2	DG JW6	1			66.126337	1.866	0.514	21
VT0502		DG_VT2	DG JW6	1			66.126370	2.065	0.582	21
KI0205 ***GPB***		DG_MKKI5		1		64.7 ± 0.9	66.127370	1.919	0.480	21
KI0108		DG_MKKI5		1			66.127470	1.438	0.418	20
SI2107		DG_SI2		1			66.128470	1.515	0.462	20
SI2204		DG_SI2		1			66.128570	1.494	0.429	19
SI1805				1			66.129570	2.052	0.600	19
SI2308		DG_SI1	DG JW5	1			66.130570	1.743	0.478	18
SI2403		DG_SI1	DG JW5	1		64.9 ± 0.9	66.130595	1.783	0.472	16
SI2603		DG_SI1	DG JW5	1			66.130620	1.847	0.498	16
SI2506		DG_SI1	DG JW5	1		64.9 ± 0.9	66.130645	1.819	0.511	16
MK01			DG JW5				66.130670			16
SI1304				1			66.131670	2.174	0.643	16
SI1704			DG JW4	1			66.132670	2.044	0.561	16
KI12		DG_MKKI4	DG JW4				66.132695			15
MK10		DG_MKKI4	DG JW4				66.132720			15
MK02		DG_MKKI4	DG JW4				66.132745			15
VT04			DG JW4				66.132770			15
MK09							66.133770			15
MK04							66.134770			14
SI0402				1			66.135770	2.007	0.589	14
VT06		DG_VT1					66.136770			13
VT0302		DG_VT1		1			66.136870	2.158	0.558	13
SI05							66.137870			13
KI11							66.138870			12
KI10							66.139870			12
VT0205				1	C29r		66.140870	1.712	0.502	11
SI06			DG JW3				66.141870			10
KI0308		DG_MKKI3	DG JW3	1			66.141895	1.740	0.504	9
KI0405		DG_MKKI3	DG JW3	1			66.141920	1.739	0.496	9
MK11		DG_MKKI3	DG JW3				66.141945			9
VT01		Excluded	DG JW3		Unusual direction		66.141970			9
MK0604				1			66.142970	1.757	0.500	9
KI0808				1			66.143970	1.759	0.502	8
KI08c				1			66.143970	1.743	0.509	8
MK08		DG_MKKI2	DG JW2				66.144970			7
KI0905		DG_MKKI2	DG JW2	1			66.145020	2.236	0.690	6
KI0603		DG_MKKI2	DG JW2	1			66.145070	2.211	0.673	6
KI0707		DG_MKKI1	DG JW1	1	C29r		66.146070	1.587	0.426	6
KI0507		DG_MKKI1	DG JW1	1			66.146103	1.579	0.426	5
MK07		DG_MKKI1	DG JW1				66.146137			5
MK0508a		DG_MKKI1	DG JW1	1			66.146170	1.620	0.444	5
MK0508b		DG_MKKI1	DG JW1	1			66.146170	1.613	0.438	5
SI1001	Latifwadi (?)	DG_SI4		1	C30r / C30n		68.650800	2.179	0.593	5
SI0908		DG_SI4		1	C30r / C30n		68.650817	2.159	0.597	3
SI0705		DG_SI4		1	C30r / C30n		68.650833	2.203	0.574	3
SI0804		DG_SI4		1	C30r / C30n		68.650850	2.178	0.593	3
SI11		DG_SI4			C30r / C30n		68.650867			3

Sample *(Red boles)*	Formation	SEE (section)	SEE (formation)	Deccan Group	Magneto-stratigraphy	^{40}K-^{40}Ar age (Ma)	Timeframe (Ma)	Gd/Yb_n	Nb/La_n	Cumulative volume (%)
SI12		DG_SI4			C30r / C30n		68.650883			3
NA03		DG_SI4			C30r / C30n	67.4 ± 1.0	68.650900			3
SI1403a		DG_SI3		1	C30r / C30n		68.651900	2.126	0.587	3
SI1403b		DG_SI3		1	C30r / C30n		68.651900	2.161	0.597	1
NA04		DG_SI3			C30r / C30n		68.651933			1
SI1508		DG_SI3		1	C30r / C30n		68.651967	2.122	0.586	1
SI1602		DG_SI3		1	C30r / C30n		68.652000	2.140	0.596	1
SI2001				1	C30r / C30n		68.653000	1.529	0.412	1

III. Electron Probe Micro Analyser (EPMA) – Basic principles and high-precision analysis

Most of the dataset presented in this thesis has been acquired on a JEOL JXA-8230 EPMA at ISTerre (Grenoble, France) using combined Energy Dispersive Spectroscopy (EDS) and Wavelength Dispersive Spectroscopy (WDS) at high current, acceleration voltage and counting times.
After providing the reader with the basics of electron microscopy and electron-probe microanalysis, the high-precision EPMA analysis method will be described in details.

III.1. Electron-Probe Micro Analysis – From electrons to X-ray

EPMA is a technique of electron microscopy allowing in-situ elemental analysis for elements ranging from $_{4}$Be to $_{92}$U (this range of atomic numbers results from the capacity of an element to emit x-rays and on how easily it can be detected. See further in the text) at concentrations down to ~10ppm (depending on the analysed specimen and the operating conditions) and spatial resolution of about 1µm (also depending on the specimen and the operating conditions).

Electron microscopy is one of the most versatile sets of techniques for analysing (composition) and/or observing (shape/morphology) fine structures. It stems from the multitude of signals emanating from the interaction of an electron beam with matter. Electron microscopy is a mostly non-destructive technique insofar as it does not require any ablation of material from the analysed specimen. However, the stability (i.e. capacity to withstand the energy of the electron beam) of the latter depends on its composition and structure. Figure 1.1 shows some of the signals that arise from the interaction of an electron beam with matter.
These emissions or signals convey compositional as well as morphological and structural information about the specimen under observation. For example, the latter may be used to create images up to very high magnification powers (up to ca. two million) or to find out the structure and orientation of a crystal lattice if the specimen happens to be in a crystallized state (*Secondary Electrons Image* (SEI), *CathodoLuminescence* (CL), *Electron BackScatter Diffraction* (EBSD), respectively). On the other hand, the compositional information can be used to resolve the chemical composition of a sample in various ways: in-situ point analysis, mapping (as a series of points or as a raster scan) or atomic number contrast (*Energy* and *Wavelength Dispersive Spectroscopy* (EDS/WDS), *BackScattered Electron* image (BSE), respectively). Note that electron microscopy cannot be used for acquiring isotopic data.

So how is it possible that a single particle, or rather a bundle of them – the electron beam – can spark all these different types of emissions?

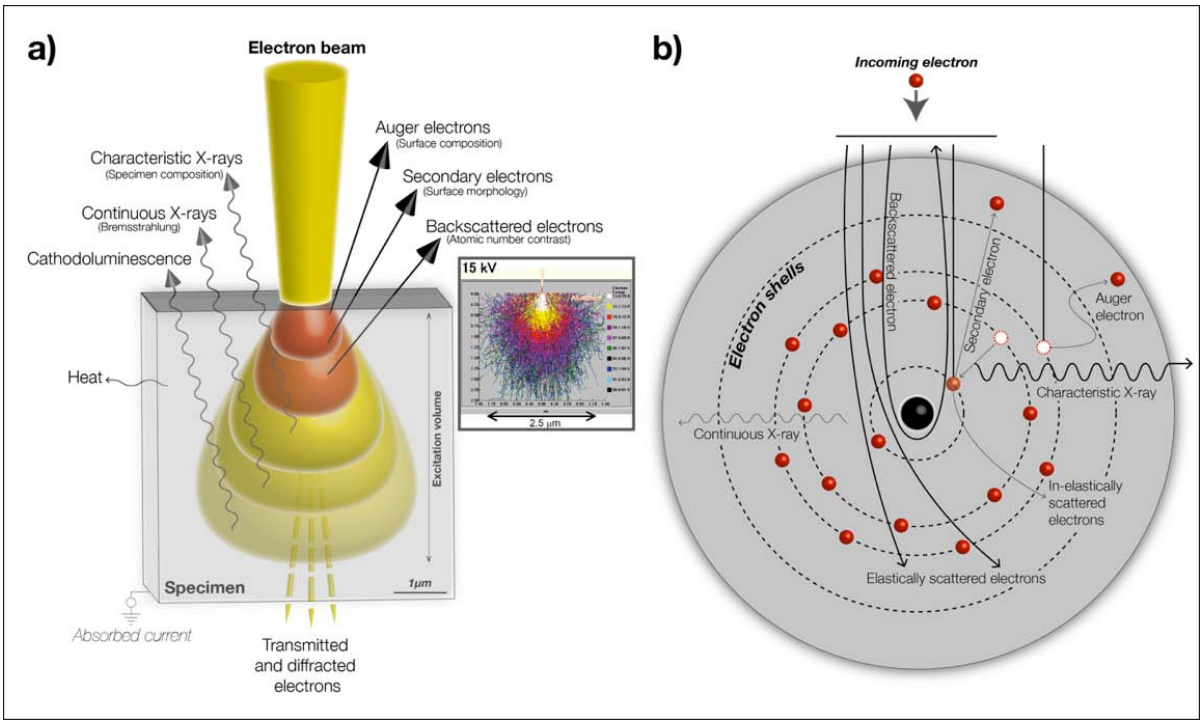

Figure 1.1 - Illustration of the various types of signals resulting from the interaction of an electron beam with matter. a) Distribution of emissions within the specimen. b) Illustration of the phenomena responsible for these signals within an atom. Adapted from © JEOL ltd.

The interactions an electron (beam) can have with the targeted material fall into two categories.

First, electrons may travel through the sample with virtually no energy loss. This is called *elastic interaction*. Coulomb forces (positive charge of the nuclei versus the negative charge of the electron) may nonetheless influence the path of these electrons so that they will either go straight through the specimen or follow a deflected trajectory (Figure 1.1a). When Coulomb forces are strong enough (e.g. high atomic number and/or in the vicinity of the nuclei), the path can become deflected to the point of sending the electron back in the direction it came from. It is a *Backscattered* electron. The backscattering process being more efficient for higher atomic numbers, *BackScattered Electron (BSE)* images offer atomic-number contrasts (averaged within the excitation volume, Figure 1.1). Hence, in the case of *elastic interactions*, only the changes in the path of the incoming electron convey information. In the second case however, energy is transferred from the electrons to the specimen (*inelastic interactions*). Depending on where and how(much) energy is exchanged, various kinds

secondary signals will be emitted (Figure 1.1). For example, an electron can collide with another one to the point of removing it from its shell. The removed electron becomes a *secondary electron*. Subsequently, another electron from another shell of the same atom will replace the missing one (vacancy). Transitions always occur from outer shells towards inner, higher-energy ones. During this substitution process, *characteristic X-ray fluorescence* will be emitted. Furthermore, s*econdary electrons* may still be strong enough to spark further fluorescence either belonging to the *X-ray continuum* (*Background*, *Continous X-ray* or *Bremsstrahlung*) or triggering other *characteristic X-ray* emissions of lower energies (*secondary fluorescence*). Removal of outer shell electrons will not spark characteristic X-ray emission. Instead, this will merely modify the overall electronic charge of the atom, a phenomenon that will easily be compensated for by electrons wandering in the surroundings. Outer shell electrons nonetheless do carry some compositional information (*Auger* electron). Finally, at lower energies and for luminescent materials, interactions with the atomic nuclei will result in *cathodoluminscence*.

It is important to keep in mind that the electrons (transmitted or scattered, elastically or inelastically) and the photons emitted whether they be infra-red (heat), visible light (cathodoluminscence), or X-rays (characteristic or background) do not all come from the same depth/volume of the specimen and hence in electron microscopy, one does not analyse a 2D-point on the surface of a sample but rather a small volume (μm^3) of it. This volume is generally referred to as *excitation volume* (Figure 1.1). The size of this volume depends 1 – on the signal or emission considered (e.g. secondary electrons will only provide the user with information on the surface of the specimen whereas characteristic X-rays will be emitted from a much larger volume) and 2 – the overall excitation volume varies with the acceleration voltage of the electron beam as well as with the average atomic number or density of the specimen (Figure 1.2). Although generally illustrated as a pear-like structure, the excitation volume is rather messier in reality. A Monte Carlo simulation of electron trajectories within a given specimen is presented in the inset of (Figure 1.1a). The beam current on the other hand has consequences solely on the intensity of what happens within the excitation volume, but not on its dimensions.

It therefore appears that the observation or analysis of a specimen by electron microscopy cannot be undertaken without considering what the previous is made of as well as what the latter is used for. In other words, if one wishes to obtain high-resolution images of the surface of a sample (secondary electrons), low acceleration voltages should be used (smaller

excitation volume thus enhancing the spatial resolution). Alternatively, as in the case of EPMA, if the user wants to unveil the chemical characteristics of the specimen (characteristic X-ray), the acceleration voltage may have to be set higher in order to encompass the *critical ionization energies* (i.e. the energy that is needed to spark a characteristic X-ray emission which is always higher than the corresponding characteristic line) of the elements contained within the specimen, as well as the beam current (though only up to what the sample can endure without being volatized). Yet this setting would be inappropriate if the specimen's density is low, in which case the acceleration voltage must remain low (Figure 1.2). Everything in electron microscopy is a matter of tradeoffs.

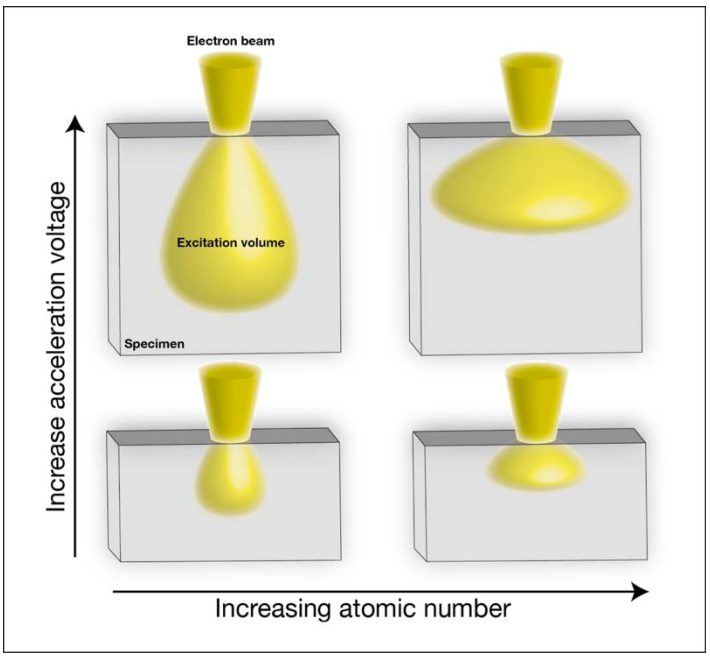

Figure 1.2 - Changes in the size and geometry of the excitation volume as a function of the acceleration voltage of the beam with respect to the atomic number or density of the specimen. Adapted from © JEOL ltd.

Among all the signals mentioned in the above, the most important to this work (carried out using EPMA) is the characteristic X-ray emission insofar as it enables quantitative analysis. Each element of the periodic table has a unique X-ray spectra (Moseley, 1913, 1914) formed by the electronic transitions between its electron shells. In other words, each element of the periodic table (Z higher than 2 (He) for electronic transitions cannot happen with only one shell) has a unique electronic configuration that reacts to external excitations in a specific and unchanging way, namely by releasing a typical X-ray signature. The higher energy X-rays are emitted upon electronic transitions within inner (higher energy) shells while transitions between lower energy (outer) shells will result in lower energy X-rays. All the possible transitions have been assigned a set of letters, one referring to the shell where the electron was

removed from and the other, a Greek character often accompanied by an index, indicates where the replacing electron comes form (Figure 1.3).

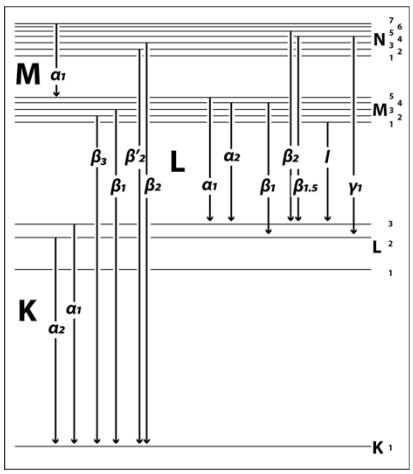

Figure 1.3 – Some of the electronic transitions giving rise to emission lines (Thompson *et al.*, 2009)

However, a specimen is not made of a single atom so that many will be excited in the fashion described above (Figure 1.1 and Figure 1.2). Moreover, the actual characteristic X-ray signature will be superimposed to the continuous X-ray or background emission (Figure 1.1 and Figure 1.4).

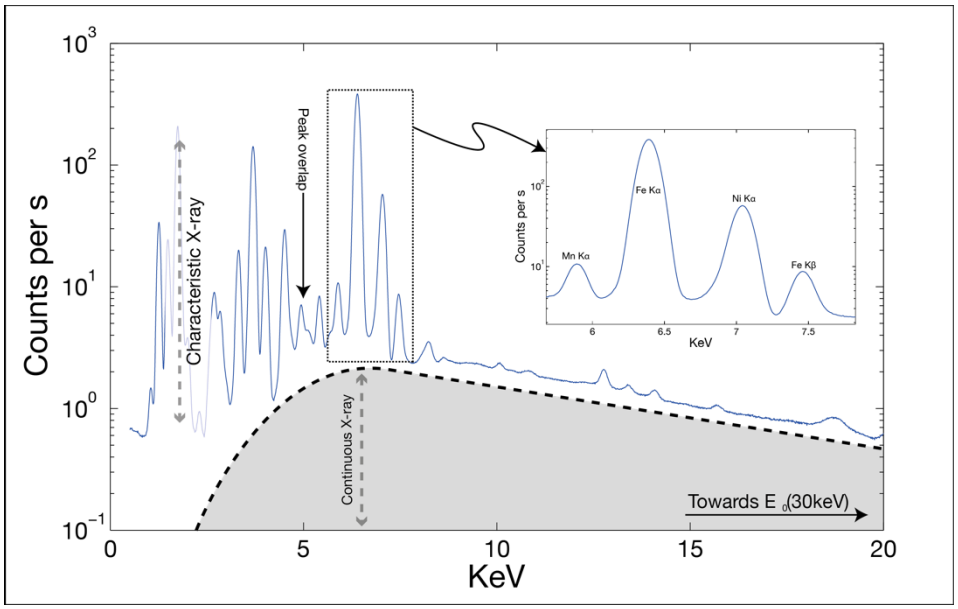

Figure 1.4 - Example of an X-ray fluorescence (EDS) spectra superimposed to the continuous X-ray. The inset shows the first emission lines (K) of Mn, Fe and Ni in details

There are two important aspects of Figure 1.4: First, the X-ray lines or peaks do not all have the same height (in counts per s or X-ray photon per s). This is not directly indicative of the element concentration in the sample but it is a place to start. Secondly, some lines overlap (see, for example around 5 and 2.5 keV on Figure 1.4). This phenomenon renders both the

identification of an element and its quantification a little trickier. The X-ray spectra of Figure 1.4 being no more than a histogram of X-ray photons for a given unit energy range divided in a number of bins, the energy resolution (the width the bins) and the amount (height) of signal within each bin become the two very critical variables in improving the identification and quantification of X-ray spectra. In short, the previous is addressed by choosing *Wavelength Dispersive Spectroscopy* (WDS) over *Energy Dispersive Spectroscopy* (EDS) while the latter pertains to both the use EDS versus WDS and to the analytical conditions (operating conditions of the apparatus and nature of the specimen).

X-ray spectra can be acquired following two different ways. They may be acquired in the energy space (*Energy Dispersive Spectroscopy*) or in the wavelength space (*Wavelength Dispersive Spectroscopy*) (Figure 1.5).

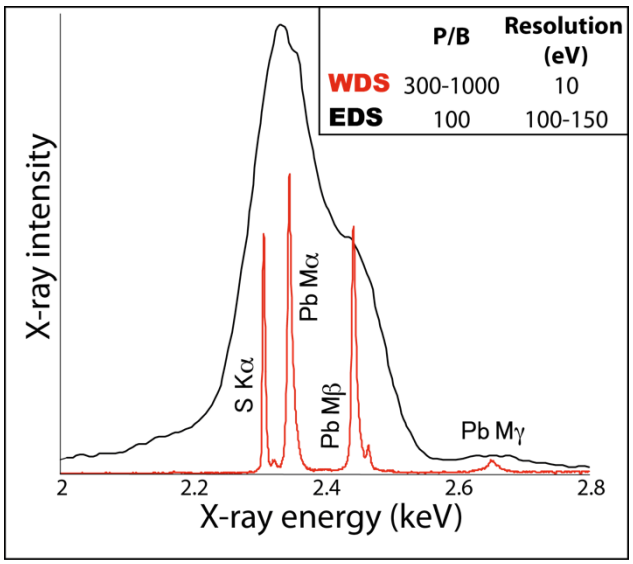

Figure 1.5 - Comparison of the EDS and WDS spectra of PbS. The inset (upper right) shows the main differences between EDS and WDS. P/B: Peak-to-Background ratio. Adapted from © JEOL ltd.

Energy Dispersive Spectroscopy (EDS) involves recording a histogram for the full energy range from E_0 – the source's acceleration voltage – downward (see Figure 1.4). The sensor records the entire energy range at once. An incident X-ray from the specimen enters the EDS detector and photoelectrons are released out of this interaction. The photoelectrons (charges) are then converted into a voltage so that the voltage pulses are proportional to the energy of the incident X-ray photons. It is fast, simple and provides the user with the full X-ray spectra of the specimen allowing fast *qualitative* identification of its components. However, the peak-to-background ratio is not outstanding (in the order of 100, Figure 1.5). Moreover, the energy resolution is fairly coarse (one order of magnitude lower than the width – actually, the *Full-*

Width-Half-Maximum of a peak intensity – of an actual X-ray line, which is typically 10eV wide or less) so that EDS often fails to single out peaks that are close to one another (Figure 1.4, Figure 1.5, Table 1–1). Finally, the user must be aware of some artefacts. These include peak broadening; peak distortion; escape peak; absorption edges; sum peak and system peak. *Peak broadening* results from the convolution of a detector system response with a natural peak. The natural peak appears wider and the quantification is biased. In brief:

- *Peak distortion*: the collection of charge carriers (photoelectrons) from some regions (edges) of the detector is not perfect and results in a deviation from the Gaussian shape of the low-energy side of a peak
- *Escape peak* is an artificial peaks that can appear close to any natural one as a result of K X-ray photons being released within the sensor (e.g. silicon K-lines for a detector made of silicon. In this case escape peaks could occur at E - $K_{\alpha}Si$)
- *Absorption edge*: an EDS detector is isolated from the specimen chamber by a thin layer or window (typically made of beryllium). Absorption takes place for low energy photons (the lower energy, the more absorption) and reduces the number of photons reaching the detector but not their energies. Hence, peak-to-background ratios can become extremely poor at low energies
- *Sum peak* occurs during pre-amplification in the detector and results from several pulses being fully or partially processed at the same time. This is directly linked to the frequency or counting rate at which the sensor's pre-amplifier operates
- Finally, *system peak* is due to the X-ray fluorescence of the detector itself. If it is made of silicon, $K_{\alpha}Si$ may be detected. This is also true of X-ray tubes (source) used in X-ray fluorescence instruments – another way of generating EDS spectra is to excite the specimen with X-rays instead of electrons. For example, Figure 1.4 was recorded on an Eagle III X-ray fluorescence apparatus that uses a rhodium X-ray tube as a source. Therefore in the final spectrum rhodium lines will occur (around 20 and 22 keV, not seen on Figure 1.4)

An exhaustive and accurate review of the mechanisms by which these artefacts are generated is beyond the scope of this chapter. It is nonetheless critical that the user be aware of these.

Finally, note that EDS and/or *Electron Energy Loss Spectroscopy* (EELS) are the only options in the case of Transmission Electron Microscopy (small area of interest) and high-resolution Scanning Electron Microscopy (low beam current). EELS is based on measuring the energy lost by the electron beam upon elastic and inelastic interactions while travelling through the

specimen. In addition to very high energy resolutions (~1eV) EELS also provides information as to the state of the material analysed (e.g. EELS can make the difference between two crystalized polymorphs).

Table 1–1 – Common peak overlaps in X-ray microanalysis

S Kα	*Mo Lα*	*Pb Mα*	
Na Kα	*Zn Lα*		
Ni Lα	*La Mα*		
Zr Lα	*Pt Mα*	*P kα*	*Ir Mα*
Nb Lα	*Hg Mα*		
Si Kα	*W Mα*	*Ta Mα*	*Rb Lα*
Al Kα	*Br Lα*		
Y Lα	*Os Mα*		
O Kα	*V Lα*		
Mn Lα	*Fe Lα*	*F kα*	

Wavelength Dispersive Spectroscopy (WDS) was proposed for the first time in the very comprehensive PhD thesis of Raymond Castaing (Castaing, 1951) and aims at increasing both the peak-to-background ratios and the spectral resolution. It is more complex than EDS and does not provide the user with a full X-ray spectrum as seen on Figure 1.4. On the other hand, it enables very accurate quantitative analysis.

With WDS, one looks at X-rays from a wavelength point of view. Energy and wavelength are related following:

$$E = h\frac{c}{\lambda} \qquad (1)$$

Where E is the energy in J (1eV = $1.602.10^{-19}$ J), h the Planck constant ($6.63\ 10^{-34}$ m^2 kg/s), c the speed of light in vacuum in ($2.99\ 10^{8}$ $m.s^{-1}$) and λ the wavelength in m.

The reason for considering wavelengths instead of energies is that they can be filtered (or analysed) upon diffraction by crystallized matter following Bragg's law:

$$2d \sin\theta = n\lambda \qquad (2)$$

Where d is the lattice spacing of the *analysing crystal*, θ is the angle of the incident X-ray with respect to the crystal's surface, n is an integer and λ the wavelength of the characteristic X-ray (Figure 1.6). Therefore, by diffracting X-ray using specific crystals with appropriate d it becomes possible to analyse one specific peak at a time. The spectral resolution becomes very high (Figure 1.5)

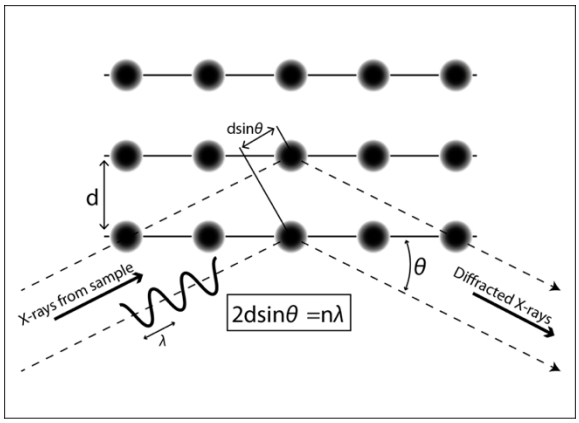

Figure 1.6 - Illustration of an analysing crystal or monochromator. Adapted from © JEOL ltd.

The diffracted X-ray enters a gas-filled counting sensor where its interaction with the gas contained within the sensor produces photoelectrons. This is followed by a cascade of voltage pulses of various energies that are filtered and summed up by the electronic of the probe as *counts* or *counts per seconds*. The filtering carried out at this point is twofold. First, the low voltage pulses are excluded because they arise from secondary interactions within the sensor itself. Furthermore, n in equation (2) indicates that multiples of λ can be diffracted as well. Voltage pulses higher than that of the desired X-ray are thus excluded as well. This process is set up through *Pulse Height Analysis* whereby two energy thresholds are defined: a *baseline* and a *window*. Consequently, any signal lower than the baseline and higher than the window is filtered out. Anything within this range is used for statistical counting. Peak interference may nonetheless happen for lines that are very close to one another (e.g. a few tens of eV apart, Table 1–1).

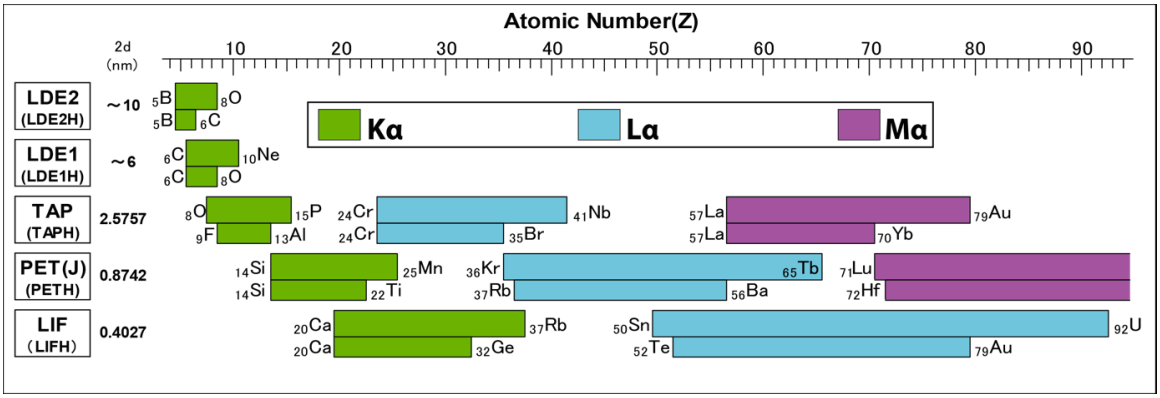

Figure 1.7 - Example (non-exhaustive) of various analysing crystals (left) and their elemental ranges. Adapted from © JEOL ltd.

An analysing crystal with its own *d* will only allow a certain range of wavelength (λ) to be diffracted, θ being the limiting variable. Several crystals with different *d* are required to cover most of the periodic table in terms of characteristic X-ray (Figure 1.7). Moreover, while more than one crystal type may diffract the same given wavelength, they may not all provide an output signal of equal quality (Figure 1.8).

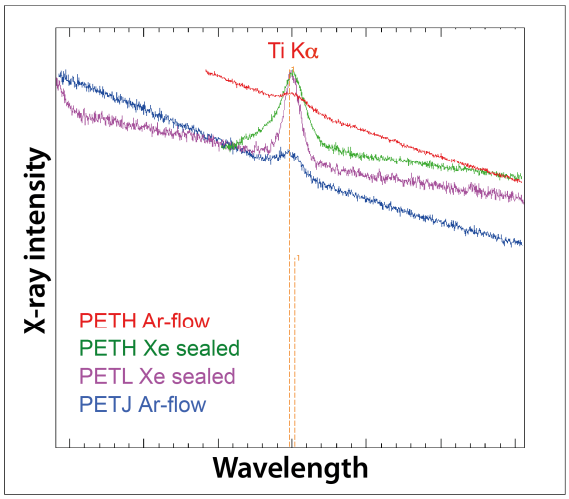

Figure 1.8 - Ti K⍰ for 200ppm of Ti in olivine analysed by 4 different PET crystals (PET = Pentaerythritol) and 2 kinds of counters (Ar flow-through vs. Xe sealed). Adatped from (Batanova & Sobolev, 2013)

Finally, lithium is not within the range of elements accessible to WDS for two reasons. First, its ionization energy is low meaning that the peak-to-background ratio of Li *Kα* would be very poor. But most importantly, there exist no crystal for analysing Li *Kα* X-ray as the lattice spacing required would be too large. This shortcoming may nonetheless be compensated for by the use of a *Soft X-ray Emission Spectrometer* (SXES). SXES uses diffraction gratings and a CCD camera instead of analysing crystals and gas counters. It works exclusively at low energies with resolutions of less than 1eV and detection limits comparable or better than that of high-precision EPMA (a few ppm and sub-ppm level in some cases). SXES may be coupled to TEM as well as EPMA and used for lights elements *K* lines (Li to F) or low energy *L* lines (Mg to P). (© JEOL ltd.).

III.2. Electron Probe Micro Analysis – quantification

This section is intended as an introduction to how quantitative data can be extracted from the X-ray line intensities.

Raymond Castaing's first approximation (Castaing, 1951) was:

$$\frac{C_i}{C_i'} = \frac{I_i}{I_i'} \quad (3)$$

Where C_i is the concentration of an element i and I_i is the intensity of the characteristic line of element i. However, there are three reasons to explain why (3) is not appropriate: *secondary fluorescence*, *absorption*, *density or atomic number.*

III.2.1. Secondary fluorescence and absorption

Let us consider a 40% Fe alloy with Cr, Mn or Ni, (Figure 1.9):

- Fe in Fe-Ni is overestimated because Ni *Kα* is higher than Fe K_{edge} (the critical ionization energy of Fe *Kα*). Consequently, X-ray released from Ni *Kα* transitions will have enough energy to spark Fe lines (*secondary fluorescence*) and Fe will thus be overestimated
- Fe in Fe-Cr is underestimated because Cr K_{edge} is lower than Fe *Kα*. Hence, opposite to the previous example, it is X-ray released from Fe *Kα* transitions that will have enough energy to spark Cr *Kα* and hence, Fe *Kα* X-ray will be *absorbed* in this process and Fe concentrations will be underestimated
- In the case of the Fe-Mn alloy, there is proportionality of intensities and concentrations as neither X-ray from Fe or Mn can match the ionization energy of the other element

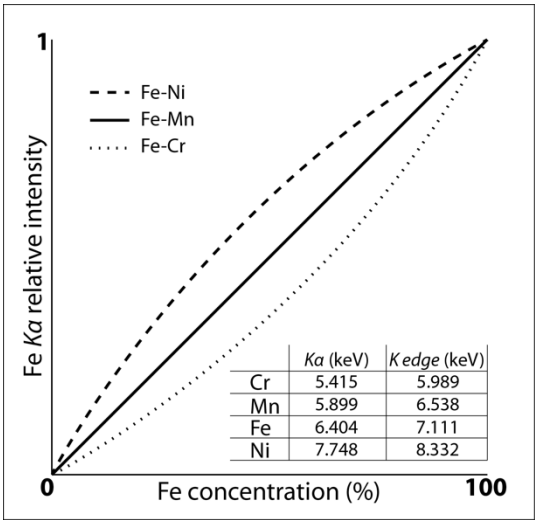

Figure 1.9 – Comparison of Fe concentration versus Fe K□ relative intensity for Cr, Mn and Ni alloys (40% Fe). Adapted from (Reed, 1993)

III.2.2. Density or atomic number

Figure 1.10 is a simplified illustration of what happens within a specimen made of atoms of different atomic weights under given observation conditions. One can see that within the binary compound (middle), the amount of high-Z atoms (grey) in the excitation volume (red) is equal to that of the pure high-Z compound (right). On the other hand, low-Z atoms (white) are under-represented in this same binary material compared to the excitation volume of the pure low-Z material (left).

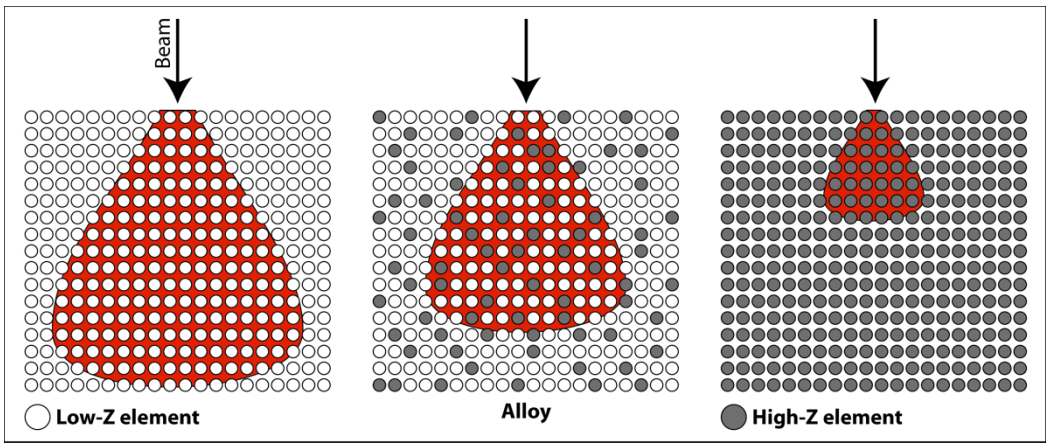

Figure 1.10 - Excitation volume (red) for a low Z material (left), a higher Z material (right) and an alloy of both (middle). Modified from (Reed, 1993)

This induces a disproportionality of the characteristic X-ray: the intensity of the high-Z lines will be similar for the alloy and the pure high-Z specimen while that of the lower-Z lines will appear smaller even though low-Z are actually more concentrated. Furthermore, it could be that one of those elements has a characteristic X-ray close to the ionization energy of the other (secondary fluorescence/absorption). Not to mention that electron backscattering is more efficient at high Z and beam penetration at low Z. In the end, one can see that proportionality between intensities and concentrations (3) almost never occurs. A correction based atomic number and specimen composition is therefore needed.

Equation (3) thus becomes:

$$C_i = \frac{I_i}{I_{i(\text{pure})}} \cdot ZAF$$

Where ZAF is a compound correction coefficient that accounts for the atomic number through electron penetration and backscattering (Z), absorption (A) and secondary fluorescence (F)

Equation (4) shows that a different ZAF is applied to both the specimen and the standard. At this stage, accuracy hinges upon how well these coefficients have been determined for both the specimen and the standard. This entails two ways of considering the standards. One way to proceed is to utilize a standard which composition is as close as possible to that of the unknown specimen. Indeed, in the extreme case where they both have the exact same composition, ZAF will be equal to 1. The other way to proceed is by using pure element or simple oxides. Accuracy will then depend on how well the ZAF corrections of those pure compounds have been defined.

Explaining these correction procedures in details is beyond the scope of this introduction to EPMA. Nonetheless, equation (4) is to be kept in mind by any EPMA user: measuring the composition of a sample shall not be done without an idea of what this sample is made of and a careful choice of standard.

III.3. High-precision EPMA for olivines

Improving the precision (repeatability) and accuracy (truthfulness) of EPMA quantification hinges upon several aspects:

Table 1–2 - Aspects to consider for high-precision EPMA

	Excitation volume	***P/B***	***ZAF***	***Peak overlap***	***PHA***	***Signal processing***	***Precision of mechanical parts***	***Lab environment*****
Beam characteristics*	×	×	×					
Specimen composition	×		×	×				
Analysing crystals		×		×	×	×		
Counters		×			×	×		
Standard materials			×					
Instrument design							×	
Laboratory design								×

**Beam diameter, acceleration voltage and current*

*** Temperature and humidity control, electromagnetic and mechanical perturbations*

All of these aspects are not equally important and more often than not appear in tradeoffs. For example, high current and acceleration voltage can dramatically improve the peak-to-background ratios and the counting statistics whilst the size of the excitation volume will increase, the spatial resolution decrease and the specimen may be damaged. Moreover, increasing the beam power (power = current × voltage) may simply decrease the precision for low-density samples, as the energy from the beam would simply be dispersed within a large volume thereby decreasing the net intensities of characteristic lines (Figure 1.2, Figure 1.10 and Figure 1.12). The same is true of alkali elements like sodium and potassium. They are volatized by the electron beam and must therefore be measured before any other element, at low current and acceleration voltages with a defocalized beam (large diameter).

The high-precision method used to analyse olivines in this PhD project is based on a combination of optimized lab design, probe operating conditions, analysing crystals and well-known standards.

III.3.1. Lab design

The lab is fitted with a high-performance air-conditioning system keeping the room temperature within ±0.5°C and ±4%RH (Relative Humidity). Maintaining a stable temperature is important, especially for the analysing crystals as temperature variations may imply small changes (dilation) in the lattice spacing which is directly linked to the diffracted wavelength (equation 2).
Along with temperature and humidity controls, low electromagnetic and mechanic perturbations help the stability of the electron beam.

III.3.2. - Operating conditions

The ultimate goal of optimized operating conditions is to reduce the peak-to-background ratios in order to improve the counting statistics. Let us first consider a few more simple equations.

X-ray lines or peaks are detected when:

$$P - B > 3\sqrt{B}$$

Where:

- *P*: peak intensity in *photons/µA*
- *B*: background intensity in *photons/µA*

And an X-ray line is considered to give reliable (99.8%) quantitative information when:

$$P - B > 10\sqrt{B}$$

This is illustrated in (Figure 1.11).

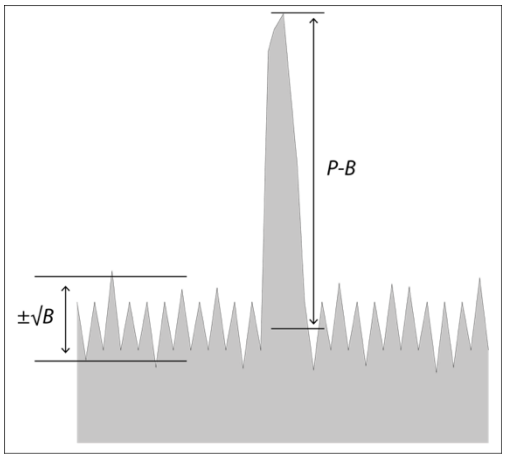

Figure 1.11 - Relationship between the background (B) and a peak (P). Adapted from © JEOL ltd.

P and *B* can also be used to describe the detection limit of a give X-ray line:

$$Dl = \frac{3\sqrt{2B}}{(P - B)\sqrt{t}} C_{std}$$

Where:

- *Dl* : Detection limit in *weight%*
- *P* : Peak intensity in *photons/µA*
- *B* : Background intensity in *photons/µA*
- C_{std} : Concentration of the sample in the element considered in *weight%*

- *ZAF* : Matrix correction factor(s)
- i : Probe current in μA
- t : Counting time in s

Finally, equation (7) can be reformulated as follows:

$$\frac{3\sqrt{2}\,\sigma_{bkg}}{\sqrt{\frac{P^2}{B}\,i\,t}}$$

Equations (7) and (8) show that the easiest way to decrease *Dl* is to reduce the peak-to-background ratio (P^2/B) and that this is best achieved by increasing i and t, namely, the probe current and the counting time. P/B is also enhanced by higher acceleration voltage although this depends on the atomic number of the atoms targeted. For light elements (Z<10), the acceleration voltage should not be higher than about 10kV (Figure 1.12).

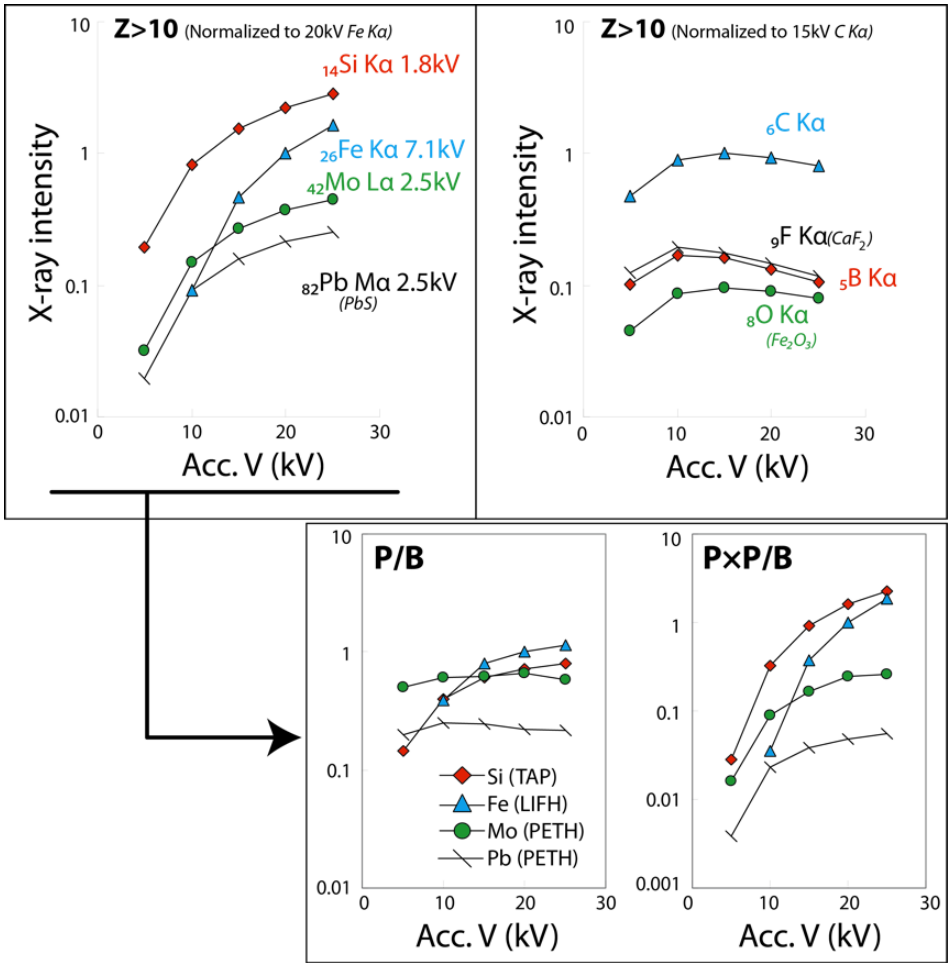

Figure 1.12 - X-ray intensities as a function of the accelerating voltage and atomic number (Z>10 and Z<10). Adapted from © JEOL ltd.

Olivine turns out to be resistant to high beam power. Moreover, it is not a low-density material and it is made of elements which atomic numbers are generally higher than 10. Therefore, the acceleration voltage it set to 25kV and the probe current to several hundreds of nano-amperes with counting times of several minutes.

The early version of this high-precision method has been explained in (Sobolev *et al.*, 2007). In this paper, Sobolev and co-workers explained the capabilities of high-precision EPMA and published the first high-precision dataset for olivines form various geological settings. They illustrated the strength of high-precision EPMA in the following figure (Figure 1.13).

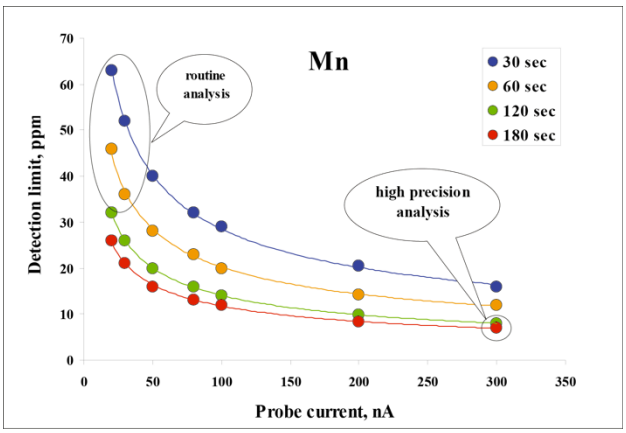

Figure 1.13 - The detection limits of olivine high-precision EPMA confronted to those of routine analysis. Modified from (Sobolev *et al.*, 2007)

Figure 1.13 shows that Sobolev and co-workers did not increase the probe current higher than 300nA yet most of the olivine dataset presented in this thesis has been acquired at 900nA. This improvement was made possible by combining EDS and WDS. While this was not possible on the probe used by Sobolev and colleagues in 2007, the new EPMA (JEOL JXA 8230) installed at ISTerre in 2011 is fully capable of combining both types spectrometers. The reason behind this technical aspect is that at beam currents higher than 300nA X-ray lines of major elements (Si, Fe and Mg) are so intense they overshoot the saturation point of the WDS counters and cannot be measured at all. Upon combining WDS and EDS however, one can analyse those major elements with EDS which saturation level is much higher than that of WDS spectrometers. The low spectral resolution and peak-to-background ratios are partially compensated for by high counting statistics. Minor and trace elements on the other hand, are

measured by WDS. This allows to move farther towards the bottom right of Figure 1.13 thereby reaching detection limits of a few (<10) ppm for Mn and other elements.

Under these conditions, the spatial resolution (max diameter of the excitation volume) is about 2µm^3. Upon comparing this value to the resolution capabilities of another analytical tool capable of similar accuracies and precisions, namely that of Laser Ablation-Inductively Coupled Mass Spectrometry (LA-ICP MS, Figure 1.14), the advantages of EPMA become obvious. In the case of Figure 1.14, not only does LA-ICP MS fail to resolve the fine zoning of this olivine grain, and will not return meaningful and reproducible (precise) compositional data either. Finally, note that Figure 1.14 was acquired at 300nA, not 900nA. Indeed, it is a qualitative (i.e. not quantitative) specimen map were counting statistics do not really matter as soon as a significant peak can be detected above the background (equation 6). Moreover, in order to obtain such a map, the high-current beam stays on the same specimen grain for several hours and over-heating is an issue (melting of the epoxy resin holding the specimen). Therefore, it has been decided to lower the beam current for this acquisition.

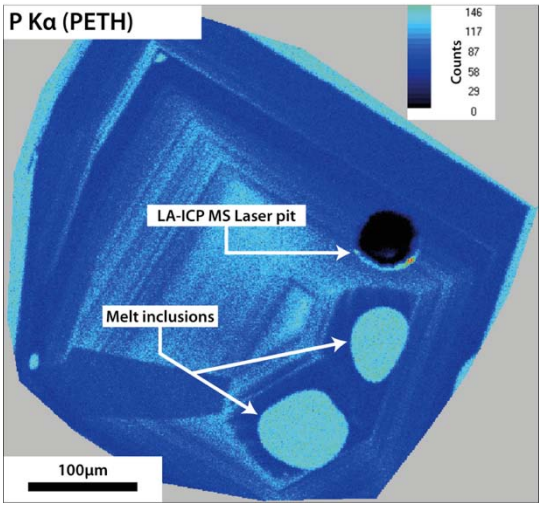

Figure 1.14 - WDS map of phosphorus K (PETH analysing crystal) at 300nA and 25kV with a 2ms dwell time for a San Carlos olivine grain and comparison of the resolution power of EPMA (1 pixel) versus that of Laser Ablation Inductively Coupled Mass Spectrometer (LA-ICP MS, black laser pit indicated on the image). Modified from (Batanova & Sobolev, 2013)

III.3.3. Standards

The high-precision EPMA protocol for olivine uses standard specimens in two different ways. First and foremost, a combination of natural and pure oxide standards is used in the calibration of the apparatus whereby both the spectrometers and the statistical processing are adjusted for all the elements analysed (Table 1–3).

Table 1–3 - List of standard specimens for high-precision olivine analysis

Element	*Standard*
Si	*Olivine San Carlos (USNM111312-44)*
Mg	*Olivine San Carlos (USNM111312-44)*
Fe	*Olivine San Carlos (USNM111312-44)*
Al	*Pure Al2O3*
Na	*Albite*
Ca	*Wollastonite*
P	*Apatite Durango*
Co	*Pure CoO*
Zn	*ZnS*
Ti	*Pure TiO2*
Ni	*Pure NiO*
Mn	*Rhodonite*
Cr	*Pure Cr2O3*

All these reference specimens are internationally recognized and their respective compositions are either simple (pure oxides) or well established (i.e. analysed many times by different techniques). Major elements (Si, Fe and Mg) are calibrated using a natural olivine standard (San Carlos olivine, (DeHoog *et al.*, 2010)) as the matrix corrections (ZAF) will be close to that of the unknown sample being processed, namely olivine. Additionally, the matrix corrections of major elements have more consequences on the final quantitative result than minor and trace elements. It is therefore important to use natural specimens at this stage. Minor and trace elements on the other hand are calibrated using either pure oxides or natural samples (for those which are not easily synthesised as simple compounds). Matrix effects of minor and trace elements have much less effects on the overall quantification simply because of their lower concentrations.

In addition to this calibration stage, standard specimens are used during the quantitative analysis sequence by intercalating three San Carlos olivine standards every forty unknown specimens. By doing so the user is able to closely monitor changes in the repeatability of the measurements (precision) and adjust the final results accordingly.

III.3.4. - Summary of the high-precision protocol

Table 1–4 is a summary of the high-precision EPMA protocol for olivine. Table 1–4 also mentions that olivine being non-conductive specimens must be coated with conductive matter in order to drain away the beam current (otherwise the specimen would turn into a capacitor). A thin carbon film of about 15nm deposited by sputtering under high vacuum takes on this task. It is worth noting that all the standard specimens must have a coating thickness similar to that of the specimen. Indeed this thin layer at the surface of the sample absorbs some of the signals from both the beam and the analysed material. It is therefore important that this absorption be equal everywhere. As for the choice of carbon over other coating materials like gold, it appears carbon is easy to use, fairly cheap and absorbs far less signal than e.g. gold.

Table 1–4 - Summary of the olivine high-precision EPMA protocol

Element	*Dwell time (s)*	*Standard*	*Crystal*	*Counter*	*Detection limit (ppm)*	*1σ error (ppm)*
Si	*500*	*Olivine San Carlos (USNM111312-44)*	*EDS (SDD)*			*800*
Mg	*500*	*Olivine San Carlos (USNM111312-44)*	*EDS (SDD)*			*90*
Fe	*500*	*Olivine San Carlos (USNM111312-44)*	*EDS (SDD)*			*100*
Al	*180*	*Pure Al2O3*	*TAPJ*	*Ar gas flow*	*5*	*8 - 10*
Na	*160*	*Albite*	*TAPJ*	*Ar gas flow*	*9*	*10*
Ca	*160*	*Wollastonite*	*TAPH*	*Ar gas flow*	*4*	*3 - 5*
P	*180*	*Apatite Durango*	*PETH*	*Ar gas flow*	*5*	*6 - 10*
Co	*160*	*Pure CoO*	*LIFL*	*Xe sealed*	*5*	*4 - 6*
Zn	*180*	*ZnS*	*LIFL*	*Xe sealed*	*6*	*4 - 7*
Ti	*180*	*Pure TiO2*	*PETH*	*Xe sealed*	*3*	*2 - 4*
Ni	*160*	*Pure NiO*	*LIFH*	*Xe sealed*	*4*	*8 - 10*
Mn	*180*	*Rhodonite*	*LIFH*	*Xe sealed*	*3*	*2 - 4*
Cr	*160*	*Pure Cr2O3*	*LIFH*	*Xe sealed*	*4*	*2 - 4*
Operating conditions: 25kV, 900nA						
Carbon coating by sputtering in high-vacuum: 15 ±3 nm						

III.3.5. Comparison with LA-ICP MS data

LA-ICP MS is an in-situ adaptation of ICP MS (Inductively Coupled Plasma Mass Spectrometry, whereby elements are separated according to their mass (instead of there X-ray signature as in EPMA) upon laser ablation (LA). This paragraph is intended to show that LA-ICP MS has limitations that may be counterbalanced by the advantages of EPMA and vice versa. In short, combining EPMA and LA-ICP MS may prove to be the most efficient set of analytical techniques for petrology and geochemistry.

While EPMA probes the composition of a specimen by analysing its response to an external excitation (non-destructive), mass spectrometry is fundamentally different in that it measures concentrations by sampling a tiny fraction of the analysed specimen, turning it into plasma and then separating and counting the various elements in presence according to their mass. This technique is therefore destructive: a tiny fraction of the original specimen has to be removed and destroyed. Moreover, the integrated signal received by the counters of an ICP MS depends on the number of atoms of a given element it receives. Therefore, the lower the concentration of this element in the specimen, the more material needed and, in the case of LA-ICP MS, the larger the laser spot and the lower the spatial resolution. It has indeed been shown (Figure 1.14) that EPMA has a much higher (about one order of magnitude higher) spatial resolution than LA-ICP MS. This is a drawback since the fine phosphorus zoning (linked to the crystal's growth rate) of the olivine grain presented in this figure is not accounted for. Not being able to resolve this, or any other zoning for that matter, not only prevents the user to access this information – which may prove critical – it also decreases the precision (repeatability) of the measurement: analysing the grain of Figure 1.14 with laser ablation mass spectroscopy several times on several locations means not having an equal proportion of P-rich and P-poor zones in all these locations and hence, precision will decrease.

Figure 1.15 shows the error bars (precision) of high-precision EPMA versus LA-ICP MS for a large range of minor and trace elements in olivine. It appears that the precision of EPMA is better than that of LA-ICP MS down to concentrations of about 100ppm where the both precisions are similar. At lower concentrations, LA-ICP MS turns out to be more precise (Figure 1.15 a and b). Nonetheless, Figure 1.15c shows that in some cases, EPMA may have precisions similar to LA-ICP MS down to 60ppm. The reasons behind these changes in precisions with concentrations from one instrument to the other are as follows: First LA-ICP

MS has an overall detection limit that is much lower than in the case of EPMA (in the order of ppb versus a few ppm). Laser ablation spectroscopy therefore allows much lower concentrations to be measured. Secondly however, LA-ICP MS suffers from low spatial resolution (Figure 1.14) and poorly known matrix corrections which lower the precision where they become large, i.e. at higher concentrations.

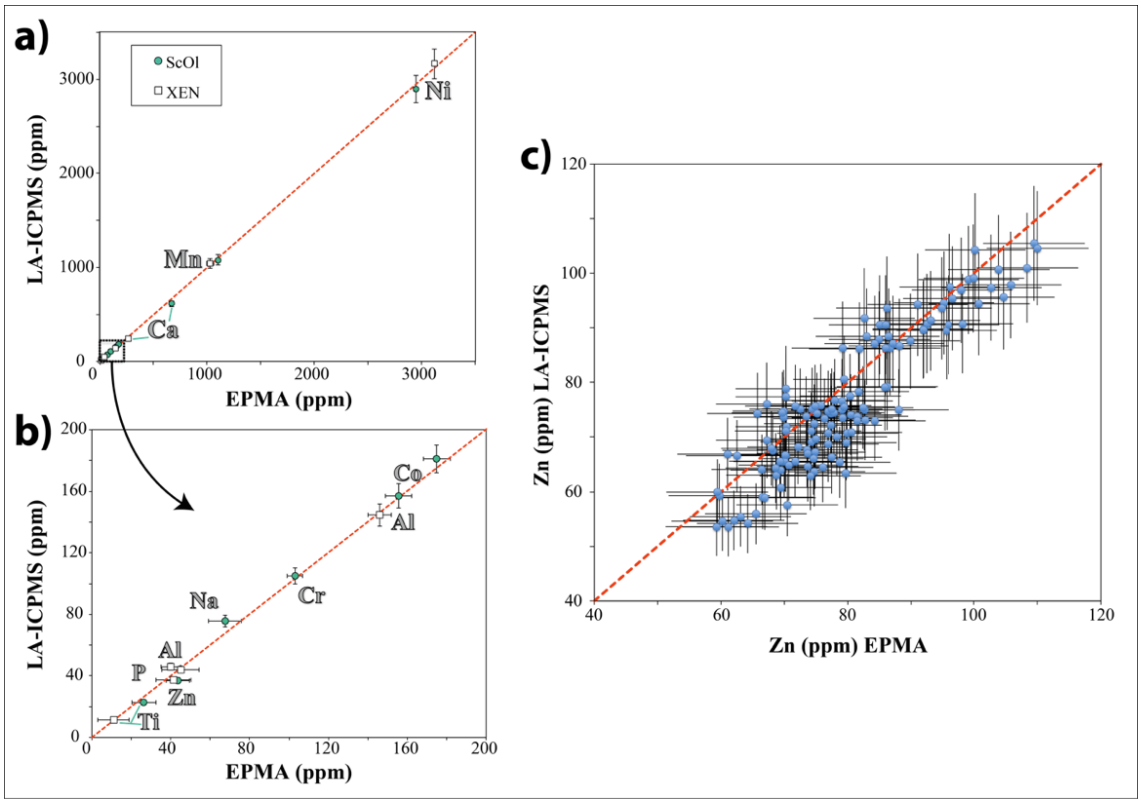

Figure 1.15 - Comparison of quantitative analysis results from EPMA and LA-ICP MS. a) and b): comparison of various minor and trace elements in the San Carlos olivine standard (LA-ICP MS values from (DeHoog *et al.*, 2010)) and a xenolith olivine standard (XEN) internal to the laboratory. c) is a comparison for Zn in MORB olivines from the Gakkel Ridge (North Atlantic Ocean) LA-ICP MS data acquired at the Max Planck Institute, Mainz, Germany. Modified from (Batanova & Sobolev, 2013)

Therefore, LA-ICP MS and EPMA are utterly complementary: EPMA is capable of providing very precise quantitative data down to trace concentrations of about 60-100ppm while offering a very high spatial resolution (2µm). On the other hand, LA-ICP MS, although suffering from lower spatial resolution and poorly constrained matrix effects, very well supplements electron microprobe at the trace and ultra-trace levels. Finally, LA-ICP MS is fully capable of analysing lithium, which, in the case of olivine being used as a proxy for mantle processes, is of particular interest (e.g. Foley *et al.*, 2013).

III.4. EPMA protocols for specimens other than olivines

Not only has EPMA been used in this project for high-precision olivine analysis, important proxies within the olivine itself, namely spinels and melt inclusions, have also been analysed this way. Olivine spinel inclusions afford information about the crystallisation temperatures and the oxygen fugacity and melt inclusions are proxies for both magmatic temperatures and primary melt compositions (section 7). None of these inclusions may be analysed at high current and acceleration voltage for they are not stable under such conditions (i.e. they would be volatized).

Table 1–5 gathers the analytical conditions and standard specimens used for analysing melt inclusions. All elements are analysed at low current first. This allows for good estimates of the average composition. Moreover, alkalis are not volatized under these conditions. The same inclusions are then processed one more time at higher current for better quantification of volatiles (S and Cl are proxies for SO_2 and HCl contents and K_2O is assumed to be close to the water content of the parental magma). Mn and Fe are re-analysed for correlating high and low current datasets. Fe is also critical in correcting the melt inclusion composition for crystallisation and inter-diffusion with olivine (section 7.1.1).

Table 1–5 - Summary of the analytical protocol for melt inclusions

Melt inclusions - low current				***Melt inclusions - high current***			
Element	***Dwell time (s)***	***Crystal***	***Standard***	***Element***	***Dwell time (s)***	***Crystal***	***Standard (20kV / 20nA)***
Si	*60*	*TAP*	*VG-2 glass*	***K***	*120*	*PETJ*	*Orthoclase*
Al	*60*	*TAP*	*VG-2 glass*	***Cl***	*120*	*PETL*	*Cancrinite*
Cl	*40*	*PETL*	*Cancrinite*	***S***	*120*	*PETH*	*ZnS*
S	*40*	*PETL*	*ZnS*	***Fe***	*120*	*LIFH*	*VG-2 glass*
P	*40*	*PETL*	*Apatite*	***Mn***	*120*	*LIFH*	*Rhodonite*
Na	*30*	*TAPH*	*Albite*	***Operating conditions: 20kV, 200nA***			
Mg	*60*	*TAPH*	*VG-2 glass*				
Ca	*60*	*PETH*	*VG-2 glass*				
K	*40*	*PETH*	*Orthoclase*				
Ti	*60*	*PETH*	*TiO_2 (rutile)*				
Fe	*60*	*LIFH*	*VG-2 glass*				
Mn	*60*	*LIFH*	*Rhodonite*				
Operating conditions: 15kV, 12nA							

Finally, Table 1–6 shows the analytical conditions of the olivine spinel inclusion protocol.

Table 1–6 - Summary of the analytical protocol for olivine spinel inclusions

Spinel			
Element	***Dwell time (s)***	***Crystal***	***Standard (20kV / 20nA)***
Cr	*160*	*PETJ*	Cr_2O_3
V	*40*	*PETL*	V_2O_3
Ti	*30*	*PETL*	TiO_2
Si	*60*	*PETL*	*Wollastonite*
Al	*70*	*TAPH*	Al_2O_3
Mg	*60*	*TAPH*	*Chromite*
Zn	*100*	*LIFH*	*ZnS*
Ni	*60*	*LIFH*	*NiO*
Mn	*100*	*LIFH*	$MnSiO_3$
Fe	*60*	*LIFH*	Fe_2O_3
Operating conditions: 20kV, 50nA			

III.5. Specifications of the JEOL JXA-8230 at ISTerre, Grenoble (France)

Electron gun

- Tungsten filament
- Probe current range: 10^{-12} to 10^{-5}A
- Beam stability: ±0.05%/h or ±0.3%/12h
- Acceleration voltage: 0.2 to 30kV
- Magnification: x40 to x300 000

Spectrometers

- 5 WDS spectrometers:

	Channel 1	Channel 2	Channel 3	Channel 4	Channel 5
X-ray spectrometer	FCS	L	H	H	H
Crystal 1	TAPJ	LIFL	TAPH	LIFH	LIFH
Crystal 2	PETJ	PETL	PETH	PETH	PETH
Crystal 3	LDE1	-	-	-	-
Crystal 4	LDE2	-	-	-	-
Rowland circle (mm)	140	140	100	100	100
Analysis range (2θ)	29-136°	29-136°	36-118.5°	36-118.5°	36-118.5°
Spectrometer drive range (mm)	70-260	69-259	86-240	86-240	86-240
Counter type	P10 gas flow	Sealed Xe	P10 gas flow	Sealed Xe	Sealed Xe

  - EDS spectrometer: Silicon Drift Detector. Energy resolution (FWHM) of 125eV for Mn Kα at $2x10^4$cps. Remote-controlled aperture mechanism enables simultaneous WDS/EDS analysis

Imagery

- Secondary Electron image resolution: 6nm
- High-resolution backscattered electron detector
- Panchromatic cathodoluminescence

The EPMA lab is fitted with air conditioning system maintaining 22±0.5°C as well as a humidity control keeping the room at 50±5%.

III.6. Historical references

Moseley (1913, 1914): Relationship between the wavelength of the characteristic emission of individual elements and their atomic number

Knoll and Ruska (1932): Means to focus an electron beam. Magnetic lenses

Castaing (1951): First comprehensive framework of electron-probe microanalysis. Theory, design, construction as well as practical methods for converting the measured intensities of characteristic lines into weight concentrations

First commercial microprobe built by Cameca (France) in 1958

McMullen (1953): First electron micrograph using secondary electrons (surface image). Prototype of many commercial instruments for the next 40 years

Duncumb and Melford (1957): Scanning technique applies to microanalysis

Long (1958) and Agrell and Long (1960): First application to geological samples

Mulvey (1960): first commercial instrument designed specifically for geological applications "Geoscan"

IV. Résumé en français

IV.1. Objectifs de la thèse

L'objectif général de cette thèse est de participer à l'étude du rôle des Trapps du Deccan vis-à-vis de l'extinction de masse de la limite Crétacé-Paléogène (K-Pg). Plus précisément, il s'agit de comprendre les processus magmatiques capables de générer des provinces magmatiques telles que les Trapps du Deccan et d'en évaluer les conséquences à la surface de la Terre : en reconstruisant la composition et l'environnement physique des sources magmatiques des Trapps du Deccan au cours du temps, de nouvelles contraintes peuvent être obtenues quant à la fusion de ces dernières et au dégazage des magmas. Ces données peuvent ensuite être confrontées à la littérature existante afin d'estimer les conséquences environnementales de telles éruptions.

Cette thèse est une application des travaux d'Alexander V. Sobolev sur les Trapps de Sibérie (Sobolev *et al.*, 2011) à un contexte radicalement différent. En effet, les Trapps de Sibérie ont été mises en place dans un contexte tectonique compressif à une époque au cours de laquelle l'océan mondial était vulnérable à l'acidification par les retombées volcaniques. A l'inverse, les Trapps du Deccan ont été mises en place dans un contexte tectonique extensif, lors d'une des plus rapide dérive continentale de l'histoire de la Terre (celle de l'Inde à travers l'Océan Indien), alors que la chimie des océans était relativement plus stable et moins vulnérable à l'acidification. La combinaison de l'éruption des Trapps du Deccan avec l'impact de Chicxulub (Alvarez *et al.*, 1980) à la limite Crétacé-Paleogène, et l'absence d'impact majeur connu à la limite Permien-Trias (Trapps de Sibérie), constituent une différence supplémentaire entre les deux évènements.

Cette thèse aborde la formation des Trapps du Deccan en quatre chapitres (la modélisation des conséquences climatiques de la mise en place des provinces magmatiques n'y est cependant pas abordé. Cette thématique fait l'objet d'une thèse en cours à l'Institut de Physique du Globe de Paris) :

- La durée et l'intensité de l'éruption des Trapps du Deccan sont des paramètres essentiels à l'évaluation des conséquences environnementales du volcanisme. Un nouveau scénario temporel, exclusivement basé sur la réinterprétation des travaux de thèse d'Anne-Lise Chenet et collaborateurs en radiochronologie et paléomagnétisme dans les Western Ghats (Chenet *et al.*, 2007, 2008, 2009), ainsi que sur une synthèse de la littérature existante est proposé.

- Ce scénario temporel est ensuite couplé à des données de chimie roche totale en éléments majeurs et traces (Bonnefoy, 2005). Cette étape permet de mettre en évidence les variations de profondeur des sources et de contamination crustale des magmas au cours du temps. Elle permet aussi d'évaluer les conséquences en terme de productivité magmatique et de dégazage.
- Des échantillons picritiques à phénocristaux d'olivines provenant du Deccan (stade précoce du panache mantellique) et de la Réunion (stade final de ce même panache) ont permis de mettre en évidence : 1) L'existence d'une lithologie ne contenant pas d'olivine dans les sources des Trapps du Deccan et de l'île de la Réunion, ce qui a des répercussions importantes sur la productivité magmatique, les interactions lithosphère-panache et sur le dégazage. 2) La composition en volatiles (K_2O, H_2O, Cl, SO_2) des magmas et 3) la composition et la température des liquides primaires à l'origine des magmas.
- Enfin, les données obtenues par analyse des phénocristaux d'olivines sont combinées aux observations des sections précédentes (épaisseur lithosphérique, pression, contamination crustale) et utilisées pour reconstituer les sources magmatiques des Trapps du Deccan (tête de panache) et de l'île de la Réunion (queue de panache).

IV.2. Scénario temporel continu de l'éruption des Trapps du Deccan et couplage à la géochimie roche totale

IV.2.1. Scénario temporel continu de l'éruption des Trapps du Deccan

Les données de paléomagnétisme haute résolution de Chenet et al (2008, 2009) et les datations radiochronologiques de Chenet et al (2007) on été réinterprétées et comparées à diverses études en liens avec la durée de mise en place des Trapps du Deccan (horizons d'altération ou red boles, Giant Plagioclase Basalts et données paléoenvironnementales), dans le but d'obtenir un scénario continu de l'éruption de cette province magmatique (Figure 3.1).

La mise en place des Trapps du Deccan – ou tout au moins de la province principale – s'est déroulée en trois étapes (Chenet *et al.*, 2007) :

- La première phase (phase 1) correspond à environ 10 % du volume total des Trapps et s'est produite à la transition C30r-C30n, il y a environ 68.65 Ma
- La seconde (phase 2) implique la mise en place de 70 à 80 % du volume de la province principale des Trapps du Deccan en environ 50 ka il y a environ 66.10 Ma (C29r). La fin de cette phase éruptive principale semble coïncider avec la limite Crétacé-Paléogène
- La phase finale (phase 3) représente 10 à 20 % du volume totale quelques 300 ka après la limite Crétacé Paléogène, de transition C29r-C29n et se prolongeant dans C29n (~65.8 Ma)

Les épisodes éruptifs précoces (Gujarat), périphériques (Subba Rao, 1972), ou tardifs (formations plus récentes que Mahabaleshwar) ne sont pas intégrés au scénario présenté ici. Le volume de ces épisodes volcaniques n'est généralement pas considéré comme supérieur à 10% du volume total des Trapps du Deccan (Paul *et al.*, 2008, Hooper *et al.*, 2010).

A elle seule, la seconde et principale phase éruptive (phase 2) pourrait avoir été responsable de l'extinction de masse de la fin du Crétacé (Keller *et al.*, 2012). Cette phase représenterait la mise en place de 8.10^5 km^3 de laves (Sen, 2001, Courtillot & Renne, 2003) en 50 ka (Figure 3.1). Ceci correspond à environ 160 fois le flux de lave actuel de l'archipel volcanique d'Hawaii (Courtillot *et al.*, 1986). De plus, la phase 2 est constituée de 25 épisodes de très courte durée (~100 ans) identifiés grace aux données paléomagnétiques (Directional Groups) Le plus important Directional Groupd identifié aurait pu correspondre à un flux moyen d'environ $160km^3$/an (formation Thakurvadi : Chenet *et al.*, 2009). Ce résultat est en accord avec des données récentes de diffusion isotopique du strontium dans les Giant Plagioclase Basalts, impliquant la mise en place de formations entières des Trapps du Deccan en moins de 1 ka (Borges *et al.*, 2013).

Les horizons d'altérations, ou red boles (les red bole d'épaisseur centimétrique, ou thin red boles se forment en une dizaine d'années alors que leurs homologues d'épaisseurs métriques nécessiteraient 50 ka pour se former : Chenet *et al.*, 2008, 2009), apparaissent à la fin de la phase principale (phase 2, Ambenali). Il est intéressant de noter que d'une part les red bole centimétriques (thin red boles) sont les premiers à apparaître dans Thakurvadi. Ils semblent ensuite être remplacés par des red boles métriques (thick red boles) dans Ambenali et Mahabaleshwar, puis à nouveau remplacés par des red boles centimétriques dans

Mahabaleshwar. D'autre part, aucun « red bole » métrique (thick) n'est inclus dans un des 25 courts épisodes volcaniques (Directional Group : Chenet *et al.*, 2008, 2009) identifiés grace au paléomagnétisme. En revanche, des « red boles » centimétriques (thin), décrits comme pouvant se former en quelques années (Chenet *et al.*, 2008, 2009, Sayyed, 2013) ont été observés au sein de ces groupes directionnels ou directional groups, ce qui atteste d'un processus d'altération rapide.

Le scénario éruptif proposé en Figure 3.1 est ensuite comparé aux paléotempératures des océans (Li & Keller, 1998) ainsi qu'à l'évolution du rapport $^{187}Os/^{188}Os$ dans les carbonates pélagiques (Robinson *et al.*, 2009) (Figure 3.2).

Figure 3.1 montre que l'augmentation de la fréquence des red boles et de leur épaisseur est associée à un épisode éruptif cataclysmique (phase 2). Figure 3.2 indique que cette phase éruptive majeure est aussi associée à une baisse du rapport $^{187}Os/^{188}Os$, et à des variations de température dans les eaux intermédiaires de l'océan global. Il est possible que ces variations puissent avoir été causées par un changement climatique, lui-même induit par une intense activité volcanique (relargage dans l'atmosphère de grandes quantités de CO_2 et SO_2 durant la phase 2). Ce changement climatique aurait affecté l'intensité moyenne des précipitations et accéléré les processus d'érosion. Une forte érosion tend à réduire le rapport $^{187}Os/^{188}Os$ dans les carbonates pélagiques. Ce même rapport isotopique aurait aussi baissé grâce à la couverture d'un craton (le craton indien dont le rapport $^{187}Os/^{188}Os$ est haut) par des basaltes (bas $^{187}Os/^{188}Os$), eux mêmes très sensibles à l'érosion. (Robinson *et al.*, 2009).

L'interprétation de la Figure 3.2 n'est néanmoins pas si simple.
D'abord, bien que la transition C30r-C30n ait été enregistrée à la fois par les Trapps du Deccan et par la section composite dans les carbonates pélagiques (Chenet *et al.*, 2007, Robinson *et al.*, 2009), la phase 1 n'est pas visible dans l'enregistrement du rapport $^{187}Os/^{188}Os$ (Figure 3.2). Il est proposé que la faible intensité de la phase 1 n'a pas été suffisante pour affecté le climat global.
D'autre part, le début du refroidissement général de la fin du Crétacé (Late-Cretaceous Cooling, ex : Li & Keller, 1998), contemporain de l'excursion en $^{187}Os/^{188}Os$ rapportée par Robinson et al, ainsi que des biozones CF2 et CF1 (Keller *et al.*, 2012), semble s'être produit environ 0.5 Ma avant le début de la phase 2 de l'éruption des Trapps du Deccan. Or les

excursions de températures (Li & Keller, 1998) et de rapports isotopiques (Vonhof & Smit, 1997, MacLeod *et al.*, 2001, Ravizza & Peucker-Ehrenbrink, 2003, Robinson *et al.*, 2009) ont aussi été interprétés comme des conséquences de l'intense volcanisme du Deccan. La réinterprétation des évènements liés aux Trapps du Deccan proposée dans cette section est en accord avec un scénario dans lequel le réchauffement de la fin du Crétacé et la première excursion de $^{187}Os/^{188}Os$ observée par Robinson et al – laquelle est aussi observée dans d'autres systèmes isotopiques (Li & Keller, 1998, Ravizza & Peucker-Ehrenbrink, 2003) – aurait été la conséquence d'une intense activité volcanique. Cependant, la durée de la première excursion en $^{187}Os/^{188}Os$ notée par Robinson et al (~0.3 Ma), elle-même similaire à celle du réchauffement tardif de la fin du Crétacé, n'est compatible ni avec la durée de la phase 2 de l'éruption du Deccan (Chenet *et al.*, 2007), ni avec la survenue de la limite K-Pg à la fin de cette dernière (Keller *et al.*, 2011). De plus, Robinson et al ont souligné que la première excursion en $^{187}Os/^{188}Os$ n'est associée à aucune conséquence environnementale majeure et en concluent que la mise en place des Trapps du Deccan n'a probablement pas eu de rôle majeur dans l'extinction de la fin du Crétacé. Cette conclusion est en contradiction avec ce qui est observé dans le bassin Krishna-Godavari, à l'Est du Deccan. D'une part, les Trapps du Deccan sont clairement associées à une perte de biodiversité dans le biozone CF1. D'autre part, la phase 2 du Deccan (phase principale) apparaît clairement contenir la limite K-Pg (Keller *et al.*, 2011, 2012). Parallèlement, la durée et l'intensité de la première excursion en $^{187}Os/^{188}Os$ de Robinson et al ne paraît pas non plus en accord avec l'existence d'éruptions paroxysmales indiquées par les groupes directionnels observés en paléomagnétisme et par les « Giant Plagioclase Basalt flows ». Enfin, le faible nombre de « red boles » observés dans la première moitié de la phase 2 indique que l'activité volcanique y était très soutenue. Par conséquent, l'hypothèse selon laquelle la première excursion en $^{187}Os/^{188}Os$ aurait été causée par la phase éruptive principale des Trapps du Deccan paraît très incertaine.
La seconde excursion en $^{187}Os/^{188}Os$ décrite par Robinson et al (2009) (Figure 3.2) semble d'avantage compatible avec la phase 2 de l'éruption des Trapps du Deccan.

A ce stade, il est important de garder en tête que l'existence d'importantes divergences dans les modèles d'âges utilisés en sédimentologie, ne peut être écartée. Par exemple, Ravizza et Peucker-Ehrenbrink (2003) placent la phase principale de l'éruption des Trapps du Deccan à la transition C30n-C29r alors que Chenet et al (2009) la place dans C29r.

Si la seconde éruption en $^{187}Os/^{188}Os$ de Robinson et al correspond effectivement à la phase 2 des Trapps du Deccan (ce qui serait alors en accord avec un grand nombre d'observations indépendantes, telles que les groupes directionnels paléomagnétiques, les « Giant Plagioclase Basalts », les biozones, et les « red boles »), il reste à trouver une explication pour l'existence de le première excursion en $^{187}Os/^{188}Os$ (Figure 3.2). Cette excursion a été mesurée dans des échantillons montrant une orientation paléomagnétique inverse. Si cette excursion est une trace de l'activité précoce des Trapps du Deccan, cette polarité inverse devrait être celle de C30r. Ceci impliquerait une discordance de plus de 2 Ma soit entre les âges modèles sédimentologiques, soit dans les données radiométriques (Chenet *et al.*, 2007). Un intervalle de 2 Ma représente deux fois la barre d'erreur moyenne des résultats de Chenet et al. Il est également peu probable qu'une telle erreur soit possible alors que les âges sédimentaires sont couplés à des données paléomagnétiques (Robinson *et al.*, 2009). D'autre part, comme il a été dit plus haut, plusieurs auteurs ont observé des excursions isotopiques sur des périodes similaires. Il est donc probable qu'une baisse en $^{187}Os/^{188}Os$ dans les carbonates pélagiques se soit produite dans C29r, au cours des derniers 0.5 Ma du Crétacé.
Dès lors, comment est-il possible d'accommoder l'intervalle entre les phases 1 et 2 du Deccan (>2 Ma) et l'existence d'une excursion en $^{187}Os/^{188}Os$ avant la phase éruptive principale (phase 2)? Il a été suggéré que l'impact de Chicxulub pourrait être plus âgé que la limite K-Pg d'environ 0.3 Ma (Keller *et al.*, 2004a, 2004b, Schulte *et al.*, 2008). Cependant, Alvarez (2003) souligne qu'un intervalle d'une durée supérieure à 0.1 Ma entre la phase principale de l'éruption du Deccan et l'impact de Chicxulub serait facilement identifiable dans les sections sédimentaires contenant la limite K-Pg. Il est aussi possible que plusieurs impacts météoritiques aient pu se produire aux alentours de la limite K-Pg (Keller *et al.*, 2003). Pourtant, de multiples impacts auraient certainement résulté en d'importantes excursions isotopiques, plus importantes que celles présentées par Robinson et al (2009). Sans oublier que l'observation conjointe d'excursion en $^{187}Os/^{188}Os$ ainsi que dans le système isotopique du Strontium exclue l'implication de matériel extraterrestre (voir section 3.5.2 du manuscrit).

Une autre possibilité consisterait à attribuer les excursions isotopiques au panache du Deccan. Sobolev et al (2011) ont montré que l'incubation d'un panache mantellique sous la lithosphère pouvait être à l'origine d'un dégazage significatif et suffisant pour créer d'importants dommages à l'environnement, avant même qu'une quelconque éruption se soit produite. Tester la validité d'une telle hypothèse nécessite de connaître la concentration des magmas en

éléments volatiles. Cet aspect est traité en section 6.5. Ce scénario implique aussi qu'un simple dégazage serait capable d'affecter les systèmes isotopiques sensibles au volcanisme. Si il est raisonnable de penser que l'injection de grandes quantités de CO_2, SO_2 et HCl dans l'atmosphère affecterait profondément le climat global, l'apparition d'une source de bas $^{187}Os/^{188}Os$ et $^{87}Sr/^{86}Sr$ (telle que des basaltes) disponible au processus d'érosion et/ou la disparition d'une autre source de haut $^{187}Os/^{188}Os$ et $^{87}Sr/^{86}Sr$ (telles que le craton indien, recouvert par les basaltes des Trapps du Deccan) demeure inexpliquée.

Enfin, la non-exhaustivité de l'échantillonnage ne peut pas être exclue. Au vu de l'étendue et du volume des Trapps du Deccan, il est possible que des coulées (ou des « red boles ») aient pu être omises entre phase 1 et 2, ou même dans la phase 2 elle même. Par exemple, la transition Bushe-Poladpur de Chenet et al n'est pas complète (Chenet *et al.*, 2009). De plus, les calculs de volume proposés par Chenet et al ne permettent d'expliquer que moins de 30% du volume totale des Trapps du Deccan (Sen, 2001). Une part importante de ce volume manquant pourrait se trouver à l'ouest de l'Inde (Minshull *et al.*, 2008, Owen-Smith *et al.*, 2013). Par ailleurs, les essaims de dykes et des études de modélisation des paléo-stresses dans la plaque indienne (Vanderkluysen *et al.*, 2011, Ju *et al.*, 2013) combinées à des données de paléo-topographie (Hooper *et al.*, 2010, Sheth & Pande, 2013) indiquent que l'emplacement des Trapps du Deccan aurait du être symétrique de part et d'autre de l'escarpement des « Western Ghats ». Dans ce cas, la sous-estimation du volume de Chenet et al (2009) serait entièrement due à une sous-estimation de l'étendue latérale de la province magmatique, et non pas à la non-exhaustivité potentielle de l'échantillonnage. Il apparaît donc peu probable que l'existence de coulées cachées sous les Trapps pourrait expliquer l'important volume manquant ainsi que l'excursion précoce en $^{187}Os/^{188}Os$.

IV.2.2. Couplage à la géochimie roche totale

Le scénario temporel de la mise en place des Trapps du Deccan présenté dans la section précédente a été couplé aux compositions en éléments majeurs et traces des échantillons utilisés en paléomagnétisme de haute résolution par Chenet et al (2008, 2009). Ces données géochimiques ont été acquises à l'occasion du stage de master de Benjamin Bonnefoy à l'IPGP, Paris (Bonnefoy, 2005).

Il apparaît que la composition de ces échantillons, notamment en terme d'éléments traces, n'est pas homogène (Figure 5.3).

Les échantillons ont été divisés en deux classes, Deccan1 et Deccan2. Celles-ci diffèrent par leurs enrichissements en éléments incompatibles et leurs anomalies en Nb, Pd, Sr et Ti. Malgré ces différences, les signatures en éléments compatibles sont remarquablement parallèles. Deccan1 montre par exemple, un Nb/La_n moyen plus bas et un enrichissement en éléments incompatibles plus fort, que Deccan2. Ces deux sous ensembles partagent cependant un enrichissement en éléments compatibles comparable et par conséquent, un rapport Gd/Yb_n moyen relativement identique. De manière plus générale, les indices de contamination crustale (ex : Nb/La_n) semblent anti-corrélés avec ceux qui indiquent une composition primitive des laves (ex : Mg#, Figure 5.5). Une telle observation a déjà été rapportée dans la littérature au sujet des Trapps du Deccan (Cox & Hawkesworth, 1985, Devey & Cox, 1987). Deccan1 semble ainsi plus primitive (et beaucoup plus hétérogène) que Deccan2 malgré des indices montrant une contamination crustale plus importante.

Les données roche totale et, plus particulièrement, des rapports élémentaires témoignant de paramètres géodynamiques importants tels que la contamination crustale (Nb/La_n) et la profondeur de la source (Gd/Yb_n), peuvent à présent être ajoutés à la Figure 3.1 pour donner la Figure 5.7. Cette figure permet d'observer que les signatures Deccan1 et Deccan2 sont séparées le long de la séquence de Trapps du Deccan. Deccan1 constitue principalement les formations inférieures, jusqu'à Poladpur, alors que Deccan2 n'est exprimée que dans les formations supérieures. La transition entre Deccan1 et Deccan2 s'opère entre les formations Khandala et Poladpur. Nb/La_n augmente alors d'environ 0.4 à plus de 0.8. Gd/Yb_n augmente aussi d'environ 1.4 à plus de 1.9 mais la valeur moyenne de ce rapport entre Deccan1 et Deccan2 reste comparable (Figure 5.5). Ceci implique une diminution importante de la contamination crustale entre Deccan1 et 2. Les variations importantes de Gd/Yb_n durant la mise en place des formations Khandala, Bushe et Poladpur implique que les sources mantelliques des Trapps du Deccan se sont, au moins momentanément, retrouvées à des profondeurs suffisamment faibles pour être en dehors du champ de stabilité du Grenat ($P < 2.4$ GPa). De plus, si le scénario temporel est correct, cette transition entre Deccan 1 et 2 n'aurait duré que 20 ka.

L'excursion négative de Gd/Yb_n et Nb/La_n des formations Khandala, Bushe et Poladpur n'est pas unique dans les Trapps du Deccan. En effet, plusieurs excursions similaires, quoi que de

moins forte intensité, peuvent être remarquées en Figure 5.7 dans les formations Jawhar (inférieure et supérieure) et Poladpur (supérieure).

Toutes les coulées faisant partie de ces excursions ne portent aucun signe d'érosion ou d'altération et contiennent des groupes directionnels paléomagnétiques. Ceci indique avec une quasi-certitude que les excursions négatives en Gd/Yb_n et Nb/La_n se sont produites sur de très courts intervalles de temps.

Les rapports élémentaires présentés ici peuvent être comparés à d'autres provinces magmatiques, telles que les Trapps de Sibérie (Figure 5.6).

Il peut être noté qu'à l'exception de quelques coulées appartenant à la base de la section de Norislk, l'ensemble des laves sibériennes ne montre aucun signe de signature du grenat ($Gd/Yb_n > 1.6$). Il s'agit d'une différence majeure entre les Trapps du Deccan et celles de Sibérie.

Sobolev et al (2011) ont montré qu'un panache mantellique était capable d'éroder la lithosphère et de réduire son épaisseur d'environ 50 % en 50 Ma. De plus, Sobolev et al ont proposé que, dans le cas de Trapps de Sibérie, l'érosion intense et généralisée de la lithosphère explique la forte baisse du rapport Gd/Yb_n (depuis des valeurs supérieures à 1.6 à inférieures à 1.5), laquelle implique que les sources magmatiques ne se trouvaient plus dans le champ de stabilité du grenat après cet épisode d'érosion. Enfin, Sobolev et al notent qu'une telle réduction de l'épaisseur de la lithosphère n'aurait pu avoir lieu si cette dernière avait eu une épaisseur initiale plus importante.

Les variations de rapports d'éléments traces dans les laves du Deccan sont compatibles avec les propositions de Sobolev et al (2011) : le panache du Deccan est entré en contact avec une lithosphère épaisse (~140 km) et les premiers magmas ont été émis de manière plus précoce que dans le cas sibérien, en empruntant des zones de faiblesses préexistantes à travers le craton indien (Murthy, 2002, Biwas, 2005). Dans ce contexte, l'érosion de la lithosphère induite par l'activité du panache mantellique doit être plus limitée et plus localisée que dans le cas d'une lithosphère moins épaisse et plus imperméable aux magmas émis pas le panache (Trapps de Sibérie). Dans le cas Sibérien, il a effectivement été noté que l'érosion généralisée du craton sibérien n'avait été possible que parce que la lithosphère était notablement imperméable aux magmas produits par le panache. A l'inverse, l'érosion localisée de la lithosphère indienne aurait tout de même pu favoriser la remontée de matériel mantellique proche de la croute. L'importante advection thermique aurait alors participé à une accentuation de la fusion par décompression et de l'assimilation crustale par assimilation et

transport turbulent (Huppert & Sparks, 1985). L'échelle de temps nécessaire à ces phénomènes a été estimée, sur la base de calculs numériques, aux alentours de 50 ka. Cette durée est parfaitement compatible avec la durée de la phase 2 de l'éruption des Trapps du Deccan (~70 % du volume total en 50 ka, Figure 5.7). Il est proposé ici que les trois ou quatre excursions de faible Gd/Yb_n et Nb/La_n pourraient témoigner d'un unique épisode d'érosion lithosphérique. Le retour rapide à des valeurs moyennes de ces deux rapports dans la formation Poladpur peut être expliqué par la formation d'un bouchon de restite (ex Harzburgite), plus légère que la péridotite fertile et la pyroxenite du panache et/ou du manteau environnant. La formation d'un tel bouchon entrainerait une augmentation de la profondeur de fusion de la tête du panache. Parallèlement, la baisse associée des indices de contamination crustale serait expliquée par la maturation des conduits magmatiques causée par le passage des précédents magmas.

Les formations supérieures (Wai) ont été mises en place suivant ce même régime final (source profonde, faible contamination crustale), comme le suggèrent les périodes de quiescence volcanique (« red boles ») et les volumes de lave plus faibles. Il doit cependant être noté que le sous-groupe Wai a une extension spatiale considérable sur le terrain (Self *et al.*, 2008b, Vanderkluysen *et al.*, 2011).

Bhattacharya et al (2013) ont identifié de fortes valeurs de $\delta^{18}O$ et de $^{87}Sr/^{86}Sr(t)$ combinées à des faibles $\varepsilon Nd(t)$, compatibles avec des épisodes isolés de forte contamination crustale dans les formations Poladpur supérieure et Mahabaleshwar inférieure. Figure 5.7 suggère que ces événements sont sans commune mesure avec ceux des formations inférieures (bas Gd/Yb_n et Nb/La_n simultanés). Bhattacharya et al ont proposé que seuls deux phénomènes pourraient expliquer ces mesures : 1) Les systèmes de conduits magmatiques sont propres à chaque formation (sauf pour Ambenali). De fait, la contamination crustale baisse une fois que le nouveau système de conduits est à maturation (réaction complète avec les magmas ascendants). 2) Tous les magmas proviennent de la même chambre magmatique. Cette chambre est approvisionnée par des magmas de différentes sources et/ou ayant subis des processus de contamination crustale variables. Les laves mises en place à la surface sont issues de mélanges de degrés variables des ces différents magmas dans la chambre magmatique commune.

Il est probable que la première proposition soit incorrecte dans la mesure où il a été montré que les trois principaux essaims de dykes ont été actifs à peu près simultanément au cours de l'emplacement de la province principale des Trapps du Deccan (Vanderkluysen *et al.*, 2011).

La deuxième proposition semble, quand à elle, plus appropriée. D'une part, la composition du groupe Deccan2 est, en moyenne, plus évoluée et plus homogène que celle de Deccan1 (Figure 5.5). Ceci indique qu'il est probable que les magmas à l'origine de Deccan2 aient été stockés suffisamment longtemps pour acquérir cette composition. D'autre part, les tendances des rapports isotopiques des formations Mahabaleshwar et Poladpur sont différentes (Poladpur possède un rapport $^{87}Sr/^{86}Sr_{(t)}$ plus élevé). Les épisodes de contamination que ces magmas ont subi doivent dès lors être différents.

Enfin, l'idée selon laquelle l'érosion de la lithosphère aurait été seulement localisée dans le Deccan est en accord avec les mesures de l'épaisseur actuelle de la lithosphère indienne (Artemieva, 2006, Priestley & McKenzie, 2006, Arora *et al.*, 2012), les modélisations de paléo-contraintes dans la plaque indienne (Ju *et al.*, 2013), ainsi qu'avec la structure en bouclier et les coulées complexes centrées sur l'essaim Nasik-Pune (Subbarao *et al.*, 2000).

IV.3. Analyse pétrologique des olivines des Trapps du Deccan et de l'île de la Réunion

Les données pétrologiques sur olivines présentées dans ce manuscrit constituent la base de données nécessaire à la reconstitution des processus magmatiques profonds liés à la mise en place des Trapps du Deccan et de l'île de la Réunion. Les principales caractéristiques de cette base de données peuvent être résumées de la manière suivante :

- Les magmas primaires à partir desquels les laves du Deccan et de la Réunion ont été fractionnées sont issus d'un mélange de produits de fusions de péridotite et de pyroxenite. La contribution de la pyroxenite à la génération des magmas peut être mesurée par l'intermédiaire de l'enrichissement en éléments compatibles (ex : Ni) et de l'appauvrissement en éléments incompatibles (ex : Mn, compatible avec le pyroxène) avec l'olivine (Sobolev *et al.*, 2005, 2007). Il a été estimé que les olivines riches en Mg des Trapps du Deccan ont cristallisé à partir d'un magma primaire lui-même composé de liquide pyroxénitique à 65%. Les olivines de la Réunion, quant à elles, ont été produites à partir d'un magma composé à 50% de liquides pyroxénitiques. Cependant, il semble que cette contribution de la pyroxénite ait été légèrement moins importante dans le cas du Piton des Neiges (35-45 %). Cette

observation nécessitera une analyse plus précise afin de déterminer les causes de cette différence. Figure 6.5.

- La composition des inclusions vitreuses des olivines est utilisée pour reconstituer les magmas primaires des Trapps du Deccan et de l'île de la Réunion ainsi que les caractéristiques de leurs sources.
- Les concentrations en éléments volatiles (S, Cl) dans les inclusions vitreuses sont compatibles avec les données publiées (Sobolev & Nikogosian, 1994, Sobolev, 1996, Bureau *et al.*, 1998a, 1998b, Self *et al.*, 2008a). Ces nouvelles données forment une tendance similaire à celle des MORB et des laves hawaiiennes, clairement différente de celle des Trapps de Sibérie (Sobolev *et al.*, 2009a). Une différence significative en Cl/K_2O entre les inclusions du Deccan et celles de la Réunion (Piton de la Fournaise) peut être notée et implique probablement une variation des processus de dégazage magmatique entre les deux stades d'évolution du panache du Deccan. Cette variation pourrait aussi s'expliquer par une contribution différente de la pyroxénite et du matériel recyclé à la génération des magmas primaires. Figure 6.7.
- L'absence de données sur les concentrations en volatiles des roches totales n'a pas permis de quantifier le dégazage des magmas du Deccan et de la Réunion. Il est néanmoins possible de proposer que ces nouvelles données sont en accord avec celles de Self et al (2008a) et que, par conséquent, les estimations publiées par ces auteurs sont valables pour le cas présent (S = 3.5 Tg/km^3 et Cl = 1 Tg/km^3). Cependant, les très fortes concentrations de chlore mesurées dans les inclusions sibériennes (jusqu'à 0.2 wt.% Sobolev *et al.*, 2009a) sont sans commune mesure avec celles du Deccan et de la Réunion. Cette différence importante devra être étudiée en détail afin de réévaluer les conséquences environnementales de la mise en place des Trapps du Deccan à la fin du Crétacé. Figure 6.7.
- L'analyse des inclusions de spinels dans les olivines magnésiennes a permis de déterminer l'état d'oxydation du fer dans les laves étudiées (Réunion, Piton de la Fournaise : Fe^{2+}/Fe^{3+}_{liq} = 6, Trapps du Deccan : Fe^{2+}/Fe^{3+}_{liq} = 11.5). Ce paramètre est important pour l'application des modèles pétrologiques nécessaires à la reconstruction des magmas primaires et des sources des deux localités. De plus, il apparaît que Fe^{2+}/Fe^{3+}_{liq} et Fo sont corrélés entre le Piton de la Fournaise et le Piton des Neiges. Ceci suggère que le degré d'oxydation des magmas est corrélé avec leur fractionnement. Figure 6.9.

- Les inclusions spinels ont aussi été utilisées pour appliquer le thermomètre de Sobolev et al (2013) basé sur le partitionnement de l'aluminium entre le spinel en inclusion et l'olivine encaissante (Figure 6.11). Les températures magmatiques obtenues sont les suivantes :

  Trapps du Deccan : 1107 – 1223 °C

  Réunion (Piton des Neiges): 1226 – 1283 °C

  Réunion (Piton de la Fournaise): 1165 – 1213 °C
- La température à laquelle les inclusions spinels se sont formées est égale à la température d'emprisonnement des inclusions vitreuses et de croissance des olivines (cumulât) qui les contiennent. Les températures dérivées de l'application de thermomètre olivine-spinels (Sobolev *et al.*, 2013) seront donc utilisées comme contraintes indépendantes sur la rééquilibration de la composition des inclusions vitreuses.

IV.4. Reconstitution des magmas primaires et des sources magmatiques des Trapps du Deccan et de l'île de la Réunion

Les résultats des modélisations pétrologiques entreprises dans le Chapitre 7 du manuscrit sont résumés dans les tableaux suivants : Table 7–7 et Table 7–9. Ces données sont compatibles avec l'interprétation suivante :

Les magmas des Trapps du Deccan ont été produits par un panache mantellique chaud (Tp ~1600 °C), composé de matériel primitif (moins de 20 % de DMM et 300 ppm d'eau) et contenant de 10 à 15% de matériel crustale recyclé (XRC). Le panache du Deccan est entré en contact avec la lithosphère indienne (épaisseur 140 à 250 km) quelques Ma avant la limite K-Pg, probablement aux alentours de 68-70 Ma (Mahoney *et al.*, 2002, Chenet *et al.*, 2007). La source hybride (éclogite + pyroxénite + péridotite) est entrée en fusion à hauteur de 10 à 15 % à une profondeur de 150 km (4.5GPa). Enfin, les magmas primaires sont issus d'une mixture de 65 % de liquides d'origine pyroxénitiques (Xpx).

Ces chiffres sont en accord avec un diamètre de la tête de panache supérieur à 1000 km (White & McKenzie, 1995) et un volume initial des Trapps du Deccan de l'ordre de 1 à $3.10^6 km^3$ (Sen, 2001). La température potentielle (1600 °C), la composante de matériel

crustale recyclé (XRC = 10-15 %) et la contribution de la pyroxénite (Xpx = 65 %) correspondent au contexte « WPM-THICK » de la classification de Sobolev et al (2007). L'interaction de la tête de panache avec la lithosphère a engendré une réduction partielle et hétérogène de l'épaisseur de la lithosphère indienne (2.4). Cette réduction d'épaisseur est observée dans les signatures en éléments traces sur roche totale (Gd/Yb_n et Nb/La_n) à quatre reprises le long de la section des Trapps du Deccan (Jawhar inférieur et supérieur, Khandala-Bushe et Bushe-Poladpur, Figure 5.7). Ces quatre excursions correspondent probablement à un seul et unique épisode d'érosion/délamination lithosphérique (50 ka, Sobolev *et al.*, 2011) périodiquement interrompu par la formation de bouchons de restite (5.5).

En moyenne, le taux d'éruption de la province principale des Trapps du Deccan aurait pu être équivalent à environ deux cent fois le taux d'éruption actuel de l'île volcanique d'Hawaii. Une telle activité magmatique aurait perduré environ 50 ka (3.6).

Il est tentant d'associer l'érosion de la plaque indienne à un contexte tectonique extensif et/ou au rifting le long de la côte ouest de l'Inde. Pourtant, il a été observé que l'extension le long de cette côte (séparation de la Laxmi Ridge et, plus tard, de Seychelles) était clairement postérieure à l'emplacement du Deccan (Hooper *et al.*, 2010). De plus, Sobolev et al (2011) ont montré qu'un régime tectonique extensif n'était pas nécessaire à la mise en place des processus d'érosion lithosphérique par un panache mantellique.

Quelques 60 Ma après l'éruption des Trapps du Deccan, le panache du même nom est toujours actif et s'exprime sous l'île de la Réunion, dont il est l'origine. A partir des données compositionnelles sur olivines, les différentes étapes de modélisation pétrologique ont permis de mettre en évidence d'importants changements entre le stade initial (Deccan) et final (Réunion) de l'activité du panache du Deccan. Les calculs de températures potentielles révèlent que le panache s'est refroidit de 50 à 150 °C au cours des soixante derniers millions d'années ($Tp_{Réunion}$ ~ 1450-1500 °C). Il s'avère aussi que la proportion de matériel recyclé transporté est moins importante ($XRC_{Réunion}$ ~ 7 %), que le taux de fusion des sources magmatiques est moins élevé d'une dizaine de pourcents ($F_{Réunion}$ = 3 à 5 %) et que la contribution des liquides pyroxénitiques à la formation des magmas primaires est moins forte d'environ 15 % (Xpx = 50 %). Cette interprétation va dans le sens de la proposition d'Herzberg & Gazel (2009) selon laquelle les panaches mantelliques liés à l'épanchement des provinces magmatiques paléocènes étaient plus chauds et ont fondu davantage que ceux qui sont à l'origine de la formation des îles volcaniques modernes. Herzberg & Gazel ont attribué

ce changement général de régime thermique à des variations compositionnelles des hétérogénéités du manteau inférieur.

Les conclusions de cette thèse sont en accord général avec les connaissances actuelles sur les processus géodynamiques internes de la Terre. Plusieurs aspects de ce travail de modélisation gagneraient néanmoins à être affinés. Les phénocristaux d'olivines magnésiennes sont la principale source d'information utilisée dans cette étude. Ces olivines ont été cristallisées dans des chambres magmatiques crustale et ont été collectées à la surface de la Terre. Le principale proxy utilisé ici (les olivines) est donc très éloigné, aussi bien dans l'espace (>100 km) qu'en terme d'évolution chimique (fractionnement, contamination crustale), de l'objet qu'il aide à décrire (le manteau terrestre). Il est donc particulièrement important de considérer et d'examiner chaque hypothèse et chaque source d'incertitude de cette approche. Ce travail de validation et de test des différentes sources d'incertitudes est abordé dans la dernière partie du chapitre 7 (7.3).

IV.5. Conclusions

Cette thèse apporte de nouveaux éléments quant à la mise en place des Trapps du Deccan à la limite Crétacé-Paléocène (K-Pg) d'une part, et quant à l'évolution au cours du temps du panache du Deccan d'autre part, depuis un stade initial de tête de panache durant la fin du Crétacé et l'éruption des Trapps du Deccan, jusqu'à un stade final actuel de « queue de panache », sous l'île de la Réunion dans l'Océan Indien.

En s'appuyant sur les précédents travaux d'Anne-Lise Chenet à l'IPGP, Paris (Chenet, 2006, 2007, 2008, 2009), il a été montré que la mise en place des Trapps du Deccan à la fin du Crétacé s'est traduite par un épisode d'activité volcanique paroxysmal dont la phase éruptive principale s'est achevée précisément à la transition K-Pg. Chenet et al ont apporté des contraintes exceptionnelles sur la durée et la dynamique de mise en place des Trapps du Deccan. D'une part, Chenet et al (2007) ont identifié trois phases volcaniques principales à partir de datation ^{40}K-^{40}Ar : Phase 1 précède la limite K-Pg de 2 Ma, phase 2 s'est produite juste avant, et s'est achevée à, la limite K-Pg (Keller *et al.*, 2012) et phase 3 a eu lieu quelques 2-300 ka plus tard, dans le Danien inférieur. D'autre part, Chenet et al (2008, 2009) ont publié une base de données quasi-exhaustive de paléomagnétisme de haute résolution pour les « Western Ghats » (Province principale des Trapps du Deccan). Ces données ont permis

l'identification de groupes directionnels correspondant à des séquences de coulées de laves portant des orientations paléomagnétiques similaires. Cette similarité dans les orientations paléomagnétiques implique une mise en place de chacunes de ces séquences de coulées en une centaine d'années au plus. 30 directionnels et 41 coulées individuelles (n'appartenant à aucun groupe directionnel) ont été observées le long de la séquence éruptive complète de la province principale du Deccan. Ceci suggère un temps d'éruption de 300 à 3000 ans pour les groupes directionnels uniquement, et 1000 à 7000 ans pour la mise en place complète de la province magmatique principale du Deccan. Récemment, des durées d'éruptions très courtes et compatibles avec les résultats de Chenet et al ont été obtenus indépendamment par modélisation de la diffusion/relaxation du rapport $^{87}Sr/^{86}Sr$ dans les phénocristaux de plagioclase des « Giant Plagioclase Basalts » (Borges *et al.*, 2013). Chenet et al en concluent que la quantification des épisodes de quiescence volcanique devenait dès lors, l'enjeu principal de la détermination de la durée totale de l'éruption des Trapps du Deccan. Chenet et al (2008) et Gérard et al (2006) ont tenté d'adresser ce problème en se basant sur les horizons altérés et autres paléosols (Sayyed, 2013) intercalés dans la séquence des Trapps du Deccan. En faisant l'hypothèse que les « thin red boles » pouvaient se former en une dizaine d'années alors que les « thick red boles » impliquaient une quiescence d'environ 50 ka, ces auteurs ont proposés que les 38 « thin red boles » et les 6 « thick red boles » observés dans les « Western Ghats » correspondaient à un temps de quiescence total d'environ 300 ka.

Le travail de Chenet et al a été réinterprété au cours de cette thèse de manière à produire un scénario continu de mise en place des Trapps du Deccan (Figure 3.1). Ce scénario continu a ensuite été comparé à des données paléo-environnementales de la littérature (Figure 3.2) et couplé à des données en éléments majeurs et traces sur roche totale (Bonnefoy, 2005) (Figure 5.7). Ce nouveau scénario continu montre une bonne corrélation avec les indicateurs paléo-environnementaux tels que les paléo-températures marines (Li & Keller, 1998) et les données récentes en $^{187}Os/^{188}Os$ dans les carbonates pélagiques (Robinson *et al.*, 2009), malgré les incertitudes importantes quand à l'étendue et la durée des périodes de quiescence volcanique. Il en est conclu que la phase 2 de l'éruption des Trapps du Deccan (Chenet *et al.*, 2007) fut un événement cataclysmique correspondant à la mise en place d'environ 8.10^5 km^3 de laves en 50 ka. Le taux d'épanchement moyen correspondant aurait été équivalent à 20 km^3/yr, soit 200 fois le taux d'éruption actuel de l'île d'Hawaii (Courtillot *et al.*, 1986). Occasionnellement, ce taux d'éruption aurait pu atteindre la valeur impressionnante de 160 km^3/yr (Chenet *et al.*, 2009). Cet évènement catastrophique (phase 2) apparaît aussi correspondre à une forte

anomalie négative en $^{187}Os/^{188}Os$ dans les carbonates pélagiques (Robinson *et al.*, 2009). La phase 2 fut probablement suivie d'une période d'activité volcanique de moindre intensité, comme en témoigne le grand nombre « thick red bole » observé entre les formations Poladpur et Mahabaleshwar (Figure 3.1). Les « thick red boles » suggèrent environ 300 ka de volcanisme de faible intensité précédant la phase 3 (Chenet *et al.*, 2007). Il est intéressant de noter que cette durée est équivalente à celle suggérée par les observations paléontologiques (Biozone P1a, Keller *et al.*, 2012). Enfin, il est aussi proposé ici que la formation des « thick red boles » aurait pu être favorisée par un climat plus humide et plus frais, lui-même conséquence de l'intense activité volcanique de la phase 2 (Figure 3.2).

Le scénario continu de l'éruption des « Western Ghats » a ensuite été couplé à des données géochimiques élémentaires (majeurs et traces) (Bonnefoy, 2005).
Deux signatures élémentaires distinctes ont pu être identifiées le long de cette section. Deccan1 correspond aux formations inférieures (Jawhar à Bushe) et montre une implication claire de la croûte continentale (contamination/assimilation). Deccan2 (Poladpur à Mahabaleshwar) apparaît, à l'inverse, moins contaminée par la croûte continentale, plus homogène et plus évolué que Deccan1 (Figure 5.5). La transition entre Deccan1 et 2 s'est produite au cours de l'éruption de la formation Poladpur (Figure 5.7) et correspond à la fin de la phase 2 (Chenet *et al.*, 2007).
Les signatures élémentaires de Deccan 1 et 2 indiquent une origine en moyenne profonde, dans le champ de stabilité du grenat ($Gd/Yb_n > 1.6$, Figure 5.6). Néanmoins, Deccan1 montre quatre excursions de bas Gd/Yb_n et Nb/La_n dans les formations Jawhar inférieure et supérieure, Khandala-Bushe et Poladpur supérieure compatibles avec des sources magmatiques à plus faible profondeur, hors du champ de stabilité du grenat ($Gd/Yb_n < 1.8$), et avec d'intenses épisodes d'assimilation crustale ($Nb/La_n \sim 0.5$) (Figure 5.7). Le caractère ponctuel de ces excursions est confirmé par leur association systématique avec des groupes directionnels (Chenet *et al.*, 2009) impliquant une durée de l'ordre de quelques centaines d'années. Il est proposé ici que ces excursions correspondent à des processus d'érosion/délamination lithosphériques localisés. En effet, la mise en place localisée d'intenses réactions panache-lithosphère aurait résulté, à ces endroits, en une forte production magmatique par décompression ($Gd/Yb_n < 1.8$). De plus, la proximité locale du matériel mantellique (panache) avec la croûte continentale aurait engendré des épisodes de forte assimilation crustale ($Nb/La_n < 0.6$). Ces chenaux d'érosion lithosphérique localisée auraient

ensuite été simplement bouchés par les restites issues de la fusion par décompression. Ce phénomène aurait artificiellement augmenté la profondeur des sources magmatiques au point de revenir dans le champ de stabilité du grenat ($Gd/Yb_n > 1.6$). L'épuisement des conduits magmatiques par ces épisodes de forte assimilation crustale aurait, parallèlement, résulté en l'augmentation du rapport Nb/La_n. Ces excursions sont réparties au cours de la phase 2 (50 ka), ce qui correspond aux résultats numériques de Sobolev et al (2011). Outre la contrainte temporelle apportée par ces derniers, Sobolev et al ont aussi montré, numériquement, que l'interaction entre un panache mantellique et une lithosphère de 140 km d'épaisseur (2.4) ne pouvait résulter qu'en une érosion/délamination localisée de la lithosphère. L'érosion localisée de la lithosphère indienne est aussi confirmée par des mesures actuelles (Figure 2.7), ainsi que par la localisation des principaux essaims de dykes (Vanderkluysen *et al.*, 2011). Enfin, il est probable que l'importante assimilation crustale indiquée par les excursions en Gd/Yb_n et Nb/La_n – lesquelles précèdent la limite K-Pg – ait eu une répercussion majeure sur le dégazage magmatique (Self *et al.*, 2008a, Ganino & Arndt, 2009, Sobolev *et al.*, 2011).

L'analyse par microsonde électronique d'olivines magnésiennes des Trapps du Deccan et de l'île de la Réunion a permis de reconstruire les magmas primaires et les sources magmatiques de pour ces deux localités, elles-mêmes respectivement représentatives des stades précoce (tête de panache) et tardif (queue de panache) du panache mantellique du Deccan.
La composition des phénocristaux d'olivine de la formation Thakurvadi des Trapps du Deccan et de l'île de la Réunion montre un excès de nickel (Ni) et un appauvrissement en manganèse (Mn) (Figure 6.3). Ce type d'anomalie compositionnelle (par rapport à des olivines issues d'un produit de fusion de la péridotite) est caractéristique de la présence d'une source hybride (pyroxenite + péridotite) dans la tête du panache du Deccan. Il est possible de relier ces anomalies en Ni en Mn à la fraction (Xpx) de liquide pyroxénitique dans les magmas primaires (Sobolev *et al.*, 2005) : Xpx (Deccan) = 65%, Xpx (Réunion) = 50% (Fig. 6.5).
Les inclusions vitreuses de ces olivines ont été analysées. Celles du Deccan (formation Thakurvadi) montrent des concentrations en volatiles comparables à celles publiées par Self et al (2008a) (valeurs moyennes : K_2O = 0.48 wt%, Cl = 0.02 wt%, S = 0.05 wt%, Figure 6.7). Ces concentrations sont beaucoup plus basses que celles rapportées pour les Trapps de Sibérie (Sobolev *et al.*, 2009a). Il est néanmoins possible et probable que, lors de la mise en place des Trapps du Deccan, le dégazage magmatique ait été beaucoup plus important pendant, ou juste

avant (Sobolev *et al.*, 2011), les épisodes de forte assimilation crustale mentionnés plus haut (excursions en Gd/Yb_n et Nb/La_n, Figure 5.7). Les inclusions vitreuses de la Réunion montrent une composition en volatiles légèrement différente de celles du Deccan (valeurs moyennes : K_2O=0.70 wt%, Cl = 0.02 wt%, S = 0.09 wt%). Il est intéressant de noter que le rapport Cl/K_2O varie entre le Deccan et la Réunion (0.40 et 0.30, respectivement). Plus précisément, pour une concentration de S donnée, Cl/K_2O est deux fois plus élevé dans les inclusions vitreuses du Deccan que dans celles de la Réunion (Figure 6.7). Cette observation suggère soit une influence de la contamination crustale (Figure 5.7), soit une influence du matériel crustale recyclé dans le panache du Deccan (Sobolev *et al.*, 2009b, 2011).

Les inclusions de spinels (dans ces mêmes olivines) ont été analysées afin de contraindre certains paramètres magmatiques importants tels que la température et l'état d'oxydation des magmas. Ces résultats ont ensuite été utilisés pour reconstituer les magmas primaires à l'origine des olivines du Deccan et de la Réunion (7.1). Puis les compositions et les paramètres physiques de ces magmas primaires ont été intégrés à deux modèles pétrologiques indépendants permettant de reconstituer les sources magmatiques des deux localités (Deccan et Réunion). L'un de ces modèles repose entièrement sur la géochimie (Sobolev *et al.*, 2005), l'autre repose sur la thermodynamique (Katz *et al.*, 2003) (7.2).

Les résultats de ces diverses étapes de modélisation convergent et révèlent des différences notables entre le stade « tête de panache » du Deccan et le stade tardif (« queue de panache ») de la Réunion. Durant la mise en place des Trapps du Deccan, le panache était chaud (Tp ~1590-1600 °C) et transportait, en comparaison avec d'autres localités (Sobolev *et al.*, 2007), une importante quantité de matériel crustale recyclé (XRC ~ 14%). Cette importante composante recyclée dans les sources des Trapps du Deccan exclue la possibilité d'une surrection syn-volcanique importante (Sobolev *et al.*, 2011), et, de fait, réconcilie les observations contradictoires de plusieurs auteurs (ex : Saunders *et al.*, 2007, Sheth, 2007). Les sources magmatiques hybrides (éclogite + pyroxénite + péridotite) des laves du Deccan ont endurées un taux de fusion de l'ordre de 12% à 4.5 GPa et la contribution des produits de fusion de la pyroxénite à la génération des magmas primaires fut de 65% (Table 7–9). La forte signature du grenat dans la plupart des laves du Deccan (Figure 5.6) implique que la lithosphère indienne n'ait été que peu affectée par l'activité du panache. Cette particularité est expliquée par 1) l'importante épaisseur initiale de la lithosphère indienne (140 km, 2.4) et 2) par l'étendue limitée des processus d'érosion/délamination due à l'existence de zones de

faiblesses préexistantes dans la plaque indienne (Murthy, 2002) permettant l'évacuation rapide des produits de fusion (Sobolev *et al.*, 2011).

Quelques 66 Ma plus tard, le panache du Deccan est toujours actif (île de la Réunion). Il est à présent plus froid d'une centaine de degrés (Tp ~1490-1450 °C) et transporte de plus faibles quantités de matériel crustale recyclé (XRC ~7 %). Les sources magmatiques de la Réunion entrent actuellement en fusion à hauteur de 4 % à 3.5 GPa et la contribution des produits de fusion de la pyroxénite à la génération des magmas primaires de la Réunion s'élève à 50 % (Table 7–9).

Figure 8.1 est une illustration, basée sur les résultats numériques de Sobolev et al (2011), de la différence entre les Trapps du Deccan et l'île de la Réunion. Cette figure inclut aussi une comparaison avec les Trapps de Sibérie.

IV.6. Perspectives

Dans les conclusions de sa thèse, Anne-Lise Chenet (Chenet, 2006) propose les perspectives suivantes :

- Confirmer que l'éruption des Trapps du Deccan s'est produite en deux phases distinctes en datant les échantillons à polarité transitionnelle de la formation Latifwadi et en étudiant la zone nord de la province principale du Deccan (Rivière Tapti), qui n'a pas encore été datée
- Ré-échantillonner la transition entre les formations Khandala et Bushe ainsi que Bushe et Poladpur dans la mesure ou les affleurements de Bushe sont de piètre qualité et n'ont par permis, pour l'instant, de construire une section continue à cet endroit
- Etudier les formations inférieures, spécialement dans la région nord (Narmada) pour contraindre les phases d'activité précoce du Deccan
- Les conséquences environnementales de l'éruption des Trapps du Deccan devraient être examinées à l'aide de modèles numériques d'étendue globale (planétaire) prenant en compte la chimie et la physique de la stratosphère
- Enfin, il serait intéressant de comparer les Trapps du Deccan avec la province magmatique de Karoo (Afrique su Sud, 180 Ma), pour laquelle les signes d'extinction de masse associés sont absents, malgré des volumes éruptés similaires

La présente thèse a été commencée en janvier 2011 et avait pour objectif initial de combiner les approches géochimiques, pétrologiques et géodynamiques en construisant un modèle numérique précis du panache du Deccan au cours du temps, similaire à celui de Sobolev et al (2011) pour les Trapps de Sibérie. Ce projet aurait donc pu adresser les trois premiers points des perspectives d'Anne-Lise Chenet mentionnées ci-dessus. Néanmoins, des difficultés et retards dans l'avancement de ce projet, dus à la mise en place d'une nouvelle microsonde électronique JEOL JXA 8230 à ISTerre ainsi qu'à la difficulté d'obtenir des contacts sur le terrain en Inde n'ont pas permis de mener à bien le travail de terrain nécessaire. Cependant, l'aide précieuse de Frédéric Fluteau et Vincent Courtillot de l'Insitut de Physique du Globe de Paris (IPGP), l'accès à leur collection d'échantillon (Chenet *et al.*, 2008, 2009), et à leur base de données à permis de participer à l'étude des Trapps du Deccan de la manière suivante :

- Réinterprétation des données de paléomagnétisme de haute résolution et des âges $^{39}Ar/^{40}Ar$ de Chenet et al (2007, 2008, 2009) par la mise en place d'un scénario continu de la mise en place des Trapps du Deccan
- Couplage de ce scénario continu avec des données paléoenvironnementales (Li & Keller, 1998, Robinson *et al.*, 2009) ainsi qu'avec des données géochimiques en éléments majeurs et traces sur roche totale (Bonnefoy, 2005)
- Application des méthode pétrologiques sur olivine (Sobolev *et al.*, 2005, 2007) et reconstitution des magmas primaires à l'origine des laves des Trapps du Deccan et de l'île de la Réunion ainsi que de leur sources

L'auteur de ce manuscrit espère fournir quelques éléments nouveaux permettant l'avancement de la compréhension de la mise en place des Trapps du Deccan.

Ce travail bénéficierait largement de l'approfondissement des points suivants :

- Des travaux de terrain permettraient de répondre aux trois premiers points des perspectives proposées dans la thèse d'Anne-Lise Chenet (Chenet, 2006). Ils permettraient également de collecter d'avantage de basaltes picritiques, aussi bien dans la province principale du Deccan que dans les régions périphériques (ex : Gujarat, 2.3.2)
- De manière plus spécifique, les excursions de bas Gd/Yb_n et Nb/La_n (Figure 5.7) devraient être étudiées en détail afin de mieux contraindre leurs durées, leurs origines et le dégazage magmatique associé

- Des travaux de terrains seraient aussi nécessaires aux Seychelles où des intrusions de compositions similaires à celles de la formation Bushe ont été observées (Owen-Smith *et al.*, 2013).
- Les résultats des modèles pétrologiques (7.2) devraient être intégrés dans un modèle numérique similaire à celui de Sobolev et al (2011) et comparés à d'autres contextes, tels que celui des Trapps de Sibérie.

10. References

Abouchami, W., Hofmann, A. W., Galer, S. J. G., Frey, F. A., Eisele, J. & Feigenson, M. D. (2005). Lead isotopes reveal bilateral asymetry and vertical continuity in the Hawaiian mantle plume. *Nature* **434**, 851-856.

Abramov, O. & Kring, D. K. (2007). Numerical modelling of impact-induced hydrothermal activity at the Chicxulub crater. *Meteoritics & Planetary Science* **42**, 93-112.

Agrell, S. O. & Long, J. V. P. (1960). The application of the scanning X-ray microanalyser to mineralogy. In: Engström, A., Cosslett, V. E. & Pattee, H. H. (eds.) *X-ray Microscopy and Microanalysis*. Amsterdam: Elsevier, 391-400.

Albarède, F., Luais, B., Fitton, G., Semet, M., Kaminski, E., Upton, B. G. J., Bachlèlery, B. & Cheminée, J.-L. (1997). The Geochemical Regimes of Piton de la Fournaise Volcano (Réunion) During the Last 530 000 Years. *Journal of Petrology* **38**, 171-201.

Albarède, F. & Tamagnan, V. (1988). Modelling the recent geochemical evolution of the Piton de la Fournaise volcano, Réunion Island, 1931-1986. *Journal of Petrology* **29**, 997-1030.

Allègre, C. J., Brick, J. L., Capmas, F. & Courtillot, V. (1999). Age of the Deccan traps using 187Re-187Os systematics. *Earth and Planetary Science Letters* **170**, 197-204.

Allègre, C. J. & Luck, J. M. (1980). Osmium isotopes as petrogenetic and geological tracers. *Earth and Planetary Science Letters* **48**, 148-154.

Allègre, C. J. & Turcotte, D. L. (1986). Implications of a two-component marble-cake mantle. *Nature* **323**, 123-127.

Almeev, R. R., Holtz, F., Koepke, J., Parat, F. & Botcharnikov, R. E. (2007). The effect of H2O on olivine crystallization in MORB: Experimental calibration at 200 MPa. *American Mineralogist* **92**, 670-674.

Alvarez, L. W., Alvarez, W., Asaro, F. & Michel, H. V. (1980). Extraterrestrial Cause for the Cretaceous-Tertiary Extinction. *Science* **208**, 1095-1108.

Alvarez, W. (2003). Comparing the Evidence Relevant to Impact and Flood Basalt at Times of Major Mass Extinctions. *Astrobiology* **3**, 153-161.

Anderson, D. L. (1994). The sublithospheric mantle as a source of continental flood basalts; the case against the continental lithosphere and plume head reservoirs. *Earth and Planetary Science Letters* **123**, 269-280.

Anderson, D. L. (2000a). The Thermal State of the Upper Mantle; No Role for Mantle Plumes. *Geophysical Research Letters* **27**, 3623-3626.

Anderson, D. L. (2000b). The thermal state of the upper mantle: no role for mantle plumes. *Geophysical Research Letters* **27**, 3623-3626.

Anderson, D. L. (2006). Speculations on the nature and cause of mantle heterogeneity. *Tectonophysics* **416**, 7-22.

Armitage, J. J., Collier, J. S., Minshull, T. A. & Henstock, T. J. (2011). Thin oceanic crust and flood basalts: India-Seychelles breakup. *Geochemistry Geophysics Geosystems* **12**, 25pp.

Arndt, N. T., Czamanske, G. K., Wooden, J. L. & Fedorenko, V. A. (1993). Mantle and crustal contributions to continental flood volcanism. *Tectonophysics* **223**, 39-52.

Arora, K., Tiwari, V. M., Singh, B., Mishra, D. C. & Grevemeyer, I. (2012). Three dimensional lithospheric structure of the western continental margin of India constrained from gravity modelling: implications for tectonic evolution. *Geophysical Journal International* **190**, 131-150.

Artemieva, I. M. (2006). Global 1° x 1° thermal moodel TC1 for the continental lithosphere: Implications for lithosphere secular evolution. *Tectonophysics* **416**, 245-277.

Artemieva, I. M. (2009). The continental lithosphere: Reconciling thermal, seismic, and petrologic data. *Lithos* **109**, 23-46.

Bajpai, S., Holmes, J., Bennett, C., Mandal, N. & Khosla, A. (2013). Palaeoenvironement of Northwestern India during the late-Cretaceous Deccan volcanic episode from trace-element and stable-isotope geochemistry of intertrappean ostracod shells. *Global and Planetary Change* **107**, 82-90.

Bajpai, S. & Prasad, G. V. R. (2000). Cretaceous age for Ir-rich Deccan intertrappean deposits: palaeontological evidence from Anjar, western India. *Journal of the Geological Society, London* **157**, 257-260.

Baksi, A. K. (2001). The Rajahmundry Traps, Andhra Pradesh: Evaluation of their petrogenesis relative to the Deccan Traps. *Proceedings of the Indian Academy of Sciences* **110**, 397-407.

Baksi, A. K. (2005). Comment on "40Ar/39Ar dating of the Rajahmundry Traps, eastern India and their relationship to the Deccan Traps" by Knight et al. *Earth and Planetary Science Letters* **239**, 368-373.

Baksi, A. K., Byerly, G. R., Chan, L. H. & Farrar, E. (1994). Intracanyon flows in the Deccan province, India: case history of the Rajahmundry Traps. *Geology* **22**, 605-608.

Banerjee, P. K., Ghose, N. C., Ravikumar, V. & Chacko, S. (1996). Petrography, geomagnetism, and rare-earth element abundances of the Rajahmundry lavas, eastern India. *Journal of Southeast Asian Earth Sciences* **13**, 139-143.

Basu, A. R., Renne, P. R., DasGupta, D. K., Teichmann, F. & Poreda, R. J. (1993). Early and Late Alkali Igneous Pulses and a High-3He Plume Origin for the Deccan Flood Basalts. *Science* **261**, 902-906.

Batanova, V. & Sobolev, A. V. (2013). A new analytical protocol for high precision EPMA of olivine. *Goldschmidt conference*.

Batanova, V. G., Belousov, I. A., Savelieva, G. N. & Sobolev, A. V. (2011). Consequences of Channelized and Diffuse Melt Transport in Supra-subduction Zone Mantle: Evidence from the Voykar Ophiolite (Polar Urals). *Journal of Petrology* **52**, 2483-2521.

Beane, J. E. (1988). Flow stratigraphy, chemical variation and petrogenesis of Deccan flood basalts from the Western Ghats, India. Washington State University.

Beane, J. E., Turner, C. A., Hooper, P. R., Subbarao, K. V. & Walsh, J. N. (1986). Stratigraphy, composition and form of the Deccan Basalts, Western Ghats, India. *Bulletin of Volcanology* **48**, 61-83.

Belcher, C. M., Collinson, M. E., Sweet, A. R., Hildebrand, A. R. & Scott, A. C. (2003). Fireball passes and nothgin burns - The role of thermal radiation in the Cretaceous-Tertiary event: Evidence from the charcoal record of North America. *Geology* **31**, 1061-1064.

Bennett, K. D. (1990). Milankovitch cycles and their effects on species in ecological and evolutionary time. *Paleobiology* **16**, 11-21.

Bhattacharji, S., Sharma, R. & Chatterjee, N. (2004). Two- and three-dimensional gravity modeling along western continental margin and intraplate Narmada-Tapti rifts: Its relevance to Deccan flood basalt volcanism. *Proceedings of the Indian Academy of Sciences* **113**, 771-784.

Bhattacharya, G. C., Chaubey, A. K., Murty, G. P. S., Srinivas, K., Sarma, K. V. L. N. S., Subrahmanyam, V. & Krishna, K. S. (1994). Evidence for seafloor spreading in the Laxmi Basin, northeastern Arabian Sea. *Earth and Planetary Science Letters* **125**, 211-220.

Bhattacharya, S. K., Ma, G. S.-K. & Matsuhisa, Y. (2013). Oxygen isotope evidence for crustal contamination in Deccan Basalts. *Chemie der Erde* **73**.

Biwas, S. K. (2005). A review of structure and tectonics of Kutch basin, western India, with special reference to earthquakes. *Current Science* **88**, 1592-1600.

Blanford, W. T. (1867). On the Traps and intertrappean beds of western and central India. *Memoir - Geological Survey of India* **6**, 137-162.

Boehler, R. (1993). Temperatures in the Eath's core from melting-point measurements of iron at high static pressures. *Nature* **363**, 534-536.

Bogue, S. W. & Glen, J. M. G. (2010). Very rapid geomagnetic field change recorded by the partial remagnetization of a lava flow. *Geophysical Research Letters* **37**.

Bonnefoy, B. (2005). Evolution géochimique des laves des trapps du Deccan et détermination des concentrations en S, F et Cl dans des inclusions vitreuses de Rajahmundry. *Institut de Physique du Globe de Paris*. Paris: Université Paris VI.

Borges, M. R. (2007). Life Cycle of Deccan Trap Magma Chambers: A Crystal Scale Elemental and Strontium Isotopic Investigation. *FIU Electronic Theses and Dissertations* **Paper 10**.

Borges, M. R., Sen, G., Hart, G. L., Wolff, J. A. & Chandrasekharam, D. (2013). Plagioclase as recorder of magma chamber processes in the Deccan Traps: Sr-isotope zoning and implications for Deccan eruptive event. *Journal of Asian Earth Sciences* **in press**.

Borisov, A. A. & Shapkin, A. I. (1990). A new empirical equation rating Fe3+/Fe2+ in magmas to their composition, oxygen fugacity, and temperature. *Geochemistry International* **27**, 111-116.

Boulila, S., Galbrun, B., Miller, K. G., Pekar, S. F., Browning, J. V., Laskar, J. & Wright, J. D. (2011). On the origin of Cenozoic and Mesozoic "third-order" eustatic sequences. *Earth-Science Reviews* **109**, 94-112.

Bowen, N. L. (1928). *The evolution of igneous rocks*: Princeton University Press.

Buffetaut, E. (1987). On the age of dinosaur fauna from Lameta Formation; Upper Cretaceous of Central India. *Newsletter on Stratigraphy* **18**, 1-6.

Bureau, H., Métrich, N., Pineau, F. & Semet, M. P. (1998a). Magma-conduit interaction at Piton de la Fournaise volcano (Réunion Island): a melt and fluid inclusion study. *Journal of Volcanology and Geothermal Research* **84**, 39-60.

Bureau, H., Pineau, F., Métrich, N., Semet, M. P. & Javoy, M. (1998b). A melt and fluid inclusion study of the gas phase at Piton de la Fournaise volcano (Réunion Island). *Chemical Geology* **147**, 115-130.

Burke, K. & Torsvik, T. H. (2004). Derivation of Large Igneous Provinces of the past 200 million years from long-term heterogeneities in the deep mantle. *Earth and Planetary Science Letters* **227**, 531-538.

Burke, W. H., Denison, R. E., Hetherington, E. A., Koepnick, R. B., Nelson, H. F. & Otto, J. B. (1982). Variation of seawater 87Sr/86Sr throughout Phanerozoic time. *Geology* **10**, 516-519.

Campbell, C. E., Oboh-Ikuenobe, F. E. & Eifert, T. L. (2008). Chapter 11: Megatsunami deposit in Cretaceous-Paleogene boundary interval of southeastern Missouri. In: Evans, K. R., Horton-Jr, J. W., King-Jr, D. T. & Morrow, J. R. (eds.) *SPE437: The Sedimentary Record of Meteorite Impacts*. Boulrder: The Geological Society of America, 189-198.

Campbell, I. H. (2005). Large Igneous Provinces and the Mantle Plume Hypothesis. *Elements* **1**, 265-269.

Campbell, I. H. & Griffiths, R. W. (1990). Implications of mantle plume structure for the evolution of flood basalts. *Earth and Planetary Science Letters* **99**, 79-93.

Cande, S. C. & Kent, D. V. (1995). Revised calibration of the geomagnetic polarity timescale for the Late Cretaceous and Cenozoic. *Journal of Geophysical Research* **100**, 6093-6095.

Carlson, R. W., Graham-Pearson, D. & James, D. E. (2005). Physical, chemical, and chronological characteristics of continental mantle. *Reviews of Geophysics* **43**.

Castaing, R. (1951). Applications des sondes électroniques à une méthode d'analyse ponctuelle chimique et cristallographique. Université de Paris.

Cazenave, A., Souriau, A. & Dominh, K. (1989). Global coupling of Earth surface topography with hotspots, geoid and mantle heterogeneities. *Nature* **340**, 54-57.

Chalapathi Rao, N. V., Burgess, R., Lehmann, B., Mainkar, D., Pande, S. K., Hari, K. R. & Bodhankar, N. (2011a). 40Ar/39Ar ages of mafic dykes from the Mesoproterozoic Chhattisgarh basin, Bastar craton, Central India: Implications for the origin and spatial extent of the Deccan Large Igneous Province. *Lithos* **125**, 994-1005.

Chalapathi Rao, N. V. & Lehmann, B. (2011). Kimberlites, flood basalts and mantle plumes: New insights from the Deccan Large Igneous Province. *Earth-Science Reviews* **107**, 315-324.

Chalapathi Rao, N. V., Lehmann, B. & Balaram, V. (2013). Platinum-group element (PGE) geochemistry of Deccan orangeites, Bastar craton, central India: Implication for a non-terrestrial origin for iridium enrichment at the K_Pg boundary. *Journal of Asian Earth Sciences* **in press**.

Chalapathi Rao, N. V., Lehmann, B., Mainkar, D. & Belyatski, B. (2011b). Pretogenesis of the end-Cretaceous diamondiferous Behradih orangeite pipe: implication for mantle plume-lithosphere interaction in the Bastar craton, Central India. *Contribution to Mineralogy and Petrology* **161**, 721-742.

Chalapathi Rao, N. V., Rao, C. V. D. & Das, S. (2012). Petrogenesis of Lamprophyres from Chhota Udepur area, Narmada rift zone, and its relation to Deccan magmatism. *Journal of Asian Earth Sciences* **45**, 24-39.

Chandrasekharam, D., Mahoney, J. J., Sheth, H. C. & Duncan, R. A. (1999). Elemental and Nd-Sr-Pb isotope geochemistry of flows and dikes from the Tapi rift, Deccan flood basalt province, India. *Journal of Volcanology and Geothermal Research* **93**, 111-123.

Channell, J. E. T. & Lehman, B. (1997). The last two geomagnetic polarity reversals recorded in high-deposition-rate sediment drifts. *Nature* **389**, 712-715.

Chase, C. G. (1981). Oceanic island Pb: two-stage histories and mantle evolution. *Earth and Planetary Science Letters* **52**, 277-284.

Chatterjee, N. & Bhattacharji, S. (2008). Trace Element Variations in Deccan Basalts: Roles of Mantle Melting, Fractional Crystallization and Crustal Assimilation. *Journal Geological Society of India* **71**, 171-188.

Chatterjee, S., Goswami, A. & Scotese, C. R. (2012). The longest voyage: Tectonic, magmatic, and paleoclimatic evolution of the Indian plate during its northward flight from Gondwana to Asia. *Gondwana Research* **23**, 238-267.

Chatterjee, S., Guven, N., Yoshinobu, A. & Donofrio, R. (2006). Shiva Structure: a possible KT boundary impact crater on the western shelf of India. *Museum of Texas Tech University Special Publications* **50**, 39pp.

Chenet, A.-L. (2006). Reconstruction de la structure de la séquence éruptive des Traps du Deccan, Inde : conséquences climatiques et environnementales. *Equipe de Paléomagnétisme*. Paris: Institut de Physique du Globe de Paris, 359.

Chenet, A.-L., Courtillot, V., Fluteau, F., Gérard, M., Quidelleur, X., Khadri, S. F. R., Subbarao, K. V. & Thordarson, T. (2009). Determination of rapid Deccan eruptions across the Cretaceous-Tertiary boundary using paleomagnetic secular variation: 2. Constraints from analysis of eight new sections and synthesis for a 3500-m-thick composite section. *Journal of Geophysical Research* **114**.

Chenet, A.-L., Fluteau, F., Courtillot, V., Gérard, M. & Subbarao, K. V. (2008). Determination of rapid Deccan eruptions across the Cretaceous-Tertiary boundary using paleomagnetic secular variation: Results frim a 1200-m-thick section in the Mahabaleshwar escarpment. *Journal of Geophysical Research* **113**.

Chenet, A.-L., Quidelleur, X., Fluteau, F., Courtillot, V. & Bajpai, S. (2007). ^{40}K-^{40}Ar dating of the Main Deccan large igneous province: Further evidence of KTB age and short duration. *Earth and Planetary Science Letters* **263**, 1-15.

Class, C. & Goldstein, S. L. (2005). Evolution of helium isotopes in the Earth's mantle. *Nature* **436**, 1107-1112.

Coccioni, R., Ferraro, E., Lirer, L., Luciani, F., Marsili, V. & Spezzaferri, S. (2004). New Insights on the Late Cretaceous-Eocene Foraminiferal Record from the Classical Bottaccione and Contessa Pelagic Tethyan Sections (Gubbio, Central Italy): Results from High Resolution Study and a New Sample Preparation Technique. *32nd IGC*, 340.

Coe, R. S., Prévot, M. & Camps, P. (1995). New evidence for extraordinarily rapid change of the geomagnetic field during a reversal. *Nature* **374**, 687-692.

Coffin, M. F. & Eldholm, O. (1994). Large Igneous Provinces: Crustal Structure, Dimensions, and External Consequences. *Reviews of Geophysics* **32**, 1-36.

Cohen, A. S. & Coe, A. L. (2002). New geochemical evidence for the onset of volcanism in the Central Altantic magmatic province and environmental change at the Triassic-Jurassis boundary. *Geology* **30**, 267-270.

Collier, J. S., Sansom, V., Ishizuka, O., Taylor, R. N., Minshull, T. A. & Whitmarsh, R. B. (2008). Age of Seychelles-India break-up. *Earth and Planetary Science Letters* **272**, 264-277.

Coogan, L. A., Saunders, A. D. & Wilson, R. N. (2014). Aluminium-in-olivine thermometry of primitive basalts: Evidence of an anomalously hot mantle source for large igneous provinces. *Chemical Geology* **in press**.

Courtillot, V., Besse, J., Vandamme, D., Montigny, R., Jaeger, J.-J. & Cappetta, H. (1986). Deccan flood basalts at the Cretaceous/Tertiary boundary? *Earth and Planetary Science Letters* **80**, 361-374.

Courtillot, V., Davaille, A., Besse, J. & Stock, J. (2003). Three dstinct types of hotspots in the Earth's mantle. *Earth and Planetary Science Letters* **205**.

Courtillot, V., Féraud, G., Maluski, H., Vandamme, D., Moreau, M. G. & Besse, J. (1988). Deccan flood basalts and the Cretaceous/Tertiary boundary. *Nature* **333**.

Courtillot, V. & Fluteau, F. (2010). Cretaceous Extinctions: The Volcanic Hypothesis. *Science* **328**, 973-974.

Courtillot, V., Gallet, Y., Rocchia, R., Féraud, G., Robin, E., Hofmann, C., Bhandari, N. & Ghevariya, Z. G. (2000). Cosmic markers, 40Ar/39Ar dating and paleomagnetism of the KT sections in the Anjar Area of the Deccan large igneous province. *Earth and Planetary Science Letters* **182**, 137-156.

Courtillot, V. E. & Renne, P. R. (2003). On the ages of flood basalt events - Sur l'âge des trapps basaltiques. *Comptes Rendus de l'Académie des Sciences* **335**, 113-140.

Cox, K. G. & Hawkesworth, J. (1985). Geochemical Stratigraphy of the Deccan Traps at Mahabaleshwar, Western Ghats, India, with Implications for Open System Magmatic Processes. *Journal of Petrology* **26**, 355-377.

Cramer, B. S., Miller, K. G., Barrett, P. J. & Wright, J. D. (2011). Late Cretaceous-Neogene trends in deep ocean temperature and continental ice volume: Reconciling records of benthic foraminiferal geochemistry (d18O and Mg/Ca) with sea level history. *Journal of Geophysical Research* **116**.

Cripps, J. A., Widdowson, M., Spicer, R. A. & Jolley, D. W. (2005). Coastal ecosystem responses lo late stage Deccan Trap volcanism: the post K-T boundary (Danian) palynofacies of Mumbai (Bombay), west India. *Palaeogeography, Palaeoclimatology, Palaeoecology* **216**, 303-332.

Cullen, A., Vicenzi, E. & McBirney, A. R. (1989). Plagioclase-ultraphyric basalts of the Galapagos archipelago. *Journal of Volcanology and Geothermal Research* **37**, 325-337.

Czamanske, G. K., Gurevitch, A. B., Fedorenko, V. & Simonov, O. (1998). Demise of the Siberian plume: Paleogeographic and paleotectonic reconstruction from the prevolcanic and volcanic record, north-central Siberia. *International Geology Review* **40**, 95-115.

Damuth, J. E. & Johnson, D. A. (1989). Morphology, sediments and structure of the Amirante Trench, Western Indian Ocean: implications for trench origin. *Marine and Petroleum Geology* **6**, 232-242.

Danyushevsky, L. V. (2001). The effect of small amounts of H2O on crystallisation of mid-ocean ridge and backarc basin magmas. *Journal of Volcanology and Geothermal Research* **110**, 265-280.

Danyushevsky, L. V., Della-Pasqua, F. N. & Sokolov, S. (2000a). Re-equilibration of melt inclusions trapped by magnesian olivine phenocrysts from subduction-related magmas: petrological implications. *Contribution to Mineralogy and Petrology* **138**, 68-83.

Danyushevsky, L. V., Eggins, S. M., Falloon, T. J. & Christie, D. M. (2000b). H2O Abundance in Depleted to Moderately Enriched Mid-ocean Ridge Magmas; Part I: Incompatible Behaviour, Implications for Mantle Storage, and Origin of Regional Variations. *Journal of Petrology* **41**, 1329-1364.

Danyushevsky, L. V., McNeill, A. W. & Sobolev, A. (2002a). Experimental and petrological studies of melt inclusions in phenocrysts from mantle-derived magmas: an overview of techniques, advantages and complications. *Chemical Geology* **183**, 5-24.

Danyushevsky, L. V. & Plechov, P. (2011). Petrolog3: Integrated software for modeling crystallization processes. *Geochemistry Geophysics Geosystems* **12**, Q07021.

Danyushevsky, L. V. & Sobolev, A. V. (1996). Ferric-ferrous ratio and oxygen fugacity calculations for primitive mantle-derived melts: calibration of an empirical technique. *Mineralogy and Petrology* **57**, 229-241.

Danyushevsky, L. V., Sokolov, S. & Falloon, T. J. (2002b). Melt inclusions in olivine phenocrysts: using diffusive re-equilibration to determine the cooling history of a crystal, with implications for the origin of olivine-phyric volcanic rocks. *Journal of Petrology* **43**, 1651-1671.

DeHoog, J. C. M., Gall, L. & Cornell, D. H. (2010). Trace-element geochemistry of mantle olivine and application to mantle petrogenesis and geothermobarometry. *Chemical Geology* **270**, 196-215.

DeMets, C., Gordon, R., Argus, D. & Stein, S. (1994). Effect of recent revisions to the geomagnetic reversal time scale on estimates of current plate motion. *Geophysical Research Letters* **21**.

Deniel, C., Kieffer, G. & Lecointre, J. (1992). New 230th-238U and 14C age determinations from Piton des Neiges volcano, Réunion - A revised chronology for the Differentiated Series. *Journal of Volcanology and Geothermal Research* **51**, 253-267.

DePaolo, D. J. (1981). Trace element and isotopic effects of combined wallrock assimilation and fractional crystallization. *Earth and Planetary Science Letters* **53**, 189-202.

DePaolo, D. J. & Ingram, B. L. (1985). High-resolution stratigraphy with strontium isotopes. *Science* **227**, 938-941.

Deshmukh, S. S., Aramaki, S., Shimizu, N., Kurasawa, N. & Konda, T. (1977). Petrography of the basalt flows exposed along Mahabaleshwar and Amboli sections in Western Ghats, India. *Records of the Geological Survey of India* **108**, 81-103.

Dessai, A. G. & Bertrand, H. (1995). The "Panvel Flexure" along the Western Indian continental margin: an extensional fault structure related to Deccan magmatism. *Tectonophysics* **241**, 165-178.

Dessert, C., Dupré, B., François, L. M., Schott, J., Gaillardet, J., Chakrapani, G. & Bajpai, S. (2001). Erosion of Deccan Traps determined by river geochemistry: impact on the global climate and the 87Sr/86Sr ratio of seawater. *Earth and Planetary Science Letters* **188**, 459-474.

Dessert, C., Dupré, B., Gaillardet, J., François, L. M. & Allègre, C. J. (2003). Basalt weathering laws and the impact of basalt weathering on the global carbon cycle. *Chemical Geology* **202**, 257-273.

Devey, C. W. (1986). Stratigraphy and geochemistry of the Deccan Traps lavas, Western India. University of Oxford.

Devey, C. W. & Cox, K. G. (1987). Relationship between crustal contamination and crystallisation in continental flood basalt magmas with special reference to the Deccan Traps of the Western Ghats, India. *Earth and Planetary Science Letters* **84**, 59-68.

Devey, C. W. & Stephens, W. E. (1991). Tholeiitic dykes in the Seychelles and the original spatial extent of the Deccan. *Journal of the Geological Society, London* **148**, 979-983.

Devey, C. W. & Stephens, W. E. (1992). Deccan-related magmatism west of the Seychelles-India rift. In: Storey, B. C., Alabaster, T. & Pankhurst, R. J. (eds.) *Magmatism and Causes of Continental Break-up*: Geological Society Special Publication, 271-291.

Dietmar Müller, R., Gaina, C., Roest, W. R. & Lundbek Hansen, D. (2002). A recipe for microcontinent formation. *Geology* **29**, 203-206.

Dietz, R. S. & Holden, J. C. (1970). Reconstruction of Pangea: Breakup and dispersion of continents, Permian to Present. *Journal of Geophysical Research* **75**, 4939-4956.

Dixon, J. E., Leist, L., Langmuir, C. H. & Schilling, J.-G. (2002). Recycled dehydrated lithosphere observed in plume-influenced mid-ocean-ridge basalt. *Nature* **420**, 385-389.

Donnelly, K. E., Goldstein, S. L., Langmuir, C. H. & Spiegelman, M. (2004). Origin of enriched ocean ridge basalts and implications for mantle dynamics. *Earth and Planetary Science Letters* **226**, 347-366.

Duncan, R. A. (1990). The volcanic record of the Réunion hotspot. In: Duncan, R. A., Backman, J., Peterson, L. C. & et.al. (eds.) *Proceedings of the Ocean Drilling Program, Scientific Restuls 115*. College Station, TX: Ocean Drilling Program, 3-10.

Duncan, R. A. & Pyle, D. G. (1988). Rapid eruption of the Deccan flood basalt at the Cretaceous/Tertiary boundary. *Nature* **333**, 841-844.

Duncan, R. A. & Richards, M. A. (1991). Hot spots, mantle plumes, flood basalts, and true polar wander. *Reviews of Geophysics* **29**, 31-50.

Duncumb, P. & Melford, D. A. (1957). A scanning microscope for X-ray emission pictures. In: Cosslett, V. E., Engström, A. & Pattee, H. H. (eds.) *X-ray microscopy and microradiography*. New York: Academic Press, 374-380.

Duraiswami, R. A., Bondre, N. R. & Dole, G. (2004). Possible lava tube system in a hummocky lava flow at Daund, western Deccan Volcanic Province, India. *Proceedings of the Indian Academy of Sciences* **113**, 819-829.

Duraiswami, R. A., Dole, G. & Bondre, N. (2003). Slabby pahoehoe from the western Deccan Volcanic Province: evidence for incipient pahoehoe-aa transitions. *Journal of Volcanology and Geothermal Research* **121**, 195-217.

Duraiswami, R. A., Gadpallu, P., Shaikh, T. N. & Cardin, N. (2013). Pahoehoe-a'a transitions in the lava flow fields of the western Deccan Traps, India-implications for emplacement dynamics, flood basalt architecture and volcanic stratigraphy. *Journal of Asian Earth Sciences* **in press**.

Eagles, G. & Hoang, H. H. (2014). Cretaceous to present kinematics on the Indian, African and Seychelles plates. *Geophysical Journal International* **196**, 1-14.

Eaton, D. W., Darbyshire, F., Evans, R. L., Grütter, H., Jones, A. G. & Yuan, X. (2009). The elusive lithosphere-asthenosphere boundary (LAB) beneath cratons. *Lithos* **109**, 1-22.

Ellam, R. M. (1992). Lithospheric thickness as a control on basalt geochemistry. *Geology* **20**, 153-156.

Ernst, R. E. & Bell, K. (2010). Large igneous provinces (LIPs) and carbonatites. *Mineralogy and Petrology* **98**, 55-76.

Famin, V., Welsch, B., Okumura, S., Bachèlery, P. & Nakashima, S. (2009). Three differentiation stages of a single magma at Piton de la Fournaise volcano (Reunion hot spot). *Geochemistry Geophysics Geosystems* **10**.

Farnetani, C. G. & Richards, M. A. (1994). Numerical investigations of the mantle plume initiation model for flood-basalt events. *Journal of Geophysical Research-Solid Earth* **99**, 13813-13833.

Farnetani, C. G. & Samuel, H. (2005). Beyond the thermal plume paradigm. *Geophysical Research Letters* **L03711**.

Fisk, M. R., Upton, B. G. J. & Ford, C. E. (1988). Geochemical and Experimental Study of the Genesis of Magmas of Reunion Island, Indian Ocean. *Journal of Geophysical Research* **93**, 4933-4950.

Foley, S. F. (2008). Rejuvenation and erosion of the cratonic lithosphere. *Nature Geoscience* **1**, 503-510.

Foley, S. F., Prelevic, D., Rehfeldt, T. & Jacob, D. E. (2013). Minor and trace elements in olivines as probes into early igneous and mantle melting processes. *Earth and Planetary Science Letters* **363**, 181-191.

Ford, C. E., Russell, D. G., Craven, J. A. & Fisk, M. R. (1983). Olivine-Liquid Equilibira: Temperature, Pressure and Composition Dependence of the Crystal/Liquid Cation Partition Coefficients for Mg, Fe2+n Ca and Mn. *Journal of Petrology* **24**, 256-266.

Foulger, G. R., Natland, J. H., Prescall, D. C. & Anderson, D. L. (2005). *Plates, plumes and paradigms*. Boulder, Colorado: The Geological Survey of America Inc.

Fretzdorff, S. & Haase, K. M. (2002). Geochemistry and petrology of lavas from the submarine flanks of Réunion Island (western Indian Ocean): implications for magma genesis and the mantle source. *Mineralogy and Petrology* **75**, 153-184.

Füri, E., Hilton, D. R., Bramley, J. M., Hémond, C., Dyment, J. & Day, J. M. D. (2011). Helium isotope variations between Réunion Island and the Central Indian Ridge (17°-21°S), New evidence for ridge-hot spot interaction. *Journal of Geophysical Research* **116**.

Furman, T., Frey, F. A. & Park, J.-H. (1991). Chemical constraints on the petrogenesis of mildly alkaline lavas from Vestmannaeyjar, Iceland: the Eldfell (1973) and Surtsey (1963-1967) eruptions. *Contribution to Mineralogy and Petrology* **109**, 19-37.

Ganerød, M., Torsvik, T. H., Hinsbergen, D. J. J. v., Gaina, C., Corfu, F., Werner, S., Owen-Smith, T. M., Ashwal, L. D., Webb, S. J. & Hendriks, B. W. H. (2011). Palaeoposition of the Seychelles microcontinent in relation to the Deccan Traps and the Plume Generation Zone in Late Cretaceous-Early Palaeogene time. *Geological Society, London, Special Publications* **357**, 229-252.

Ganino, C. & Arndt, N. T. (2009). Climate changes caused by degassing of sediments during the emplacement of large igneous provinces. *Geology* **37**, 323-326.

Garzione, C. N. (2008). Surface uplift of Tibet and Cenozoic global cooling. *Geology* **36**, 1003-1004.

Gérard, M., Caquineau, S., Chenet, A.-L., Fluteau, F., Courtillot, V. & Subbarao, K. V. (2006). Red Boles in the Deccan traps: Time constraints from alteration processes. In: Abstracts, G. R. (ed.) *European Geosciences Union*.

Ghosh, P., Sayeed, M. R. G., Islam, R. & Hundekari, S. M. (2006). Inter-basaltic clay (bole bed) horizons from Deccan traps of India: Implications for palaeo-weathering and palaeo-climate during Deccan volcanism. *Palaeogeography, Palaeoclimatology, Palaeoecology* **242**, 90-109.

Gillot, P.-Y., Lefèvre, J.-C. & Nativel, P. E. (1994). Model for the structural evolution of the volcanoes of Réunion island. *Earth and Planetary Science Letters* **122**, 291-302.

Gradstein, F., Ogg, J. & Smith, A. (2004). *A Geologic Time Scale*. Cambridge, UK: Cambridge University Press.

Green, D. H. & Ringwood, A. E. (1967). The genesis of basaltic magmas. *Contribution to Mineralogy and Petrology* **15**, 103-190.

Gregory, L. C., Meert, J. G., Pradhan, V., Pandit, M. K., Tamrat, E. & Malone, S. J. (2006). A paleomagnetic and geochronologic stury of the Majhgawan kimberlite, India: Implications for the age of the Uppper Vindhyan Supergroup. *Precambrian Research* **149**, 65-75.

Griffin, W. L., O'Reilly, S. Y., Afonso, J. C. & Begg, G. C. (2009). The Composition and Evolution of Lithospheric Mantle: a Re-evaluation and its Tectonic Implications. *Journal of Petrology* **50**, 1185-1204.

Guha, D., Das, S., Srikarni, C. & Chakraborty, S. K. (2005). Alkali Basalt of Kachchh: Its Implication in the Tectonic Framework of Mesozoic of Western India. *Journal Geological Society of India* **66**, 599-608.

Gwalani, L. G., Rock, N. M. S., Chang, W.-J., Fernandez, S., Allègre, C. J. & Prinzhofer, A. (1993). Alkaline Rocks and Carbonatites of Amba Dongar and Adjacent Areas, Deccan Igneous Province, Gujarat, India: 1. Geology, Petrography and Petrochemistry. *Mineralogy and Petrology* **47**, 219-253.

Hallam, A. & Wignall, P. B. (1999). Mass extinctions and sea-level changes. *Earth-Science Reviews* **48**, 217-250.

Hammond, J. O. S., Collier, J. S., Kendall, J.-M., Helffrich, G. & Rümpker, G. (2012). Plume scar in the mantle lithosphere beneath the Seychelles revealed by seismic imaging. *Earth and Planetary Science Letters* **355-356**, 20-31.

Hart, S. R., Hauri, E. H., Oschmann, L. A. & Whitehead, J. A. (1992). Mantle Plumes and Entrainement: Isotopic Evidence. *Science* **256**, 517-520.

Hartnady, C. J. H. (1986). Amirante Basin, western Indian Ocean: Possible impact site of the Cretaceous/Tertiary extinction bolide? *Geology* **14**, 423-426.

Haywood, J. & Boucher, O. (2000). Estimates of the direct and indirect radiative forcing due to tropospheric aerosols: a review. *Reviews of Geophysics* **38**, 513-543.

Herzberg, C. (2011). Identification of Source Lithology in the Hawaiian and Canary Islands: Implications for Origins. *Journal of Petrology* **52**, 113-146.

Herzberg, C., Asimow, P. D., Arndt, N. T., Niu, Y., Lesher, C. M., Fitton, J. G., Cheadle, M. J. & Saunders, A. D. (2007). Temperature in ambient mantle and plumes: Constraints from basalts, picrites, and komatiites. *Geochemistry Geophysics Geosystems* **8**.

Herzberg, C., Asimow, P. D., Ionov, D. A., Vidito, C., Jackson, M. G. & Geist, D. (2013). Nickel and helium evidence for melt above the core-mantle boundary. *Nature* **493**, 393-397.

Herzberg, C. & Gazel, E. (2009). Petrological evidence for secular coolig in mantle plumes. *Nature* **458**, 619-622.

Herzberg, C. & O'Hara, M. J. (2002). Plume-Associated Ultramafic Magmas of Phanerozoic Age. *Journal of Petrology* **43**, 1857-1883.

Hess, J., Bender, M. & Schilling, J.-G. (1986). Seawater 87Sr/86Sr evolution from Cretaceous to present. *Science* **231**, 979-984.

Higgins, M. D. & Chandrasekharam, D. (2007). Nature of Sub-volcanic Magma Chambers, Deccan Province, India: Evidence from Quantitative Textural Analysis of Plagioclase Megacrysts in the Giant Plagioclase Basalts. *Journal of Petrology* **48**, 885-900.

Hodell, D. A. (1994). Editorial: Progress and paradox in strontium isotope stratigraphy. *Paleoceanography* **9**, 395-398.

Hodell, D. A., Mueller, P. A., McKenzie, J. A. & Mend, G. A. (1989). Strontium isotope stratigraphy and geochemistry of the late Neogene ocean. *Earth and Planetary Science Letters* **92**, 165-178.

Hofmann, A. W. (1988). Chemical differentiation of the Earth: the relationship between mantle, continental crust, and oceanic crust. *Earth and Planetary Science Letters* **90**, 297-314.

Hofmann, A. W. & White, W. M. (1982). Mantle plumes from ancient oceanic crust. *Earth and Planetary Science Letters* **57**, 421-436.

Hooper, P., Widdowson, M. & Kelley, S. (2010). Tectonic setting and timing of the final Deccan flood basalt eruptions. *Geology* **38**, 839-842.

Hooper, P. R. (1990). The timing of crustal extension and the eruption of continental flood basalts *Nature* **349**, 246-249.

Hooper, P. R., Subbarao, K. V., Beane, J. E. & Subbarao, K. V. (1988). The giant plagioclase basalts (GPBs) of the Western Ghats, Deccan Traps. *Memoir - Geological Society of India* **10**, 135-144.

Huang, S., Hall, P. S. & Jackson, M. G. (2011). Geochemical zoning of volcanic chains associated with Pacific hotspots. *Nature Geoscience* **4**, 874-878.

Huber, B. T., Norris, R. D. & MacLeod, K. G. (2002). Deep-sea paleotemperature record of extreme warmth during the Cretaceous. *Geology* **30**, 123-126.

Huismans, R. & Beaumont, C. (2011). Depth-dependent extension, two-stage breakup and cratonic underplating at rifted margins. *Nature* **473**, 74-78.

Huppert, H. E. & Sparks, S. J. (1985). Cooling and contamination of mafic and ultramafic magmas during ascent through continental crust. *Earth and Planetary Science Letters* **74**, 371-386.

Jaiprakash, B. C., Sungh, J. & Raju, D. S. N. (1993). Foraminiferal events across the K/T boundary and age of Deccan volcanism in Palakollu area, Krishna-Godavari Basin, India. *Journal of the Geological Society of India* **41**, 105-117.

James, D. E., Fouch, M. J., VanDecar, J. C. & Lee, S. v. d. (2001). Tectospheric structure beneath southern Africa. *Geophysical Research Letters* **28**.

Jay, A. E. & Widdowson, M. (2008). Stratigraphy, structure and volcanology of the south-easts Deccan continental flood basalt province: implications for eruptive extent and volumes. *Journal of the Geological Society, London* **165**, 177-188.

Jerram, D. A. & Widdowson, M. (2005). The anatomy of Continental Flood Basalt Provinces: geological constraints on the processes and products of flood volcanism. *Lithos* **79**, 385-405.

Ju, W., Hou, G. & Hari, K. R. (2013). Mechanics of mafic dyke swarms in the Deccan Large Igneous Province: Palaeostress field modelling. *Journal of Geodynamics* **66**, 79-91.

Kaila, K. L., Reddy, P. R., Dixit, M. M. & Koteswara-Rao, P. (1985). Crustal structure across the Narmada-Son lineament, Central India from deep seismic soundings. *Journal of the Geological Society of India* **26**, 465-480.

Kaneoka, I. & Haramura, H. (1973). K/Ar ages of successive lava flows from the Deccan Traps, India. *Earth and Planetary Science Letters* **18**, 229-236.

Karmalkar, N. R., Rege, S., Griffin, W. L. & O'Reilly, S. Y. (2005). Alkaline magmatism from Kutch, NW India: Implications for plume-lithosphere interaction. *Lithos* **81**, 101-119.

Katz, R. F., Spiegelman, M. & Langmuir, C. H. (2003). A new parameterization of hydrous mantle melting. *Geochemistry Geophysics Geosystems* **4**.

Kelemen, P. B., Dick, H. J. B. & Quick, J. E. (1992). Formation of harzburgite by pervasive melt/rock reaction in the upper mantle. *Nature* **358**, 635-641.

Kelemen, P. B., Hirth, G., Shimizu, N., Spiegelman, M. & Dick, H. J. (1997). A review of melt migration processes in the adiabatically upwelling mantle beneath oceanic spreading ridges. *Philosophical Transactions of the Royal Society, London A* **355**, 283-318.

Kelemen, P. B., Whitehead, J. A., Aharonov, E. & Jordahl, K. A. (1995). Experiments on flow focusing in soluble porous media, with applications to melt extraction from the mantle. *Journal of Geophysical Research* **100**, 475-496.

Keller, G. (2005). Impacts, volcanism and mass extinction: random coincidence or cause and effect? *Australian Journal of Earth Sciences* **52**, 725-757.

Keller, G., Adatte, T., Baum, G. & Berner, Z. (2008). Reply to 'Chicxulub impact predates K-T boundary: New evidence from Brazos, Texas' Comment by Schulte et al. *Earth and Planetary Science Letters* **269**, 621-629.

Keller, G., Adatte, T., Berner, Z., Harting, M., Baum, G., Prauss, M., Tantawy, A. & Stueben, D. (2007). Chicxulub impact predates K-T boundary: New evidence from Brazos, Texas. *Earth and Planetary Science Letters* **255**, 339-356.

Keller, G., Adatte, T., Bhowmick, P. K., Upadhyay, H., Dave, A., Reddy, A. N. & Jaiprakash, B. C. (2012). Nature and timing of extinctions in Cretaceous-Tertiary planktic foraminifera preserved in Deccan intertrappean sediments of the Krishna-Godavari Basin, India. *Earth and Planetary Science Letters* **341-344**, 211-221.

Keller, G., Adatte, T., Gardin, S., Bartolini, A. & Bajpai, S. (2008a). Main Deccan volcanism phase ends near the K-T boundary: Evidence from the Krishna-Godavari Basin, SE India. *Earth and Planetary Science Letters* **268**, 293-311.

Keller, G., Adatte, T., Stinnesbeck, W., Rebolledo-Vieyra, M., Fucugauchi, J. U., Kramar, U. & Stüben, D. (2004a). Chicxulub impact predates the K-T boundary mass extinction. *PNAS* **101**, 3753-3758.

Keller, G., Adatte, T., Stinnesbeck, W., Stüben, D., Berner, Z., Kramar, U. & Harting, M. (2004b). More evidence that the Chicxulub impact predates the K/T mass extinction. *Meteoritics & Planetary Science* **39**, 1127-1144.

Keller, G., Bhowmick, P. K., Upadhyay, H., Dave, A., Reddy, A. N., Jaiprakash, B. C. & Adatte, T. (2011). Deccan Volcanism Linked to the Cretaceous-Tertiary Boundary Mass Extinction: New Evidence from ONGC Wells in the Krishna-Godavari Basin. *Journal Geological Society of India* **78**, 399-428.

Keller, G., Li, L. & MacLeod, N. (1995). The Cretaceous/Tertiary boundary stratotype section at El Kef, Tunisia: how catastrophic was the mass extinction? *Palaeogeography, Palaeoclimatology, Palaeoecology* **119**, 221-254.

Keller, G., Sahni, A. & Bajpai, S. (2009c). Deccan volcanism, the KT mass extinction and dinosaurs. *Journal of Biosciences* **34**, 709-728.

Keller, G., Stinnesbeck, W., Adatte, T. & Stüben, D. (2003). Multiple impacts across the Cretaceous-Tertiary boundary. *Earth Science Reviews* **62**, 327-363.

Kennett, B. L. N. & Widiyantoro, S. (1999). A low seismic wavespeed anomaly beneath northwestern India: a seismic signature of the Deccan plume? *Earth and Planetary Science Letters* **165**, 145-155.

Kent, D. V. & Muttoni, G. (2013). Modulation of Late Cretaceous and Cenozoic climate by variable drawdown of atmospheric pCO2 from weathering of basaltic provinces on continents drifting through the equatorial humid belt. *Climate of the Past* **9**, 525-546.

Kerr, A. C., Khan, M., Mahoney, J. J., Nicholson, K. N. & Hall, C. M. (2010). Late Cretaceous alkaline sills of the south Tethyan suture zone, Pakistan: Initial melts of the Réunion hotspot? *Lithos* **117**, 161-171.

Khosla, A. & Sahni, A. (2003). Biodiversity during the Deccan volcanic eruptive episode. *Journal of Asian Earth Sciences* **21**, 895-908.

Klaus, A., Norris, R. D., Kroon, D. & Smit, J. (2000). Impact-induced mass wasting at the K-T boundary: Blake-Nose, western North Atlantic. *Geology* **28**, 319-322.

Knight, K. B., Renne, P. R., Halkett, A. & White, N. (2003). 40Ar/39Ar dating of the Rajahmundry Traps, Eastern India and their relationship to the Deccan Traps. *Earth and Planetary Science Letters* **208**, 85-99.

Knoll, M. & Ruska, E. (1932). Das Elektronenmikroskop. *Zeitschrift für physik* **78**, 318-339.

Kogiso, T., Hirose, K. & Takahashi, E. (1998). Melting experiments on homogeneous mixtures of peridotite and basalt: application to the genesis of ocean island basalts. *Earth and Planetary Science Letters* **162**, 45-61.

Kogiso, T. & Hirschmann, M. M. (2006). Partial melting experiments of bimineralic eclogite and the role of recylcled mafic oceanic crust in the genesis of ocean island basalts. *Earth and Planetary Science Letters* **249**, 188-199.

Kogiso, T., Hirschmann, M. M. & Frost, D. J. (2003). High-pressure partial melting of garnet pyroxenite: possible mafic lithologies in the source of ocean island basalts. *Earth and Planetary Science Letters* **216**, 603-617.

Kogiso, T., Hirschmann, M. M. & Pertermenn, M. (2004). High-pressure Partial Melting of Mafic Lithologies in the Mantle. *Journal of Petrology* **45**, 2407-2422.

Korenaga, J. (2011). Velocity-depth ambiguity and the seismic structure of large igneous provinces: a case study from the Ontong Java Plateau. *Geophysical Journal International* **185**, 1022-1036.

Krassilov, V. A. (1973). Climatic changes in eastern Asia as indicated by fossil floras. I. Early Cretaceous. *Palaeogeography, Palaeoclimatology, Palaeoecology* **13**, 261-273.

Krassilov, V. A. (1975). Climatic changes in eastern Asia as indicated by fossil floras. II. Late Cretaceous and Danian. *Palaeogeography, Palaeoclimatology, Palaeoecology* **17**.

Krishnamurthy, P. & Cox, K. G. (1977). Picrite Basalts and Related Lavas from the Deccan Traps of Western India. *Contribution to Mineralogy and Petrology* **62**, 53-75.

Krishnamurthy, P., Gopalan, K. & Macdougall, J. D. (2000). Olivine Compositions in Picrite Basalts and the Deccan Volcanic Cycle. *Journal of Petrology* **41**, 1057-1069.

Krivolutskaya, N. A., Sobolev, A. V., Mikhailov, V. N., Plechova, A. A., Kostitsyn, Y. A., Roschina, I. A. & Fekiacova, Z. (2012). Parental melt of the Nadezhdinsky Formation: Geochemistry, petrology and connection with Cu-Ni deposits (Noril'sk area, Russia). *Chemical Geology* **302-303**, 87-105.

Krogh, T. E., Kamo, S. L., Sharpton, V. L., Marin, L. E. & Hildebrand, A. R. (1993). U-Pb ages of single shocked zircons linking distal K/T ejecta to the Chicxulub crater. *Nature* **366**, 731-734.

Kumar, P., Yuan, X., Kumar, M. R., Kind, R., Li, X. & Chadha, R. K. (2007). The rapid drift of the Indian tectonic plate. *Nature* **449**, 894-897.

Kyte, F. T., Leinen, M., Heath, G. R. & Zhou, L. (1993). Cenozoic sedimentation history of the central North Pacific: Inferences from the elemental geochemistry of core LL44-GPC3. *Geochimica et Cosmochimica Acta* **57**, 1719-1740.

Lambart, S., Laporte, D. & Schiano, P. (2009). An experimental study of pyroxenite partial melts at 1 and 1.5 GPa: Implications for the major-element composition of Mid-Ocean Ridge Basalts. *Earth and Planetary Science Letters* **288**, 225-347.

Lambart, S., Laporte, D. & Schiano, P. (2013). Markers of the pyroxenite contribution in the major-element compositions of oceanic basalts: Review of the experimental constraints. *Lithos* **160-161**, 14-36.

Le Bas, M. J., Le Maitre, R. W., Streckeisen, A. & Zanettin, B. (1986). A Chemical Classification of Volcanic Rocks Based on the Total Alkali-Silica Diagram. *Journal of Petrology* **27**, 745-750.

Le Friant, A., Lebas, E., Clément, V., Boudon, G., Deplus, C., De Voogd, B. & Bachèlery, P. (2011). A new model for the evolution of La Réunion volcanic complex from complete marine geophysical surveys. *Geophysical Research Letters* **38**.

Lee, C.-T. A., Luffi, P., Plank, T., Dalton, H. & Leeman, W. P. (2009). Constraints on the depths and temperatures of basaltic magma generation on Earth and other terrestrial planets using new thermobarometers for mafic magmas. *Earth and Planetary Science Letters* **279**, 20-33.

Lehmann, B., Burgess, R., Frei, D., Belyatski, B., Mainkar, D., Rao, N. V. C. & Heaman, L. M. (2010). Diamondiferous kimberlites in central India synchronous with Deccan flood basalts. *Earth and Planetary Science Letters* **290**, 142-149.

Leitch, A. M. & Davies, G. F. (2001). Mantle plumes and flood basalts: Enhanced melting from plume ascent and an eclogite component. *Journal of Geophysical Research* **106**, 2047-2059.

Lénat, J.-F., Gibert-Malengreau, B. & Galdéano, A. (2001). A new model for the evolution of the volcanic island of Réunion (Indian Ocean). *Journal of Geophysical Research* **184**, 1-13.

Li, L. & Keller, G. (1998). Abrupt deep-sea warming at the end of the Cretaceous. *Geology* **26**, 995-998.

Li, X., Kind, R., Priestley, K., Sobolev, S. V., Tilmann, F., Yuan, X. & Weber, M. (2000). Mapping the Hawaiian plume conduit with converted seismic waves. *Nature* **405**, 938-941.

Lightfoot, P. (1985). Isotope and trace element geochemistry of the South Deccan lavas, India. The Open University.

Lightfoot, P. & Hawkesworth, C. (1988). Origin of the Deccan Trap lavas: evidence from combined trace element and Sr- Nd- and Pb-isotope studies. *Earth and Planetary Science Letters* **91**, 89-104.

Lightfoot, P., Hawkesworth, C., Devey, C. W., Rogers, N. W. & Calsteren, P. W. C. v. (1990). Source and differentiation of Deccan Trap lavas: implications of geochemical and mineral chemical variations. *Journal of Petrology* **31**, 1165-1200.

Lightfoot, P. C., Hawkesworth, C. J. & Sethna, S. F. (1987). Petrogenesis of rhyolites and trachytes from the Deccan Trap: Sr, Nd, and Pb isotope and trace element evidence. *Contribution to Mineralogy and Petrology* **95**, 44-54.

Long, J. V. P. (1958). Microanalysis with X-rays. University of Cambridge.

Ludden, J. N. (1978). Magmatic evolution of the basaltic shield volcanoes of Reunion island. *Journal of Volcanology and Geothermal Research* **7**, 171-198.

MacLeod, K. G., Fullagar, P. D. & Huber, B. T. (2003). 87Sr/86Sr test of the degree of impact-induced slope failure in the Maastrichtian of the western North Atlantic. *Geology* **31**, 311-314.

MacLeod, K. G., Huber, B. T. & Fullagar, P. D. (2001). Evidence for a small (~0.000030) but resolvable increase in seawater 87Sr/86Sr ratios across the Cretaceous-Tertiary boundary. *Geology* **29**, 303-306.

Mahoney, J. J. (1984). Isotopic and chemical studies of the Deccan and Rajmahal traps, India: mantle sources and petrogenesis. University of California, San Diego.

Mahoney, J. J. (1988). Deccan Traps. In: Macdougall, J. D. (ed.) *Continental flood basalts*: (Dorrecht: Kluwer-Academic), 151-194.

Mahoney, J. J., Duncan, R. A., Khan, W., Gnos, E. & McCormick, G. R. (2002). Cretaceous volcanic rocks of the South Tethyan suture zone, Pakistan: implications for the Réunion hotspot and Deccan Traps. *Earth and Planetary Science Letters* **203**, 295-310.

Mahoney, J. J., Natland, J. H., White, W. M., Poreda, R. J., Bloomer, S. H., Fisher, R. L. & Baxter, A. N. (1989). Isotopic and Geochemical Provinces of the Western indian Ocean Spreading Centers. *Journal of Geophysical Research* **94**, 4033-4052.

Mahoney, J. J., Sheth, H. C., Chandrasekharam, D. & Peng, Z. X. (2000). Geochemistry of Flood Basalts of the Toranmal Section, Northern Deccan Traps, India: Implications for Regional Deccan Stratigraphy. *Journal of Petrology* **41**, 1099-1120.

Maimon, O., Lyakhovsky, V., Melnik, O. & Navon, O. (2012). The propagation of a dyke driven by gas-saturated magma. *Geophysical Journal International* **189**, 956-966.

Malod, J. A., Droz, L., Mustafa Kemal, B. & Patriat, P. (1997). Early sreading and continental to oceanic basement transition beneath the Indus deep-sea fan: northeastern Arabian Sea. *Marine Geology* **141**, 221-235.

Marsh, B. D. (2007). Magmatism, Magma, and Magma Chambers. *Treatise on Geophysics Volume 6: Crust and Lithosphere Dynamics*: Elsevier, 275-333.

Maurel, C. & Maurel, P. (1982). Etude experimentale de l'equilibre Fe2+-Fe3+ dans les spinelles chromiferes et les liquides silicates basiques coexistants à 1atm. *Comptes Rendus de l'Académie des Sciences* **285**, 209-215.

McArthur, J. M., Thirlwall, M. F., Engkilde, M., Zinsmeister, W. J. & Howarth, R. J. (1998). Strontium isotope profiles across K/T boundary sequences in Denmark and Antarctica. *Earth and Planetary Science Letters* **160**, 179-192.

McElwain, J. C. & Punyasena, S. W. (2007). Mass extinction events and the plant fossil record. *TRENDS in Ecology and Evolution* **22**, 548-557.

McMullen, D. (1953). An improved scanning electron microscope for opaque specimens *Proceedings of the IEE* **100**, 254-256.

Médard, E. & Grove, T. L. (2008). The effect of H2O on the olivine liquidus of basaltic melts: experiments and thermodynamic models. *Contribution to Mineralogy and Petrology* **155**, 417-432.

Medvedev, M. V. & Melott, A. L. (2007). Do extragalactic cosmic rays induce cycles in fossil diversity? *The Astrophysical Journal* **664**, 879-889.

Meert, J. G., Pandit, M. K., Pradhan, V. R., Banks, J., Sirianni, R., Stroud, M., Newstead, B. & Gifford, J. (2010). Precambrian crustal evolution of Peninsular India: A 3.0 billion year odyssey. *Journal of Asian Earth Sciences* **39**, 483-515.

Melluso, L., Beccaluva, L., Brotzu, P., Gregnanin, A., Gupta, A. K., Morbidelli, L. & Traversa, G. (1995). Constraints on the Mantle Sources of the Deccan Traps from the Petrology and Geochemistry of the Basalts of Gujarat State (Western India). *Journal of Petrology* **36**, 1393-1432.

Melluso, L., Mahoney, J. J. & Dallai, L. (2006). Mantle sources and crustal input as recorded in high-Mg Deccan Traps basalts of Gujarat (India). *Lithos* **89**, 259-274.

Melluso, L., Sethna, S. F., D'Antonio, M., Javeri, P. & Bennio, L. (2002). Geochemistry and petrogenesis of sodic and potassic mafic alkaline rocks in the Deccan Volcanic Province, Mumbai Area (India). *Mineralogy and Petrology* **74**, 323-342.

Minshull, T. A., Lane, C. I., Collier, J. S. & Whitmarsh, R. B. (2008). The relationship between rifting and magmatism in the northeastern Arabian Sea. *Nature Geoscience* **1**, 463-467.

Mitchell, C. & Widdowson, M. (1991). A geological map of the southern Deccan Traps, India and its structural implications. *Journal of the Geological Society, London* **148**, 495-505.

Molnar, P. & England, P. (1990). Late Cenozoic uplift of mountain ranges and global climate change: chicken or egg? *Nature* **346**, 29-34.

Moore, G., Vennemann, T. & Charmichael, I. S. E. (1998). An empirical model for the solubility of H2O in magmas to 3 kilobars. *American Mineralogist* **83**, 36-42.

Moore, J. G. & Clague, D. (1992). Volcano growth and evolution of island of Hawaii. *Geological Society of America Bulletin* **104**, 1471-1484.

Morgan, J. P., Reston, T. J. & Ranero, C. R. (2004). Contemporaneous mass extinctions, continental flood basalts, and 'impact signals': are mantle plume-induced lithospheric gas explosions the causal link? *Earth and Planetary Science Letters* **217**, 263-284.

Morgan, W. J. (1971). Convection plumes in the lower mantle. *Nature* **230**, 42-43.

Morgan, W. J. (1972). Deep Mantle Convection Plumes and Plate Motions. *The American Association of Petroleum Geologists Bulletin* **56**, 203-213.

Moseley, H. J. G. (1913). The high-frequency spectra of the elements. *Philosophical Magazine* **26**, 1024-1034.

Moseley, H. J. G. (1914). The high-frequency spectra of the elements; part II. *Philosophical Magazine* **27**, 703-713.

Moulin, M., Fluteau, F., Courtillot, V., Marsh, J., Delpech, G., Quidelleur, X., Gérard, M. & Jay, A. E. (2011). An attempt to constrain the age, duration, and eruptive history of the Karoo flood basalt: Naude's Nek section (South Africa). *Journal of Geophysical Research* **116**.

Mulvey, T. (1960). A new microanalyser. In: Engström, A., Cosslett, V. E. & Pattee, H. H. (eds.) *X-ray Microscopy and Microanalysis*. Amsterdam: Elsevier, 372-378.

Murthy, Y. S. (2002). On the correlation of seismicity with geophysical lineaments over the Indian subcontinent. *Current Science* **83**, 760-766.

Murton, B. J., Tindle, A. G., Milton, J. A. & Sauter, D. (2005). Heterogeneity in southern Central India Ridge MORB: Implications for ridge-hot spot interaction. *Geochemistry Geophysics Geosystems* **6**.

Naslund, H. R. (1984). Petrology of the Upper Border Series of the Skaergaard Intrusion. *Journal of Petrology* **25**, 185-212.

Nikolaev, G. S., Borisov, A. A. & Ariskin, A. A. (1996). Calculation of the Ferric-Ferrous Ratio in Magmatic Melts: Testing and Additional Calibration of Empirical Equations for Various Magmatic Series. *Geochemistry International* **34**, 641-649.

Nordt, L., Atchley, S. & Dworkin, S. I. (2002). Paleosol barometer indicates extreme fluctuations in atmospheric CO2 across the Cretaceous-Tertiary boundary. *Geology* **30**, 703-706.

Norris, R. D., Firth, J., Blusztajn, J. S. & Ravizza, G. (2000). Mass failure of the North Atlantic margin triggered by the Cretaceous-Paleogene bolide impact. *Geology* **28**, 1119-1122.

Oehler, J.-F., Lénat, J.-F. & Labazuy, P. (2008). Growth and collapse of the Reunion Island volcanoes. *Bulletin of Volcanology* **70**, 717-742.

Olsson, R. K., Miller, K. G., Browning, J. V., Habib, D. & Sugarman, P. J. (1997). Ejecta layer at the Cretaceous-Tertiary boundary, Bass River, New Jersey (Ocean Drilling Program Leg 174AX. *Geology* **25**, 759-762.

Owen-Smith, T. M., Ashwal, L. D., Torsvik, T. H., Ganerød, M., Nebel, O., Webb, S. J. & Werner, S. C. (2013). Seychelles alkaline suite records the culmination of Deccan Traps continental flood volcanism. *Lithos* **182-183**, 33-47.

Oxburgh, R. (1998). Variations in the osmium isotope composition of sea water over the past 200,000 years. *Earth and Planetary Science Letters* **159**, 183-191.

Pande, K. (2002). Age and duration of the Deccan Traps, India: A review of radiometric and paleomagnetic constraints. *Proceedings of the Indian Academy of Sciences* **111**, 115-123.

Parthasarathy, G., Bhandari, N., Vairamani, M. & Kunwar, A. C. (2008). High-pressure phase of natural fullerene C60 in iridium-rich Cretaceous-Tertiary boundary layers of Deccan intertrappean deposits, Anjar, Kutch, India. *Geochimica et Cosmochimica Acta* **72**.

Patino, L. C., Velbel, M. A., Price, J. R. & Wade, J. A. (2003). Trace element mobility during spheroidal weathering of basalts and andesites in Hawaii and Guatemala. *Chemical Geology* **202**, 343-364.

Paul, D. K., Ray, A., Das, B., Patil, S. K. & Biswas, S. K. (2008). Petrology, geochemistry and paleomagnetism of the earliest magmatic rocks of Deccan Volcanic Province, Kutch, Northwest India. *Lithos* **102**, 237-259.

Pavlov, V., Fluteau, F., Veselovskiy, R., Fetisova, A. M. & Latyshev, A. V. (2011). Secular Geomagnetic Variations and Volcanic Pulses in the Permian-Triassic Traps of the Norilsk and Maimecha-Kotui Provinces. *Physics of the Solid Earth* **47**, 402-417.

Payne, J. A., Jackson, M. G. & Hall, P. S. (2012). Parallel volcano trends and geochemical asymetry of the Society Islands hotspot track. *Geology* **41**, 19-22.

Payne, J. L., Turchyn, A. V., Paytan, A., DePaolo, D. J., Lehrmann, D. J., Yu, M. & Wei, J. (2010). Calcium isotope constraints on the end-Permian mass extinction. *Proceedings of the National Academy of Sciences, USA* **107**, 8543-8548.

Peate, I. U. & Bryan, S. E. (2008). Re-evaluating plume-induced uplift in the Emeishan large igneous province. *Nature Geoscience* **1**, 625-629.

Pegram, W. J., Krishnaswami, S., Ravizza, G. E. & Turekian, K. K. (1992). The record of seawater 187Os/186Os variation through the Cenozoic. *Earth and Planetary Science Letters* **113**, 569-576.

Peng, Z. X. & Mahoney, J. J. (1995). Drillhole lavas from the northwestern Deccan Traps, and the evolution of Réunion hotspot mantle. *Earth and Planetary Science Letters* **134**, 169-185.

Peng, Z. X., Mahoney, J. J., Hooper, P. R., Harris, C. & Beane, J. E. (1994). A role for lower continental crust in flood basalt genesis? Isotopic and incompatible element study of the lower six formations of the western Deccan traps. *Geochimica et Cosmochimica Acta* **58**, 267-288.

Peng, Z. X., Mahoney, J. J., Hooper, P. R., Macdougall, J. D. & Krishnamurthy, P. (1998). Basalts of the northeastern Deccan Traps, India: Isotopic and elemental geochemistry

and relation to southwestern Deccan stratigraphy. *Journal of Geophysical Research* **103**, 29,843-829,865.

Peucker-Ehrenbrink, B. & Ravizza, G. (2000). The marine osmium isotope record. *Terra Nova* **12**, 205-219.

Pierazzo, E., Hahmann, A. N. & Sloan, L. C. (2003). Chicxulub and Climate: Radiative Perturbations of Impact-Produced S-Bearing Gases. *Astrobiology - Rubey Colloquium Paper* **3**, 99-118.

Prasad, J. N., Patil, S. K., Venkateshwarlu, M., Saraf, P. D., Tripathi, S. C. & Rao, D. R. K. (1998). Palaeomagnetic results from the Cretaceous Bagh Group in the Narmada Basin, central India: evidence of pervasive Deccan remagnetization and its implications for Deccan volcanism. *Geophysical Journal International* **133**, 519-528.

Premoli-Silva, I. & Sliter, W. (1995). Cretaceous planktonic foraminiferal biostratigraphy and evolutionary trends from the Bottaccione section, Gubbio, Italy. *Palaeontogr. Ital.* **82**, 1-89.

Priestley, K. & McKenzie, D. (2006). The thermal structure of the lithosphere from shear wave velocities. *Earth and Planetary Science Letters* **244**, 285-301.

Raju, D. S. N., Jaiprakash, B. C. & Kumar, A. (1996). Paleoenvironmental set-up and age of basin floor just prior to the spread of Deccan volcanism in the Krishna-Godavari Basin, India. *Memoir - Geological Society of India* **37**, 285-295.

Raju, D. S. N., Jaiprakash, B. C., Kumar, A., Saxena, R. K., Dave, A., Chatterjee, T. K. & Mishra, C. M. (1995). Age of Deccan volcanism across KTB in Krishna-Godavari Basin: new evidences. *Journal of the Geological Society of India* **45**, 229-233.

Rampino, M. R. & Stothers, R. (1988). Flood basalt volcanism during the past 250 million years. *Science* **241**, 663-668.

Rapp, R. P., Shimizu, N., Norman, M. D. & Applegate, G. S. (1999). Reaction between slab-derived melts and peridotite in the mantle wedge: experimental constraints at 3.8 GPa. *Chemical Geology* **160**, 335-356.

Raup, D. M. (1987). Mass extinction: A commentary. *Palaeontology* **30**, 1-13.

Raup, D. M. & Sepkoski, J. J. (1982). Mass Extinction in the Marine Fossil Record. *Science* **215**, 1501-1503.

Ravizza, G. & Peucker-Ehrenbrink, B. (2003). Chemostratigraphic Evidence of Deccan Volcanism from the Marine Osmium isotope Record. *Science* **302**, 1392-1395.

Ray, J. S., Pande, K. & Pattanayak, S. K. (2003). Evolution of the Amba Dongar Carbonatite Complex: Constraints from 40Ar–39Ar Chronologies of the Inner Basalt and an Alkaline Plug. *International Geology Review* **45**, 857-862.

Ray, R., Shukla, A. D., Sheth, H. C., Ray, J. S., Duraiswami, R. A., Vanderkluysen, L., Rautela, C. S. & Mallik, J. (2008). Highly heterogenous Precambrian basement under the central Deccan Traps, India: Direct evidence from xenoliths in dykes. *Gondwana Research* **13**, 375-385.

Reed, S. J. B. (1993). *Electron Probe Analysis*. Cambridge: Cambridge University Press.

Renne, P. R., Deino, A. L., Hilgen, F. J., Kuiper, K. F., Mark, D. F., Mitchell, W. S., Morgan, L. E., Mundil, R. & Smit, J. (2013). Time Scales of Critical Events Around the Cretaceous-Paleogene Boundary. *Science* **339**, 684-687.

Richards, M. A., Duncan, R. A. & Courtillot, V. E. (1989a). Flood Basalts and Hot-Spot Tracks: Plume Heads and Tails. *Science* **246**, 103-107.

Ridgwell, A. (2005). A Mid Mesozoic Revolution in the regulation of ocean chemistry. *Marine Geology* **217**, 339-357.

Ritsema, J. & Allen, R. M. (2003). The elusive mantle plume. *Earth and Planetary Science Letters* **207**, 1-12.

Robinson, N., Ravizza, G., Coccioni, R., Peucker-Ehrenbrink, B. & Norris, R. (2009). A high-resolution marin 187OS/188Os record for the late Maastrichtian: Distinguishing the chemical fingerprints of Deccan volcanism and the KP impact event. *Earth and Planetary Science Letters* **281**, 159-168.

Robock, A. (2000). Volcanic eruptions and climate. *Reviews of Geophysics* **38**, 191-219.

Roddaz, M., Said, A., Guillot, S., Antoine, P.-O., Montel, J.-M., Martin, F. & Darrozes, J. (2011). Provenance of Cenozoic sedimentary rocks from the Sulaiman fold and thrust belt, Pakistan: implications for the palaeogeography of the Indus drainage system. *Journal of the Geological Society, London* **168**, 499-516.

Roeder, P. L. & Emslie, R. F. (1970). Olivine-Liquid Equilibrium. *Contribution to Mineralogy and Petrology* **29**, 275-289.

Rohde, R. A. & Muller, R. A. (2005). Cycles in fossil diversity. *Nature* **434**, 208-210.

Roy, A. B. (2003). Geological and Geophysical Manifestations of the Reunion Plume-Indian Lithosphere Interactions - Evidence from Northwest India. *Gondwana Research* **6**, 487-500.

Roy-Barman, M. & Allègre, C. J. (1995). 187Os/186Os in oceanic island basalts: tracing crust recycling in the mantle. *Earth and Planetary Science Letters* **129**, 145-161.

Royer, J.-Y., Chaubey, A. K., Dyment, J., Bhattacharya, G. C., Srinivas, K., Yatheesh, V. & Ramprasad, T. (2002). Paleogene plate tectonic evolution of the Arabian and Eastern Somali basins. *Geological Society, London, Special Publications* **195**, 7-23.

Rudnick, R. L. & Gao, S. (2003). 3.01 Composition of the Continental Crust. *Treatise on Geochemistry* **3**, 1-64.

Salaün, A., Villemant, B., Semet, M. & Staudacher, T. (2010). Cannibalism of olivine-rich cumulate xenoliths during the 1998 eruption of Piton de la Fournaise (La Réunion hotspot): Implications for the generation of magma diversity. *Journal of Volcanology and Geothermal Research* **198**, 187-204.

Salil, M. S., Shrivastava, J. P. & Pattanayak, S. K. (1997). Similarities in the mineralogical and geochemical attributes of detrital clays of Maastrichtian Lameta Beds and weathered Deccan basalt, Central India. *Chemical Geology* **136**, 25-32.

Sandwell, D. T. & Smith, W. H. F. (1997). Marine gravity anomaly from Geosat and ERS-1 altimetry. *Journal of Geophysical Research* **102**, 10,039-010,054.

Santosh, M. (2010). A synopsis of recent conceptual models on supercontinent tectonics in relation to mantle dynamics, life evolution and surface environment. *Journal of Geodynamics* **50**, 116-133.

Saunders, A. D. (2005). Large Igneous Provinces: Origin and Environmental Consequences. *Elements* **1**, 259-263.

Saunders, A. D., Jones, S. M., Morgan, L. A., Pierce, K. L., Widdowson, M. & Xu, Y. G. (2007). Regional uplift associated with continental large igneous provinces: The roles of mantle plumes and the lithosphere. *Chemical Geology* **241**, 282-318.

Sayyed, M. R. G. (2013). Flood basalt hosted palaeosols: Potential palaeoclimatic indicators of global climate change. *Geoscience Frontiers* **in press**.

Sayyed, M. R. G. & Hundekari, S. M. (2006). Preliminary comparison of ancient bole beds and modern soils developed upon the Deccan Volcanic Basalts around Pune (India): Potential for Palaeoenvironmental Reconstruction. *Quaternary International* **156-157**, 189-199.

Schiano, P. (2003). Primitive mantle magmas recorded as silicate melt inclusions in igneous minerals. *Earth Science Reviews* **63**, 121-144.

Schulte, P., Alegret, L., Arenillas, I., Arz, J. A., Barton, P. J., Bown, P. R., Bralower, T. J., Christeson, G. L., Claeys, P., Cockell, C. S., Collins, G. S., Deutsch, A., Goldin, T. J.,

Goto, K., Grajales-Nishimura, J. M., Grieve, R. A. F., Gulick, S. P. S., Johnson, K. R., Kiessling, W., Koeberl, C., Kring, D. A., MacLeod, K. G., Matsui, T., Melosh, J., Montanari, A., Morgan, J. V., Neal, C. R., Nichols, D. J., Norris, R. D., Pierazzo, E., Ravizza, G., Rebolledo-Vieyra, M., Reimold, W. U., Robin, E., Salge, T., Speijer, R. P., Sweet, A. R., Urrutia-Fucugauchi, J., Vajda, V., Whalen, M. T. & Willumsen, P. S. (2010). The Chicxulub Asteroid Impact and Mas Extinction at the Cretaceous-Paleogene Boundary. *Science* **327**, 1214-1218.

Schulte, P., Speijer, R. P., Brinkhuis, H., Kontny, A., Claeys, P., Galeotti, S. & Smit, J. (2008). Comment on the paper "Chicxulub impact predates K-T boundary: New evidence from Brazos, Texas" by Keller et al. (2007). *Earth and Planetary Science Letters* **269**, 614-620.

Self, S., Blake, S., Sharma, K., Widdowson, M. & Sephton, S. (2008a). Sulfur and Chlorine in Late Cretaceous Deccan Magmas and Eruptive Gas Release. *Science* **319**, 1654-1657.

Self, S., Jay, A. E., Widdowson, M. & Keszthelyi, L. P. (2008b). Correlation of the Deccan and Rajahmundry Trap lavas: Are these the longestand the largest lava flows on Earth? *Journal of Volcanology and Geothermal Research* **172**, 3-19.

Self, S., Widdowson, M., Thordarson, T. & Jay, A. E. (2006). Volatile fluxes during flood basalt eruptions and potential effects on the global environment: A Deccan perspective *Earth and Planetary Science Letters* **248**, 518-532.

Sen, G. (1995). A simple petrologic model for the generation of Deccan Traps magmas. *International Geology Review* **37**, 825-850.

Sen, G. (2001). Generation of Deccan Trap magmas *Proceedings of the Indian National Science Academy* **110**, 409-431.

Sen, G. (2002). Giant Plagioclase Basalts, eruption rate versus time. Response to Sheth's comments and some additional thoughts. *Proceedings of the Indian Academy of Sciences* **111**, 487-488.

Sen, G., Bizimis, M., Das, R., Paul, D. K., Ray, A. & Biswas, S. (2009). Deccan plume, lithosphere rifting, and volcanism in Kutch, India. *Earth and Planetary Science Letters* **277**, 101-111.

Sen, G., Borges, M. R. & Marsh, B. (2006). A case for short durtaion of Deccan Traps eruption. *EOS Transactions, American Geophysical Union* **87**, 197-198.

Sen, G. & Chandrasekharam, D. (2011). Chapter 2: Deccan Traps Flood Basalt Province: An Evaluation of the Thermochemical Plume Model. In: Ray, J., Sen, G. & Ghosh, B. (eds.) *Topics in Igneous Petrology*: Springer Science.

Sethna, S. F. (1999). Geology of Mumbai and Surrounding Areas and its Position in the Deccan Volcanic Stratigraphy, India. *Journal Geological Society of India* **53**, 359-365.

Shaw, D. M. (1970). Trace element fractionation during anatexis. *Geochimica et Cosmochimica Acta* **34**, 237-243.

Sheth, H. C. (1998). A reappraisal of the coastal Panvel fl exure, Deccan Traps, as a listricfault–controlled reverse drag structure. *Tectonophysics* **294**, 143-149.

Sheth, H. C. (2005). From Deccan to Réunion: No trace of a mantle plume. In: G.R., F., J.H., N., D.C., P. & D.L., A. (eds.) *Plates, Plumes and Paradigms*: Geological Society of America Special Paper, 477-501.

Sheth, H. C. (2007). Plume-related regional prevolcanic uplift in the Deccan Traps: Absence of evidence, evidence of absence. *The Geological Society of America Special Paper* **430**, 785-813.

Sheth, H. C. & Melluso, L. (2008). The Mount Pavagadh volcanic suite, Deccan Traps: Geochemical stratigraphy and magmatic evolution. *Journal of Asian Earth Sciences* **32**, 5-21.

Sheth, H. C. & Pande, K. (2013). Geological and 40Ar/39Ar age contraints on late-stage Deccan rhyolitic volcanism, inter-volcanic sedimentation, and the Panvel flexure from the Dongri area, Mumbai. *Journal of Asian Earth Sciences* **in press**.

Sheth, H. C., Zellmer, G. F., Demonterova, E. I., Ivanov, A. V., Kumar, R. & Patel, R. K. (2013). The Deccan tholeiite lavas and dykes of ghatkopar-Powai area, Mumbai, Panvel flexure zone: Geochemistry, stratigraphic status, and tectonic significance. *Journal of Asian Earth Sciences* **in press**.

Shrivastava, J. P. & Pattanayak, S. K. (2002). Basalts of the Eastern Deccan Volcanic Province, India. *Gondwana Research* **5**, 649-665.

Simonetti, A., Bell, K. & Viladkar, S. G. (1995). Isotopic data from the Amba Dongar Carbonatite Complex, west-central India: Evidence for an enriched mantle source. *Chemical Geology* **122**, 185-198.

Simonetti, A., Goldstein, S. L., Schmidberger, S. S. & Viladkar, S. G. (1998). Geochemical and Nd, Pb, and Sr Isotope Data from Deccan Alkaline Complexes - Inferences for Mantle Sources and Plume - Lithosphere interaction. *Journal of Petrology* **39**, 1847-1864.

Singh, R. S., Stoermer, E. F. & Kar, R. (2007). Earliest freshwater diatoms from the Deccan Intertrappean (Maastrichtian) sediments of India. *Micropaleontology* **52**, 545-551.

Smietana, M. (2011). Pétrologie, geochronologie (K-Ar) et géochimie élémentaire et isotopique (Sr, Nd, Hf, Pb) de laves anciennes de la Réunion : Implications sur la construction

de l'édifice volcanique. Université de la Réunion - Laboratoire GéoSciences Réunion, Université de Brest - Laboratoire Domaines Océaniques, 371.

Smit, J. (2004). The section of the Barranco del Gredero (Caravaca, SE Spain): a crucial section for the Cretaceous/Tertiary boundary impact extinction hypothesis. *Journal of Iberian Geology* **31**, 181-193.

Sobolev, A. V. (1996). Melt Inclusions in Minerals as a Source of Principle Petrological Information. *Petrology* **4**, 209-220.

Sobolev, A. V., Batanova, V., Krasheninnikov, V. G., Borisov, A. A., Arndt, N. T., Kuzmin, D. V., Krivolutskaya, N. A. & Sushchevskaya, N. M. (2013). Potential Temperatures of Sources of MORB, OIB and LIPs based on Al Partitioning Between Olivine and Spinel. *AGU, Fall Meeting 2013* **V11C-06**.

Sobolev, A. V. & Chaussidon, M. (1996). H2O concentrations in primary melts from supra-subduction and mid-ocean ridges: Implications for H20 storage and recycling in the mantle. *Earth and Planetary Science Letters* **137**, 45-55.

Sobolev, A. V. & Danyushevsky, L. V. (1994). Petrology and Geochemistry of Boninites from the North Termination of the Tonga Trench: Constraints on the Generation Conditions of Primary High-Ca Boninite Magmas. *Journal of Petrology* **35**, 1183-1211.

Sobolev, A. V., Hofmann, A., Sobolev, A. V. & Nikogosian, I. K. (2005). An olivine-free mantle source of Hawaiian shield basalts. *Nature* **434**, 590-597.

Sobolev, A. V., Hofmann, A. W., Brügmann, G., Batanova, V. G. & Kuzmin, D. V. (2008). A Quantitative Link Between Recycling and Osmium Isotopes. *Science* **321**, 536.

Sobolev, A. V., Hofmann, A. W., Kuzmin, D. V., Yaxley, G. M., Arndt, N. T., Chung, S.-L., Danyushevsky, L. V., Elliott, T., Frey, F. A., Garcia, M. O., Gurenko, A. A., Kamenetsky, V. S., Kerr, A. C., Krivolutskaya, N. A., Matvienkov, V. V., Nikogosian, I. K., Rocholl, A., Sigurdsson, I. A., Sushchevskaya, N. M. & Teklay, M. (2007). The Amount of Recycled Crust in Sources of Mantle-Derived Melts. *Science* **316**, 412-417.

Sobolev, A. V., Krivolutskaya, N. A. & Kuzmin, D. V. (2009a). Petrology of the Parental Melts an Mantle Sources of Siberian Trap Magmatism. *Petrology* **17**, 253-286.

Sobolev, A. V. & Nikogosian, I. K. (1994). Petrology of Long-Lived Mantle Plume Magmatism: Hawaii, Pacific, and Reunion Island, Indian Ocean. *Petrology* **2**, 131-168.

Sobolev, A. V., Sobolev, S. V., Kuzmin, D. V., Malitch, K. N. & Petrunin, A. G. (2009b). Siberian meimechites: origin and relation to flood basalts and kimberlites. *Russian Geology and Geophysics* **50**, 999-1033.

Sobolev, S. V., Sobolev, A. V., Kuzmin, D. V., Krivolutskaya, N. A., Petrunin, A. G., Arndt, N. T., Radko, V. A. & Vasiliev, Y. R. (2011). Linking mantle plumes, large igneous provinces and environmental catastrophes. *Nature* **477**, 312-316.

Srivastava, P., Sangode, S. J., Meshram, D. C., Gudadhe, S. S., Nagaraju, E., Kumar, A. & Venkateshwarlu, M. (2012). Paleoweathering and depositional conditions in the inter-flow sediments units (bole beds) of Deccan Volcanic Province, India: A mineral magnetic approach. *Geoderma* **177-178**, 90-109.

Steinberger, B. (2000). Plumes in a convecting mantle: models and observations for individual hotspots. *Journal of Geophysical Research* **105**, 11127-11152.

Subba Rao, S. (1972). Alkaline Rock of the Deccan Traps. *Bulletin Volcanologie* **35**, 983-997.

Subbarao, K. V., Bodas, M. S., Khadri, S. F. R., Beane, J. E., Kale, V., Widdowson, M., Hooper, P. R. & Walsh, J. N. (2000). Penrose Deccan 2000 - Field Excursion Guide to the Western Deccan Basalt Province. *Geological Society of India & Geological Society of America*.

Subbarao, K. V., Hooper, P. R., Dayal, A. M., Walsh, J. N. & Gopalan, K. (1999). Narmada dykes. *Geological Society of India, Memoirs* **43**, 891-902.

Subbarao, K. V. & Pathak, S. (1993). Reversly magnetized flows, Rajahmundry, Andhra Pradesh. *Journal Geological Society of India* **41**, 71-72.

Sun, C. & Liang, Y. (2013). The importance of crystal chemistry on REE partitioning between mantle minerals (garnet, clinopyroxene, orthopyroxene, and olivine) and basaltic melts. *Chemical Geology* **358**, 23-36.

Sun, S. & McDonough, W. F. (1989). Chemical and isotopic systematics of oceanic basalts: implications for mantle composition and processes. In: Saunders, A. D. & Norry, M. J. (eds.) *Magmatism in the Ocean Basins*. London: Geological Society Special Publication, 313-345.

Talusani, R. V. R. (2010). Bimodal tholeiitic and midly alkalic basalts from Bhir area, central Deccan Volcanic Province, India: Geochemistry and petrogenesis. *Journal of Volcanology and Geothermal Research* **189**, 278-290.

Talwani, M. & Reif, C. (1998). Laxmi Ridge - A continental sliver in the Arabian Sea. *Marine Geophysical Researches* **20**, 259-271.

Tatsumi, Y. & Hanyu, T. (2003). Geochemical modeling of dehydration and partial melting of subducting lithosphere: Toward a comprehensive understanding of high-Mg andesite formation in the Setouchi volcanic belt, SW Japan. *Geochemistry Geophysics Geosystems* **4**.

Thompson, A., Attwood, D., Gullikson, E., Howells, M., Kim, K.-J., Kirz, J., Kortright, J., Lindau, I., Liu, Y., Pianetta, P., Robinson, A., Scofield, J., Underwood, J., Williams, G. & Winick, H. (2009). *X-ray data booklet*. Berkeley: Lawrence Berkeley National Laboratory - University of California.

Thordarson, T. & Self, S. (1998). The Roza Member, Columbia River Basalt Group: A gigantic pahoehoe lava flow field formed by endogenous processes? *Journal of Geophysical Research* **103**, 27,411-427,447.

Todal, A. & Edholm, O. (1998). Continental margin off Western India and Deccan Large Igneous Province. *Marine Geophysical Researches* **20**, 273-291.

Torsvik, T. H., Burke, K., Steinberger, B., Webb, S. J. & Ashwal, L. D. (2010). Diamonds sampled by plumes from the core-mantle boundary. *Nature* **466**, 352-355.

Torsvik, T. H. & Cocks, L. R. M. (2004). Earth Geography from 400 to 250 Ma: a palaeomagnetic, faunal and facies review. *Journal of the Geological Society* **61**, 555-572.

Turgeon, S. C. & Creaser, R. A. (2008). Cretaceous anoxic event 2 triggered by a massive magmatic episode. *Nature* **454**, 323-326.

Upton, B. G. J. & Wadsworth, W. J. (1965). Geology of Réunion Island, Indian Ocean. *Nature* **207**, 151-154.

Valet, J.-P., Laj, C. & Tucholka, P. (1986). High-resolution sedimentary record of a geomagnetic reversal. *Nature* **322**, 27-32.

Vanderkluysen, L., Mahoney, J. J., Hooper, P. R., Sheth, H. C. & Ray, R. (2011). The Feeder System of the Deccan Traps (India): Insights from Dike Geochemistry. *Journal of Petrology* **52**, 315-343.

Venkatesan, T. R., Pande, K. & Gopalan, K. (1993). Did Deccan volcanism pre-date the Cretaceous/Tertiary transition? *Earth and Planetary Science Letters* **119**, 181-189.

Venkaya, E. (1949). Deccan trap outliers of the Godavari districts. *Proceedings of the Indian Academy of Sciences* **29**, 431-441.

Viladkar, S. G. & Schidlowski, M. (2000). Carbon and Oxygen Isotope Geochemistry of the Amba Dongar Carbonatite Complex, Gujarat, India. *Gondwana Research* **3**, 415-424.

Villemant, B., Salaün, A. & Staudacher, T. (2009). Evidence for a homogeneous primary magma at Piton de la Fournaise (La Réunion): A geochemical study of matrix glass, melt inclusions and Pélé's hairs of the 1998-2008 eruptive activity. *Journal of Volcanology and Geothermal Research* **184**, 79-92.

Vlastélic, I., Deniel, C., Bosq, C., Télouk, P., Boivin, P., Bachèlery, P., Famin, V. & Staudacher, T. (2009). Pb isotope geochemistry of Piton de la Fournaise historical lavas. *Journal of Volcanology and Geothermal Research* **184**, 63-78.

Vlastélic, I., Peltier, A. & Staudacher, T. (2007). Short-term (1998-2006) fluctuations of Pb isotopes at Piton de la Fournaise volcano (Réunion Island): Origins and constraints on the size and shape of the magma reservoir. *Chemical Geology* **244**, 202-220.

Vlastélic, I., Staudacher, T. & Semet, M. (2005). Rapid Change of Lava Composition from 1998 to 2002 at Piton de la Fournaise (Réunion) Inferred from Pb Isotopes and Trace Elements: Evidence for Variable Crustal Contamination. *Journal of Petrology* **46**, 79-107.

Vogt, P. R. (1972). Evidence for a global synchronism in mantle plume convection, and possible significance for geology. *Nature* **240**, 338-342.

Vonhof, H. B. & Smit, J. (1997). High-resolution late Maastrichtian-early Danian oceanic 87Sr/86Sr record: Implications for Cretaceous-Tertiary boundary events. *Geology* **25**, 347-350.

Walter, M. J. (1998). Melting of Garnet Peridotite and the Origin of Komatiite and Depleted Lithosphere. *Journal of Petrology* **39**, 29-60.

Walter, M. J. (2014). 3.10 - Melt Extraction and Compositional Variability in Mantle Lithosphere. *Treatise on Geochemistry (Second Edition)* **3**, 393-419.

Wan, Z., Coogan, L. A. & Canil, D. (2008). Experimental calibration of aluminium partitioning between olivine and spinel as a geothermometer. *American Mineralogist* **93**, 1142-1147.

Wang, Z. & Gaetani, G. A. (2008). Partitioning of Ni between olivine and siliceous eclogite partial melt: experimental constraints on the mantle source of Hawaiian basalts. *Contribution to Mineralogy and Petrology* **156**, 661-678.

Watson, S. & McKenzie, D. (1991). Melt Generation by Plumes - a Study of Hawaiian Volcanism. *Journal of Petrology* **32**, 501-537.

Weis, D., Garcia, M. O., Rhodes, J. M., Jellinek, A. M. & Scoates, J. S. (2011). Role of the deep mantle in generating the compositional asymetry of the Hawaiian mantle plume. *Nature Geoscience* **4**, 831-838.

White, R. & McKenzie, D. (1989). Magmatism at Rift Zones: The Generation of Volcanic Continental Margins and Flood Basalts. *Journal of Geophysical Research* **94**, 7685-7729.

White, R. S. & McKenzie, D. (1995). Mantle plumes and flood basalts. *Journal of Geophysical Research* **100**, 17543-17585.

White, R. V. (2002). Earth's biggest 'whodunnit': unravelling the clues in the case of the end-Permian mass extinction. *Philosophical Transactions of the Royal Society, London A* **360**, 2963-2985.

White, R. V. & Saunders, A. D. (2005). Volcanism, impact and mass extinctions: incredible or credible coincidences? *Lithos* **79**, 299-316.

White, W. M. & Klein, E. M. (2014). 4.13 Composition of the Oceanic Crust. *Treatise on Geochemistry (Second Edition)*, 457-496.

Widdowson, M., Pringle, M. S. & Fernandez, O. A. (2000). A Post K-T Boundary (Early Palaeocene) Age for Deccan-type Feeder Dykes, Goa, India. *Journal of Petrology* **41**, 1177-1194.

Widdowson, M., Walsh, J. N. & Subbarao, K. V. (1997). The geochemistry of Indian bole horizons: palaeoenvironmental implications of Deccan intravolcanic palaeo surfaces. *Geological Society, London, Special Publications* **120**, 269-281.

Wignall, P. B. (2001). Large igneous provinces and mass extinctions. *Earth Science Reviews* **53**, 1-33.

Wilf, P., Johnson, K. R. & Huber, B. T. (2003). Correlated terrestrial and marine evidence for global climate changes before mass extinction at the Cretaceous-Paleogene boundary. *Proceedings of the National Academy of Sciences, USA* **100**, 599-604.

Willenbring, J. K. & Blanckenburg, F. v. (2010). Long-term stability of global erosion rates and weathering during late-Cenozoic cooling. *Nature* **211-214**.

Wilson, J. T. (1963). A possible origin of the Hawaian Islands. *Canadian Journal of Physics* **41**, 863-870.

Wimpenny, J., Gannoun, A., Burton, K. W., Widdowson, M., James, R. H. & Gislason, S. R. (2007). Rhenium and osmium isotope and elemental behaviour accompanying laterite formation in the Deccan region of India. *Earth and Planetary Science Letters* **261**, 239-258.

Wolbach, W. S., Lewis, R. S. & Anders, E. (1985). Cretaceous Extinctions: Evidence for Wildfires and Search for Mateoritic Material. *Science* **230**, 167-170.

Wolfe, J. A. (1990). Palaeobotanical evidence for a temperature increase following the Cretaceous/Tertiary boundary. *Nature* **343**, 153-156.

Wolfe, J. A. & Upchurch-Jr, G. R. (1986). Vegetation, climatic and floral changes at the Cretaceous-Tertiary boundary. *Nature* **324**, 148-152.

Woolley, A. R. & Kjarsgaard, B. A. (2008). Carbonatite occurrences of the world: map and database: map and database. *Geological Survey of Canada, Open File 5796*.

Workman, R. K. & Hart, S. R. (2005). Major and trace element composition of the depleted MAROB mantle. *Earth and Planetary Science Letters* **231**, 53-72.

Yasuda, A., Fujii, T. & Kurita, K. (1994). Melting phase relations of an anhydrous mid-ocean ridge basalt from 3 to 20 GPa: Implications for the behavior of subducted oceanic crust in the mantle. *Journal of Geophysical Research* **99**, 9401-9414.

Yaxley, G. M. (2000). Experimental study of the phase and melting relations of homogeneous basalt + peridotite mixtures and implications for the petrogenesis of flood basalts. *Contribution to Mineralogy and Petrology* **139**, 326-338.

Yaxley, G. M. & Green, D. H. (1998). Reactions between eclogite and peridotite: mantle refertilisation by subduction of oceanic crust. *Schweizer Mineralogische und Petrographische Mitteilungen* **78**, 243-255.